IN VITRO FLUID DYNAMICS OF PROSTHETIC AORTIC HEART VALVES IN STEADY AND PULSATILE FLOW

Thesis by

Daniel Dale Hanle

In Partial Fulfillment of the Requirements

for the Degree of

Doctor of Philosophy

California Institute of Technology

Pasadena, California

1984

(Submitted November 28, 1983)

I dedicate this thesis to my wife,

Carolyn,

and to my parents,

Don and Dorothy Hanle.

ACKNOWLEDGEMENTS

The untimely death of Dr. William Harrison Corcoran does not allow me to express to him my deep gratitude for his genuine interest in my development as a student at the California Institute of Technology. Dr. Corcoran exemplified true professionalism and did so on a very consistent basis. He expected no less from his students. His many insights into the project reported on herein, his occasional "close the door . . ." exhortations, and his well-timed encouragement were beneficial beyond measure.

The close collaboration, interest, and encouragement of Dr. Earl C. Harrison of the Los Angeles County - University of Southern California Medical Center were greatly appreciated.

Discussions with Dr. Ajit Yoganathan, Dr. David Suobank, and Dr. L. Gary Leal were very helpful in the course of the work.

Expertise in fabricating the experimental apparatus was provided by Hollis Reamer, George Griffith, Seichi Nakawatase (Chic), Ray Reed, John Yehle, and Mike Nagy. Their innovative ideas were invaluable.

Thanks also go to the numerous undergraduate chemical engineering students, American Heart Association fellows, and high school students who helped with the project. Jeff Atherton, Lorna Anderson, Ed Lambert, Cheryl Robertson, Mike Grimmett, Costas Hamakiotes, Bill Marshall, and Monica Alexiu were especially helpful.

I would also like to express my gratitude to Donna Johnson for her consistently high-quality and cheerful administrative assistance throughout the project.

A very special thanks goes to my wife Carolyn for the innumerable hours she helped with this manuscript.

The funding for this project was provided by the Donald E. Baxter Foundation, the Children's Heart Foundation of Southern California and the American Heart Association, Los Angeles Affiliate. That support is gratefully acknowledged.

Shiley Laboratories, Sutter Biomedical, and St. Jude Medical, Inc. generously contributed the prostheses for this project.

ABSTRACT

Velocity measurements were made *in vitro* using a laser-Doppler anemometer downstream from prosthetic aortic heart valves with distinctly different designs. The valves studied were an Ionescu-Shiley tri-leaflet bioprosthesis, a Björk-Shiley convexo-concave tilting-disc prosthesis, a Smeloff caged-ball prosthesis, and a St. Jude bi-leaflet prosthesis. Velocity measurements were made in steady and in pulsatile flow using a Newtonian fluid with a viscosity of 0.001 kg/m·s. Velocity components in all three coordinate directions were measured at 305 locations distibuted systematically across a cross section of the flow system at an axial distance of 31.8 mm downstream from the valve mount. This systematic approach to the data acquisition allowed a detailed analysis of the disturbed flow fields generated by each of the four valves. Large shear stresses were estimated in the bulk flow which were potentially hemolytic and which could potentially activate platelet chemical-release reactions.

A well-controlled, comparative analysis of the steady-flow and pulsatile-flow velocity results revealed that measurements made in steady flow could be used to approximate the dynamics of pulsatile flow during the middle of the pulse cycle only. Shear stresses estimated for steady flow were found to be an upper bound on those estimated for pulsatile flow.

A comparison of the pressure-drop and regurgitant-flow characteristics of these four valves showed that there was a significant range in the hydrodynamic performance of these prostheses. The St. Jude prosthesis generated the lowest pressure drop among the four valves studied while the Smeloff prosthesis generated the largest. The St. Jude prosthesis also allowed the least amount of regurgitant flow of the three valve designs which, when closed, did not totally occlude their orifice for flow. Because it has a totally-occluding design, the

Ionescu-Shiley bioprosthesis allowed the least regurgitant flow of the valves studied. The Smeloff prosthesis allowed the largest amount of regurgitant flow of the valves studied.

TABLE OF CONTENTS

	ACKNOWLEDGEMENTS	iv
	ABSTRACT	vi
	TABLE OF CONTENTS	viii
	LIST OF ILLUSTRATIONS	xiii
	LIST OF TABLES	xx
	LIST OF SYMBOLS	xxii
Chapter 1	INTRODUCTION AND BACKGROUND	1
1.1	The Normal Aortic Valve	1
1.2	Aortic Valve Replacement	3
1.3	Complications of Aortic Valve Prostheses	5
1.3.1	Thrombus Formation	6
1.3.2	Intravascular Hemolysis	8
1.4	Engineering Considerations	16
1.5	Previous *In Vitro* Investigations	20
1.6	Goals and Approach of the Present Investigation	24
Chapter 2	APPARATUS AND METHODOLOGY	29
2.1	Flow Apparatus	29
2.1.1	Aortic-Valve Flow Section	29
2.1.2	Steady-Flow Loop	33
2.1.3	Pulsatile-Flow Loop	39
2.2	Aortic Prostheses Studied	44
2.2.1	Ionescu-Shiley Bioprosthesis	44
2.2.2	Björk-Shiley Convexo-Concave Prosthesis	48
2.2.3	Smeloff Prosthesis	48
2.2.4	St. Jude Prosthesis	49

2.3	Laser-Doppler Anemometer	49
2.3.1	Description of Apparatus	49
2.3.2	Operational Characteristics	54
2.3.3	Velocity Measurements	63
2.4	Computer Interface	69
2.4.1	Laboratory Hardware	69
2.4.2	Data Collection	74
2.4.3	Data Reduction	79
2.5	Preliminary Results	87
Chapter 3	EXPERIMENTAL RESULTS AND DISCUSSION	93
3.1	Experimental Uncertainties	93
3.2	Empty Aortic-Valve Flow Section	96
3.3	Ionescu-Shiley Bioprosthesis	101
3.3.1	Introduction	101
3.3.2	Methodology and Apparatus	103
3.3.3	Results	103
3.3.3.1	Pressure and Volumetric-Flow Results	103
3.3.3.2	Velocity Results	108
3.3.4	Discussion	139
3.3.4.1	Discussion of the Pressure and Volumetric-Flow Results	139
3.3.4.2	Discussion of the Velocity Results	147
3.3.4.3	Steady Versus Pulsatile Flow	161
3.3.5	Conclusions	173

3.4	Björk-Shiley Convexo-Concave Prosthesis	176
3.4.1	Introduction	176
3.4.2	Methodology and Apparatus	178
3.4.3	Results	178
3.4.3.1	Pressure and Volumetric-Flow Results	178
3.4.3.2	Velocity Results	178
3.4.4	Discussion	203
3.4.4.1	Discussion of the Pressure and Volumetric-Flow Results	203
3.4.4.2	Discussion of the Velocity Results	207
3.4.4.3	Steady Versus Pulsatile Flow	215
3.4.5	Conclusions	218
3.5	Smeloff Prosthesis	221
3.5.1	Introduction	221
3.5.2	Methodology and Apparatus	223
3.5.3	Results	223
3.5.3.1	Pressure and Volumetric-Flow Results	223
3.5.3.2	Velocity Results	223
3.5.4	Discussion	244
3.5.4.1	Discussion of the Pressure and Volumetric-Flow Results	244
3.5.4.2	Discussion of the Velocity Results	248
3.5.4.3	Steady Versus Pulsatile Flow	251
3.5.5	Conclusions	254

3.6	St. Jude Prosthesis	257
3.6.1	Introduction	257
3.6.2	Methodology and Apparatus	258
3.6.3	Results	258
3.6.3.1	Pressure and Volumetric-Flow Results	258
3.6.3.2	Velocity Results	263
3.6.4	Discussion	279
3.6.4.1	Discussion of the Pressure and Volumetric-Flow Results	279
3.6.4.2	Discussion of the Velocity Results	283
3.6.4.3	Steady Versus Pulsatile Flow	286
3.6.5	Conclusions	290
Chapter 4	VALVE COMPARISON STUDIES	292
4.1	Comparison of Pressure and Volumetric-Flow Results	292
4.1.1	Pressure-Drop Comparison	292
4.1.2	Flow-Rate Comparison	295
4.1.3	Hydraulic Performance Comparison	298
4.1.4	Regurgitant-Flow Comparison	304
4.2	Comparison of Velocity Results	309
4.2.1	Forward-Flow Results	309
4.2.2	Reverse-Flow Results	324
4.3	Comparative Shear-Stress Analysis	331

Chapter 5	SUMMARY AND RECOMMENDATIONS	340
5.1	Summary	340
5.2	Recommendations	343
	REFERENCES	347
	APPENDIX	A-1

LIST OF ILLUSTRATIONS

		Page
Figure 1.	Aortic-valve flow section depicted with an Ionescu-Shiley bioprosthesis mounted.	30
Figure 2.	Schematic of the steady-flow loop showing the location of the LDA laser beams for velocity measurements in the fully developed turbulent pipe flow.	34
Figure 3.	Schematic of the pulse-duplicator showing the location of the LDA laser beams for the pulsatile-flow studies.	40
Figure 4.	Aortic-pressure (AP), ventricular-pressure (VP), and volumetric-flow (VF) data for the Björk-Shiley convexo-concave (25 mm) prosthesis in the pulse-duplicator.	45
Figure 5a.	Prosthetic aortic heart valves used in the present investigation.	46
Figure 5b.	Prosthetic aortic heart valves used in the present investigation.	47
Figure 6.	Diagram of the laser-Doppler anemometer apparatus used for the present investigation.	51
Figure 7.	LDA laser beams crossing in a cylindrical flow channel for velocity-component measurements in the axial and non-axial directions.	64
Figure 8.	Detail of the aortic-valve flow section showing the location of the data plane.	67
Figure 9.	Index numbers for the grid points on the data plane.	68
Figure 10.	Diagram of the interface of the laboratory computer to the data collection equipment.	70
Figure 11a.	LDA data-ready signal leaving the tracker (left) and arriving at the computer (right) after passing through the 15-meter cable between the two apparatus.	73
Figure 11b.	"Enhanced" LDA data-ready signal leaving the "A/D Sync" electronic box (left) and arriving at the computer (right) after passing through the 15-meter cable between the two apparatus.	73
Figure 12.	Velocity, pressure, and volumetric-flow data from a pulsatile-flow experiment showing the raw data as one-second records.	77
Figure 13.	Mean axial velocities for fully developed turbulent pipe flow showing characteristic blunted flow profile.	88

Page

Figure 14. Mean axial velocities for fully developed turbulent pipe flow showing good agreement with 1/7-power law. 90

Figure 15. Mean non-axial velocities (top) and rms axial velocities (bottom) for fully developed turbulent pipe flow. 91

Figure 16. Comparison of mean axial velocities for fully developed turbulent pipe flow with those downstream from the empty aortic-valve flow section at z = 31.8 mm. 97

Figure 17. Comparison of the mean non-axial velocities (top) and rms axial velocities (bottom) for fully developed turbulent pipe flow with those downstream from the empty aortic-valve flow section z = 31.8 mm. 98

Figure 18. Idealized volumetric-flow curve showing temporal location of pulsatile-flow windows 6 through 25, 30, and 40 for the Ionescu-Shiley (25 mm) bioprosthesis. 109

Figure 19. Mean axial velocities in 3-D perspective for pulsatile-flow windows 6 through 23, 25, and 30 downstream from the Ionescu-Shiley (25 mm) bioprosthesis at z = 31.8 mm. 110

Figure 20. Mean axial velocities in 3-D perspective for steady flow and pulsatile-flow windows 8, 14, 18, and 21 downstream from the Ionescu-Shiley (25 mm) bioprosthesis at z = 31.8 mm. 112

Figure 21. Mean axial velocities in 3-D perspective for pulsatile-flow windows 25, 30, and 40 downstream from the Ionescu-Shiley (25 mm) bioprosthesis at z = 31.8 mm. 114

Figure 22. Mean axial velocities as contours for steady flow and pulsatile-flow windows 8, 14, and 18 downstream from the Ionescu-Shiley (25 mm) bioprosthesis at z = 31.8 mm. 115

Figure 23. Mean axial velocities as contours for pulsatile-flow windows 25, 30, and 40 downstream from the Ionescu-Shiley (25 mm) bioprosthesis at z = 31.8 mm. 118

Figure 24. Mean non-axial velocities as resultants for steady flow and for pulsatile-flow windows 8, 14, and 18 downstream from the Ionescu-Shiley (25 mm) bioprosthesis at z = 31.8 mm. 120

Figure 25. Mean non-axial velocities as resultants for pulsatile-flow windows 25, 30, and 40 downstream from the Ionescu-Shiley (25 mm) bioprosthesis at z = 31.8 mm. 122

Page

Figure 26. Root-mean-square (rms) axial velocities as contours for steady flow and pulsatile-flow windows 8, 14, and 18 downstream from the Ionescu-Shiley (25 mm) bioprosthesis at z = 31.8 mm. 124

Figure 27. Root-mean-square (rms) velocities in the axial (z) direction and non-axial (y and x) directions as contours for steady flow downstream from the Ionescu-Shiley (25 mm) bioprosthesis at z = 31.8 mm. 125

Figure 28. Comparison of mean axial velocities for data plane located at z = 31.8 mm with those for data plane located at z = 55.9 mm downstream from the Ionescu-Shiley (25 mm) bioprosthesis. 127

Figure 29. Comparison of the mean non-axial velocities (top) and rms axial velocities (bottom) for data plane located at z = 31.8 mm with those for data plane located at z = 55.9 mm downstream from the Ionescu-Shiley (25 mm) bioprosthesis. 128

Figure 30. Total estimated shear stresses, τ_{zx}, as contours for steady flow and for pulsatile-flow windows 8, 14, and 18 downstream from the Ionescu-Shiley (25 mm) bioprosthesis at z = 31.8 mm. 133

Figure 31. Total estimated shear stresses τ_{zx}, τ_{zy}, and τ_{xy}, for steady flow downstream from the Ionescu-Shiley (25 mm) bioprosthesis at z = 31.8 mm. 134

Figure 32. Volumetric-flow rate (top) and average rms velocity (bottom) calculated from the mean and rms velocities, respectively, at the data plane as a function of pulsatile-flow window number for the Ionescu-Shiley (25 mm) bioprosthesis. 135

Figure 33. Idealized volumetric-flow curve showing temporal location of pulsatile-flow windows 6 through 25, 30, and 40 for the Björk-Shiley convexo-concave (25 mm) prosthesis. 181

Figure 34. Mean axial velocities in 3-D perspective for pulsatile-flow windows 6 through 23, 25, and 30 downstream from the Björk-Shiley convexo-concave (25 mm) prosthesis at z = 31.8 mm. 182

Figure 35. Mean axial velocities in 3-D perspective for steady flow and pulsatile-flow windows 8, 13, 17, and 20 downstream from the Björk-Shiley convexo-concave (25 mm) prosthesis at z = 31.8 mm. 184

Figure 36. Mean axial velocities in 3-D perspective for pulsatile-flow windows 25, 30, and 40 downstream from the Björk-Shiley convexo-concave (25 mm) prosthesis at z = 31.8 mm. 186

Page

Figure 37. Mean axial velocities as contours for steady flow and pulsatile-flow windows 8, 13, and 17 downstream from the Björk-Shiley convexo-concave (25 mm) prosthesis at z = 31.8 mm. 187

Figure 38. Mean axial velocities as contours for pulsatile-flow windows 25, 30, and 40 downstream from the Björk-Shiley convexo-concave (25 mm) prosthesis at z = 31.8 mm. 190

Figure 39. Mean non-axial velocities as resultants for steady flow and for pulsatile-flow windows 8, 13, and 17 downstream from the Björk-Shiley convexo-concave (25 mm) prosthesis at z = 31.8 mm. 191

Figure 40. Mean non-axial velocities as resultants for pulsatile-flow windows 25, 30, and 40 downstream from the Björk-Shiley convexo-concave (25 mm) prosthesis at z = 31.8 mm. 194

Figure 41. Root-mean-square (rms) axial velocities as contours for steady flow and pulsatile-flow windows 8, 13, and 17 downstream from the Björk-Shiley convexo-concave (25 mm) prosthesis at z = 31.8 mm. 195

Figure 42. Total estimated shear stresses, τ_{zx}, as contours for steady flow and for pulsatile-flow windows 8, 13, and 17 downstream from the Björk-Shiley convexo-concave (25 mm) prosthesis at z = 31.8 mm. 197

Figure 43. Total estimated shear stresses, τ_{zy}, as contours for steady flow and for pulsatile-flow windows 8, 13, and 17 downstream from the Björk-Shiley convexo-concave (25 mm) prosthesis at z = 31.8 mm. 198

Figure 44. Volumetric-flow rate (top) and average rms velocity (bottom) calculated from the mean and rms velocities, respectively, at the data plane as a function of pulsatile-flow window number for the Björk-Shiley convexo-concave (25 mm) prosthesis. 200

Figure 45. Idealized volumetric-flow curve showing temporal location of pulsatile-flow windows 6 through 25, 30, and 40 for the Smeloff (24 mm) prosthesis. 226

Figure 46. Mean axial velocities in 3-D perspective for pulsatile-flow windows 6 through 23, 25, and 30 downstream from the Smeloff (24 mm) prosthesis at z = 31.8 mm. 228

Figure 47. Mean axial velocities in 3-D perspective for steady flow and pulsatile-flow windows 8, 13, 17, and 20 downstream from the Smeloff (24 mm) prosthesis at z = 31.8 mm. 229

Page

Figure 48. Mean axial velocities in 3-D perspective for pulsatile-flow windows 25, 30, and 40 downstream from the Smeloff (24 mm) prosthesis at z = 31.8 mm. 230

Figure 49. Mean axial velocities as contours for steady flow and pulsatile-flow windows 8, 13, and 17 downstream from the Smeloff (24 mm) prosthesis at z = 31.8 mm. 232

Figure 50. Mean axial velocities as contours for pulsatile-flow windows 25, 30, and 40 downstream from the Smeloff (24 mm) prosthesis at z = 31.8 mm. 234

Figure 51. Mean non-axial velocities as resultants for steady flow and for pulsatile-flow windows 8, 13, and 17 downstream from the Smeloff (24 mm) prosthesis at z = 31.8 mm. 235

Figure 52. Mean non-axial velocities as resultants for pulsatile-flow windows 25, 30, and 40 downstream from the Smeloff (24 mm) prosthesis at z = 31.8 mm. 237

Figure 53. Root-mean-square (rms) axial velocities as contours for steady flow and pulsatile-flow windows 8, 13, and 17 downstream from the Smeloff (24 mm) prosthesis at z = 31.8 mm. 238

Figure 54. Total estimated shear stresses, τ_{zx}, as contours for steady flow and for pulsatile-flow windows 8, 13, and 17 downstream from the Smeloff (24 mm) prosthesis at z = 31.8 mm. 240

Figure 55. Volumetric-flow rate (top) and average rms velocity (bottom) calculated from the mean and rms velocities, respectively, at the data plane as a function of pulsatile-flow window number for the Smeloff (24 mm) prosthesis. 241

Figure 56. Idealized volumetric-flow curve showing temporal location of pulsatile-flow windows 6 through 25, 30, and 40 for the St. Jude (25 mm) prosthesis. 262

Figure 57. Mean axial velocities in 3-D perspective for pulsatile-flow windows 6 through 23, 25, and 30 downstream from the St. Jude (25 mm) prosthesis at z = 31.8 mm. 263

Figure 58. Mean axial velocities in 3-D perspective for steady flow and pulsatile-flow windows 8, 13, 17, and 20 downstream from the St. Jude (25 mm) prosthesis at z = 31.8 mm. 264

Figure 59. Mean axial velocities in 3-D perspective for pulsatile-flow windows 25, 30, and 40 downstream from the St. Jude (25 mm) prosthesis at z = 31.8 mm. 266

		Page
Figure 60.	Mean axial velocities as contours for steady flow and pulsatile-flow windows 8, 13, and 17 downstream from the St. Jude (25 mm) prosthesis at z = 31.8 mm.	267
Figure 61.	Mean axial velocities as contours for pulsatile-flow windows 25, 30, and 40 downstream from the St. Jude (25 mm) prosthesis at z = 31.8 mm.	269
Figure 62.	Mean non-axial velocities as resultants for steady flow and for pulsatile-flow windows 8, 13, and 17 downstream from the St. Jude (25 mm) prosthesis at z = 31.8 mm.	271
Figure 63.	Mean non-axial velocities as resultants for pulsatile-flow windows 25, 30, and 40 downstream from the St. Jude (25 mm) prosthesis at z = 31.8 mm.	272
Figure 64.	Root-mean-square (rms) axial velocities as contours for steady flow and pulsatile-flow windows 8, 13, and 17 downstream from the St. Jude (25 mm) prosthesis at z = 31.8 mm.	274
Figure 65.	Total estimated shear stresses, τ_{zx}, as contours for steady flow and for pulsatile-flow windows 8, 13, and 17 downstream from the St. Jude (25 mm) prosthesis at z = 31.8 mm.	275
Figure 66.	Volumetric-flow rate (top) and average rms velocity (bottom) calculated from the mean and rms velocities, respectively, at the data plane as a function of pulsatile-flow window number for the St. Jude (25 mm) prosthesis.	277
Figure 67.	Prosthetic aortic heart valves used in the present investigation showing area available for regurgitant flow through the closed prostheses.	307
Figure 68.	Mean axial velocities for steady flow and during maximum forward flow for pulsatile flow downstream from the Ionescu-Shiley (25 mm) and Björk-Shiley convexo-concave (25 mm) prostheses at z = 31.8 mm.	310
Figure 69.	Mean axial velocities for steady flow and during maximum forward flow for pulsatile flow downstream from the Smeloff (24 mm) and St. Jude (25 mm) prostheses at z = 31.8 mm.	311
Figure 70.	Mean non-axial velocities for steady flow and during maximum forward flow for pulsatile flow downstream from the Ionescu-Shiley (25 mm) and Björk-Shiley convexo-concave (25 mm) prostheses at z = 31.8 mm.	315

Page

Figure 71. Mean non-axial velocities for steady flow and during maximum forward flow for pulsatile flow downstream from the Smeloff (24 mm) and St. Jude (25 mm) prostheses at z = 31.8 mm. 316

Figure 72. Root-mean-square (rms) axial velocities for steady flow and during maximum forward flow for pulsatile flow downstream from the Ionescu-Shiley (25 mm) and Björk-Shiley convexo-concave (25 mm) prostheses at z = 31.8 mm. 320

Figure 73. Root-mean-square (rms) axial velocities for steady flow and during maximum forward flow for pulsatile flow downstream from the Smeloff (24 mm) and St. Jude (25 mm) prostheses at z = 31.8 mm. 321

Figure 74. Mean axial velocities at z = 31.8 mm in 3-D perspective during maximum reverse flow for the four prostheses studied in the present investigation. 325

Figure 75. Mean axial velocities at z = 31.8 mm as contours during maximum reverse flow for the four prostheses studied in the present investigation. 326

Figure 76. Mean non-axial velocities at z = 31.8 mm as resultants during maximum reverse flow for the four prostheses studied in the present investigation. 328

Figure 77. Root-mean-square (rms) axial velocities at z = 31.8 mm as contours during maximum reverse flow for the four prostheses studied in the present investigation. 330

Figure 78. Total estimated shear stresses, τ_{zx}, for steady flow and during maximum forward flow for pulsatile flow downstream from the Ionescu-Shiley (25 mm) and Björk-Shiley convexo-concave (25 mm) prostheses at z = 31.8 mm. 332

Figure 79. Total estimated shear stresses, τ_{zx}, for steady flow and during maximum forward flow for pulsatile flow downstream from the Smeloff (24 mm) and St. Jude (25 mm) prostheses at z = 31.8 mm. 333

Figure A1. Mean axial velocities for steady flow downstream from the Ionescu-Shiley (25 mm) bioprosthesis at z = 31.8 mm. A-3

LIST OF TABLES

		Page
Table 1.	Tolerance of Platelets and Red Blood Cells to Fluid Shear Stress.	9
Table 2.	Standard Performance Settings for the Pulse-Duplicator.	43
Table 3.	Data Rejection Criteria for Pulsatile-Flow Experiments.	86
Table 4.	Parameters Computed from the Pressure Data for the Ionescu-Shiley (25 mm) Bioprosthesis.	104
Table 5.	Parameters Computed from the Volumetric-Flow Data for the Ionescu-Shiley (25 mm) Bioprosthesis.	106
Table 6.	Parameters Computed from the Pressure Data for the Björk-Shiley Convexo-Concave (25 mm) Prosthesis.	179
Table 7.	Parameters Computed from the Volumetric-Flow Data for the Björk-Shiley Convexo-Concave (25 mm) Prosthesis.	180
Table 8.	Parameters Computed from the Pressure Data for the Smeloff (24 mm) Prosthesis.	224
Table 9.	Parameters Computed from the Volumetric-Flow Data for the Smeloff (24 mm) Prosthesis.	225
Table 10.	Parameters Computed from the Pressure Data for the St. Jude (25 mm) Prosthesis.	259
Table 11.	Parameters Computed from the Volumetric-Flow Data for the St. Jude (25 mm) Prosthesis.	260
Table 12.	Comparison of Pressure-Drop Results for the Four Prosthetic Aortic Heart Valves Studied in the Present Investigation.	293
Table 13.	Comparison of Flow-Rate Results for the Four Prosthetic Aortic Heart Valves Studied in the Present Investigation.	296
Table 14.	Comparison of the Effective Orifice Areas and Performance Indices in Steady Flow for the Four Prosthetic Aortic Heart Valves Studied in the Present Investigation.	301
Table 15.	Comparison of the Effective Orifice Areas and Performance Indices in Pulsatile Flow for the Four Prosthetic Aortic Heart Valves Studied in the Present Investigation.	303
Table 16.	Comparison of Regurgitant-Flow Results for the Four Prosthetic Aortic Heart Valves Studied in the Present Investigation.	305

Page

Table 17. Comparison of the Maximum Acceleration of the Fluid through the Four Prosthetic Aortic Heart Valves Studied in the Present Investigation. 314

Table 18. Comparison of the Magnitude of the Secondary-Flow Structure Generated Downstream from the Four Prosthetic Aortic Heart Valves Studied in the Present Investigation. 319

Table 19. Comparison of the Magnitude of the Fluctuating Velocities Generated Downstream from the Four Prosthetic Aortic Heart Valves Studied in the Present Investigation. 323

Table 20. Comparison of the Magnitude of the Estimated Total Shear Stresses, τ_{zx}, Generated Downstream from the Four Prosthetic Aortic Heart Valves Studied in the Present Investigation. 335

Table A1. Mean Axial Velocities at z = 31.8 mm for the Ionescu-Shiley (25 mm) Bioprosthesis in Steady Flow. A-2

LIST OF SYMBOLS

A	Cross-sectional area of the modeled ascending aorta (m^2)
A_1	Area available for flow upstream from a pipe expansion (m^2)
A_2	Area available for flow downstream from a pipe expansion (m^2)
$\overline{AP}$	Mean aortic pressure (kPa)
C	Constant in Equation (12) ($kPa \cdot s^2/m^6$)
E_f	Rate at which mechanical energy is irreversibly converted to thermal energy per unit mass (m^2/s^2)
$E_{f,se}$	Rate at which mechanical energy is irreversibly converted to thermal energy per unit mass at a sudden expansion in a pipe (m^2/s^2)
g	Gravitational constant (m/s^2)
h_i	Height of the flow section at station i (m)
k_c	Correlation coefficient used in Equation (7)
K_{tot}	Total kinetic energy per unit mass (m^2/s)
$\overline{KE}$	Average kinetic energy ($kg \cdot m^2/s$)
L	Distance between pressure taps (m)
P	Fluid pressure (kPa)
p_i	Fluid pressure in the flow section at station i (kPa)
P_{x1}	Pressure at the earlier crossing of the aortic and ventricular pressure curves during the cycle (kPa)
P_{x2}	Pressure at the later crossing of the aortic and ventricular pressure curves during the cycle (kPa)
Q	Volumetric-flow rate (L/min)
$\overline{Q}$	Mean volumetric-flow rate for steady flow (L/min)
$\overline{Q^2}$	Mean-square volumetric-flow rate during systole (L/min)
Q_C	Volumetric-flow rate associated with the closure-flow phase (L/min)
Q_F	Volumetric-flow rate associated with the forward-flow phase (L/min)
Q_L	Volumetric-flow rate associated with the leakage-flow phase (L/min)

Q_{max}	Maximum volumetric-flow rate for pulsatile flow (L/min)
Q_{min}	Minimum volumetric-flow rate for pulsatile flow (L/min)
Q_{rms}	Root-mean-square volumetric-flow rate during systole (L/min)
t	Time (s)
T	Total time of data interval for LDA measurements (s)
u	Velocity component (cm/s)
u'	Fluctuating velocity component (cm/s)
u_1	Mean velocity across the pipe upstream from a pipe expansion (cm/s)
u_{rms}	Root-mean-square of the velocity component u (cm/s)
v	Velocity component (cm/s)
$\bar{v}$	Average velocity across the flow section (cm/s)
$\tilde{v}$	Statistical contribution of an imposed wave function to the instantaneous velocity (cm/s)
v'	Fluctuating velocity component (cm/s)
$\overline{v'^2}$	Mean-square of the fluctuating velocity across the flow section (cm/s)
v_i	Velocity of ith LDA measurement in data interval (cm/s)
$\bar{v}_i$	Average velocity across the flow section at station i (cm/s)
v_{rms}	Root-mean-square of the velocity component v (cm/s)
$< v >$	True mean of the velocity (cm/s)
$< v >_{PA}$	Phase-averaged mean of the velocity (cm/s)
$< v >_{TA}$	Time-averaged mean of the velocity (cm/s)
VP_{max}	Maximum ventricular pressure (kPa)
α	Ratio of cross-sectional area of orifice to that of flow section.
δt_i	Time between successive LDA velocity measurements (s)
ΔP	Pressure drop in flowing system (kPa)
$\overline{\Delta P}$	Mean pressure drop for steady flow (kPa)
ΔP_{max}	Maximum pressure drop for pulsatile flow (kPa)

$\overline{\Delta P}_{dias}$	Mean diastolic pressure drop (kPa)
$\overline{\Delta P}_{sys}$	Mean systolic pressure drop (kPa)
μ	Fluid viscosity (kg/m·s)
Φ_{tot}	Total potential energy per unit mass (m^2/s)
ρ	Fluid density (kg/m^3)
τ_{ij}^{lam}	Laminar shear stress for the velocity component in the i direction relative to the j direction (N/m^2)
τ_{ij}^{turb}	Turbulent (Reynolds) shear stress for velocity components in the i and j directions (N/m^2)

1. INTRODUCTION AND BACKGROUND

1.1 THE NORMAL AORTIC VALVE

The function of the healthy aortic valve is extremely efficient. It is a one-way check valve which produces little resistance to forward flow, requires negligible retrograde flow to close, and does not leak once it is closed. The natural aortic valve consists of three equal-sized, non-muscular cusps which are only about one-tenth of a millimeter thick (Bellhouse and Talbot, 1969). These three cusps, or leaflets, which are very flexible in the axial direction, form the occluding mechanism for the valve. In response to forward flow, they open into the aortic root and move almost entirely out of the valve orifice in a "hinge-like" fashion thus producing little resistance to the flow (Bellhouse, 1969; Bellhouse and Talbot, 1969; van Steenhoven and van Dongen, 1979; van Steenhoven, et al., 1982). Thus, as Yellin and Peskin (1975) note, the pressure drop across the healthy aortic valve is very small and due mainly to the inertia of the fluid. There are three permanent dilatations of the aorta called sinuses. These sinuses are located in the wall of the aortic root just downstream from the base of the valve. Each of the three leaflets opens into its corresponding sinus during forward flow and thereby avoids contact with the wall of the aorta. When the forward flow decelerates, *but before it reverses*, these leaflets begin to move away from their respective sinuses and back towards their closed position. This interesting phenomenon has been investigated and appears to be related to the fluid-dynamic interaction of the opened leaflets with the sinus geometry of the aortic root (Bellhouse, 1969; Bellhouse and Talbot, 1969; Swanson, et al., 1978; van Steenhoven and van Dongen, 1979). Alternatively, it is thought that valve closure could be initiated by the deceleration of the forward flow, as a manifestation of the so-called "breaking of the jet" phenomenon (Talukder, et al., 1977; Lee and Talbot, 1979). As Peskin (1982) has concluded after

extensively reviewing the current theories, the question of the leaflet-closure mechanism has not yet been resolved. Whatever the mechanism, very little retrograde flow is needed to complete the valve closure process. Once closed the leaflets effectively seal the valve orifice and allow no leakage flow. In addition to the above, and perhaps just as important, the forward flow that passes through the valve remains relatively undisturbed and centrally oriented in the ascending aorta. In this fashion, almost three million liters of blood per year are pumped during the systolic or contraction phase of the cardiac cycle through the opened aortic valve, during which time it opens and closes approximately forty million times.

Both congenital and acquired heart-valve disease can seriously compromise the smooth and competent functioning of the natural aortic valve. Some common causes of acquired aortic valve disease are rheumatic fever, bacterial or fungal infection, arteriosclerotic changes, connective-tissue disorders, severe hypertension, and syphilis (Roschke, 1973; Yoganathan, 1978; Figliola, 1979). Unchecked, the valve damage produced by these diseases can be fatal. A diseased and thereby defective valve generally becomes either stenotic, or regurgitant, or both (Wright, 1972b). Aortic stenosis is an effective narrowing of the valve orifice which results in an increased resistance to blood flow by increasing the pressure difference across the valve during the systolic phase of the cardiac cycle. Aortic regurgitation occurs if the aortic valve fails to close completely during the diastolic or relaxation phase. In either case the work load on the heart is increased; with stenosis the heart must work to overcome the increased pressure difference; with regurgitation it must work to "re-pump" the regurgitated flow.

When dysfunction of the aortic valve has progressed to a stage where adverse symptoms are provoked by less than normal daily activities, surgical

intervention is often indicated (Bonchek, 1981). Such patients belong to class III or IV of the New York Heart Association (NYHA) classification of organic heart disease (Casci, et al., 1977). At surgery, the diseased valve can seldom be repaired (Bonchek, 1981). Thus surgical treatment is generally limited to excision of the diseased valve and implantation of a prosthesis.

1.2 AORTIC VALVE REPLACEMENT

Replacement of a severely damaged aortic valve usually produces a marked improvement in both life expectancy and the quality of the patient's life. Life expectancy is commonly measured using an actuarial method (Bodnar, et al., 1982). This method calculates the percentage possibility of patient survival following implantation (Anderson, et al., 1974; Grunkemeier, et al., 1975; Grunkemeier and Starr, 1977; Rahimtoola, 1983). For prostheses currently being implanted the survival rate at five years has generally been reported as 75% to 85% (Bonchek and Starr, 1975; Lee, et al., 1975; Ionescu, et al., 1977; Ionescu, et al., 1982; McHenry, et al., 1978; Björk and Henze, 1979; Levang, et al., 1979; Dale, et al., 1980; Starr, et al., 1980; Karp, et al., 1981; Gonzalez-Lavin, et al., 1983). Somewhat lower rates of 65% to 75% have been reported when early operative mortality was included (Lee, et al., 1975; Dale, et al., 1980). Early mortality is defined as that which occurs within 30 days of the surgical procedure and is currently about 5% for single valve replacement (Rahimtoola, 1983). Recently Bodnar, et al. (1982) have suggested that the percentage values calculated above from the actuarial analyses do not fairly evaluate implant performance unless non-valve related deaths are excluded. The survival rate of unoperated patients can be quite variable depending upon the cardiac valve disease etiology (Schwarz, et al., 1982). Survival rates have been reported as low as 20% at two years for patients for whom surgical

intervention was indicated but was *not* performed (Schwarz, et al., 1982). The quality of life has been measured using the NYHA classifications of organic heart disease. These classifications range from I for slight disease to IV for very severe disease (Casci, et al., 1977). Several investigators have classified valve recipients both before and after surgery (Sarma, et al., 1977; Ionescu, et al., 1977; Ionescu, et al., 1982; McHenry, et al., 1978; Emery, et al., 1979; Dale, et al., 1980; Starr, et al., 1980; Chaux, et al., 1981; Karp, et al., 1981; Gonzalez-Lavin, et al., 1983). They have consistently reported that the functional classification of patients has improved by one and often two classes following surgery. Thus treatment of advanced cardiac valve disease by valve replacement has proven very successful.

Because of this success, over half a million prosthetic valves have been implanted since the first caged-ball valves were placed in the aortic and mitral positions in 1960 (Schoen, et al., 1982). Choosing a prosthesis for implantation, though, is generally not a simple matter. There have been approximately fifty different prostheses made available to the surgeon since the early 1960's (Roberts, 1976). Many of these have been subsequently discarded due to lack of success. Those valves in current use have in most cases undergone several modifications. The aortic prostheses currently in use can be categorized as i) central-flow valves, ii) semi-central flow valves, and iii) lateral-flow valves. *Central-flow valves* have occluding mechanisms which are modeled after that of the natural valve and include stented homografts, autografts, and heterografts. The central-flow valves are also known as the "bioprosthetic" valves in reference to the materials of their construction (Wallace, 1975). *Semi-central flow valves* have occluding mechanisms which divide the forward flow into unequal, non-axisymmetric portions. This category includes tilting-disc and pivoting-disc valves. *Lateral-flow valves* have occluding mechanisms which produce an annular-type flow around a centrally located poppet. This third category

includes caged-ball and caged-disc valves. The valves in these latter two categories are collectively known as the "mechanical" valves to distinguish them from the "bioprosthetic" valves of the first category. Historically, a variety of other prosthesis designs have been proposed with occluding mechanisms both similar and quite different from those mentioned here. These other valves were either never implanted or implanted in very small numbers because of limited success. Non-stented homografts have had a measure of success and popularity through the years (Ross, 1982) but are not included here since they are used so infrequently.

1.3 COMPLICATIONS OF AORTIC VALVE PROSTHESES

The wide variety of valve designs currently available attests to the fact that an ideal heart-valve substitute has not yet been developed. Despite numerous designs and modifications of those designs over the last quarter century, the problems associated with the use of aortic prostheses *in vivo* have not all been eliminated. There remains a significant fraction of prosthesis recipients in whom debilitating or fatal complications develop subsequent to surgery. The most serious complications are (Herr, et al., 1965; McHenry, et al., 1968; Yoganathan, 1978; Figliola, 1979; Hwang, et al., 1983; Silver and Wilson, 1983): thrombus formation, hemolysis associated with the damage of red blood cells (RBCs), material failure, infection, valve dehiscence, and patient/prosthesis mismatch. Many of these complications have been traced upon autopsy or explantation to the inefficiency of the prosthetic valves to replicate faithfully the efficient hemodynamic function of the healthy, natural aortic valve. In particular the problems of thrombus formation and hemolysis appear to be related to the dynamics of the flow through the prosthetic valve. As such, extensive medical and engineering research both *in vivo* and *in vitro* has been

reported on the nature of these flows in the last twenty years. In these investigations specific efforts have been made to try to understand so as to ultimately prevent the contrary dynamic mechanisms underlying these flow-related problems. Until these problems are solved, the development of an "ideal" aortic valve replacement will not be forthcoming.

1.3.1 Thrombus Formation

Prosthesis-induced formation of thrombus is probably the most serious complication of heart-valve replacement. Schoen, et al. (1982) state that thrombotic complications of prosthetic implants are a "major cause of morbidity and mortality" and "represent the most important individual prosthesis-related factor limiting the long-term success" of the replacement of cardiac valves. Thrombus formation on the superstructure of prosthetic valves has been reported by numerous investigators (Davila, et al., 1963; Cokkinos, et al., 1971; Bozer and Karamehmetoglu, 1972; Ben-Zvi, et al., 1974; Björk and Henze, 1975; Fernandez, et al., 1976; Roberts, 1976; Dale, 1977; Yoganathan, 1978; Yoganathan, et al., 1978a; Yoganathan, et al., 1981; Chaux, et al., 1979; Edmiston, et al., 1979; Shulman, et al., 1979; Venkataraman, et al., 1980). This thrombus can become extensive and lead to persistent and massive embolic events as well as interfere with the mechanical function of the prosthesis (Friedli, et al., 1971; Roberts, 1976; Kloster, 1979). Furthermore, as Silver and Wilson (1983) note, clinically significant thrombus formation can take place soon after implant or at any time subsequently.

Thrombotic complications are common to all valves currently implanted (Silver and Wilson, 1983). The incidence of thromboembolism for mechanical aortic prostheses currently in use is about 2% to 3% per patient year with careful anticoagulation therapy (Kloster, 1979). Unanticoagulated bioprosthetic

aortic valve recipients may have similar thromboembolic rates but are free from the risks associated with long term anticoagulant therapy (Silver and Wilson, 1983). This apparent freedom from anticoagulants for patients with implanted bioprosthetic valves was cause for early enthusiasm for these designs (Whalen and Keiser, 1977; Frater, et al., 1979). Unfortunately patients with tissue valves in the mitral position are not as free from thromboembolic complications as had been initially hoped. (Chaux, et al., 1979; Edmiston, et al., 1979; Gray, et al., 1979). Thus, to date, a patient who undergoes valve replacement with any type of prosthesis is not free from the prospect of associated thromboembolic complications.

Although the initiation and propagation of thrombus on these prostheses are not entirely understood (Wright, 1972a), it is generally recognized that certain flow structures can contribute to thrombogenesis. Leonard (1972) outlined several basic flow patterns which have been observed to be thrombogenetic, including stagnation and separated flows. Prosthetic surfaces near stagnant zones and flow separation regions have been shown to have increased susceptibility to thrombus formation (Dutton, et al., 1968; Petschek, et al., 1968; Madras, et al., 1971; Yoganathan, 1978; Yoganathan, et al., 1978a; Yoganathan, et al., 1981; Shulman, et al., 1979; Lindsay, et al., 1980). This flow-structure dependence of the formation of thrombus appears to be related in large part to the thrombogenetic role of the platelet, a formed element of the blood. After becoming "activated" by membrane damage, platelets can deposit on a surface (Dutton, et al., 1968) and begin a three-step process of adherence, aggregation, and chemical release which can ultimately result in thrombus formation (Sixma and Wester, 1977; Lindsay, et al., 1980; Schoen, et al., 1982). Current evidence suggests that platelets can be activated by mechanical forces. Both the forces associated with the platelet impacting on a foreign surface (Johnston,

et al., 1975; Bernstein, 1976; Bernstein, et al., 1977; Whicher, et al., 1980) and the forces associated with platelet interaction with elevated fluid shear stresses (Brown, et al., 1975a; Brown, et al., 1975b; Hung, et al., 1976; Colantuoni, et al, 1977; Turitto and Baumgartner, 1978; Ramstack, et al., 1979) can apparently result in platelet activation. Table 1 shows the results of investigations of the tolerance of platelets to fluid shear stresses. Although extremely high shear stresses were required to damage platelets structurally, very low shear stresses were required to activate the platelets causing them to release acid phosphatase, lactic dehydrogenase, and serotonin. Once released, these chemicals accelerate the thrombogenetic processes. Thus flow structures which bring the platelet into contact with a prosthetic surface or which subject the platelet to high shear stresses, or both, can be thrombogenetic. Recirculating flow structures near surfaces can aggravate this problem. They provide regions in the flow wherein platelets may experience high shear stresses for lengthened residence times. Also they can allow damaged platelets to come into contact repeatedly with nearby surfaces.

1.3.2 Intravascular Hemolysis

Intravascular hemolysis, like thromboembolism, occurs in most patients with mechanical prostheses and is reported for all commonly used prosthetic valve designs (Kloster, 1979). Most investigators have found that in the absence of paravalvular leakage around the valve base-ring, chronic intravascular hemolysis is generally mild (Brodeur, et al., 1965; Herr, et al., 1965; McHenry, et al., 1968; Walsh, et al., 1969; Roeser, et al., 1970; Eyster, et al., 1971; Crexells, et al., 1972; Henze and Fortune, 1974; Slater, et al., 1974; Sallam, et al., 1976; Santinga, et al., 1976; Dale and Myhre, 1978; Falk, et al., 1979; Levang, 1979; Febres-Roman, et al., 1980). Hemolytic anemia occurs when the magnitude of

Table 1

Tolerance of Platelets and Red Blood Cells
to Fluid Shear Stress

Investigations and Results	Shear Stress (N/m^2)	Order of Magnitude of Exposure Time (seconds)	Experimental Apparatus
Platelets:			
BROWN, et al. (1975)			concentric
acid phosphatase release	15	10^2	cylinder
HUNG, et al. (1976)			concentric
lactic dehydrogenase release	16	10^2	cylinder
COLANTUONI, et al. (1977)			
serotonin release	700	10^{-3}	capillary
lowered count	1500	10^{-3}	
BERNSTEIN, et al. (1977)			turbulent
structural damage	10000	10^{-3}	jet
Red Blood Cells:			
SUTERA, et al. (1975)			
loss of biconcavity	50	10^2	concentric
prolate ellipsoid	150	10^2	cylinder
fragmentation	250	10^2	
NEVARIL, et al. (1968)			
morphological changes	150	10^2	concentric
hemolysis	300	10^2	cylinder
LEVERETT, et al. (1972)			concentric
hemolysis	150	10^2	cylinder
ROONEY (1970)			oscillating
hemolysis	450	10^{-3}	bubble
SALLAM and HWANG (1983)			turbulent
hemolysis	400	10^{-4}	jet
WILLIAMS (1970)			oscillating
hemolysis	560	10^{-4}	wire
INDEGLIA, et al. (1968)			turbulent
hemolysis	4000	10^{-5}	jet
BLACKSHEAR (1972)			turbulent
hemolysis	4000	10^{-5}	jet

hemolysis outstrips the ability of the body to replace the RBCs. As Kloster (1979) points out, though, compensated hemolysis is much more common than clinically significant hemolytic anemia. The incidence of anemia varies from 5% to 15% depending upon the design of the implanted prosthesis. Thus hemolysis associated with prosthetic valves is, as Silver and Wilson (1983) state, usually mild, rarely causes anemia, and if it does is likely to be caused by iron or folate deficiency. Therefore hemolytic disease caused by prosthetic valves can usually be managed effectively using oral iron and folate therapy.

Compensated hemolysis is not, however, as innocuous as it might seem. Most importantly, hemolysis may play a role in thrombogenesis (Stormorken, 1971; Casci, et al., 1977; Figliola and Mueller, 1977). When RBCs are hemolyzed they release both adenosine diphosphate (ADP) and a clot-promoting factor called erythrocytin (Gaarder, et al., 1961; Stormorken, 1971). These substances promote platelet adhesion and aggregation which can ultimately result in thrombus formation. ADP, in particular, is an extremely powerful platelet-aggregating agent. Gaarder, et al. (1961) found that less than one micromolar ADP caused rapid and marked aggregation of platelets. Thus, once RBCs have been damaged to the extent that they release ADP, thrombogenesis can cascade through the aggregation step. Stagnant or recirculating zones in the flow can be detrimental if they aggravate the situation by elevating the ADP concentration within them due to lack of mixing with the main flow. Secondarily, mild prosthesis-generated hemolysis may also contribute to the formation of gallstones (cholelithiasis). Merendino and Manhas (1973) and Harrison, et al. (1978) have noted that cholelithiasis can be a frequent complication of heart valve replacement. These investigators have attributed this complication to the increased hemolysis level present in prosthetic valve recipients.

Although prosthesis-related hemolysis has been attributed to the occluding mechanism crushing RBCs (Wright, 1972a; Nworgu, et al., 1979; Silver and Wilson, 1983), the elevated fluid shear stresses associated with these prostheses are probably more important (Nevaril, et al., 1969; Hellums and Brown, 1977). RBC damage which is induced by shear stresses both in bulk flows and near prosthetic surfaces has thus been the subject of numerous investigations over the last ten or fifteen years. The findings of some of these investigations are given in Table 1 along with the work with platelets mentioned earlier. The results of these studies seem to indicate that hemolysis will result when RBCs are exposed to bulk shear stresses above a threshold value of 150 to 300 newtons per square meter (N/m^2) for longer than two to four minutes (Nevaril, et al., 1968; Nevaril, et al., 1969; Leverett, et al., 1972; Sutera, et al., 1972; Sutera and Mehrjardi, 1975; Hellums and Brown, 1977). For shorter exposure times, higher shear stresses are required for hemolysis (Blackshear, et al., 1965; Blackshear, 1972; Bernstein, et al., 1967; Indeglia, et al., 1968; Rooney, 1970; Williams, et al., 1970; Sallam and Hwang, 1983).

Blackshear, et al. (1965) have investigated the effects of several fluid mechanical factors which may influence hemolysis. Among these factors were pressure, pressure fluctuations, shear stress, and turbulence. These investigators concluded that the RBC could withstand large positive pressure excursions and only occasionally succumbed to large negative pressures. It would seem, therefore, as Blackshear concluded later (Blackshear, 1972) in a review of the state of the art, that pressure-related factors "can be rejected as not contributing to hemolysis" and that "factors that are presently in dispute" as causing hemolysis "are turbulent shear stress and laminar shear stress."

A common methodology for assessing RBC damage *in vivo* has been to tag cells with a radioactive label and measure the RBC life span (Brodeur,

et al., 1965; Herr, et al., 1965; McHenry, et al., 1968; Walsh, et al., 1969; Roeser, et al., 1970). The random-labeling technique of tagging RBCs with ^{51}Cr (Gehrman, et al., 1966) has been the most useful (Wintrobe, et al., 1981). This technique requires the radioactive tagging of the RBCs in a small volume of blood which is then introduced into the subject. The subject can be either the original donor or another with well-characterized cardiovascular health. The activity from the chromium is then followed as a function of time and the time-history of that small blood volume is determined. RBC life span is determined as that time required for the complete disappearance of the activity. Nevaril and coworkers (Nevaril, et al., 1968; Nevaril, et al., 1969) have used this technique to study the gross effects of shear on rabbit RBCs. They sheared blood removed from rabbit donors and subsequently reintroduced the traumatized blood back into the animals. RBC life spans *in vivo* were significantly reduced and correlated qualitatively with observations of the traumatized cells.

Another aspect of RBC damage induced by shear stresses, and possibly a more important one, is that significant morphological changes of the RBC can occur at lower shear stresses than those generally considered hemolytic (Nevaril, et al., 1969; Hellums and Brown, 1977). As Wright (1972a) states, the main effect of blood trauma in patients is probably reduced cell life due to sublethal damage rather than outright cell rupture. From their radioactive-labeling experiments, Nevaril and coworkers (Nevaril, et al., 1968; Nevaril, et al., 1969) reported that morphologically altered cells were rapidly removed from the circulation by the spleen and liver. Using an electron microscope, Sutera and Mehrjardi (1975) have shown various levels of sublethal RBC damage for a range of shear stresses. The exposure time was four minutes in a concentric cylinder device. At shear stresses as low as 50 N/m^2 they observed

that RBCs suffered loss of their biconcavity; at 150 N/m^2 the RBCs assumed a prolate ellipsoid shape. In their work the RBCs were "frozen" by glutaraldehyde fixation while suspended in the viscometric flow. An interesting facet of the work of Sutera and Mehrjardi (1975), therefore, as Hellums and Brown (1977) noted, is that it seems to indicate that shear effects are probably of greater importance in viscometric studies than wall effects, as was previously debated (Blackshear, et al., 1965; Blackshear, 1972; Hochmuth, et al., 1972).

Turbulence generated by an implanted prosthesis can be an additional source of sufficient forces *in vivo* to adversely affect the success of the implant. In fact, Stein, et al. (1982) have noted that the largest contribution to potentially detrimental shear stresses is probably from turbulent, or Reynolds, stresses in the highly disturbed flow generated by diseased or prosthetic valves. The shear stresses in turbulent flow are generally much greater than for laminar flow (Schlichting, 1968) and therefore can be considered more apt to damage both RBCs and platelets. Silver and Wilson (1983) state that all prostheses cause intravascular hemolysis because of turbulence. Other investigations have also indicated that turbulence-induced hemolysis can be a problem with current prosthetic valve designs (Stein and Sabbah, 1976; Stein, et al., 1982; Schoen, et al., 1982). Turbulent flow may, in addition, contribute to thrombus formation (Davila, et al., 1963; Smith, et al., 1972; Stein and Sabbah, 1974; Stein and Sabbah, 1976). As Stein, et al. (1982) state, the high shear stresses inherent in turbulent flow may have a direct effect upon platelets. Platelets so activated can then initiate thrombogenesis. Moreover, as discussed earlier, sub-lethally damaged RBCs can also affect platelet aggregation and thereby induce thrombosis.

Recently, Sallam and Hwang (1983) have addressed the question of the efficacy of Reynolds stresses in causing hemolysis. These investigators have

characterized the shear-stress field generated by a turbulent jet. They found a threshold shear for hemolysis of about 400 N/m^2, as shown in Table 1. This threshold value was comparable to the results of previous investigations (Nevaril, et al., 1968; Leverett, et al., 1972; Rooney (1970); Williams, et al., 1970) wherein laminar shear stresses were implicated in causing hemolysis. The result of Sallam and Hwang was, however, an order of magnitude less than that found previously by others using a turbulent jet (Indeglia, et al. 1968; Blackshear, 1972). Thus elevated Reynolds stresses appear to be as effective in causing hemolysis as elevated laminar stresses.

The simple fact that blood circulates may also be a factor in prosthesis-related damage of RBCs. The mean flow rate of blood for a 70-kilogram man is about 5.0 liters per minute and his total blood volume averages 4.4 liters (Wintrobe, et al., 1981). Thus, assuming sufficient mixing, an RBC makes a circuit of the cardiovascular system about once a minute. After being produced in the bone marrow, the healthy RBC has a life span of approximately 120 days before it is scavenged by the reticuloendothelium system. Hence, an RBC which lived a normal life span would encounter an implanted prosthesis about 170,000 times. The duration of each encounter would depend upon the average velocity of the flow through the valve, the profile height of the prosthesis, and the extent to which the flow through the valve disturbed the flow downstream from it. The average velocity through the valve is on the order of 100 cm/s during the forward-flow phase. Average profile heights plus the length of the significantly disturbed flow field range from about one to up to three or more centimeters. Using the conservative value of one centimeter gives an encounter duration of about ten milliseconds. The RBC above would then spend around 1700 seconds (28 minutes) of its life encountering the prosthesis. Thus the relatively short duration of a single encounter can accumulate into a significant exposure time.

Questions arise at this point, however, regarding reversibility of damage and fatigue. Lacking a nucleus and the organelles that make protein synthesis possible, the RBC is incapable of self-repair (Wintrobe, et al., 1981). Damage to the RBC is therefore cumulative. Mechanical forces which induce irreversible changes in the RBC membrane may eventually become destructive even when these forces are not of significant magnitude to cause lysis during a single encounter. The frequency of these encounters, moreover, suggests that fatigue failure of the RBC membrane due to cyclic forces may also be a factor. Several studies indicate that, though the RBC membrane can apparently withstand extremely large bending strain without suffering significant irreversible changes (Rand and Burton, 1964; Fung and Tong, 1968; Hoeber and Hochmuth, 1970; Hochmuth and Mohandas, 1972; Hochmuth, et al., 1972; Hochmuth, et al., 1973; Evans, 1973; Hung, et al., 1978), tangential stresses that result in an area increase can cause drastic changes in the membrane. None of these studies, however, has given any results for reoccurring, cyclic forces on the RBC membrane. Thus it remains unclear how repeated trauma is withstood by the RBC membrane for the magnitudes and frequencies found for blood circulating past a prosthetic valve.

Although the magnitude of the shear stresses discussed above are probably greater than those found in healthy individuals, this has not been the case for patients with implanted aortic valve prostheses. *In vitro* studies have consistently shown that the natural valve is associated with lower fluid-flow induced stresses than diseased or prosthetic valves (Love, et al., 1971; Stein and Sabbah, 1976; Hwang, 1977; Schramm, et al., 1980; Schramm, et al., 1982). Furthermore, the stresses which occur *in vivo* are probably of the same order of magnitude as those found in *in vitro* studies, as Stein, et al. (1982) concluded after studying the fluid-flow induced stresses both *in vitro* and *in vivo* using

hot-film anemometry.

It seems then, in summary, that the fluid dynamics of implanted prostheses is pivotal to the long-term success of the surgical procedure. Flow stagnation regions and separation zones can be thrombogenetic. High shear stresses in the bulk flow can cause hemolysis and activate platelets, and thereby also contribute to thrombogenesis. Turbulence with its associated larger shear stresses can further endanger the success of the implanted prosthesis. Moreover, the recirculation of the formed elements of the blood in all probability intensify these adverse effects. Therefore, as Hwang (1977) indicates, a basic understanding is needed of the characteristics of the highly disturbed, if not exactly turbulent, flow through both the natural aortic valve and the various designs of aortic-valve prostheses.

1.4 ENGINEERING CONSIDERATIONS

There have been a number of more fundamental engineering studies undertaken of significantly simplified flows and geometries which have been at least partially motivated by the flow-related problems associated with implanted prostheses. These studies have been both theoretical and experimental and have been mostly concerned with the dynamics of steady and unsteady flow through orifices, model stenoses, and various valve models. The results from these efforts must be considered in the light of their often limiting simplifications. Nonetheless, certain fundamental phenomena have been characterized from these studies which may have a direct bearing on the interpretation of results of investigations in flows and geometries which are more physiologically pertinent.

The studies of model stenoses and orifices can be thought of as studies of model valves in which the complication of the valve occluder has been removed.

Important "occluder-less" studies have been those for pulsatile-flow through both model stenoses (Cox, et al., 1979; Clark, 1976a; Clark, 1976b) and orifices (Yellin and Peskin, 1975) where the forward-phase flow could be taken as quasi-steady. That is, as quasi-steady, the flow rate and structure remained relatively constant throughout the forward-flow phase. For model stenoses, quasi-steadiness appeared to be more pronounced for the larger flow constrictions ranging up to 89% (Cox, et al., 1979) and 94% (Clark, 1976a; Clark, 1976b) of the tube cross-sectional area. This quasi-steadiness phenomenon, if it could be shown to persist after the introduction of an occluder into the flow, could greatly simplify the characterization of flows downstream from prosthetic valves. Another interesting phenomenon has been reported by Young and Tsai (1973a and 1973b). These investigators modeled stenoses as gradual constrictions in the tube diameter and found that the critical Reynolds number at which turbulence was first detected was larger for unsteady flow than for steady flow. Furthermore, the difference between the critical Reynolds numbers was greater for the milder flow constrictions. Earlier Yellin (1966) had found related results for the limiting case of no flow constriction. He reported that for certain combinations of Reynolds number, flow-amplitude ratio, and frequency parameter, the growth rate of turbulent slugs was significantly smaller for pulsatile flow than for steady flow. More recently Hussain and Stettler (Hussain, 1977; Stettler and Hussain, 1983) have reported that the transition Reynolds number can be increased by as much as 60% using sinusoidal modulation of the flow. From these results it would appear that, at least in the absence of an occluder, prosthetic valves could tend to generate less turbulence in unsteady flow than in steady flow and that, moreover, the less the valve design constricts the flow the more dramatic this difference may become.

In general, however, the studies of model stenoses and orifices have not been

that definitive relative to the problem of the flow past an implanted prosthesis. The theoretical considerations of the work cited here have generally agreed with experimental results of pressure-drop studies. For flow-field determinations, however, agreements have only been qualitative at best. Recently, the correct location of shed vortices as a function of time were predicted for bounded, pulsating flows through orifices (de Bernardis, et al., 1981). Nonetheless, the current state of these types of investigations is not far enough advanced to contribute significantly to the understanding and prediction of the forces and flows downstream from implanted prostheses.

Valve-model studies have generally been concerned with the dynamics of the flow past the occluder of the valve. As such, the valve-model studies have been more or less complementary to the orifice and model-stenosis work. Caged-disc occluder and caged-ball occluder models are most common (Au and Greenfield, 1975; Figliola and Mueller, 1976; Roschke and Harrison, 1977; Underwood and Mueller, 1977; Mazumdar and Thalassoudis, 1983). Au and Greenfield (1975) theoretically studied the opening dynamics of a simplified model of a disc-occluder valve. In their work they found that the maximum shear stresses occurred near the end of the opening phase of the valve. These maximum shear stresses occurred near the edge of the upstream face of the occluder. Roschke and Harrison (1977), on the other hand, after theoretically studying the opening sequence of both caged-ball and caged-disc model valves, concluded that the largest shear stresses would occur for these types of valves in the small annular region available for flow at the *beginning* of the opening phase of the valve. These apparently contradictory results are, however, difficult to compare, as Roschke and Harrison (1977) point out, because of differences in geometry, flow, and, perhaps most importantly, Reynolds number definitions and magnitudes. Unfortunately, no information could be deduced from these

studies regarding flow structures downstream from the model valves. Thus the application of their work beyond the short time interval just after the beginning of the forward-flow phase was not possible. Underwood and Mueller (1977) theoretically studied a model caged-disc valve in steady flow for Reynolds numbers up to 1300 based on the tube diameter. They reported a maximum shear stress of approximately 9 N/m^2 located at the edge of the upstream face of the occluder. They indicate, however, that this value would be much higher for the maximum Reynolds numbers usually found in the ascending aorta, which are typically around 6000. At the higher Reynolds number, moreover, turbulence is likely to occur with its associated Reynolds stresses. Hence, the actual total shear stresses are probably much higher than those that these investigators were able to calculate. More recently, Mazumdar and Thalassoudis (1983) have extended these types of analyses into physiological ranges of Reynolds numbers. They assumed quasi-steady laminar flow at the maximum Reynolds number of 6000 based on the tube diameter. Their results were very similar in form to those of Underwood and Mueller (1977) with the maximum shear stresses again occurring at the edge of the upstream face of the valve occluder.

Some experimental verification of higher shear stresses for flow past a model disc-occluder valve has been given by Figliola and Mueller (1976). They studied Reynolds numbers as high as 6000 based on the tube diameter. Using hot-wire anemometry in air, they were able to determine very high, localized shear stresses both in the annulus between the occluder and the aortic wall and also directly downstream from the occluder edge. Their results indicated that turbulence stresses would occur *in vivo* as high as 1000 N/m^2. These extremely high stresses were probably a result of the sharp edges of the valve model. For current prosthetic valve designs such sharp features are generally absent.

Overall, it is clear that more accuracy in theoretical and physical valve models is necessary with respect to replicating the geometry of the prosthesis and physiologic flow before clinically significant applications of these investigations would be justified.

1.5 PREVIOUS IN VITRO INVESTIGATIONS

For *in vitro* investigations a valve prosthesis is placed in a flow field similar to that which it might encounter upon implantation. Some *in vitro* work has been cited above with respect to the problems associated with implanted prosthetic valves. Here, a more comprehensive review will be given of the *in vitro* investigations reported in the literature. Emphasis will be on the characterization of the detailed flow structures downstream from the prostheses being studied. Advantages of *in vitro* tests have been that they provide the necessary control that researchers require to unravel the complex, interrelated phenomena which accompany the fluid dynamics of these valves *in vivo*. On the other hand, Roschke (1973) has given three disadvantages of *in vitro* testing. These disadvantages are that i) *in vitro* tests cannot reproduce the physiological environment in every detail, ii) *in vitro* tests are relative in that there are currently no universally accepted valve-testing standards,* and iii) in *in vitro* tests some important implant-related problems cannot be simulated at all (e.g., the formation of thrombus). Yet, as also inferred by Roschke (1973), *in vitro* studies can be extremely beneficial for determining pressure-drop and flow-regurgitation characteristics of prosthetic valves, for studying valve opening and closure dynamics, and for determining the locations and magnitudes of associated flow structure and turbulence.

---

* Recently the Association for the Advancement of Medical Instrumentation (AAMI) has published an American National Standard for Cardiac Valve Prostheses (ANSI/AAMI CVP3-1981) (Hancock, et al., 1981) which, upon gaining more wide-spread acceptance, will be a definite step in the right direction.

Early *in vitro* investigations concentrated primarily on the measurements of the pressure drop across the valve and flow regurgitation (Cartwright, et al., 1964; Smeloff, et al., 1966; Duff, 1969; Wieting, 1969; Björk and Olin, 1970; Kaster, et al., 1970; Olin, 1971; Wright, 1972b; Henze and Fortune, 1974). Flow-visualization techniques were also employed to qualitatively study the flow patterns associated with various prostheses (Davey, et al., 1966; Smeloff, et al., 1966; Duff, 1969; Wieting, 1969; Kaster, et al., 1970; Björk and Olin, 1970; Olin, 1971; Phillips, et al., 1972). Wieting (1969) went a step further using a photographic technique and obtained velocity measurements from his flow-visualization work. His results, although pioneering, were limited in spatial and temporal resolution. Nonetheless, general flow structures and their magnitudes could be deduced from his plots. More sophisticated flow-visualization work has continued, (Phillips, et al., 1976; Phillips, et al., 1979; Reul, et al., 1977; Wright, 1977; Wright and Temple, 1977; Emery, et al., 1978; Emery and Nicoloff, 1979; Gombrich, et al., 1979; Lloyd, 1979; Nicoloff and Emery, 1979; Wright 1979; Alchas, et al., 1980; Schramm, et al., 1980; Schramm, et al., 1982; Tindale, et al., 1982; Yoganathan, et al., 1983b) mainly because of its unique ability to enhance the study of the larger-scale flow structures.

Some years later, hot-wire and hot-film anemometers were used to measure local velocities near various prostheses (Swope and Falsetti, 1976; Hwang, 1977; Figliola and Mueller, 1977; Figliola, 1979; Figliola and Mueller, 1979; Figliola and Mueller, 1981). These anemometers, however, were not especially well matched to this application. The flow downstream from prosthetic valves was highly disturbed with elevated turbulence intensities and thus signal-to-noise problems were common. In addition, the flow frequently had separation regions with associated reverse flow which could not be distinguished from forward flow with these anemometers. The invasiveness of this technique has also posed a

problem. The size of the flow probe and its supporting mechanism were significant since for these studies the geometries and flow structures tend to be quite small.

The laser-Doppler anemometer (LDA), on the other hand, is well matched to the measurement of velocities in these flowing systems. In the past four or five years many investigators have turned to this tool for velocity measurements in the vicinity of prosthetic valves (Yoganathan, et al., 1977b; Yoganathan, 1978; Yoganathan, et al., 1978a; Yoganathan, et al., 1978b; Yoganathan, et al., 1979a; Yoganathan, et al., 1979c; Yoganathan, et al., 1980; Yoganathan, et al., 1981; Yoganathan, et al., 1983a; Yoganathan, et al., 1983b; Lu, et al., 1979; Figliola, 1979; Figliola and Mueller, 1979; Figliola and Mueller, 1981; Alchas, et al., 1980; Phillips, et al., 1979; Phillips, et al., 1980; Bruss, et al., 1983). Yoganathan and coworkers first used the LDA to measure axial velocities and turbulence intensities in steady flow both very close to the wall and in the bulk flow. They have reported quite detailed measurements in the near vicinity of valve occluders (Yoganathan, et al., 1977b; Yoganathan, 1978; Yoganathan, et al., 1978b; Yoganathan, et al., 1980; Yoganathan, et al., 1981; Yoganathan, et al., 1983a; Yoganathan, et al., 1983b) and have been able to correlate some of their findings with known clinical failure modes of implanted valves (Yoganathan, et al., 1977a; Yoganathan, 1978; Yoganathan, et al., 1978b; Yoganathan, et al., 1980). Figliola and Mueller (Figliola, 1979; Figliola and Mueller, 1979; Figliola and Mueller, 1981) measured velocities using the LDA and measured the Reynolds stresses using a hot-film anemometer for steady flow. They were able to obtain detailed results very close to the valve occluders. Lu, et al. (1979) measured velocities in pulsatile flow through prosthetic heart valves and reported results for the time of maximum flow in the cardiac cycle. Because of their experimental arrangement they were also able to directly

measure Reynolds stresses using the LDA and thereby to obtain some idea of the shear stresses present in the flow as a function of location. Phillips and coworkers (Phillips, et al., 1979; Phillips, et al., 1980; Alchas, et al., 1980) also used the LDA to measure velocities in pulsatile flow. From their work they were able to present results for several different times in the cardiac cycle. Most recently Bruss, et al. (1983) brought much of the above together by using the LDA to study the flow structures near the occluders of four mechanical valve prostheses in pulsatile flow at various times in the cardiac cycle. From their work several flow structures downstream from these prostheses were easily appreciated in both space and time.

The LDA has, therefore, provided a significant increase in the accuracy, precision, and resolution of the data obtained downstream from prosthetic valves *in vitro* when compared to either the flow-visualization techniques or the hot-wire and hot-film anemometers used in earlier investigations. Using the LDA, significant stagnant flow regions have been found close to valve occluders, separated-flow regions have been found to the leeward side of valve superstructure, and both laminar shear stresses near surfaces and turbulent shear stresses in the bulk flow have been found to be greatly elevated.

Until this investigation, however, the LDA was most commonly used to measure the velocity at only a few locations in the flow at a time. Hence, the identification of the large-scale structures, a strong point of flow-visualization work, was lost. The LDA can be used to determine large-scale structures in regions of interest by appropriately "mapping" those regions with a sufficient number of well-located points at which velocities are measured. The aforementioned studies most commonly located measurement points at even intervals along a diameter of the circular cross section of the flow section. A cross section of the flow, or flow "profile," was thereby generated and from it

conclusions were drawn regarding the nature of the total flow field. The conclusions made in this way were tenuous in that it was difficult to identify large-scale flow structures from one or two flow profiles. Moreover, the velocity data presented to date were mostly limited to the axial direction. Thus there was a paucity of non-axial data from which secondary-flow structures could be identified. Because such secondary-flow information could allow the prediction of the magnitudes and locations of any potentially detrimental flow structures present in the flow as a function of both time and location, a need existed for data collection at numerous well-chosen locations, both on and off the flow-section diameter, at various cross sections of the flow field for both the axial and non-axial directions.

Finally, no systematic study has been reported in which results from steady-flow experiments were compared with those from pulsatile-flow experiments in the same systems. Moreover, very little clear evidence has been reported which indicates to what extent steady-flow velocity data can be used to assess the *in vivo* performance of a prosthetic valve. Therefore, as a refinement of the recent conclusion of Bruss, et al. (1983), a more complete mapping of both steady and pulsatile flow downstream from prosthetic valves was felt to be necessary for the characterization of velocity fields which could be used to provide further specific clinical correlations.

1.6 GOALS AND APPROACH OF THE PRESENT INVESTIGATION

The primary goal of the present investigation was to gain a better understanding of the dynamics of flow through prosthetic aortic heart valves. To this end a systematic methodology for studying the fluid dynamics of these valves *in vitro* using the LDA was developed and implemented. A method was designed which provided velocity data i) at a sufficient number of locations to

map the flow structures, ii) in the non-axial directions as well as the axial, and iii) from the same experimental rig for both steady and pulsatile flow. This method provided an improved way to approach the analysis of prosthetic valve flows so that a more basic fluid mechanical understanding of these complicated flows could be attained. Mean and root-mean-square (rms) velocities were determined at each measurement location in all three coordinate directions from the instantaneous velocity data. By analyzing the velocity data obtained via this method, potentially thrombogenetic flow structures could be identified and characterized as to overall magnitude and to the extent of the effected regions of flow. Also, from this analysis some general comments were possible regarding particular drawbacks of the designs of the occluding mechanisms of the valves studied. Perhaps most importantly, the method provided for a well-controlled comparison between steady-flow and pulsatile-flow results. Thus, the efficacy of steady-flow assessment of the flow structure downstream from aortic prostheses was carefully analyzed.

For an *in vitro* study, the pertinent *in vivo* environment should be approximated as closely as possible. As Casci, et al. (1977) note, for *in vitro* studies of aortic prostheses, a very accurate physical model of the aorta is required which takes into account the physiological pressure pulse reflections and the oscillations of the blood mass. For the present investigation, the flow section was designed and constructed which geometrically modeled the human aortic root. This flow section was then incorporated into a pulse-duplicator which was designed to produce pressure and flow fields similar to those found *in vivo*.

The present investigation included the estimation of turbulent shear stresses at all locations where velocity measurements were made. Assuming a correlation coefficient, the rms velocities in two mutually orthogonal coordinate

directions allowed the estimation of the Reynolds stresses in the flow. This stress was determined for each of the three different shear components of the stress tensor. For each location where data were collected in the flow, these three components of the turbulent shear stress were summed with the respective component of the laminar shear stress. This summation was done to allow estimation of the "total" shear stress that a formed element of blood might encounter downstream from a specific valve prosthesis *in vivo*. It is not clear, however, that the separate effects of the laminar and turbulent shear stresses on a formed blood element are entirely additive. An accurate assessment of the overall effect would be difficult owing to the complex nature of the mechanical structure of the formed blood elements in general and the RBC in particular. Most probably the overall effect of the two shear stresses would be less than their sum with the maximum shear stress experienced by the formed element being that sum only infrequently if at all. Laminar shear stresses are generated by the difference in the mean velocities of two adjacent fluid "elements." Turbulent shear stresses are generated by the phase relationship of two, mutually orthogonal fluctuating velocities. A body placed in a flow field containing both relatively significant laminar and turbulent shear stresses would only experience the sum of these stresses, i.e., the total shear stress, when the two stresses were acting in the same direction. Otherwise, the total shear stress experienced by that body would be less. Hence, the total shear stress was probably an upper bound on the shear stress experienced by the formed elements of the blood. Using the total shear stresses thus estimated, comparisons were made between the magnitude of these stresses and those discussed above as potentially detrimental to the long-term success of aortic valve replacement.

Another goal of this work was to evaluate and compare four aortic prostheses

using the capabilities of the developed methodology. Both steady-flow and pulsatile-flow investigations were performed on each of the four valves. These results allowed comparisons of steady-flow to pulsatile-flow results for each valve design a well as comparisons of results between valve designs.

Pressure-drop and regurgitant-flow characteristics were also determined for the four aortic prostheses studied in the present investigation. The pressure drop was determined for each valve in both steady and pulsatile flow. These pressure and flow characteristics allowed an analysis of the relative hemodynamic performance of the four prostheses studied.

One prosthesis was chosen as a representative of each of the three categories of valve types delineated above. The Ionescu-Shiley bioprosthesis was chosen as the central-flow valve. This valve is a bovine heterograft which has become increasingly more popular since its release for general use in the U.S.A. in 1976. The Björk-Shiley convexo-concave prosthesis was chosen as the semi-central flow valve. This valve is a tilting-disc valve which is currently very popular. The first model of this valve was first used clinically in 1969 and has become the most commonly implanted prosthesis worldwide. The Smeloff prosthesis was chosen as the lateral-flow valve. The present model of this valve has been in clinical use since 1966 and as such has been available for implantation the longest of all valves currently implanted. A fourth valve, the St. Jude prosthesis, was chosen because of its current popularity, unique design, and expected growth in popularity. The flow through this valve is a cross between central flow and semi-central flow. It is a relatively new valve, having been approved for general use in the U.S.A. in 1981. Preliminary results show that this design has definite hemodynamic advantages over other designs currently available and suggest that its clinical use will probably increase significantly if neither materials failure nor thrombotic occlusion become late-developing problems.

These four valves and their function are described more completely in the next chapter on the experimental apparatus and methodology.

2. APPARATUS AND METHODOLOGY

2.1 FLOW APPARATUS

2.1.1 Aortic-Valve Flow Section

A Lucite® flow section was constructed in which the aortic prostheses were mounted for all investigations. The flow section was designed to approximate the physiologically pertinent geometries both in the near vicinity of and also downstream from the natural aortic valve. The flow section is shown with an Ionescu-Shiley valve mounted in the top of Figure 1. The bottom of Figure 1 shows the mounted valve and modeled aortic root in more detail. The sinuses of Valsalva were modeled by the Lucite® sinuses indicated in the figure. Data on sinus dimensions in adults were obtained from castings of the ascending aortas of patients at autopsy. The autopsy work was done by Earl C. Harrison, M.D., of the Los Angeles County - University of Southern California Medical Center. All dimensions thus determined were scaled appropriately for an aortic-root diameter of 25.4 mm. This diameter corresponded well with that which would call for a size 24 or 25 aortic prostheses at surgery.

Also indicated in the bottom of Figure 1 are the coordinate directions used in the present investigations. The z-direction was axially oriented. The y-direction was orthogonal to the z-direction and was oriented so that it bisected one of the sinuses. The x-direction was mutually orthogonal to the y- and z-directions. The origin of the z-axis was the downstream face of the prosthesis base-ring. The positive direction for z was defined as in the direction of the mean flow, i.e., from left to right in Figure 1.

Downstream from the sinuses a straight tube of circular cross section modeled the ascending aorta. Several concerns arose when modeling the ascending aorta in this way. The natural ascending aorta begins to curve

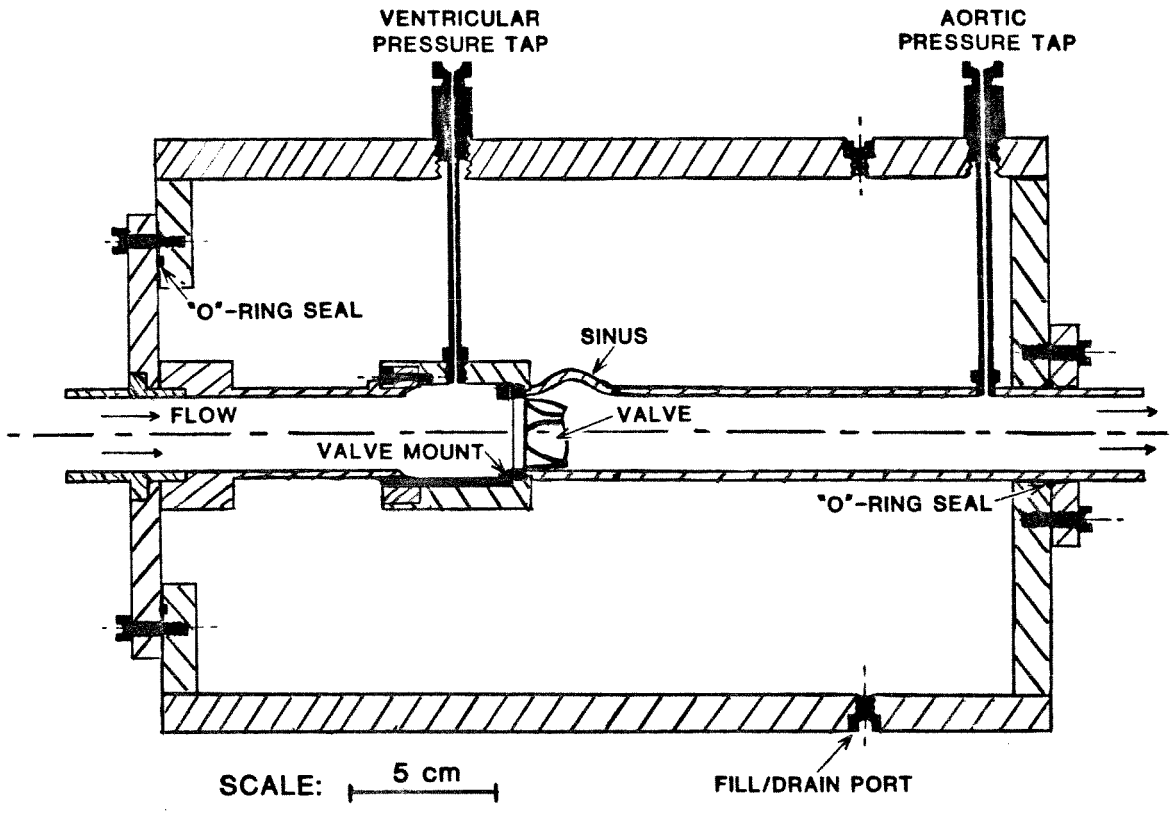

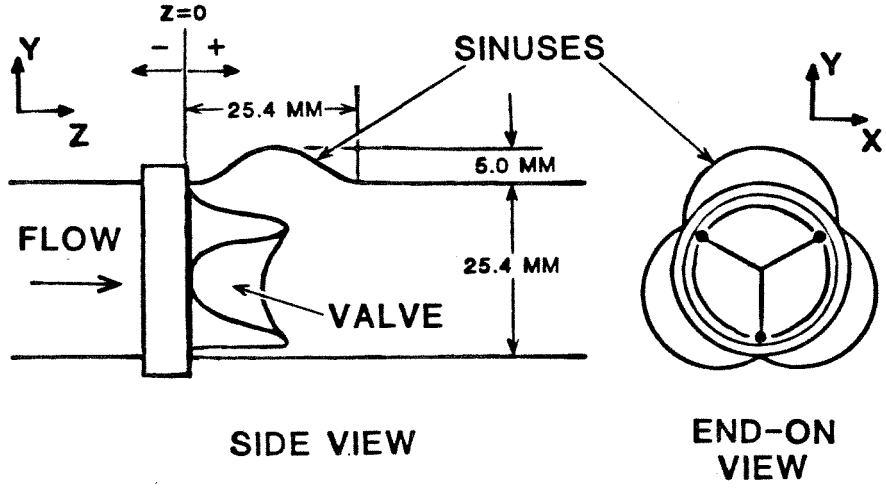

Figure 1. Aortic-valve flow section depicted with an Ionescu-Shiley bioprosthesis mounted.

significantly beyond five or six centimeters downstream from the base of the natural aortic valve (Braunwald, 1980). Also, located just beyond the beginning of this curvature is the innominate aorta, the first of three large side-branches. Thus there were significant limitations in the interpretation of data collected more than five centimeters downstream from the base-ring of the mounted valve. Furthermore, the ascending aorta tapers slightly along its length and is distensible. Thus questions regarding flow accelerations and compliance were important. Recently Walburn and Stein (1981) have studied the effect of tapering of the ascending aorta. Their results show that the effect of the tapering of the ascending aorta can be assumed to be small within the distance limit set by the curvature effects. For the steady-flow case the pulsing dynamic was ignored and hence modeling the compliance of the natural tissues was of secondary importance. For the pulsatile-flow case some provision for the compliance of the natural tissues was made by placing a Gooch-tubing section as closely as possible downstream from the flow section.

Upstream from the valve mount, the flow section was designed for the secure mounting of the valve and to provide an entrance flow of fully developed turbulent pipe flow.

Ports were tapped in the wall of the flow section to allow the measurement of the wall pressures. The ventricular pressure tap was located 20 mm upstream from the downstream face of the valve base-ring. The aortic pressure tap was located 150 mm downstream from the downstream face of the valve base-ring. The locations of the pressure taps chosen corresponded approximately with those of earlier work in our laboratory (Yoganathan, et al., 1977a; Yoganathan, 1978; Yoganathan, et al., 1979b; Suobank, 1983) and thus allowed pressure data to be readily compared. Yoganathan (1978) had earlier determined that for steady flow essentially complete recovery of the pressure

had been attained at the location of the aortic pressure tap.

The aortic-valve flow section was then placed inside a Lucite® box with a square cross section (see Figure 1). The purpose of the box was three-fold. Most importantly, when it was filled with water the box provided an optically improved path for the anemometer laser beams through the flow section. To minimize any uncertainty in the beam path and to reduce scattering of the beam, it is desirable to have the incoming beam cross through changes in the index of refraction at a high angle of incidence to the surface generating the change in the index. High incidence angles are those approaching 90° with respect to the surface. Simple optics theory (Hagelberg, 1973) dictates that in those cases where an incidence angle of 90° can not be maintained at all times, as was the case for the present investigation, the highest angles of incidence should optimally be those at the greatest differences in the indices of refraction. This requirement for optimization stems from the fact that the angle of refraction at the surface is a function of the ratio of the indices of refraction. Larger angles of refraction cause small defects in the surface to generate larger errors in the beam path. The difference in the indices of refraction was less between water and the Lucite® than between air and Lucite®. At 22° C the index of refraction of the air, water, and Lucite® were 1.000, 1.330, and 1.490, respectively. The larger change in the refractive index thus occurred along the laser beam path at the side of the box exposed to the air. Therefore, this larger change in the refractive index occurred at the surface which was at a high incidence to the incoming laser beams and which, moreover, did not change its incidence during an experiment. Otherwise, had there been no box, the change of indices from air to Lucite® would have occurred at the outer wall of the Lucite® tube modeling the ascending aorta. Depending upon the desired location of the laser-beam crossing inside the tube, the angle of incidence could become almost

prohibitively small. Secondarily, the box could be sealed watertight. Once the flow section was placed inside the box, "o"-ring seals on both ends of the box prevented leakage. The flow section itself, therefore, did not need to be sealed. Finally, the box was square in cross section and thus could readily be rotated 90°. This rotation provided a quick and accurate means of rotating the flow section along with its currently mounted valve without the need to remove, rotate, and remount the prosthesis.

2.1.2 Steady-Flow Loop

A steady-flow loop was constructed to generate a fully developed turbulent flow in a tube. The flow loop is shown schematically in Figure 2. Flow direction is indicated by the arrows. The Lucite® flow section which generated the turbulent flow had been previously developed in our laboratories by Whatley (1981). He determined that the flow conditioner generated fully developed flow in the tube at a distance of 35 tube diameters downstream. For the present investigation, therefore, velocity data were collected at 35 diameters using the LDA apparatus described below. Also, by measuring both the velocities in the flow and the pressure drop as a function of the distance down the tube, Whatley determined that the flow loop generated quite faithfully a flow which obeyed Blasius' law of friction (Bird, et al., 1960). Thus the flow loop provided a known flow in which the measurement system could be characterized.

For the present study the flow tube was fitted with a Lucite® box which served a similar purpose as the box described above for the aortic-valve flow section. The box used here differed in that it was smaller and was not sealed, since no leakage problems were anticipated.

The box and tube were then connected rigidly to a mill table so that they could be translated together in three mutually orthogonal directions. The

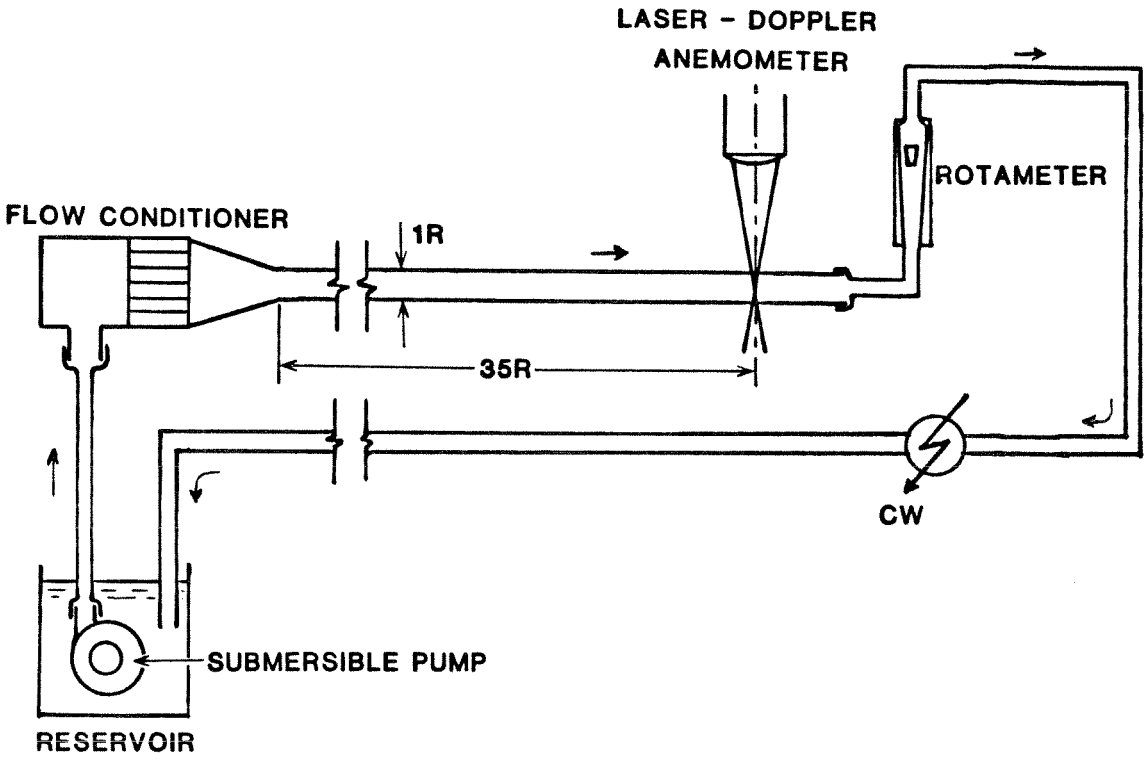

Figure 2. Schematic of the steady-flow loop showing the location of the LDA laser beams for velocity measurements in the fully-developed, turbulent pipe flow. Flow direction is indicated by the arrows. For studies of prostheses, the aortic-valve flow section was inserted immediately downstream from the location shown here of the measurements in the developed turbulence.

resolution of the mill table was 0.025 mm in each of the three coordinate directions. Translating the flow section in this way allowed velocity data to be collected from various points in the flow.

Once the work on the fully developed flow had been completed, the steady-flow apparatus was modified to include the aortic-valve flow section. The aortic-valve flow section was inserted into the flow loop immediately downstream from the flow tube. For these experiments the flow section was fastened to the mill table. Velocity data were again collected using the LDA. The pressure drops across the prostheses were also measured. Pressure measurements were not done for the developed-turbulence case. The pressure was measured at both the ventricular and aortic pressure taps by two Statham P23De physiological pressure-transducers. The frequency response of the transducers was -3 db at 100 Hz. Each transducer was connected to a Honeywell 218-1 bridge amplifier. Using the amplifiers, the pressure transducers were calibrated before use with a water-filled manometer. For the steady-flow studies, the ventricular and aortic pressure as well as their difference was obtained as a function of time via the computer interface to the transducers described below.

In addition to the prosthetic valves that were studied, a case with no valve present in the flow section was studied. Instead, a Lucite® ring with an inner diameter (ID) of 25.4 mm was inserted into the flow section. The experiments with and without a mounted valve were identical.

The blood-analog fluid used was normal saline, i.e., 0.9%-by-weight NaCl in de-ionized water, at room temperature. A normal saline solution was primarily chosen for the present work to provide continuity with earlier work in our laboratory (Yoganathan, et al., 1977a; Yoganathan, et al., 1977b; Yoganathan, 1978; Yoganathan, et al., 1978a; Yoganathan, et al., 1978b; Yoganathan, et al., 1979a; Yoganathan, et al., 1979b; Yoganathan, et al., 1979c;

Suobank, 1983; Suobank, et al., 1984a; Suobank, et al., 1984b; Suobank, et al., 1984c). Also, the normal saline solution has been the blood-analog fluid preferred by the manufacturers of bioprosthetic valves for the testing of their valves. This preference arose because bioprosthetic valves have been known to react unfavorably to other common blood-analog fluids such as solutions of glycerin in water. A normal saline solution was therefore again the blood-analog fluid of choice to maintain consistency in the present investigation wherein both mechanical and bioprosthetic valves were to be tested. Finally, as Yoganathan (1978) indicates, the use of the saline solution as the blood-analog solution was experimentally much more convenient. The NaCl was put in the water to give the solution similar electrolytic characteristics as that of whole blood. These electrolytic characteristics were required by the electromagnetic flowmeter used for the pulsatile-flow work.

The viscosity of the normal-saline solution was, however, less than the apparent viscosity of whole blood (0.001 kg/m·s vs. 0.003 to 0.004 kg/m·s). Because of this viscosity difference, blood-analog fluids such as 45%-by-weight glycerin in water and 6%-by-weight Polyol Pluracol V-10 (Wyandotte Chemicals) in water have been used by other investigators. Yoganathan and co-workers (Yoganathan, et al., 1977a; Yoganathan, 1978; Yoganathan, et al., 1979b) have shown, though, that normal-saline and 6%-by-weight Polyol® solutions give very similar pressure drop results. They studied Reynolds numbers based on the tube diameter ranging from 8400 to 25,200 for the saline solution and 2400 to 7200 for the Polyol®. The Reynolds number here was defined as $Re = \frac{\rho \bar{U} D}{\mu}$ where ρ was the density of the fluid in kg/m^3, $\bar{U}$ was the average velocity across the tube cross-section in m/s, D was the tube diameter in meters, and μ was the viscosity in kg/m·s. Hwang, et al. (1983) and Olin (1971) have also found that when fluid viscosities and Reynolds numbers are in the ranges given above,

viscosity differences have had little influence on pulsatile-flow pressure drops.

The lack of sensitivity of the pressure-drop results on the Reynolds number was because the friction and form drag in those flowing systems were relatively weak functions of the Reynolds number over the ranges studied. Friction drag is that drag caused by the wall of the flow section. Form drag is that drag caused by any flow separation produced downstream from a submerged object in a flowing fluid. Because fluid flowed past the occluding mechanism of the valves and also through the valve orifice and flow section tubes, both friction and form drag were present in the present investigation. The pressure drop across a prosthesis, therefore, was a result of the energy losses associated with these two drags. For flows which obey Blasius' law of friction, the friction drag caused by the wall of the flow section varies as $Re^{-0.25}$. Thus two flows at Reynolds numbers whose difference was fairly large would have had somewhat similar magnitudes of friction drag. For the current investigation the Reynolds number was about 25,000. The comparative Reynolds number for a blood-analog fluid with a viscosity of, say, 0.0035 kg/m·s, would have been about 7100. Thus, were Blasius' law of friction valid, the friction drag would have been 0.0063 for the higher Reynolds number and 0.0086 for the lower. It is not clear, however, what effect the prosthesis mounted in the flow would have on the exponent of -0.25 given above but if the flow then became similar to that through extremely roughened tubes the exponent would actually decrease in absolute magnitude (Bird, et al., 1960). Form drag, moreover, may have contributed significantly to the overall drag and therefore the Reynolds number dependence of the friction drag was possibly of less importance in any case. Over the Reynolds number range of interest, the form drag would be almost independent of the Reynolds number for spheres, cylinders whose axis was perpendicular to the free streaming flow, and discs that were both perpendicular and inclined to the free

streaming flow (Perry and Chilton, 1973). Thus, for most prosthetic valve designs, the form drag would probably be comparable at all viscosities in the range demonstrated by the blood-analog fluids discussed here. Because form-drag results have usually been determined for a relatively small object in the free streaming flow of a large wind tunnel, only these general comments can be made regarding this drag in the confined flows of this investigation. Nonetheless, it is reasonable to expect only small differences in pressure-drop results over the range of Reynolds numbers of interest, as has been found experimentally, and especially so if form drag predominated.

Whole blood also exhibits certain non-Newtonian characteristics which are ignored when normal saline is used. To address this aspect of the problem, Schramm and coworkers (Schramm, et al., 1980; Schramm, et al., 1982) compared a 0.14% polyacrylamide (PAA) solution with water for velocity measurements downstream from prosthetic valves *in vitro*. PAA exhibits a viscoelastic behavior comparable to whole blood at a hematocrit (RBC volumetric concentration) of 44%. The average hematocrit for a normal human male is 47% and for a female is 42% (Wintrobe, et al., 1981). The PAA had a viscosity of 0.0001 kg/m·s per 1° C for 18° C to 25° C. In their detailed flow-visualization studies, Schramm and coworkers reported that though the PAA did show somewhat blunted velocity profiles, flow formations were essentially the same for water as for PAA at the same flow rates. Thus the Newtonian nature of water used as the blood-analog fluid does not appear to seriously limit the applicability of *in vitro* findings.

Referring again to Figure 2, the flow proceeded from the flow section through a Brooks rotameter (model 10-1110) and a copper heat-exchanger to the reservoir and the submerged pump. The rotameter was calibrated using the normal-saline solution so that the flow loop could be run at a flow rate of

27 L/min. The heat exchanger removed the heat generated by the submersible pump (Little Giant). A steady-state temperature of 27° C was reached in approximately ten minutes. The density and viscosity of the normal-saline solution at this temperature are 1000 kg/m^3 and 0.00086 kg/m·s, respectively. Finally, the fluid was pumped from the reservoir into the flow conditioner and back through the flow section.

2.1.3 Pulsatile-Flow Loop

Figure 3 depicts the pulse-duplicator schematically. Flow direction is indicated by the arrows. Beginning at the liquid reservoir and proceeding in the direction of the flow, the first unit encountered is the mitral-valve flow section. This section has a one-way check valve constructed of Gooch tubing stretched over a circle of wire mesh. The Gooch tubing was slit from its center point outward to approximately 80% of its radius. Three such slits were present, each 120° from each other, thereby generating three triangular "leaflets." Forward flow opened the valve by moving the leaflets out into the flow away from the wire mesh. Reverse flow effectively closed the valve by moving the leaflets back onto the wire mesh support.

The ventricular-pump section modeled the left ventricle of the human heart. It was connected through quick-acting solenoid valves (ASCO Bulletin 8321, normally-closed) to an air-pressure line at a gauge pressure of 551.4 kilopascals (kPa), i.e., 80 psig. By activating and deactivating the solenoid valves, this section received a pulse of air. The air "squeezed" the bulbs, thereby effectively modeling the motion of the wall of the human ventricle. Regulators in the air line allowed the pressure to the section to be varied from 68.9 to 344.6 kPa (gauge), i.e., 10 to 50 psig. By regulating the air flow, the stroke volume of the ventricular-pump section could be controlled.

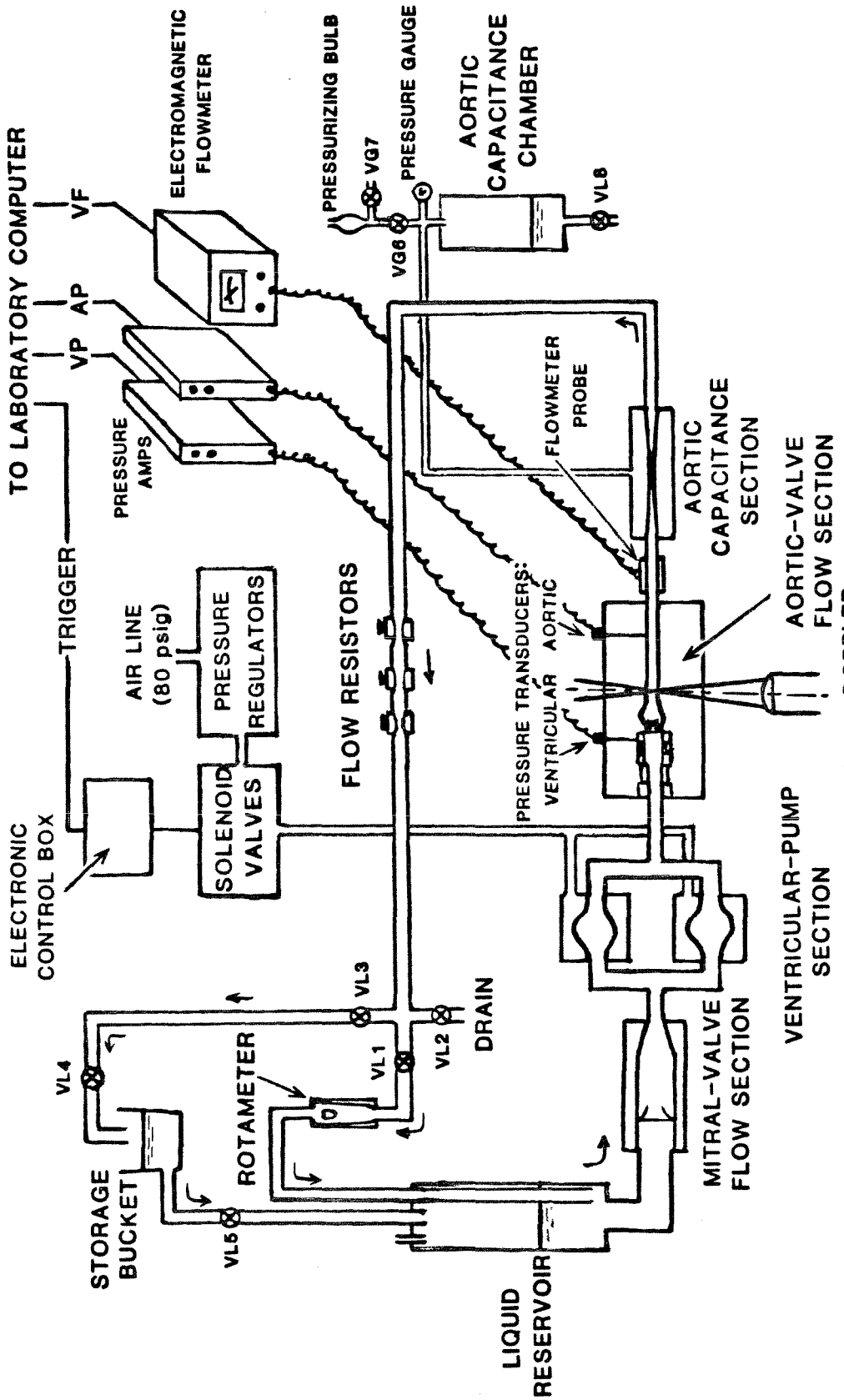

Figure 3. Schematic of the pulse-duplicator showing the location of the LDA laser beams for the pulsatile-flow studies. Flow direction is indicated by the arrows.

An electronic control box was used to set the rate and duration of the pulses. The control box had a trigger output which was read into the laboratory computer as described below so that all data collected would be synchronized with respect to the pulse timing.

The aortic-valve flow section was described earlier. Velocity data and the ventricular and aortic pressures were measured in the same way as for the steady-flow experiments. In addition, the instantaneous flow rate was measured by an electromagnetic flowmeter (Statham SP-7507-250) and its flow probe. This flowmeter was located at the downstream end of the aortic-valve flow section at $z \approx 200$ mm and was attached to the flow section rigidly so that the flow rate measured was essentially that through the valve orifice. The flowmeter measured the voltage induced by an electrolytic fluid passing through an applied magnetic field. The electrolytic fluid was a normal-saline solution, as noted earlier. The output from the two pressure amplifiers ("VP" and "AP") and the electromagnetic flowmeter ("VF") were each read into the laboratory computer via the interface described below.

The systemic capacitance system consisted of the aortic capacitance section and the aortic capacitance chamber. The capacitance section was passive and modeled the distensibility of the rest of the cardiovascular system. Varying the pressure in the capacitance system while the pulse-duplicator was operating allowed the setting of physiological pressure levels in the aortic-valve flow section. The pressure in the capacitance system could be varied by use of the capacitance chamber. A pressurizing bulb and pressure gauge were provided on the chamber to reproducibly elevate the pressure in the capacitance section. Valves VG6 and VG7 were placed so that they could maintain and vent the pressure, respectively. The total volume of the aortic capacitance section could be varied by raising or lowering the liquid level in the chamber through valve

VL8. Raising the liquid level gave the section less distensibility, and vice versa.

Flow resistors, when coupled with the effect of the systemic capacitance system, completed the modeling of the cardiovascular system. The systemic resistance could be increased or decreased by tightening down or loosening up, respectively, on the series of three resistors.

After passing through the resistors, the fluid then returned to the reservoir through a rotameter. Because of oscillations in the flow the rotameter gave only a rough estimate of the mean flow in the pulsating system. As such, the rotameter was used as a quick reference for maintaining consistent performance of the pulse-duplicator during an experiment. A branch was provided upstream from the rotameter to allow the fluid to be pumped into the storage bucket. Flow was directed into the bucket by closing valve VL1 and opening valve VL3. From the bucket the fluid could be fed by gravity back into the reservoir through valve VL5. Valve VL4 was positioned at the highest point in the flow loop and was used to prime the system at start-up. Valve VL2 was positioned at the lowest point in the flow loop and was used to drain the system.

The performance of the pulse-duplicator was maintained for all experiments at the standard settings listed in Table 2. These settings were within the ranges recommended by AAMI in their American National Standards for cardiac valve testing (Hancock, et al., 1981). The pulse rate was set at 70 beats per minute. The average flow rate was maintained at 5.4 L/min. The stroke volume averaged 0.086 liters but varied from one valve design to allow the average flow rate to be maintained. The pneumatic systolic interval, defined as the length of time that the ventricular-pump section was pressurized by the solenoid valves, was 0.300 seconds. The pneumatic diastolic interval encompassed the remainder of the pulse and was therefore 0.557 seconds. The systolic ejection interval was defined as the length of time the ventricular pressure was greater than the

Table 2

Standard Performance Settings

for the Pulse-Duplicator

Pulse Rate	70 min^{-1}
Mean Flow Rate	5.4 L/min
Stroke Volume	0.086 liters
Systolic Interval	300 ms
Diastolic Interval	557 ms
Aortic Pressure	16.0/10.7 kPa*
Peak Systolic Flow Rate	30.2 L/min

*Gauge pressure.

aortic pressure and, hence, varied somewhat between valve designs from the given pneumatic interval. The systolic ejection interval, however, varied between valve designs only as much as 2% from the average value of 0.287 seconds and, therefore, was quite close to the pneumatic interval for all four valve designs studied. The aortic pressure was set to range between 16.0 and 10.7 kPa (gauge), i.e., 120 and 80 torr (gauge). With the above settings established, the peak systolic flow rate was then maintained at an average of 29.6 L/min between valve designs by varying the form of the volumetric-flow curve. The settings were maintained by monitoring the pressures and volumetric flow with the use of the laboratory computer. During an experiment, the pressure and volumetric-flow data were used to characterize the performance of the pulse-duplicator on a pulse-to-pulse basis. Later, the pressure and volumetric-flow data were plotted to document the pulse-duplicator performance. Typical pressure and flow curves are shown in Figure 4. Again these curves are within the bounds set by AAMI. The pressure and volumetric-flow results shown here, and others presented in the next chapter, are evidence that the pulse-duplicator reproduced quite well the pressure and flow fields which the prosthetic valves studied might encounter when implanted in a patient.

2.2 AORTIC PROSTHESES STUDIED

2.2.1 Ionescu-Shiley Bioprosthesis

The Ionescu-Shiley valve is a bioprosthetic valve made of tissue from the bovine pericardial sack, as shown in Figure 5a. The occluding mechanism of this valve consists of three equal-sized leaflets of roughly semi-lunar shape. The leaflets are fixed with glutaraldehyde at high pressure and mounted on a titanium stent which is designed to provide some measure of flexibility. During forward flow the leaflets billow out in such a way as to provide an essentially

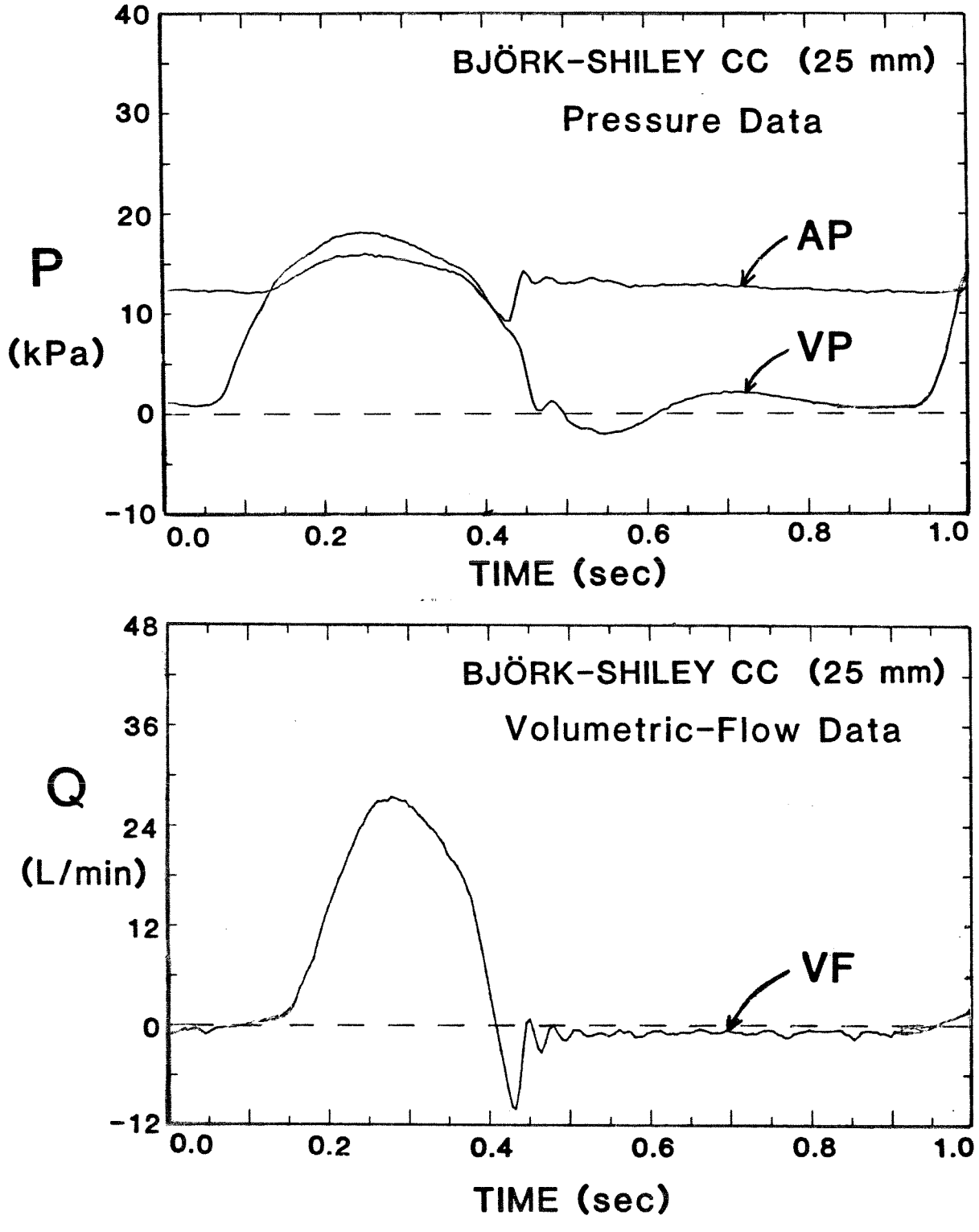

Figure 4. Aortic-pressure (AP), ventricular-pressure (VP), and volumetric-flow (VF) data for the Björk-Shiley convexo-concave (25 mm) prosthesis in the pulse-duplicator.

PROSTHETIC AORTIC VALVES

Ionescu-Shiley

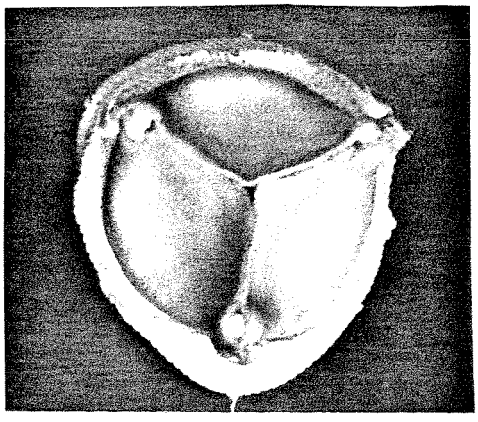

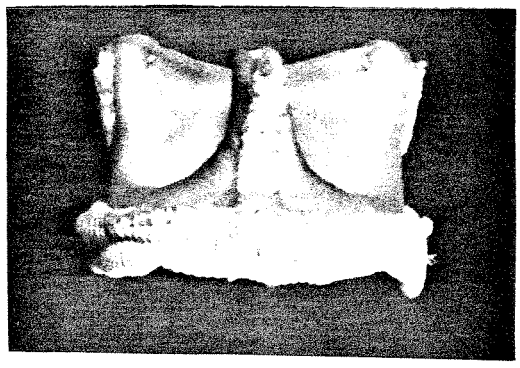

Björk-Shiley convexo-concave

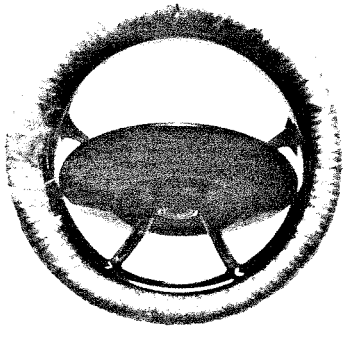

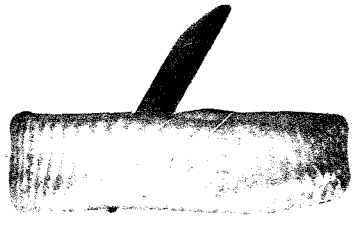

Figure 5a. Prosthetic aortic heart valves used in the present investigation.

PROSTHETIC AORTIC VALVES

Smeloff

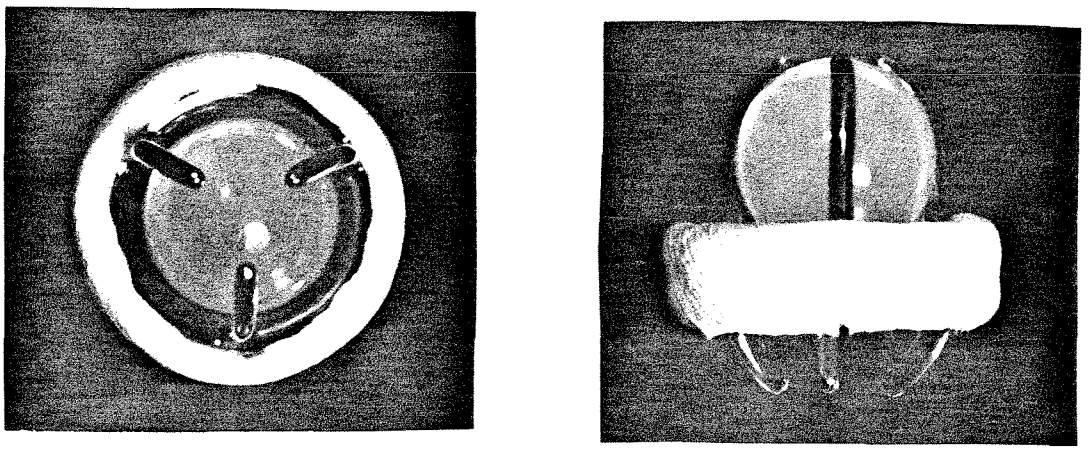

St. Jude

Figure 5b. Prosthetic aortic heart valves used in the present investigation.

circular orifice for flow. Upon deceleration and reverse flow the leaflets are pushed back to the closed position where their free edges seal the orifice by resting against one another. This valve is a totally occluding valve and therefore, for a properly operating prosthesis, there is no further reverse flow once the valve is closed.

2.2.2 Björk-Shiley Convexo-Concave Prosthesis

The Björk-Shiley convexo-concave valve consists of a stellite base-ring with a pyrolytic-carbon, tilting-disc occluder, as shown in Figure 5a. The occluding mechanism of this valve is a circular disc which tilts open to 60° in response to forward flow and tilts back to its closed position for deceleration and reverse flow. The disc is lenticular in cross section and is free to rotate about its axis while opening and closing. The convex downstream face of the disc has a shallow well in its center in which the downstream support strut rests to insure that the disc does not free itself from the valve superstructure and emobilize during forward flow. An upstream strut rests against the concave upstream face of the disc in such a way as to prevent disc emobilization during reverse flow. The disc does not totally occlude the valve orifice when closed. By design, a thin annular region remains when the disc is in the closed position. Thus there is a finite amount of reverse flow once the valve is closed. For ease of visualizing the function of the valve radiographically, a tantalum hoop is incorporated into the disc occluder.

2.2.3 Smeloff Prosthesis

The Smeloff valve is a double-caged silastic ball valve with a stellite-cage superstructure, as shown in Figure 5b. The occluding mechanism of this valve is a spherical ball which moves out away from the valve orifice in response to

forward flow and back into the orifice for reverse flow. During forward flow the ball is restrained from emobilizing by a three-pronged cage protruding downstream from the valve orifice. A similar yet shorter cage located upstream from the valve orifice restrains the ball during reverse flow. When the valve is closed, the diameter of the ball is essentially positioned at the minimum cross section of the valve base-ring. Thus a thin annular region remains between the ball and orifice on closure which allows a finite amount of reverse flow through the closed valve.

2.2.4 St. Jude Prosthesis

The St. Jude valve is a modified hinged-leaflet type valve, as shown in Figure 5b. All surfaces of the valve were covered with pyrolytic carbon. The occluding mechanism of this valve consists of two equal-sized leaflets which are individually hinged at the base ring. Each leaflet is essentially flat and approximately semicircular in shape. Four butterfly-shaped hinges, two for each leaflet, serve to both restrain the leaflets and allow for a limited range of rotation. During forward flow the two leaflets rotate out of the base ring to an angle of 85° such that their curved aspects are directed downstream. Upon deceleration and reverse flow the leaflets rotate back into the valve base-ring until their linear aspects meet and rest against each other. The valve design allows for a finite amount of reverse flow through the closed valve.

2.3 LASER-DOPPLER ANEMOMETER

2.3.1 Description of Apparatus

Velocity data were obtained through the use of a laser-Doppler anemometer (LDA) for both the steady-flow and pulsatile-flow experiments. Principles of the LDA technique have been given elsewhere (e.g., Menon, 1982; Yoganathan, 1978;

Figliola, 1979; Whatley, 1981). The LDA is a velocity-measuring apparatus that i) requires no probe in the flow, ii) requires no calibration, and iii) can measure flow reversals. In dual beam mode, as used for these investigations, the LDA operated on the principle that the crossing of two coherent laser beams created a fringe pattern at the beam crossing from the interference of the wave fronts. The distance between adjacent fringes, called the fringe spacing, could be calculated from the wavelength of the laser beams and the angle of their intersection. Particles moving through the fringe pattern produced a Gaussian-shaped intensity variation of scattered light. The scattered light was collected by a photomultiplier and converted into a voltage signal. The frequency of this voltage signal was determined using a phase-locked loop circuit. This circuit and associated controlling logic comprised the LDA signal processor which for this case was called a "tracker." The inverse of the voltage-signal frequency was the time taken by a particle to cross a pair of fringes and, since the fringe spacing was known, the velocity of the particle was obtained. Flow reversals could be measured if one of the incident laser beams was frequency shifted with respect to the other. Zero velocity then no longer corresponded to a frequency of zero but rather to the shifting frequency. Negative velocities could then be distinguished from positive ones down to that negative velocity which after the frequency shifting corresponded to a frequency of zero.

A schematic of the LDA used for these investigations is given in Figure 6. The Helium-Neon (He-Ne) laser was a Spectra-Physics model 124A with a maximum power output of 15 milliwatts and a wavelength of 632.8 nanometers. Once leaving its source, the laser beam was directed into an optic unit (DISA 55L78) in which it was split and realigned. In this beam splitter the two laser beams were separated a distance of 38 mm. One of the split beams was frequency shifted by 40 MHz in the light-modulating, acousto-optic cell (commonly called a "Bragg

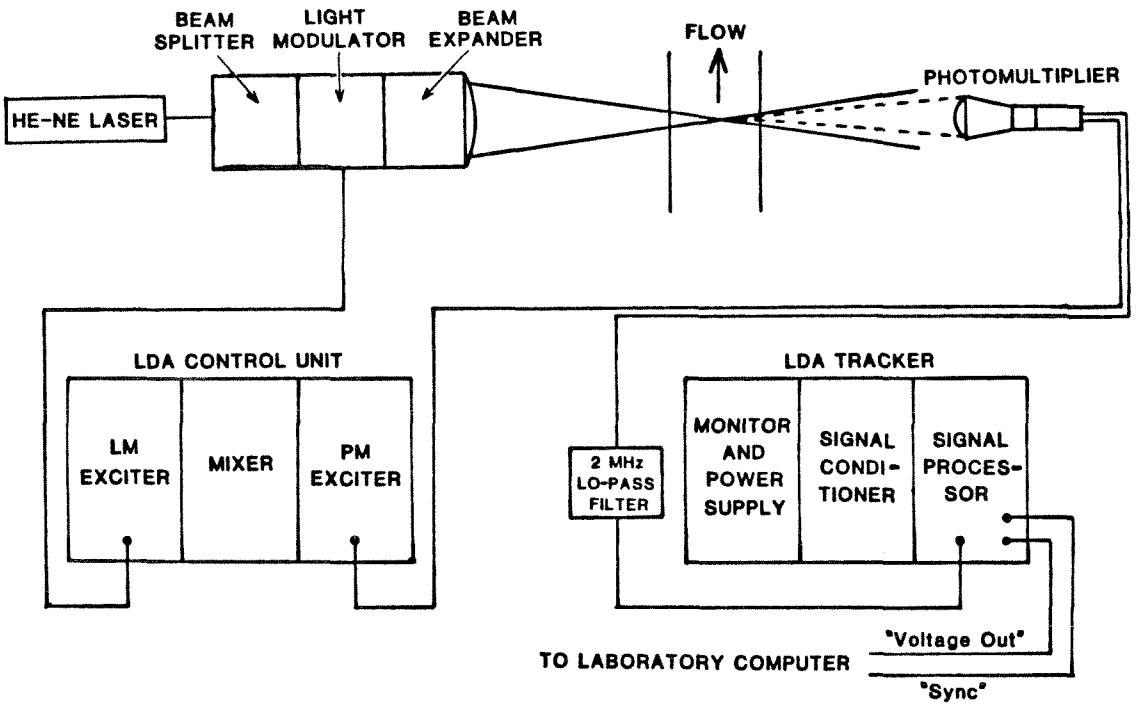

Figure 6. Diagram of the laser-Doppler anemometer apparatus used for the present investigation. The LDA was operated in the dual-beam, forward-scatter mode.

cell"). The other split beam was directed around the Bragg cell in the light modulator and remained unshifted. A beam expander (DISA 55L77) was used so that when the two split beams intersected, the ellipsoidal LDA probe volume at the beam intersection measured 0.06 mm wide and 0.2 mm long based on the $1/e^2$ intensity points. The LDA *measuring* volume was the effective fraction of the probe volume in which Doppler measurements were possible. The extent of the measuring volume was difficult to determine, however, as Buchhave, et al. (1979) relate, since it depended upon the field of view of the detector, the overall gain of the LDA, and the mode of signal processing. A lens with a focal length of 120 mm, placed after the beam expander, caused the two split beams to intersect. The half-angle between the beams upon intersection in air was 9.0°. This angle gave a calibration factor of 202 cm/s/MHz. The photomultiplier used a lens of 8.25 diopters with a focal length of 105 mm.

The LDA Control Unit (DISA 55L70) consisted of a Light-Modulator (LM) Exciter (DISA 55L74), a Range Translator or "Mixer" (DISA 55L72), and a PM Exciter (DISA 55L76),. The LM Exciter provided the 40 MHz signal which drove the Bragg cell. The Mixer was used to translate the shifted laser beam by a selectable amount. The mixing value was usually set at 39.80 MHz so that the 40 MHz shifted beam would be translated by only 0.20 MHz. For extremely high values of the mean velocity in the measuring volume, the Mixer was incremented in steps of 0.20 MHz until optimum tracking by the LDA was obtained. For extremely low and negative values of the mean velocity in the measuring volume, the Mixer was decremented in steps of 0.20 MHz. The PM Exciter modulated the voltage and current characteristics of the photomultiplier and was operated in "AUTO" mode.

The LDA Tracker consisted of a Monitor and Power Supply Unit (TSI 1091), a Signal Conditioner (TSI 1051), and a Signal Processor (TSI 1090). The Monitor

and Power Supply displayed the output from the Signal Processor after the signal had passed through the Signal Conditioner. The Signal Conditioner filtered and amplified the Signal Processor output. The Signal Conditioner, however, was not used for the present study because the laboratory computer read and displayed the velocity data directly. Reference to the monitor was therefore unnecessary and, hence, no signal conditioning was required. The input to the Signal Processor was the photomultiplier output after this output had been passed through a 2.0 MHz lo-pass filter. The meter on the Signal Processor was set on "track" and reference was made to the "samples/sec" scale to determine the tracking level during an experiment. The range of the Signal Processor was set at one volt per MHz. Tracking was set on "automatic." The gain of the input was advanced until the "out of range" indicator light was flickering. On occasion the LDA would try to track noise when the "out of range" light was flickering. In those cases the gain was turned down until the LDA was again tracking on signal. A quick check of whether the LDA was tracking on signal or noise was to simply block the optical path to the photomultiplier. If tracking ceased when the photomultiplier was blocked then the LDA was tracking on signal. Else, the LDA was tracking on noise. The outputs from the Signal Processor were "voltage out" and "sync" and were both read into the laboratory computer via the interface described below. The "voltage out" output was the voltage that was proportional to the velocity in the LDA measuring volume. This "voltage out" signal was updated only after a sufficiently strong scattering signal from a particle was collected by the photomultiplier. Otherwise, the "voltage out" output was held at the voltage of the most recent update. The "sync" output was a small voltage spike which signaled that a newly updated voltage was available at the "voltage out" output. As such, the "sync" output was also called the LDA "data-ready" signal.

2.3.2 Operational Characteristics

By its nature the LDA required that the flow section be transparent. The flowing fluid also had to be transparent and contain small, suspended particles to act as the light-scattering centers. A transparent fluid would allow the highest signal-to-noise ratio by minimizing interference with the scattered-light signal emitted from the LDA measuring volume. On the other hand, some particles were necessary in the flow to scatter the light from the measuring volume. There was, therefore, a trade-off between transparency and the density of light-scattering centers.

For the current work the normal-saline solution described earlier was adequate on both counts when "lightly" seeded with cornstarch. An amount of this cornstarch seeding was added to raise the particle density to a level which gave an LDA tracking rate of approximately 3000 Hz. During an experiment the seeding was varied when necessary to maintain the tracking rate at the desired level. In practical terms, only a very small "dash" of cornstarch seeding of about 0.1 milliliters in volume was necessary to achieve the desired tracking rate. The cornstarch particles were also quite small, being only about 10 micrometers in diameter, and thus for low particle densities did not significantly affect the transparency of the normal-saline solution.

Another constraint on the size of the particles used as the light-scattering centers was that they be small enough to faithfully follow the turbulent flow. Buchhave, et al. (1979) used the turbulent microscales of length and velocity as defined by Kolmogorov (1941) to determine the largest particle size which would introduce no more than 1% error in the velocity. They found that for turbulent pipe flow of water at 100 cm/s, the maximum particle size was around 49 micrometers. The cornstarch particles with diameters of approximately 10 micrometers were therefore small enough so that, except for perhaps the

most extreme cases of turbulence intensity, they followed the flow quite well for the present investigation.

The seeding was added to the fluid by introducing a small volume of a well-mixed, normal-saline solution having a very high-particle density into the fluid reservoirs of the two flow loops. The particles were then dispersed throughout the reservoirs by the mixing effect of the fluid-return lines. The particles remained fairly well dispersed during each of their flights of about one-minute duration through the flow loops before returning to the reservoirs. A slight level of settling out of the particles was noticeable in the flow loops over the course of several hours but was readily compensated for by the addition of another smaller "dash" of the cornstarch to the normal-saline solution.

An attribute of the LDA tracker was that the particle density could affect the tracker's mode of operation (Buchhave, et al., 1979; Kreid, 1974). The tracker could be operated in either continuous-signal mode or burst-signal mode. In continuous-signal mode the tracker output was proportionate to the velocity in the measuring volume nearly all the time. In this mode, therefore, the tracker required a signal comprised of the scattered light from many particles in the measuring volume simultaneously. That is, this mode required high-particle densities. In single-burst mode the tracker output was proportionate to the velocity in the measuring volume at those instances when a particle was present. Thus the burst-signal mode required a signal made up of the scattered light from a succession of single particles in the measuring volume. That is, this mode required low-particle densities. Usually, however, the LDA tracker attempted to operate in continuous-signal mode even for quite low-particle densities. Forcing the tracker to operate only in single-burst mode thus required that the gain on the input signal be lowered so that only the highest intensities of the scattered light from a particle were allowed to exceed the

signal drop-out level of the tracker. By keeping the level of seeding at a sufficiently low level and lowering the gain on the input signal the LDA tracker was operated in single-burst mode for the present investigations.

Verification of the single-burst mode of operation of the tracker could be made by estimating the effective particle density and determining the probability of more than one particle in the measuring volume at one time. The effective particle density could be determined from the average flux through the measuring volume and the average LDA tracking rate. As indicated earlier, however, the size of the measuring volume was difficult to determine. Since the gain of the tracker was decreased to operate in single-burst mode, the measuring volume was probably significantly smaller than the probe volume. To estimate the size of the measuring volume, therefore, the conservatively large size of the probe volume was used. For an average velocity of around 100 cm/s and a probe-volume cross-sectional area of 9.425×10^{-5} cm^2, the average flux of fluid through the probe volume was 0.009425 cm^3/s. The flux of particles through the probe volume could thus be determined from the particle density. The particle density, in turn, could be determined from the tracking rate. To determine the particle density, it was assumed that effectively only one particle was in the measuring volume at a time. That this assumption was valid is shown below. The flux of particles was therefore equal to the tracking rate. For the tracking rate of 3000 Hz, the particle density was approximately 320,000 particles per milliliter. The particle density determined in this way was an *effective* particle density because not all particles in the measuring volume generated sufficiently strong scattered signals to exceed the drop-out level of the LDA tracker. The particles ranged somewhat in size and were variously shaped and thus only a fraction of the particles at any moment may have been of optimal size and been in the optimal orientation to produce a sufficiently

strong scattered signal. Given adequate mixing, however, the ratio of the number of optimally sized and oriented particles to the total number would vary randomly about some well-defined average value.

Most of the time only one strongly scattering particle was in the measuring volume at one time. This fact can be shown using a Poisson distribution (Guttman, et al., 1971). Having effectively 320,000 such particles per milliliter and sampling 3000 of them from a measuring volume encompassing only 3.77×10^{-7} milliliters, the probability of no such particles being in the measuring volume at a given time was 0.8864; the probability of one such particle being present was 0.1069; and the probability of two such particles being present was 0.0064. The probability of three or more such particles being present was 0.0003. Thus only about six percent of the time that the measuring volume contained at least one strongly scattering particle were there two such particles and only very rarely were there three or more. On the other hand, assuming, say, ten strongly scattering particles were in the measuring volume simultaneously, the effective particle density would have been 3,180,000 particles per milliliter. This density gave the contradictory results, however, that 52 percent of the time that at least one strongly scattering particle was present in the measuring volume, only one such particle was present; 31 percent of the time, two such particles were present; 12 percent of the time, three such particles were present; and less than 5 percent of the time were four or more present. In fact, the probability of ten strongly scattering particles being in the measuring volume simultaneously would have been less than one in one million. Therefore, the basis for the calculation of the effective particle density was valid and, hence, it is clear that the tracker was operating in single-burst mode throughout the experiments.

The single-burst mode of operation for the tracker was also verified during the experiments by use of a triggering oscilloscope with storage capability. The oscilloscope was set to trigger on a Doppler burst with an amplitude greater than the tracker threshold value and was connected to the amplified input port of the tracker. Visual inspection of stored bursts revealed that by far the greatest majority of bursts were the result of a single particle passing through the measuring volume.

When using a tracker in single-burst mode, a question arose regarding the magnitude of the maximum acceleration of the flow that could be measured by the LDA. The maximum accelerations for the flows in the present investigation were those associated with the velocity fluctuations. Since it was desired to determine both the mean and root-mean-square (rms) velocities from the LDA measurements, it was important to determine the extent to which the tracker followed these highly accelerating velocity fluctuations. For the tracker used in the present investigation, the frequency of the Doppler signal was required to be within 15% of that of the previous signal. Most often the LDA mixer was set so that the average frequency of the Doppler signals was about 0.65 MHz. For an average sampling rate of 1500 Hz, and the calibration factor of 202 cm/s/MHz, the maximum acceleration that the tracker could follow was about 30,000 cm/s^2. The average sampling rate of 1500 Hz used here was the actual average sampling rate for the present investigation, as related below.

The maximum acceleration in the flows studied in the present investigation exceeded the tracker maximum only in extreme cases. Assuming there was local isotropy in the turbulent flow, microscales of length and time could be defined (Kolmogorov, 1941) and used to determine the maximum acceleration associated with a given frequency of the turbulent fluctuation. For the acceleration of 30,000 cm/s^2 the microscale frequency, defined as the velocity

scale divided by the length scale, was around 2000 Hz. Spectra measured for air in fully developed turbulent pipe flow show that at 2000 Hz the energy in the flow has decreased by more than two orders of magnitude compared to the maximum (Laufer, 1954; Sandborn, 1955; Torobin and Gauvin, 1961; Hinze, 1976; Lawn, 1970). Similar results have been found for water (Martin and Johanson, 1965; Chuang and Cermak, 1967; Komasawa, et al., 1974). The amplitude of turbulent fluctuations above 2000 Hz were quite small, therefore, and contributed little to the rms velocity of the flow. Spectra for a round turbulent jet also showed the same trend for the higher frequencies (Corrsin and Uberoi, 1951) as for the fully developed turbulent pipe flow. This similarity in trends was true even in the maximum shear region of the jet. It would appear then that the limit on the maximum acceleration of the flow measurable by the LDA tracker was rarely if ever surpassed by the flows in the present investigation on a significant basis. Thus, the rms velocities presented herein were not biased significantly as a result of the maximum acceleration limit of the LDA tracker.

There were, however, several other factors which could significantly bias the results. Biasing problems stemmed from the finite size of the measuring volume, the relationship of particle flux to mean velocity, and, for the pulsatile-flow work, the use of a finite data-window size.

Biasing problems associated with the finite size of the measuring volume have caused continuous-signal LDA measurements to suffer from random phase fluctuations known as Doppler ambiguity (Berman and Dunning, 1973; George and Lumely, 1973; George, 1974; Edwards, 1981). As George and Lumely (1973) state, these phase fluctuations were generated by the finite transit time of particles through the measuring volume as well as both mean velocity gradients and turbulent velocity fluctuations across the measuring volume. Particles arriving at the measuring volume at slightly differing and unknown times and

yet simultaneously passing through different regions of that volume produced a spectral broadening about the frequency of the mean velocity. This spectral broadening was interpreted as turbulent fluctuation even for cases where by design there was no such fluctuation.

Single-burst LDA measurements were, however, generally free from this Doppler ambiguity (Johnson, 1973). Since the scattered signal fed to the signal processor was most often that from a single particle, little ambiguity could arise.

The single-burst measurements, nonetheless, suffered from other biasing problems associated with the finite size of the measuring volume. In particular, the determination of the true velocity fluctuation in the flow was hampered. Particles passing through the measuring volume at separate intervals would, in general, pass through different portions of that volume. If there was an appreciable mean gradient across the finite measuring volume, the measured velocities from such particles would give rise to a finite fluctuation even for a case where fluctuations were absent. This bias has been shown to increase both as the square of the width of the measuring volume and as the square of the mean gradient across that volume (Karpuk and Tiederman, 1976). Karpuk and Tiederman (1976) found that in the limit of no mean gradient, no biasing occurred even for relatively large measuring volumes. Similarly, for an infinitesimal measuring volume, little biasing occurred for large mean gradients.

Single-burst LDA measurements also suffered from biasing problems associated with the relationship of the particle flux to the mean velocity. Here, the determination of both the true mean velocity and the true velocity fluctuation in the flow was hampered. The velocity was sampled only at those random times during which there happened to be a particle in the measuring volume. Biasing occurred in the randomly sampled data because a larger than

average volume of fluid passed through the measuring volume when the velocity was faster than the mean, and vice versa (McLaughlin and Tiederman, 1973). McLaughlin and Tiederman (1973) point out that for uniformly dispersed scattering centers, the arithmetic mean of the velocities of all particles passing through the measuring volume was biased towards a higher value than the true mean. On the other hand, the fluctuating velocity was biased towards a lower value. Thus the major problem with single-burst LDA measurements has been, as Buchhave, et al. (1979) noted, the extraction of unbiased statistical quantities from the randomly sampled data.

For single-burst LDA measurements, many investigators have estimated the extent of the bias which arose from both the finite measuring volume size and the relationship of particle flux to mean velocity (McLaughlin and Tiederman, 1973; Barnett and Bentley, 1974; Kreid, 1974; Karpuk and Tiederman, 1976; Buchhave, et al., 1979). When straight-forward arithmetic averaging was used, these investigators estimated that the mean velocity was in error as much as +5% at a turbulence intensity of 25% to 30% (McLaughlin and Tiederman, 1973; Barnett and Bentley, 1974; Buchhave, et al., 1979), and up to +15% at a turbulence intensity of 50% (Buchhave, et al., 1979). Similarly, the rms velocity was in error as much as -10% at a turbulence intensity of 50% (Karpuk and Tiederman, 1976; Buchhave, et al., 1979). Earlier investigations gave estimates of around -10% error in the rms velocities for turbulence intensities of only 25% to 30% (McLaughlin and Tiederman, 1973; Barnett and Bentley, 1974). Overall, the mean velocity determined from the single-burst measurements was higher than the true mean while, conversely, the velocity fluctuation determined was lower than the true fluctuation.

To completely remove the biasing described above for the single-burst LDA measurements, weighting the data by the inverse of the instantaneous velocity

vector would be required (McLaughlin and Tiederman, 1973). Since this velocity has been rarely known, the inverse of the streamwise component of the velocity was used to minimize the biasing effects (McLaughlin and Tiederman, 1973; Barnett and Bentley, 1974; Karpuk and Tiederman, 1976). Another approach has been to use time averaging of the data (Kreid, 1974; Dimotakis, 1976). When the time of each velocity sampling was available, time averaging was generally superior to arithmetic averaging. Kreid (1974) has shown that for time-averaged results, sample biasing only became significant very near the wall, especially where the measuring volume was truncated by the presence of the wall. Dimotakis (1976) has also shown that time averaging minimized sample biasing especially for high-mean sampling rates. Away from the immediate vicinity of the wall and for sufficient sampling rates, therefore, time averaging the data resulted in lower biasing than that listed above for the arithmetic-averaging case, if not eliminating it altogether.

A final source of sample bias arose in the pulsatile-flow case from the use of a finite data-window size. This bias was a result of large mean accelerations of the flow through the measuring volume and affected only the determination of the velocity fluctuations. Time averaging eliminated this bias with respect to the mean velocity. When large mean accelerations were present, as in the pulsatile-flow case, the individual LDA measurements were grouped into data windows in order to extract values of the mean and fluctuating velocity components during that time interval. A significant acceleration caused an appreciable change in the mean velocity during the finite time interval of the data window. This change in the mean velocity was then interpreted erroneously as fluctuations in the velocity.

The extent of the bias arising from the data-window size was potentially large but in practice tended to be notable only for the highest accelerations. For

reasons described below, the pulsatile-flow data were collected in 20-millisecond windows. From the pulse-duplicator flow curves, it was determined that the maximum rate of change of the flow rate over 20 milliseconds was approximately 5 L/s^2. For a cross-sectional area of 5.07 cm^2, this maximum rate of change gave a maximum flow acceleration of around 1000 cm/s^2. Using a worst-case analysis wherein measurements happened to be made at both extremes of the data window, an rms velocity of 17 cm/s was determined. During most of the acceleration phases of the flows in the present investigation the rms velocity determined by visually fitting the raw data was larger than that from this worst-case analysis. The rms velocity was generally in error from 10% to 15% high. Therefore, in practice, the bias in the rms velocities introduced by the flow acceleration was not excessive. Moreover, this bias was in the opposite sense as that from the particle flux to mean velocity relationship. Thus the errors in the rms velocities determined using time averaging of the single-burst LDA measurements were in all likelihood quite small.

2.3.3 Velocity Measurements

The velocity measurements were made at various locations in the flow by translating the aortic-valve flow section relative to the fixed laser-optics system. The relationship of the flow section to the incoming laser beams is shown in Figure 7. The top of Figure 7 depicts the case where the axial velocity is to be measured. The bottom of Figure 7 depicts the case where the velocity in the non-axial direction is to be measured. For these investigations the axial velocity was defined as parallel to the z-axis. The orthogonal, non-axial velocities were defined as parallel to the x- and y-axes. The velocities in the y-direction were measured by rotating the laser optics 90° with respect to the orientation of the optics when the data in the z-direction were collected. The velocities in the

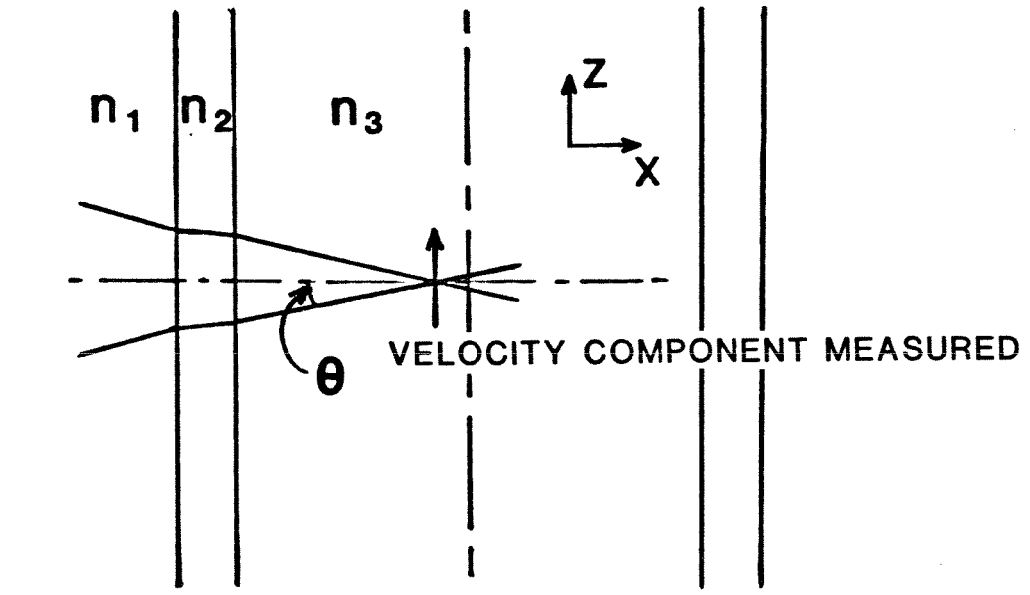

AXIAL
(Φ=0)

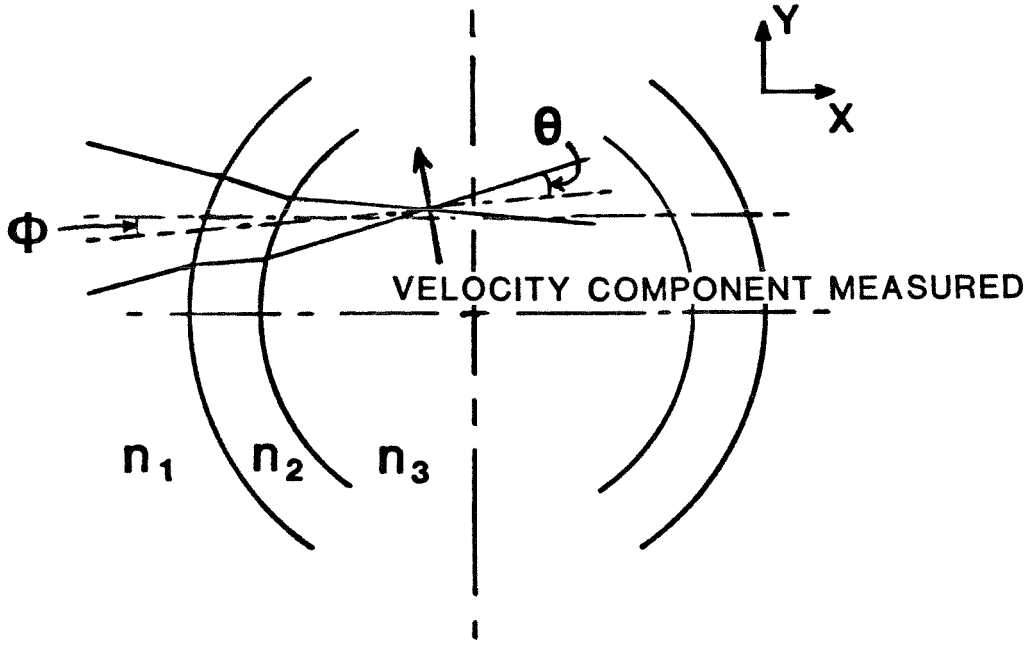

NON-AXIAL

Figure 7. LDA laser beams crossing in a cylindrical flow channel for velocity-component measurements in the axial and non-axial directions. The angle Θ is constant for all positions in the axial case but varies significantly with position for the non-axial case. The skew angle Φ, which is everywhere zero for the axial case, is generally small but non-zero for the non-axial case.

x-direction were measured by rotating the flow section 90° with respect to its orientation when the data in the z- and y-directions were collected.

For each experiment the velocity data were collected at numerous positions in a given cross section of the flow section. The positions of the beam intersection were computed as a function of the flow-section location using Snell's law (Hagelberg, 1973) and the indices of refraction of air, Lucite®, and the normal-saline solution. The refractive indices of air, Lucite®, and water were given earlier. The refractive index for the normal-saline solution differed only slightly from that for water, the former being 1.333 and the latter being 1.330. Using an iterative procedure, the computer determined the necessary translation of the flow section for a desired translation of the beam intersection inside the tube. Two different computer routines were needed, one each for the axial and non-axial orientations of the laser optics. For the axial case, the curvature of the tube had a symmetrical effect on the incoming laser beams, as can be seen in Figure 7. Thus the angle Θ remained constant for all positions of the beam intersection. The LDA calibration factor, a function of Θ, therefore also remained constant. Moreover, the calibration factor in the flow was by symmetry equal to that in air, as Yoganathan (1978) and Whatley (1981) have shown. Therefore, only a single computation of the incident-beam path was necessary to fully determine the beam-intersection position for each data-plane grid location. For the non-axial case, however, tube curvature generally affected the two laser beams asymmetrically. As a result, for the non-axial case Θ was not a constant but rather a function of the position of the beams in the flow section. The calibration factor, therefore, was in need of constant updating in the computer software for the non-axial case. In addition, for data collected in one non-axial direction (say 'y') at grid points not on the diameter of the tube in the other direction ('x'), the velocity component measured was slightly

skewed off-angle from the intended non-axial component. This skewness is shown in Figure 7 as angle Φ. Fortunately, for the large majority of the locations at which data were collected, Φ was less than 2° and only rarely was greater than 5°. Therefore the effects of this skewness was considered to introduce little significant error in the overall data-collection methodology and went unaccounted for in the present work.

The cross section of the flow section at which the velocity data were collected was called the data plane, as shown in Figure 8. For the present work, the data plane was located at z = 31.8 mm. This data-plane location was the closest to the prosthesis that reliable LDA measurements could be made over the entire data plane. Taking data closer to the prosthesis was hindered by the relatively complicated geometry of the sinuses.

The locations at which data were collected on the data plane were chosen by considering a 20-by-20 square-mesh grid imposed on the circular cross section of the tube, as depicted in the bottom of Figure 8. The grid points shown correspond to the corners of the mesh pattern with the center point of the grid coinciding with the center point of the circle. No points in the grid which lay outside of the circle defined by the inner wall of the tube are shown since no velocity data were taken at these points. As shown in Figure 8, Δ was defined as the shortest distance between nearest neighbors in the square grid. For the 20-by-20 grid Δ had a length of 1.27 mm.

For referencing purposes the grid points were indexed from 1 to 317 as shown in Figure 9. With this numbering scheme, the grid point numbered 159 was on the center line of the tube. Points numbered 1, 11, 23, 39, 55, 149, 169, 263, 279, 295, 307, and 317 lay exactly on the wall of the tube by definition and therefore the velocity at these points was always zero.

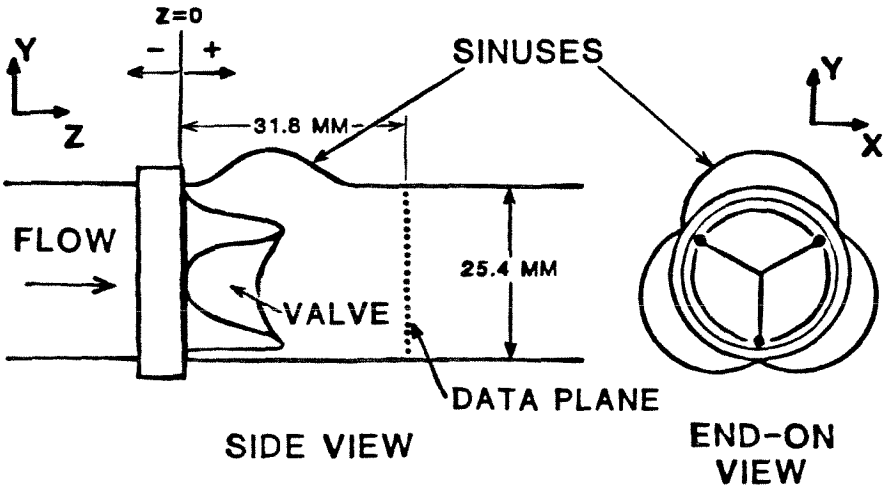

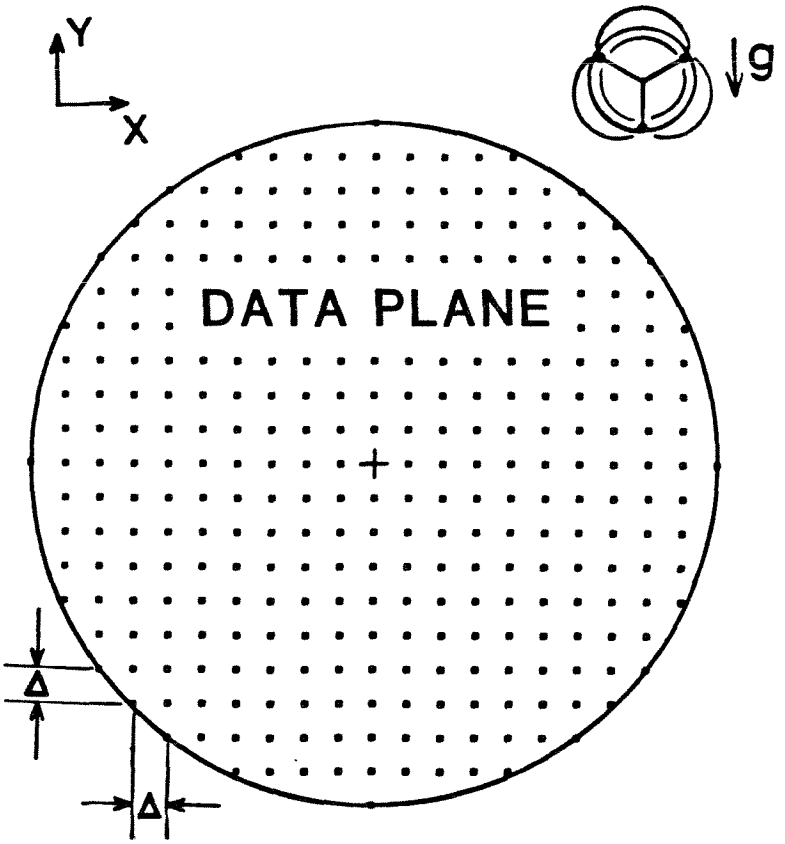

Figure 8. Detail of the aortic-valve flow section showing the location of the data plane. The data plane contains the grid points at which the velocity data were taken at that cross-section of the flow channel. Note the definition of Δ.

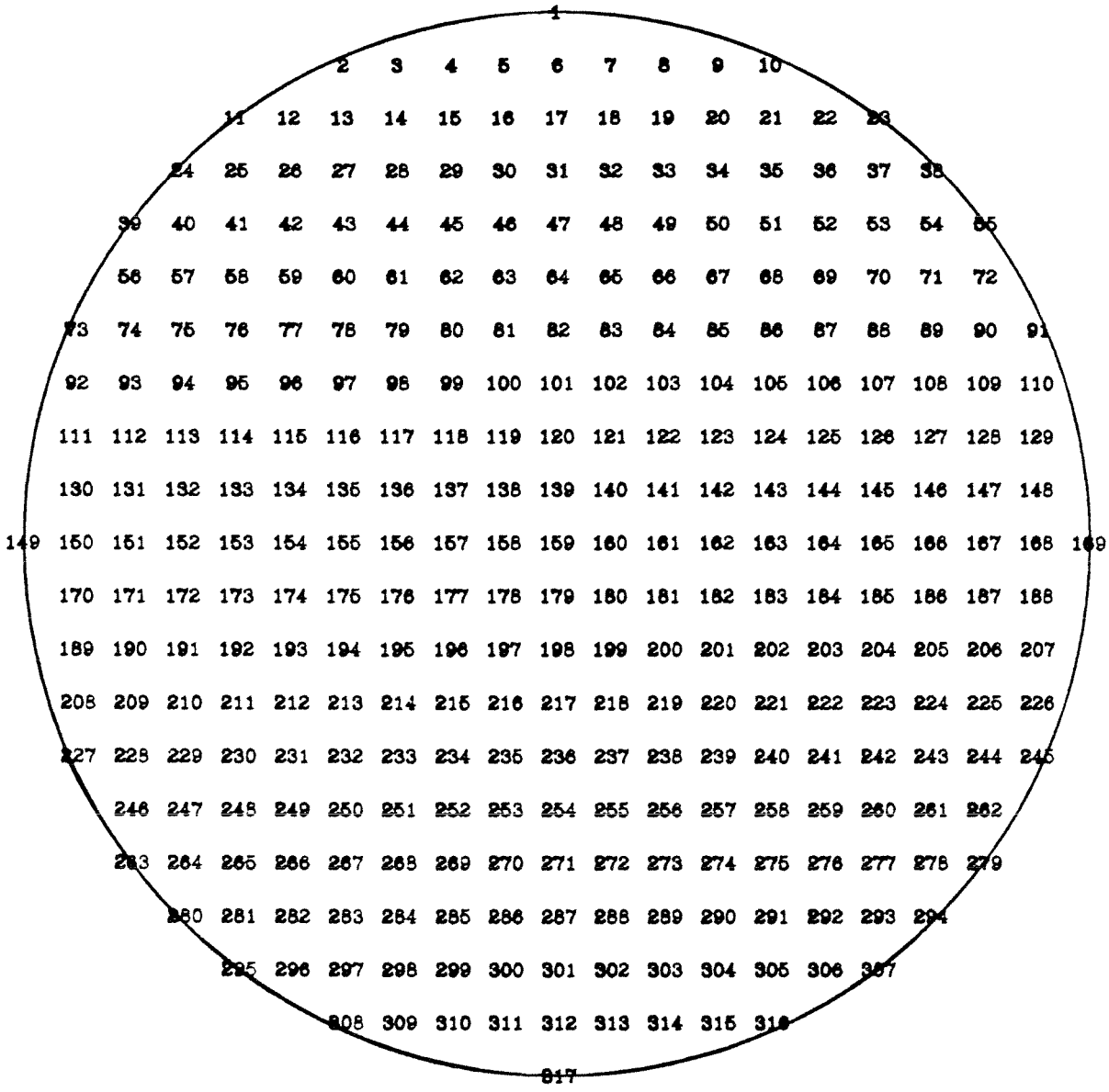

Figure 9. Index numbers for the grid points on the data plane. The point numbered 159 of the grid coincides with the centerline of the tube. Points numbered 1, 11, 23, 39, 55, 149, 169, 263, 279, 295, 307, and 317 are exactly on the wall of the tube.

A 20-by-20 grid was chosen for this work as a trade-off between resolution in space and practical limitations of time. Important flow structures studied in this work included, for example, separated-flow regions and stagnant zones. It was felt that the resolution of 1.27 mm allowed by the 20-by-20 grid was sufficient to study such structures. With respect to time limitations, the 20-by-20 grid created over 300 locations for data collection. It took approximately two minutes per grid point for the steady-flow experiments and six minutes per grid point for pulsatile-flow experiments. Thus data collection and transfer time alone amounted to roughly ten hours and thirty hours per experiment for steady-flow and pulsatile-flow experiments, respectfully. For a 25-by-25 grid, with a point-to-point resolution of 1.0 mm, the number of points at which measurements would be required was greater than 450, or approximately a 50% increase in time. It was thus felt that any further increase in the number of grid points would have been prohibitive with respect to timing requirements.

2.4 COMPUTER INTERFACE

2.4.1 Laboratory Hardware

A Digital Equipment Corporation (DEC) PDP-11/34A mini-computer was used in the laboratory for all data collection and reduction. For collecting data the computer was equipped with an analog-to-digital (A/D) converter (AD11-K) and two real-time programmable clocks (KW11-K). The AD11-K and KW11-K were connected logically to one another through the computer unibus, as shown in Figure 10. During an experiment, the AD11-K sampled the velocity data signal from the LDA, the aortic-pressure (AP) and ventricular-pressure (VP) data signals from the two pressure transducers, and the volumetric-flow (VF) data signal from the electromagnetic flowmeter. The velocity data line was connected

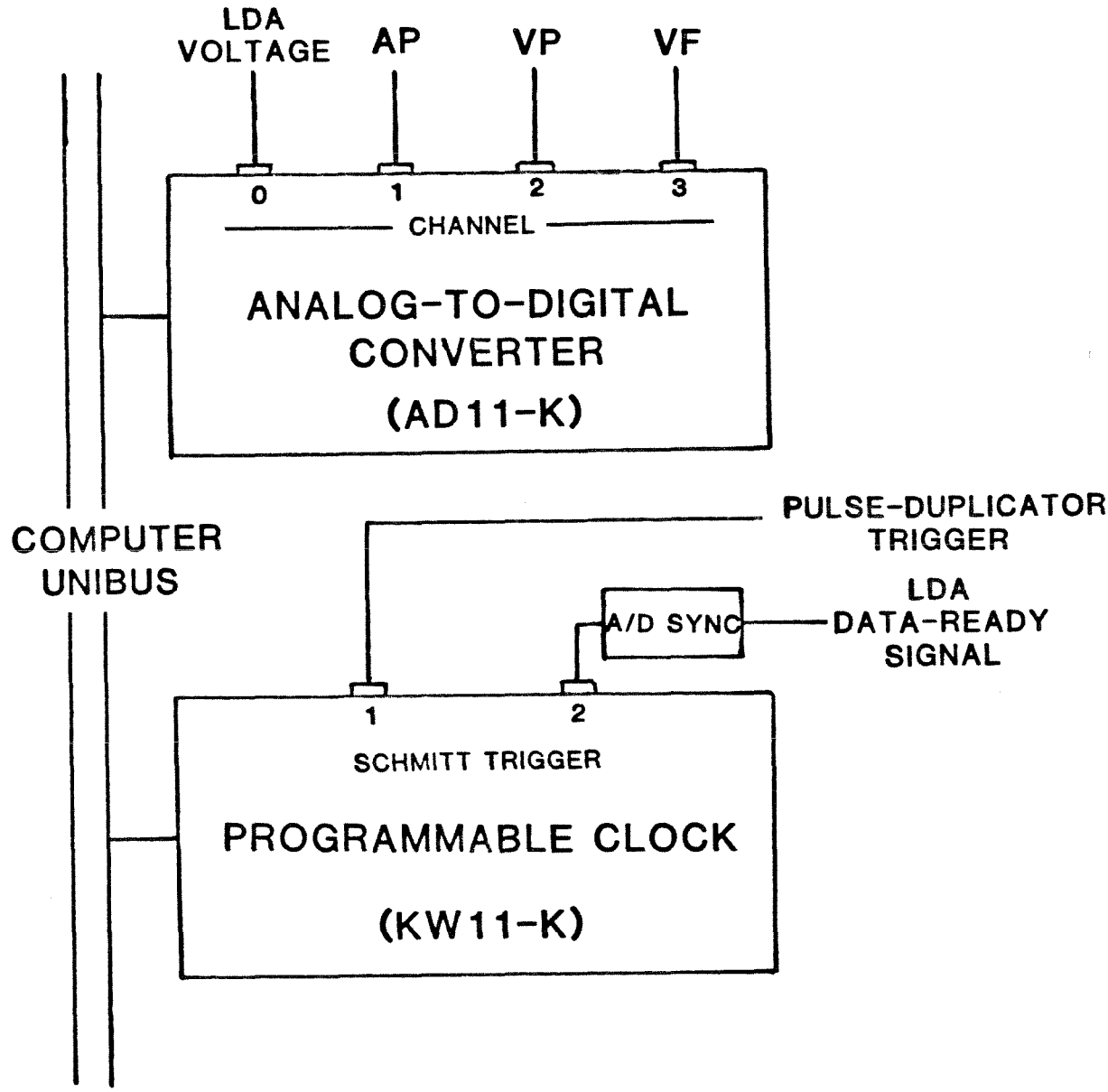

Figure 10. Diagram of the interface of the laboratory computer to the data collection equipment. Data were collected using the analog-to-digital converter under the timing control of the programmable clock.

to channel 0 of the AD11-K, the AP data line to channel 1, the VP data line to channel 2, and the VF data line to channel 3. Timing considerations were handled through two Schmitt triggers on the KW11-K. Schmitt trigger 1 (ST1) was connected to the trigger output from the pulse-duplicator control box. Using ST1, all data sampling for pulsatile-flow experiments was referenced in time to the beginning of a pulse. Schmitt trigger 2 (ST2) was connected to the data-ready signal ("sync") of the LDA tracker. Using ST2, the computer was programmed to read the velocity data from A/D channel 0 only after this data had been updated by the LDA electronics.

The resolution of the AD11-K depended upon its input voltage range and, for the velocity data, the LDA calibration factor. The input voltage to the AD11-K was set to range from -5.0 volts to +5.0 volts. As a 12-bit converter, the AD11-K divided this range into 4096 divisions. The finest resolution of the AD11-K was therefore 0.002441 volts. The pressure amplifiers were both calibrated for a conversion factor of 13.332 kPa per volt. Thus the smallest pressure difference the AD11-K could resolve was 0.0325 kPa. The electromagnetic flowmeter was calibrated for a conversion factor of 20.00 L/min/volt. Thus the smallest difference in the flow rate the AD11-K could resolve was 0.0488 L/min. For the velocity data, the LDA calibration factor was 202 cm/s/volt in air. The smallest velocity difference the AD11-K could resolve was therefore 0.493 cm/s/volt. As discussed above, however, for the non-axial case the calibration factor was a function of the location of the measuring volume in the flow. The largest the calibration factor became was 240 cm/s/volt at the grid points numbered 2 and 308. The smallest the calibration factor became was 144 cm/s/volt at the grid points numbered 10 and 316. The smallest velocity difference the AD11-K could resolve for these two cases were, respectively, 0.586 cm/s and 0.351 cm/s. For the magnitudes of the pressure, volumetric-flow, and velocity data collected in

the present investigation, these resolution limits were adequately small, that is, they did not significantly hinder the interpretation of the results.

Noise in all data signals was minimized by having the equipment share the same physical ground. When the computer was installed in the laboratory a heavy-duty ground was provided for the exclusive use of the computer power supply. All experimental equipment was subsequently connected to this power supply via the unswitched plug receptacles on the supply unit. Ground loops and other grounding problems were thereby averted.

Because the cable length required by the laboratory layout was greater than 15 meters, the relatively diminutive data-ready signal of the LDA tracker suffered significant signal-loss. This loss-of-signal problem is shown in Figure 11a. In order to be sensed by the KW11-K at its ST2 port, the data-ready signal was required to start lower than and then rise above a preset threshold value. This requirement insured that an ST2 "event" would be generated by the KW11-K in response to the incoming data-ready signal. An "event" was the modality by which the KW11-K communicated to the AD11-K and other hardware that a data-ready signal had been received. Unfortunately, the data-ready signal which arrived at the ST2 port was often too small to be reliably sensed by the KW11-K and no event would be registered. To solve this problem a signal-enhancing, electronic box, denoted "A/D Sync," was built and placed in the data line near the tracker. Upon receiving the data-ready signal, the A/D Sync box produced a 5-volt, 10-microsecond square-wave. This more robust square-wave pulse was transmitted through the BNC cable to the KW11-K ST2 port with minimal distortion, as shown in Figure 11b. The reliability of sensing the data-ready signal of the tracker was thereby greatly increased. Loss-of-signal problems were not significant for the other data lines.

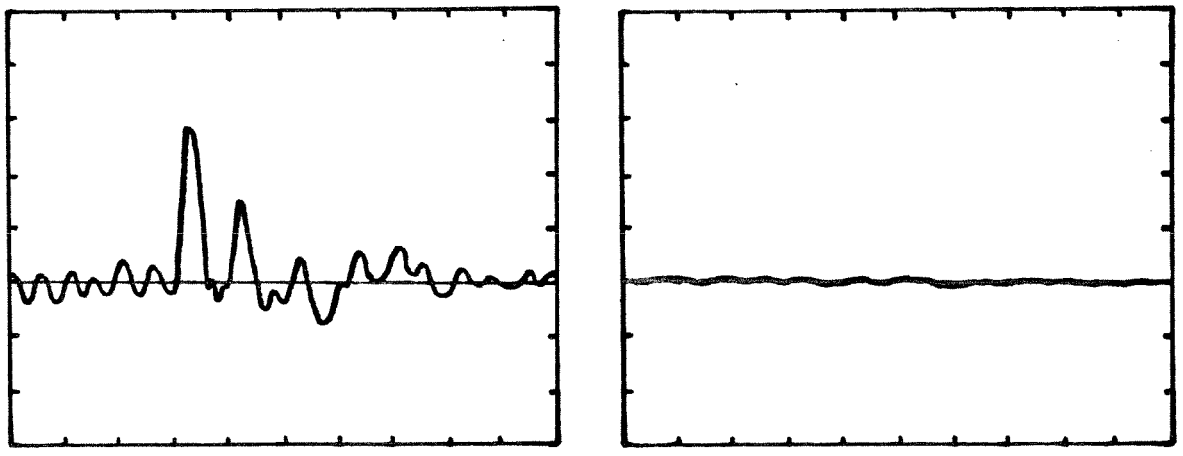

Figure 11a. LDA data-ready signal leaving the tracker (left) and arriving at the computer (right) after passing through the 15-meter cable between the two apparatus. The signal suffered significant loss-of-signal due to excessive cable length. Vertical scale is 0.5 volts per division. Horizontal scale is 0.1 microseconds per division.

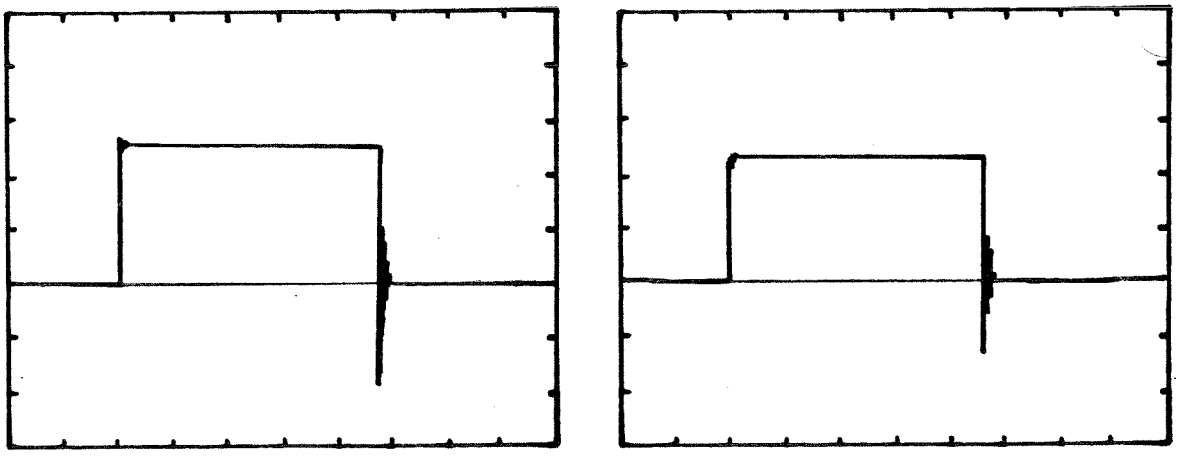

Figure 11b. "Enhanced" LDA data-ready signal leaving the "A/D Sync" electronic box (left) and arriving at the computer (right) after passing through the 15-meter cable between the two apparatus. The "A/D Sync" box enhanced the signal so that it would be sensed reliably at the computer. Vertical scale is 2.0 volts per division. Horizontal scale is 2.0 microseconds per division.

2.4.2 Data Collection

The data-collection logic was designed to collect the velocity data at a maximum sampling rate of 2500 Hz and the AP, VP, and VF data at a maximum sampling rate of 250 Hz. A timing routine insured that no two velocity samples were closer together in time than 40 microseconds. Similarly no two AP, VP, or VF samples were allowed closer together than 400 microseconds. These maximum sampling rates were the highest possible without encountering serious data-storage problems, as will be discussed below. Larger rates would not have been significantly more helpful in any event since for the present investigation only the first and second moments of the data were of interest and, in particular, no spectral analyses were done. In fact, much lower sampling rates provided adequate accuracy in the experimental results as exemplified by good reproducibility.

Actual sampling rates were somewhat lower than the maximums. The rates averaged 1500 Hz for the velocity data and 200 Hz for the AP, VP, and VF data. These lower rates were caused by the fact that the LDA could measure the velocity only when a particle was present in the LDA measuring volume. For the present investigation, particles tended to arrive at the measuring volume in a random fashion. ST2 events were thus generated only at those random times when the LDA updated its output of the measured velocity. Because of this randomness, the computer often had to wait a significant time for an ST2 event. This ST2 wait directly increased the 40-microsecond timing interval between velocity samples and hence lowered the sampling rate. The AP, VP, and VF rate was also lowered but less dramatically so because the time between these samples was much longer than that for the velocity-data case.

The sampling rates of the data signals, therefore, varied directly with the tracking level of the LDA tracker. A high tracking level shortened the ST2 waits

on the average and the sampling rate rose. A low tracking level lengthened the ST2 waits on the average and the sampling rate fell. For very high, or good, tracking levels, a sampling rate as high as 2200 Hz was possible for the velocity-data signals. For very low, or poor, tracking levels a sampling rate of 800 Hz was measured. Most of the time the sampling rate ranged between 1200 Hz and 1800 Hz. For the AP, VP, and VF data signals, the sampling rate generally ranged between 180 Hz and 220 Hz for lower and higher LDA tracking levels, respectively.

An important ramification of this tracking level to sampling-rate relationship was that it provided a way to keep the sampling rate relatively constant for all data collection. The tracking level could be raised or lowered, for example, by varying the concentration of the cornstarch seeding in the normal saline used for the experiments. Hence, to a degree, the sampling rate could be controlled by simply adding more seeding or diluting some out. Other ways to modify the tracking level included changing the "gain" on the tracker and switching the mixing frequency of the mixer. When used in concert, these controls on the tracking level could often vary the sampling rate over quite a broad range. The design of the software thus provided a way to control the sampling rate so that it could be maintained relatively constant from grid point to grid point and from experiment to experiment.

For these investigations full advantage was taken of this sampling-rate control feature of the software design. The sampling rate was kept relatively constant for all grid points and experiments so that the comparisons of the results would be for values computed from similar data bases.

All data were collected as series of one-second records. For the sampling rates used in the present investigation, dynamic-memory limitations of the computer prevented longer records. Since the time of each velocity read was

collected along with the velocity value itself, a single, one-second record required up to 5000 storage locations in dynamic memory. The AP, VP, and VF data and the time they were collected required up to 1000 additional storage locations. These requirements were close to the limit of the memory during data collection and thus restricted the record length. On the other hand, it was desirable to use record lengths long enough to encompass the entire pulse interval for the pulsatile-flow experiments. The one-second record length met this criterion. Examples of one-second data records are shown in Figure 12 for the velocity, pressure, and volumetric-flow data from a pulsatile-flow experiment.

Data collection for each one-second record was initiated by an ST1 event. For both steady-flow and pulsatile-flow experiments the ST1 triggering signal was generated by the electronic control box of the pulse-duplicator. For the steady-flow experiments the control box was disconnected from the pulse-duplicator. After waiting on and receiving an ST1 event, the computer then reset the programmable clock and began waiting for an initial ST2 event to start the data-sampling loop.

After each data record had been collected, the data in the dynamic memory from that record were written onto the computer disc and a new record was collected. This write process took approximately five seconds. Successive data records were, therefore, not contiguous in time but rather about six seconds apart.

A concern therefore arose that any naturally occurring periodicities of the steady flow with periods longer than one second were ignored. Flow-visualization studies in our laboratories, however, have suggested that such longer-time-scale events did not occur. These longer periodicities were of less immediate interest in any case, since the application of this work was to implanted prosthesis where

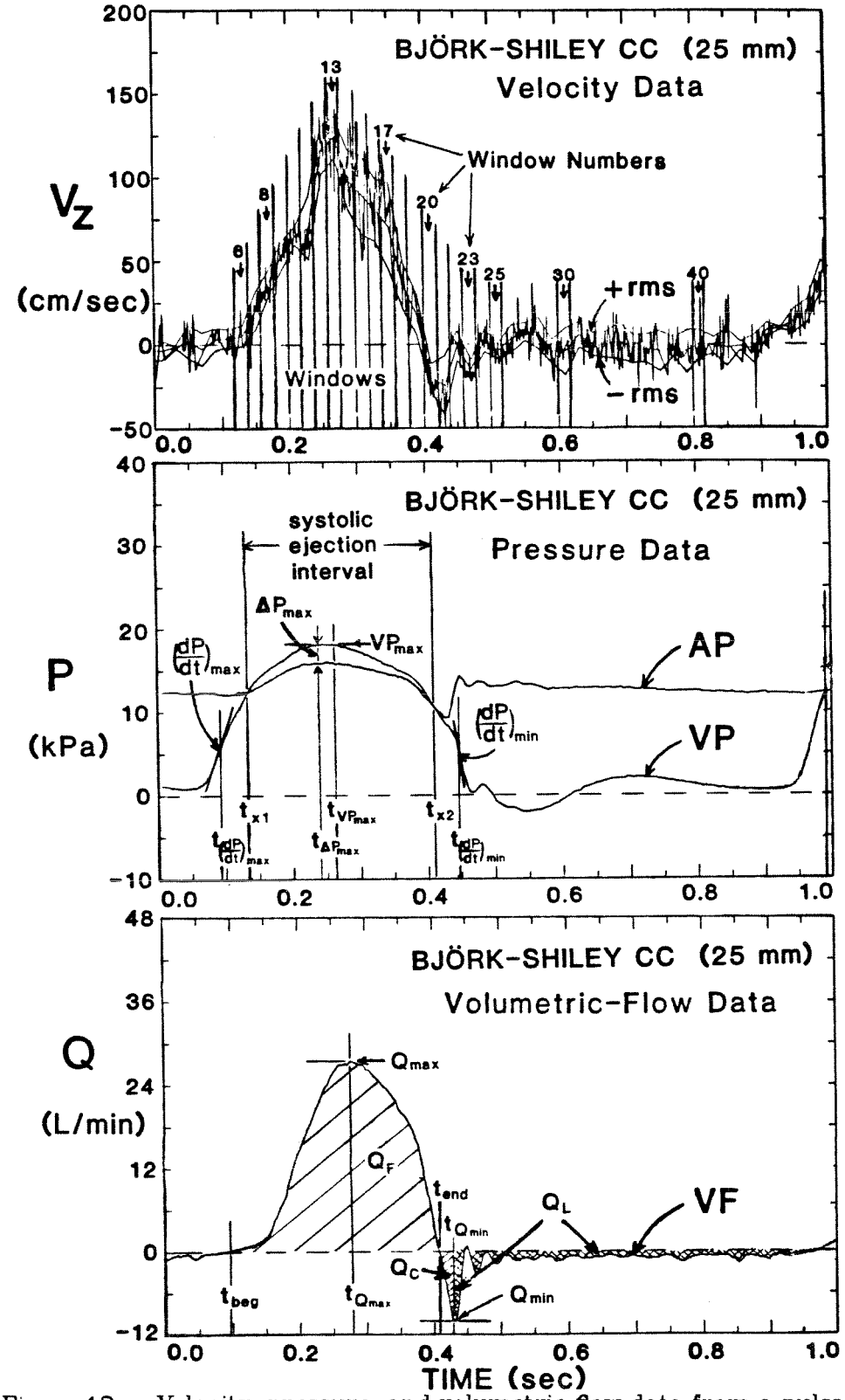

Figure 12. Velocity, pressure, and volumetric-flow data from a pulsatile-flow experiment showing the raw data as one-second records. For the velocity data, the record has been divided into 20-millisecond windows. For the pressure and flow data, several parameters are defined that were reduced from the raw data for each pulse.

there is an imposed periodicity of about one second. Hence, for the present work, collecting data as a series of one-second data records was an acceptable way to collect more data at a given grid point than the computer memory could retain at one time.

For the pulsatile-flow case, the data in the one-second data records were divided into 20-millisecond windows, as shown in Figure 12. Two opposing constraints were important when deciding on this window size. The first constraint was that of resolving variations of the mean velocity during the simulated pulse. For this investigation, the smallest mean velocity variations of considerable interest were those of about 50 milliseconds in duration which were associated with valve closure. The 20-millisecond windows provided sufficient resolution of these small, closure-related features. The second constraint was that of collecting a sufficiently large data base to obtain acceptable accuracy in the reduced data. The accuracy was determined by checking for the extent of reproducibility. Whenever the reproducibility of the results became poor, the accuracy of any one reading became increasingly suspect. Whenever the reproducibility was good, the accuracy of the results was considered acceptable on the grounds that each reading would be very close to the expectation value. Experimentally it was found that good accuracy in the results could be achieved with windows as small as 20 milliseconds. Factors affecting this accuracy are discussed below. The use of 20-millisecond windows was thus determined to be the best trade-off between resolution and accuracy constraints.

As a consequence of the 20-millisecond data windows, the amount of velocity data required for good accuracy of results at a given grid point was much larger for pulsatile-flow experiments than for steady-flow experiments. For the steady-flow case, six one-second records were collected at each point in the data plane

grid. For the average sampling rate of 1500 Hz mentioned earlier, six data records gave a data base of 9000 data points at each grid point. This large data base was found to be more than sufficient for good accuracy in the results. Furthermore, the time required to collect this amount of data was not prohibitive. For the pulsatile-flow case, thirty data records were collected. For a sampling rate of 1500 Hz, thirty records gave *for each window* a data base of approximately 900 data points at each grid point. This amount of data per window, though somewhat small, did not create problems with reproducibility and hence accuracy in our work except for the most extreme cases of turbulence intensity. Collecting significantly fewer records gave rise to significant losses of reproducibility and hence unacceptably diminished accuracy. For the larger number of records, though, time requirements began to be prohibitive. Nonetheless, it was decided to use thirty records for the pulsatile-flow work while using only six records for the steady-flow work.

2.4.3 Data Reduction

Data reduction was necessary during the experiments because the amount of data collected at the sampling rates discussed above quickly became too large for the computer disc storage capacity. For a complete experiment, data was collected at 305 grid points. For each steady-flow experiment, therefore, more than 1800 data records were generated. At the average sampling rate of 1500 Hz, each record contained the 1500 velocity data plus the 1500 corresponding time data. Approximately 5.4 million data, thus, were generated for each steady-flow experiment, not including the pressure and volumetric-flow data. The entire computer disc storage capacity was 5.2 megabytes. More than one disc would have been required, then, to store all of the raw data from a single steady-flow experiment. Each pulsatile-flow experiment would have

required more than six discs. Data reduction was thus required on-line by data-manipulation (and economic) considerations.

For the case of reducing the velocity data for steady-flow experiments, the time-averaged mean of the velocity $\langle v \rangle_{TA}$ and root-mean-square (rms) v_{rms} were estimated from each of the six one-second data records. Time-averaging was possible since the time of each velocity data sampling had been obtained from the programmable clock and stored along with the velocity data. The merits of this approach to the data reduction were discussed above in the section on the operational characteristics of the LDA. Because the velocity data could be considered to have been arriving at the A/D converter in a random fashion, for N data points $\langle v \rangle_{TA}$ was estimated as

$$\langle v \rangle_{TA} \approx \frac{1}{2T} \sum_{i=2}^{N} (v_i + v_{i-1})\, \delta t_i \qquad (1)$$

where

$$T = t_N - t_1$$

and

$$\delta t_i = t_i - t_{i-1} \quad .$$

Likewise v_{rms} was estimated as

$$v_{rms}^2 \approx \frac{1}{T} \sum_{i=2}^{N} (v'_i)^2\, \delta t_i \qquad (2)$$

where

$$v'_i = v_i - \langle v \rangle_{TA} \quad .$$

Equation (1) is the trapezoidal approximation of the integral of the instantaneous velocity over time T. Equation (2) is the back-step modification of the trapezoidal approximation of the integral of the fluctuating velocity over time T. These definitions are based on the assumption that most often only one scattering particle was in the LDA measuring volume at one time

(Dimotakis, 1976). Finally, the six mean and rms velocities computed for the six data records were then arithmetically averaged to obtain a single mean and rms velocity for each grid point on the data plane.

To reduce the velocity data for pulsatile-flow experiments, it was necessary to use a modified form of phase averaging. Phase averaging of instantaneous data allowed for the recognition of a cyclic forcing function generating a wave phenomenon which was superimposed on a time-independent mean (Hussain and Reynolds, 1970; Hussain, 1977). The phase-averaging method was predicated upon the decomposition of the instantaneous velocity as

$$v(x,t) = \langle v \rangle (x) + \tilde{v}(x,t) + v'(x,t) \tag{3}$$

where x is a representative coordinate direction, t is the time, $\langle v \rangle$ is the true mean of the velocity, $\tilde{v}$ is the statistical contribution of the imposed wave function to the instantaneous velocity, and v' is the fluctuating velocity component. For the present work $\tilde{v}$ was equivalent to the mean velocity which corresponded to each data window in pulsatile flow. The phase average was defined as

$$\langle v(x,t) \rangle_{PA} \equiv \lim_{N \to \infty} \frac{1}{N} \sum_{n=0}^{N} v(x,t+n\tau) \tag{4}$$

where τ is the period of the wave. For the present pulsatile-flow investigations, however, the wave function was not sinusoidal nor did this function have a zero mean. The time-independent mean velocity for the present investigation therefore was not equal the mean velocity which would have resulted if the forcing function were to cease. If, for the present investigation, the forcing function ceased, the mean velocity was zero. Otherwise the mean velocity was decidedly not zero but some value which was proportionate to the mean flow rate. Hence it was convenient to modify Equation (3) as

$$v(x,t) = \tilde{v}(x,t) + v'(x,t) \; . \qquad (5)$$

Here the "mean" velocity was redefined as that time-independent mean velocity which would have existed *without* the influence of the cyclic forcing function. The values of $\tilde{v}$ and v' were then computed by modified phase-averaging for each window. Therefore, for steady flow one mean and one rms velocity were associated with each point of the data grid while for pulsatile flow 50 mean and 50 rms velocities were associated with each grid point.

To reduce the AP, VP, and VF data for steady-flow experiments, the data in the six one-second data records were handled in the same fashion as for the steady-flow velocity-data case. Time-averaged mean and rms values of AP, VP, and VF were determined for each of the 305 grid points at which data were taken. These 305 time-averaged mean and rms values were further reduced by taking their arithmetic mean. This further reduction was possible since the AP, VP, and VF data were not affected by the location of the LDA measuring volume in the flow. The reduced AP and VP data allowed for the determination of the average pressure drop across the flow-section orifice. The reduced VF data simply allowed for a check on the calibration of the electromagnetic flowmeter.

To reduce the AP, VP, and VF data for pulsatile-flow experiments, several parameters were computed from each signal as shown in Figure 12. These parameters were used both on-line to determine how well the pulse-duplicator was operating during an experiment and later off-line to characterize the simulated-pulse environment. The on-line use required that the reduced parameters be displayed at the terminal on a point-by-point basis. The off-line use required that the reduced parameters be stored for later reference. For the off-line use, all reduced parameters were arithmetically averaged for the 305 data-plane grid points. The standard deviation which corresponded to each average was also computed and was used as a measure of the reproducibility of

the pulse-duplicator during a given experiment. The parameters which were reduced from the raw data were as follows. From the AP data the average aortic pressure was determined. From the VP data the maximum and minimum ventricular pressures and the times of their occurrence relative to the beginning of the record were determined. Also determined from the VP data were the maximum and minimum rates of ventricular-pressure change and the times of their occurrence. Additional parameters were obtained by subtracting the AP data from the VP data. These additional parameters included the maximum pressure difference and the time of its occurrence, the two pressures and times at which the pressure curves crossed, and the average pressure differences during the systolic ejection interval and during the remainder of the pulse cycle. The systolic ejection interval was defined as that time period delineated by the two times the pressure curves crossed and during which the ventricular pressure reached its maximum. The time period between two succeeding systolic ejection intervals consisted mostly of the diastolic interval. From the VF data, the maximum and minimum flow rates and the times of their occurrence were determined. Also the times of the beginning and end of the forward-flow phase of the cycle were determined. The time of the beginning of the forward-flow phase was determined as the time of the latest zero crossing of the flow curve before it rose above a given threshold value. Typically the threshold value was set at 0.5 L/min. The time of the end of forward flow was determined as the time of the next zero of the flow curve after it had dropped below the given threshold value. For pulsatile flow, the mean flow was also determined for the complete cycle. The mean flow was determined as the sum of the forward flow and the regurgitant flow. Forward flow was that flow which occurred during the forward-flow phase of the cycle. The forward flow, therefore, was equal to the stroke volume of the ventricular-pump section of the

pulse-duplicator. Regurgitant flow was that flow which occurred during the time period of the cycle other than the forward-flow phase. The regurgitant flow was further divided up into closure flow and leakage flow. Closure flow was that flow which occurred after the aortic pressure had dropped below the ventricular pressure but before the valve had closed. The time of valve closure was estimated as the time of the minimum flow rate. By simultaneously displaying the aortic-pressure and the volumetric-flow curves on the oscilloscope it was determined that the time the minimum flow rate occurred corresponded to the sharp minimum in the aortic pressure known as the dicrotic notch. The dicrotic notch is a pressure-wave reflection generated by the rapid flow deceleration upon valve closure. Thus the time of occurrence of the dicrotic notch has long been recognized as the time of valve closure. Leakage flow was that flow which occurred after the valve had closed but before the beginning of the next forward-flow phase. Finally, the root-mean-square of the flow rate during the systolic ejection interval was calculated. For each cycle, these sixteen parameters and the times associated with them were stored, the raw data was deleted, and another cycle of data was collected.

For the pulsatile-flow experiments it became necessary to provide data-rejection capabilities. The reasons for the data-rejection capabilities were two-fold. First, the velocity data from the LDA tracker suffered occasional loss of tracking. As discussed above, the LDA tracker had certain limitations with respect to the maximum accelerations that it could follow. This maximum acceleration was surpassed on occasion leading to significant data loss. Such losses were mainly the result of very large mean accelerations of the fluid through the LDA measuring volume or extremely high turbulence intensity in the measuring volume. In either case, loss of tracking resulted from two subsequent velocity-data measurements which were too widely differing. When

this loss of tracking, or data "drop-out," occurred the tracker would begin to search again for the data signal by slewing up and down its frequency range. Data were lost during the time the tracker was searching, which could last for up to 100 milliseconds. More commonly, however, data loss would be experienced for approximately five milliseconds or less. The second reason that data-rejection capabilities were necessary was that the pulse-duplicator was not entirely precise at all times in duplicating pulses. A check was kept on the performance of the pulse-duplicator by continually monitoring the pressure and volumetric-flow data on-line during an experiment. Several criteria were developed and coded, and then referenced on a cycle-to-cycle basis. Whenever any one of these criteria was violated the offending data record was rejected.

Data-rejection criteria were developed from each of the three data types: the velocity, volumetric flow, and pressure. These criteria are summarized in Table 3. For the velocity, a data drop-out which lasted longer than approximately 50 milliseconds in a given cycle was sufficient grounds for rejecting that entire record. For the flow, a record was rejected if the time of the occurrence of the maximum flow rate was greater than 0.3 seconds for that record, on the grounds that it was too far out of phase with previous records. Further, if the average flow rate computed from the data was greater than 0.092 L/s or less than 0.075 L/s for a given record, then that record was rejected on the grounds that the pulse-duplicator had produced an abnormally strong or weak ventricular-pump stroke, respectively. Another check on the strength of the ventricular-pump stroke was the maximum flow rate. When the maximum flow rate was greater than 0.550 L/s, the record was also rejected as having been abnormally strong. Finally, for the pressure, if the systolic time-interval was shorter than 0.25 seconds or longer than 0.35 seconds for a given record, then that record was rejected on the grounds that the calibrated zeros

Table 3

Data Rejection Criteria
for Pulsatile-Flow Experiments

Data Type	Rejection Parameter	Rejection Criterion	Rejection Basis
velocity	maximum time of data drop-out for LDA tracker	> 50 ms	excessive data loss
volumetric flow	maximum flow rate	> 0.550 L/s	abnormally strong ventricular-pump stroke
	time of maximum flow rate	> 0.3 s	data record significantly out of phase
	mean flow rate	< 0.075 L/s	abnormally weak ventricular-pump stroke
		or	
		> 0.092 L/s	abnormally strong ventricular-pump stroke
pressure	systolic interval	< 0.25 s	calibrated zeros of AP low and/or VP high
		or	
		> 0.35 s	calibrated zeros of AP high and/or VP low

of the AP and VP data signals were probably no longer balanced. That is, since the systolic interval was determined by comparing the two pressure data, AP and VP, then whenever this interval was significantly different than expected, the validity of the AP to VP comparison became suspect. Of these criteria, the average-flow constraints were most often violated while the systolic-interval constraint was the least violated. On the average, only two or three records out of the thirty were rejected per grid point.

The data from a rejected record were replaced by that from the previous record, thus giving the latter double weighting. This weighting process tended to be random and hence no difficulties arose with respect to data biasing. A problem occurred, of course, if the first record for a given point were rejected. In that case there was no previous record and all the data collected for that point was rejected, a warning was given, and the point was re-run by manual intervention.

2.5 PRELIMINARY RESULTS

Before the data were collected for the mounted prostheses, velocity measurements were made in fully developed turbulent flow in a tube. The results from the turbulent-flow studies were used to verify that the LDA measured the flow reliably and that the computer interface to the LDA was operational. The Reynolds number of the flow based on the tube diameter was 21,100. Velocity data were collected in each of the three coordinate directions at each grid point in the data plane. From these data, both mean and rms velocities in the axial and non-axial directions were calculated.

The mean axial velocity data showed that the LDA measured accurately the form and magnitude of the fully developed turbulent pipe flow. These axial data are plotted in Figure 13 both in three-dimensional (3-D) perspective and as

FULLY DEVELOPED TURBULENT PIPE FLOW

MEAN AXIAL VELOCITIES

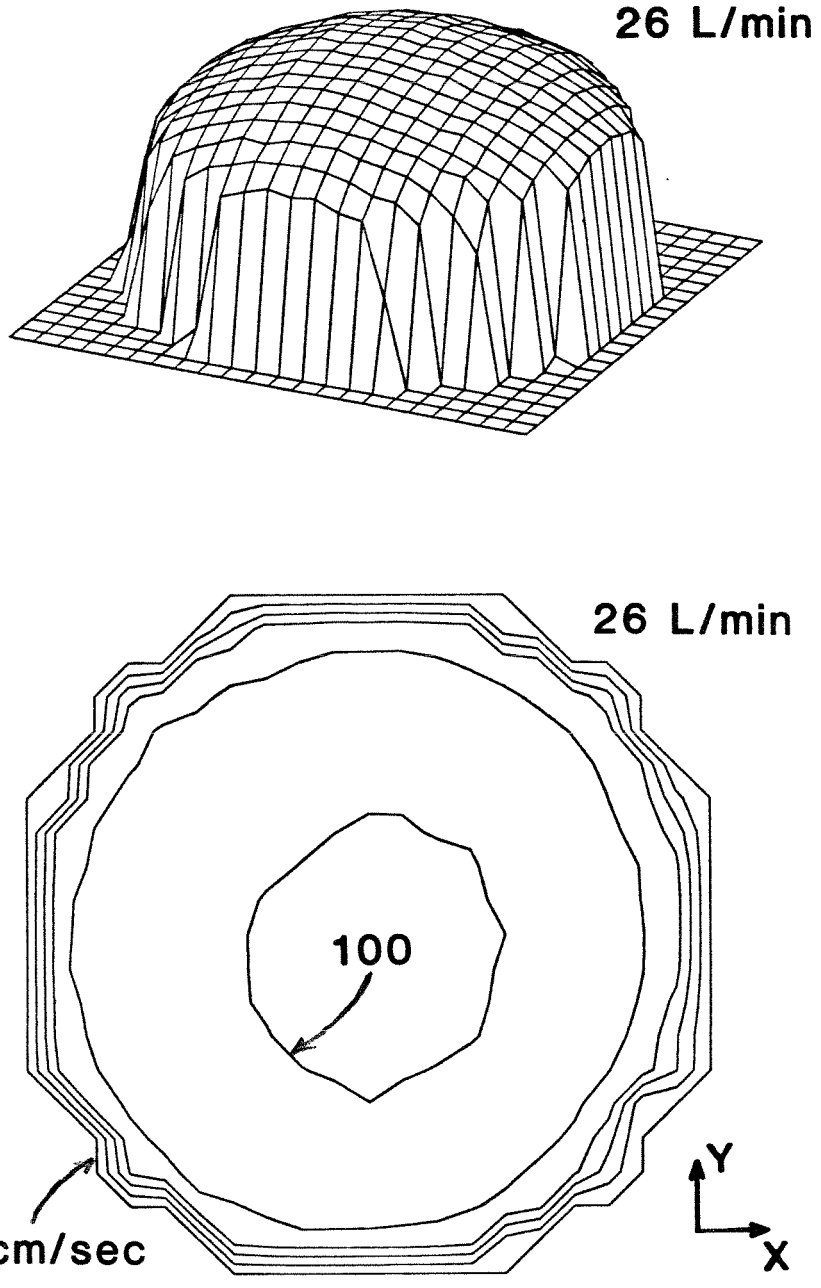

Figure 13. Mean axial velocities for fully developed turbulent pipe flow showing characteristic blunted flow profile. Contour interval: 20 cm/s.

contours. The 3-D perspective shows the characteristic blunted profile of turbulent flow in a tube. The contour plot shows the axisymmetric aspect of the flow. Small-scale abberations are noticeable near the tube wall in both plots but these can be attributed for the most part to mapping the circular cross section of the tube with a square grid. Even so, as shown in Figure 14, a profile of the results compare well to the theoretical 1/7-power law deduced from Blasius' law of friction (Bird, et al., 1960). As a comparison, Schlichting (1968) gave a value of 1/6.6 for the power law for a Reynolds number of 23,000. Thus the form of the mean velocities of the fully developed turbulent pipe flow was adequately measured by the LDA. The flow rate represented by the axial data was determined as 0.430 L/s using a two-dimensional Simpson's rule integration. This integrated flow compares well with the flow rate measured by the rotameter of 0.420 L/s. The percentage difference was only 2.4%. Thus the magnitude of the mean velocities in fully developed turbulent pipe flow was also adequately measured by the LDA.

The mean non-axial velocity data were used to determine what, if any, secondary-flow structures were present in the turbulent flow. To present these data, resultants were calculated from the two velocities corresponding to each grid point in the x- and y-directions. Had there been any secondary-flow structures in the flow, these resultants would have been shown as arrows in the "vector" plot in the top of Figure 15. Mean, non-axial velocities greater than 2.0 cm/s were, however, necessary for resultant arrows to be plotted. As can be seen from Figure 15, no mean non-axial velocities were measured greater than 2.0 cm/s in any direction at any grid point. The non-axial data therefore verified that no significant secondary flow structures were produced by the steady-flow loop for the fully developed turbulent pipe flow.

FULLY DEVELOPED TURBULENT PIPE FLOW

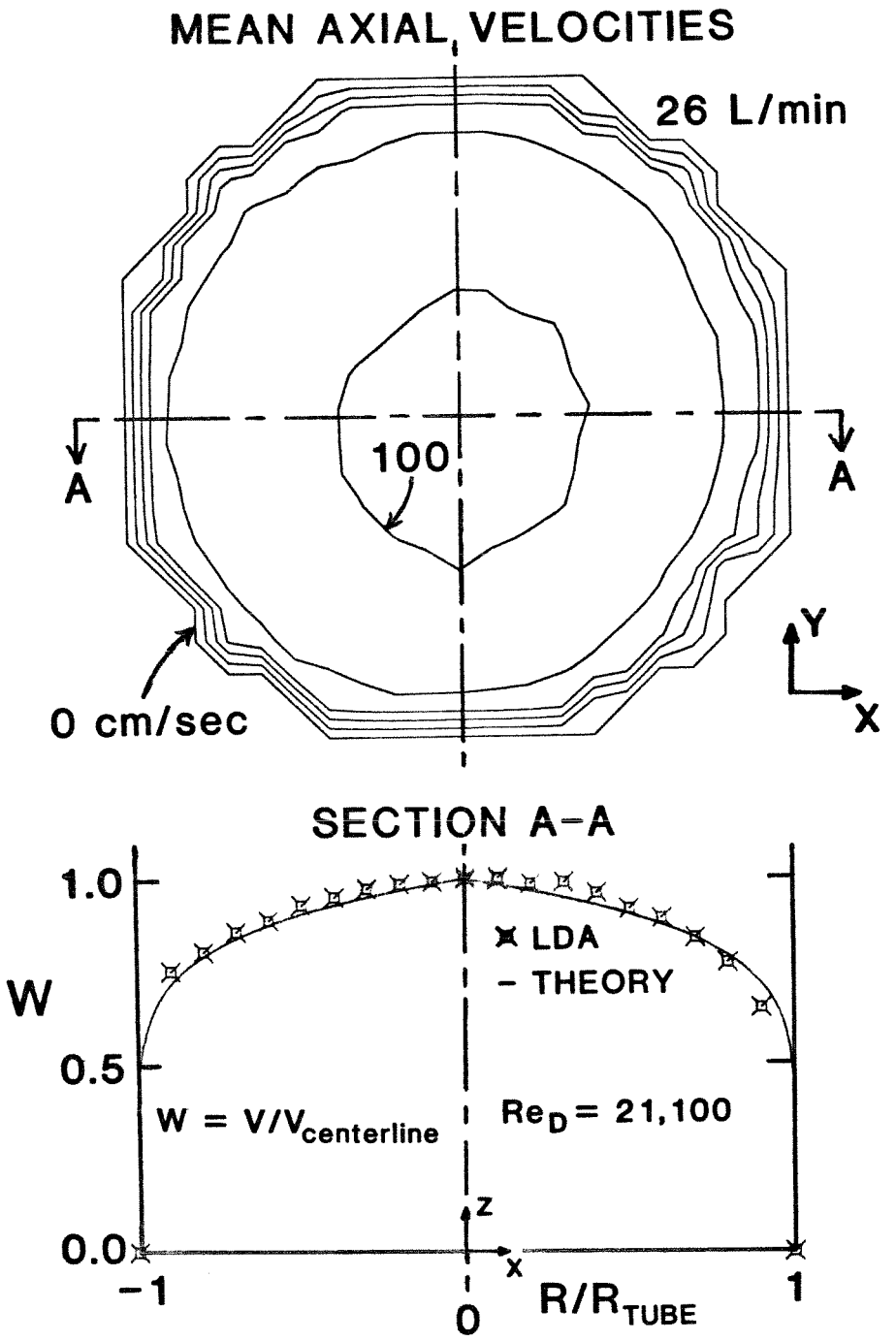

Figure 14. Mean axial velocities for fully developed turbulent pipe flow showing good agreement with 1/7-power law. Contour interval: 20 cm/s.

FULLY DEVELOPED TURBULENT PIPE FLOW

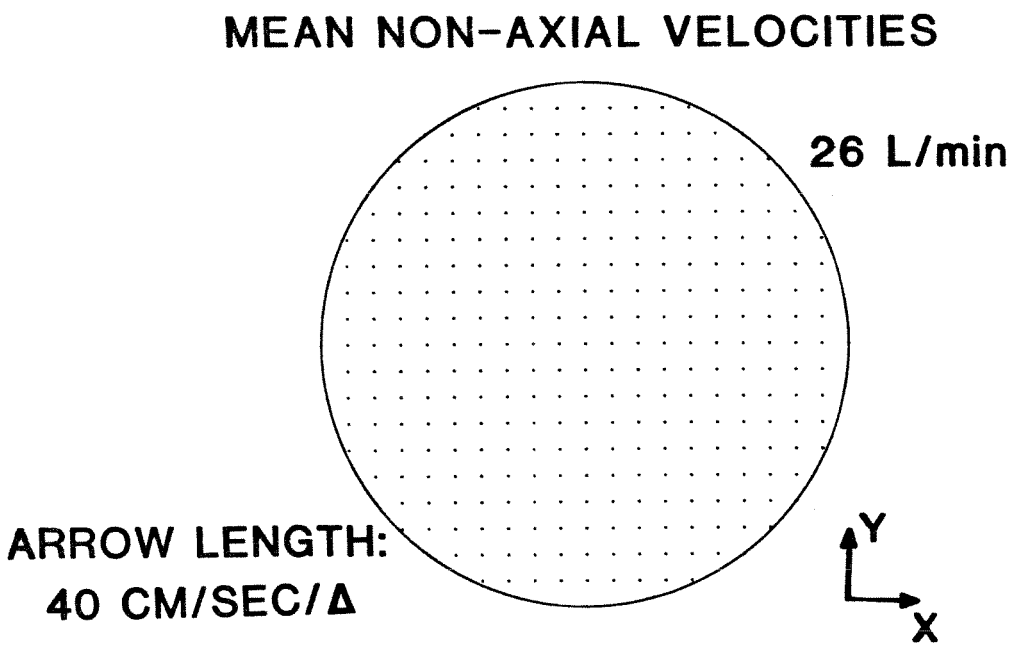

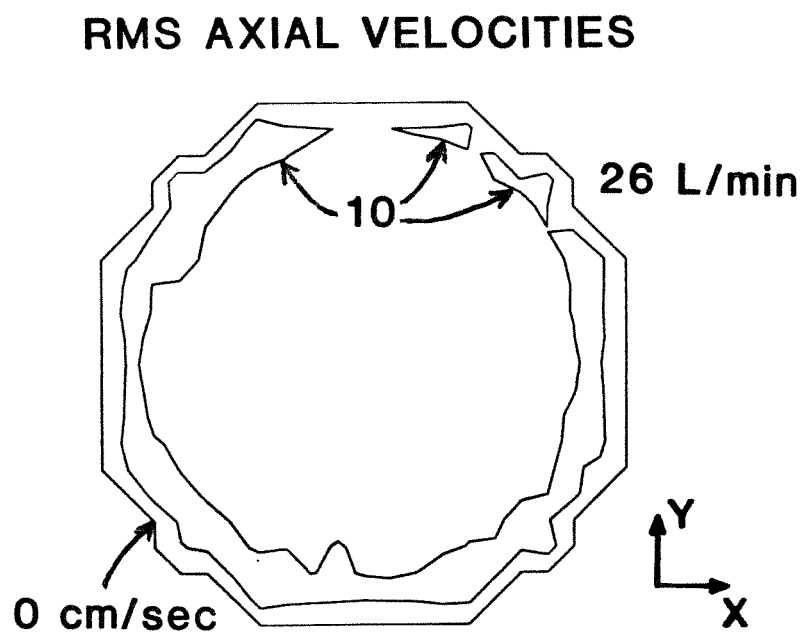

Figure 15. Mean non-axial velocities (top) and rms axial velocities (bottom) for fully developed turbulent pipe flow. Contour interval for rms velocities: 10 cm/s.

Root-mean-square (rms) velocities were calculated to verify that the experimental set-up accurately measured this aspect of the turbulent flow. These rms velocities are shown in the bottom of Figure 15. The rms velocity data in the axial direction ranged from a minimum of 6.2 cm/s at the tube center line to about 12 cm/s near the tube wall. The mean axial velocity at the tube centerline was 105 cm/s; therefore, the turbulence intensity, defined as the ratio of the rms velocity to the mean velocity at the centerline of the tube, ranged from 0.06 on the centerline to approximately 0.12 near the wall. These results are in good agreement with the findings of others at similar Reynolds numbers in both air (Laufer, 1954; Sandborn, 1955; Lawn, 1971) and water (Martin and Johanson, 1965; Chuang and Cermak, 1967; Komasawa, et al., 1974).

All results near the wall should be interpreted in light of the discussion above of the abberations of the form of the axial data results. That is, since the emphasis of the work was in the bulk region away from the wall, the region near the wall was not studied intensively. Hence, care should be taken to note that little or no information is available from Figures 13 through 15 and those like them, with respect to the region very near the wall. Within a millimeter or so of the wall, however, the results agree well with other established work for the case of fully developed turbulence in tube flow.

3. EXPERIMENTAL RESULTS AND DISCUSSION

3.1 EXPERIMENTAL UNCERTAINTIES

When discussing and interpreting the results of the present investigation, it is important that any uncertainties inherent in the experimental apparatus and methodology be delineated and, where possible, estimated. Experimental uncertainties arose from i) limitations in the capability of the laser-Doppler anemometer to collect velocity data, ii) limitations associated with the extraction of statistical information from the data collected using the laser-Doppler anemometer, and iii) limitations of the pulse-duplicator in duplicating pulses over protracted experimental runs. Uncertainties associated with the anemometer were discussed above in regards to the operational characteristics of the laser-Doppler anemometer and are summarized here. Uncertainties associated with the pulse-duplicator are discussed here in general terms and also more specifically in the sections below on the valve designs studied in the present investigation.

For both steady and pulsatile flow, as mentioned earlier, single-burst LDA measurements suffered from biasing problems associated with the relationship of the particle flux to the mean velocity. The maximum error expected in the mean velocity due to this biasing ranged from +5% at a turbulence intensity of 25% to 30% up to +15% at a turbulence intensity of 50%. The maximum error expected in the rms velocity was -10% at a turbulence intensity of 50%.

For pulsatile flow, additional experimental uncertainties arose because of the need to use data windows of finite length for data reduction. Larger data windows allowed a larger data base per grid-point location but limited the resolution of the results in time. Smaller data windows gave better temporal resolution, but, for a relatively constant data rate, required longer experimental

runs to obtain a given data-base size.

The 20-millisecond windows used in the present investigation caused some experimental uncertainty in the rms velocity results because of the magnitude of the flow acceleration during the forward-flow phase of the pulse cycle. This uncertainty in the rms velocity for a given window was estimated to be at most about +15%.

The windows used in the present investigation also caused some experimental uncertainty in both the mean and rms velocity results because of the duration of the experiments required to obtain reproducibility in the results. The duration of a pulsatile-flow experiment necessary to obtain good reproducibility was discussed in the previous chapter as being about 30 hours. As will be shown below, the mean and rms axial results from the pulsatile-flow experiments appear more "ragged" than for steady flow. Also, the resultant plots for the mean non-axial results appear to reflect more "scatter" in the data.

This "raggedness" and "scatter" can be attributed to the relative amount of data available from the pulsatile-flow experiments and the reproducibility of the flow from one cycle to the next. As discussed in Chapter 2, each mean and rms velocity result for pulsatile flow was calculated from about one-tenth the raw data available for the steady-flow calculations. Thus the data bases for the pulsatile-flow calculations were much smaller than those for steady flow. The reproducibility of the flow from cycle to cycle was generally good but details of the larger flow structures tended to reproduce less well. This intermittent pulse-to-pulse non-reproducibility was noted from flow-visualization studies and was most pronounced for low-velocity and flow-separation regions. The resultants of non-axial velocities appeared to be especially sensitive in these regions because of the combined effects from the two independently-obtained velocity results at the same grid-point location.

The extent of the experimental uncertainties associated with reproducibility considerations was, in general, unknown. Steady-flow results, of course, did not suffer these uncertainties and hence a comparison of steady-flow and pulsatile-flow results should give some idea of the magnitude of these pulsatile-flow uncertainties. It is shown below that steady-flow results resemble pulsatile-flow results during the middle portion of the forward-flow phase. The deviation of the pulsatile-flow results from those for steady flow, therefore, may be an indication of these uncertainties. If so, then the uncertainties associated with reproducibility were relatively small, being less than 5% to 10%, for much of the pulsatile-flow results. Again, for results obtained in or near low-velocity and flow-separation regions, this uncertainty may have been as much as 50% or higher in exceptional cases.

Taken together, then, pulsatile-flow experimental uncertainties could have been quite high in some cases. This fact should be considered when interpreting the results presented in this chapter.

A final consideration is that the rms velocities may be an overestimate of the fluctuating velocity component due to turbulence. No provision was made in the data-collection technique for natural frequencies in the flow. That is, shedding vortices and the like were "averaged out" and ultimately contributed to the magnitude of the rms velocities calculated from the raw data. This omission was probably more serious for steady flow because for pulsatile flow a period of about one second was imposed on the system and data were collected in phase with that period. The magnitude of the uncertainty attributed to this "averaging out" phenomenon was unknown. This uncertainty would be expected to vary considerably across the data plane, with the regions of the maximum uncertainty being those regions located directly downstream from aspects of

the superstructure of the valves which protruded into the main stream of the flow.

3.2 EMPTY AORTIC-VALVE FLOW SECTION

A Lucite® ring with an inner diameter of 25.4 mm was inserted into the valve mount of the aortic-valve flow section so that no constriction of the flow was generated. Velocity measurements were then made for steady flow across the data plane located at z = 31.8 mm (see Figure 8). Results with the Lucite® ring were used to determine the effect of the flow-section geometry on the overall flow. The results from experiments in the "empty" flow section were used to compare with those results from experiments with a mounted valve.

The mean axial data are presented in Figure 16 along with the results from the fully developed turbulent flow. The fully developed flow data represent the structure of the inlet flow to the flow section for comparison. As indicated, the flow rate through the flow section was 26 L/min. Mean non-axial data are presented in the top of Figure 17. The rms axial data are presented in the bottom of Figure 17.

Comparing the data from the empty flow section with that of the inlet flow, it can be concluded that the geometry of the flow section had a noticeable but not significant effect on the flow. That is, the results from the experiments during which prostheses were mounted can be almost entirely attributed to the valve and not to the flow section itself. Some small disturbances of the inlet stream are, however, evident in Figures 16 and 17. First, the flow through the flow section appears to have been slightly constricted. A small "bulge" can be seen in the axial data for the Lucite® ring which is not present for the fully developed flow data. This flow constriction can probably be attributed to the inlet geometry of the flow section near the valve-mounting mechanism. In addition

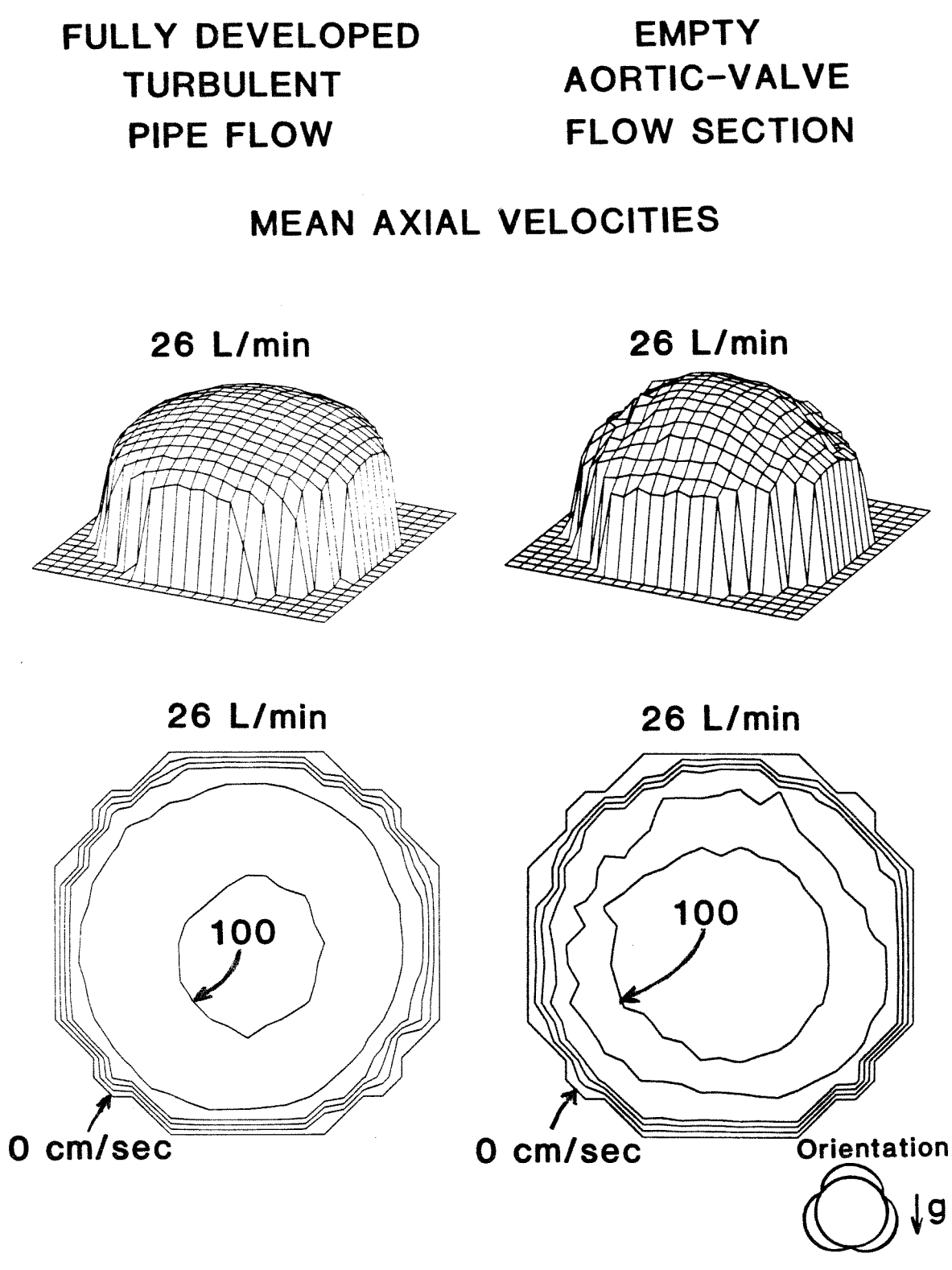

Figure 16. Comparison of mean axial velocities for fully developed turbulent pipe flow with those downstream from the empty aortic-valve flow section at z = 31.8 mm. Contour interval: 20 cm/s.

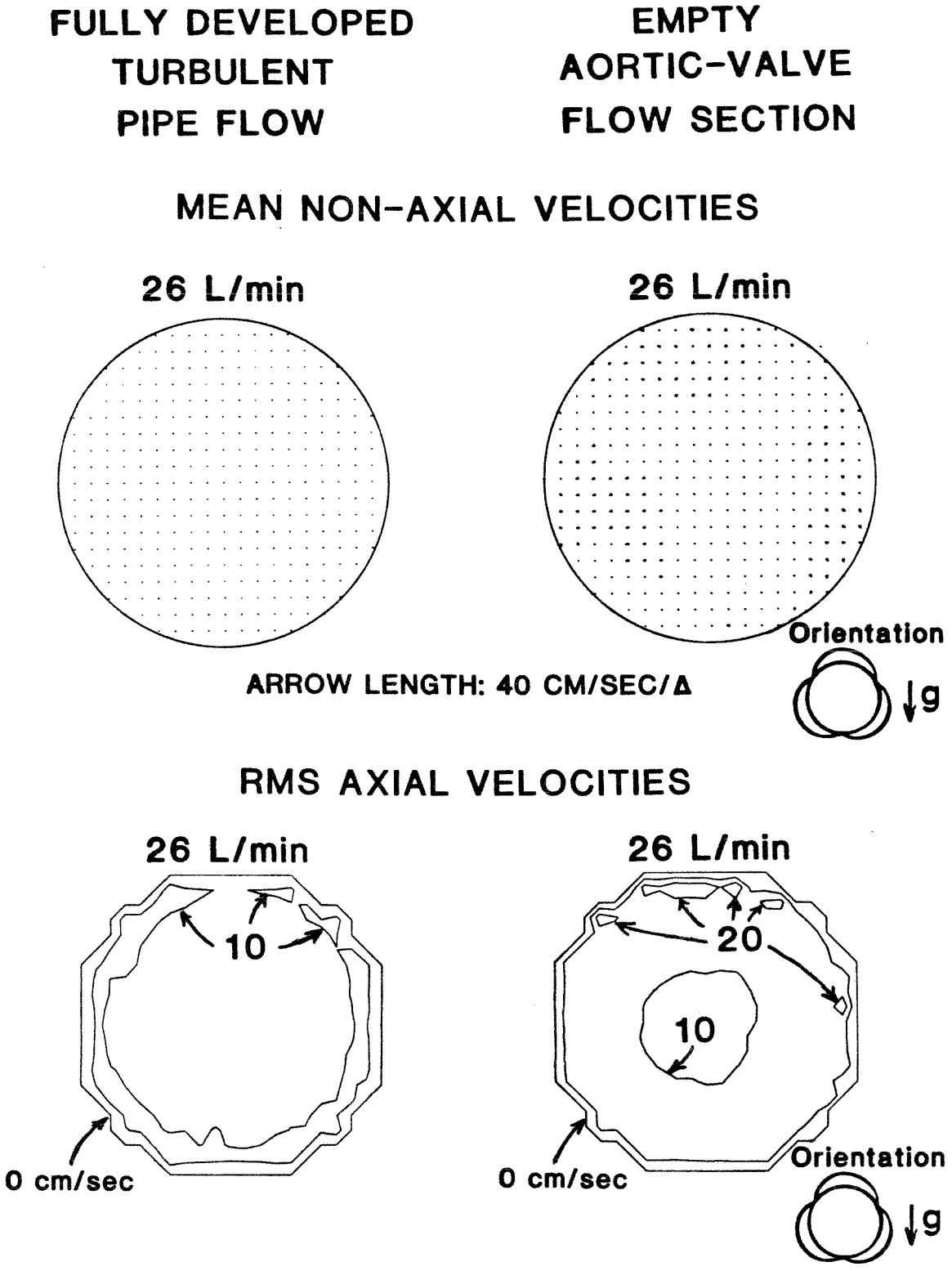

Figure 17. Comparison of the mean non-axial velocities (top) and rms axial velocities (bottom) for fully developed turbulent pipe flow with those downstream from the empty aortic-valve flow section z = 31.8 mm. Contour interval for rms velocities: 10 cm/s.

the flow through the flow section shows minor disturbances which can be attributed to the sinuses. The non-axial data in Figure 17 show this effect most definitively. The grid points at which non-axial velocity components were greater than 2.0 cm/s are spatially grouped into roughly three regions in the data plane. These regions correspond azimuthally with the orientation of the sinuses. As a result, there is a somewhat tri-symmetric aspect to the non-axial data. Slightly larger axial velocities are evident closer to the tube wall in three distinct regions which correspond to the regions delineated for the non-axial data. Thus it appears that the sinuses had the effect of accelerating the flow locally while also imparting small, non-axial components to the otherwise axially oriented velocities. It is possible that some of the "bulging" of the flow mentioned earlier could be attributed to the sinus geometry.

The sinus geometry probably accounted for the increase in the rms velocities shown in the bottom of Figure 17 for the empty flow section as compared with that for the fully developed case. The average rms across the data plane was 9.3 cm/s for the fully developed turbulent pipe flow and 14.0 cm/s for the flow through the empty flow section. The respective average turbulence intensities were 0.10 and 0.16. Flow-visualization studies have shown that the separated flow regions were present in the sinuses. At least some of the disturbances in the main flow could have originated in these separated regions had these disturbances been entrained by the main flow and convected downstream. For the most part, the effects of the sinuses in the absence of a valve were not significant. Likewise, the constriction of flow was sufficiently small to be considered inconsequential.

The flow through the empty flow section approximated fairly well the flow which occurs through the natural aortic valve of a patient at rest. Schramm, et al. (1982), in an *in vitro* study showed that an unstented aortic valve

generated a broad, smoothly diverging jet which reattached quickly as it proceeded downstream. Thus at an axial distance of z = 31.8 mm, the flow, not surprisingly, showed minimal acceleration and was only slightly constricted. The results presented by these investigators appeared to contain almost no non-axial velocities at the axial distance of z = 31.8 mm. It was thus felt that the flow through the empty flow section was enough comparable to that through a natural valve to represent a base-line for comparing flows downstream from the prostheses studied in the present investigation.

Pressure data were taken at z = -20 mm and z = 150 mm in the empty flow section. The ventricular pressure was 25.5 ± 0.2 kPa (gauge). The pressure drop across the orifice was measured as 0.4 ± 0.1* kPa. This pressure drop was simply the base-line pressure difference for the given pressure tap locations.

* Results are presented in the form: ***arithmetic mean*** ± ***standard deviation.***

3.3 IONESCU-SHILEY BIOPROSTHESIS

3.3.1 Introduction

The Ionescu-Shiley tri-leaflet bioprosthetic valve has become increasingly popular as an aortic valve replacement since being released in 1976 for general use in the United States. This central-flow valve is shown in the top of Figure 5a. Since its first clinical trials some five years earlier in 1971, this prosthesis has been reported to generate a flow field similar to that of the natural aortic valve (Ionescu, et al., 1977), to have a negligible pressure drop (Ionescu, et al., 1977; Tandon, et al., 1977), to exhibit low thromboembolic rates even when anticoagulation therapy was not employed (Ionescu, et al., 1977; Ionescu, et al., 1982; Frater, et al., 1979), and to cause very little intravascular hemolysis (Ionescu, et al., 1977).

Other *in vitro* and *in vivo* studies have obtained less favorable results. *In vitro* investigations (Schramm, et al., 1982; Yoganathan, et al., 1983b) of the flows downstream from this valve have indicated that the flow field generated is significantly different from that generated by the natural tri-leaflet aortic valve. A pronounced, jet-like flow has been found to emerge from the Ionescu-Shiley valve causing large separated regions in the flow and high mean velocity gradients (Schramm, et al., 1982; Yoganathan, et al., 1983b). Some evidence has also been reported (Frater, et al., 1979; Becker, et al., 1980; Martin, et al., 1981; Tindale, et al., 1982; Schramm, et al., 1982; Yoganathan, et al., 1983b) that the pressure drop associated with the Ionescu-Shiley prosthesis is not as small as previously reported (Ionescu, et al., 1977; Tandon, et al., 1977). *In vivo* studies by Frater, et al. (1979) and Becker, et al. (1980) indicate that the Ionescu-Shiley valve is moderately obstructive, especially so for smaller sizes. *In vitro* work (Martin, et al., 1981; Tindale, et al., 1982; Schramm, et al., 1982; Yoganathan, et al., 1983b) has also shown higher pressure drops than previously reported.

Elevated hemolysis levels associated with the use of this prosthesis *in vivo* have also been reported (Febres-Roman, et al., 1980). The levels of hemolysis reported were of comparable magnitude to that found for popular mechanical prosthetic aortic valves. It has, on the other hand, been generally agreed upon that the Ionescu-Shiley valve is associated with low thromboembolic rates. These low rates have been attributed mainly to the material of construction which apparently is non-thrombogenetic.

In the present investigation, an Ionescu-Shiley prosthesis with a TAD of 25 mm was studied *in vitro* in both steady and pulsatile flow regimes. Pressure and volumetric-flow data were collected to insure that the pressure and flow fields encountered by the valve in the experimental rig were similar to that which the valve might encounter when implanted in a patient. For pulsatile flow, the pulse-duplicator was operated at pressures and flows found *in vivo* in a resting state, i.e., as might be measured in the catheterization laboratory. After establishing these pressure and flow fields, the assessment of the *in vitro* states was extended to i) an extensive evaluation of the mean and rms velocities in the axial and non-axial directions across a data plane downstream from the mounted prosthesis, ii) the estimation of the total shear stresses at the data plane from the rms velocity results, iii) the estimation of the total regurgitant flow associated with this prosthesis to be used in comparison with other valves studied, and iv) to the comparison of steady-flow and pulsatile-flow results to give insights into the relevance of steady-flow analyses of flow fields downstream from prosthetic valves.

This extensive analysis was primarily undertaken to gain a better insight into the structure of the flow downstream from the Ionescu-Shiley prosthesis. It was expected that this extensive analysis would allow more definitive comments regarding the hydrodynamic performance of this central-flow valve prosthesis

relative to the discrepancies in the literature discussed above. In particular, the jet-like structure of the flow was to be analyzed and interpreted in light of the pressure-drop results found for this valve. Detailed estimations of shear stresses was undertaken in the hope that better correlation between *in vitro* results and *in vivo* levels of hemolysis could be achieved.

3.3.2 Methodology and Apparatus

The experimental methodology and apparatus used to obtain the results for the Ionescu-Shiley valve, were those discussed in detail in Chapter 2.

3.3.3 Results

3.3.3.1 Pressure and Volumetric-Flow Results

Several parameters were computed from the pressure data collected during each experiment. The value of each parameter and its time of occurrence in the cycle are presented in Table 4. All timing information reported in Table 4 is relative to the beginning of the systolic ejection interval. As discussed in Chapter 2 and depicted in Figure 12, the systolic ejection interval was defined as the time interval between the times of occurrence of P_{x1} and P_{x2}. Thus the time of occurrence of P_{x1} was zero by definition; i.e., P_{x1} occurred at $t = 0$. The systolic ejection interval therefore ended at the time of occurrence of P_{x2} at $t = 293 \pm 16$ milliseconds.

For pulsatile flow, the parameters calculated were the maximum pressure drop (ΔP_{max}), the maximum ventricular pressure (VP_{max}), the pressures at the two crossings of the pressure curves (P_{x1} and P_{x2}), the maximum and minimum rate of change of the (ventricular) pressure ($\left[\frac{dP}{dt}\right]_{max}$ and $\left[\frac{dP}{dt}\right]_{min}$), the mean systolic pressure drop ($\overline{\Delta P}_{sys}$), the mean diastolic pressure drop ($\overline{\Delta P}_{dias}$), and the

Table 4

Parameters Computed from the Pressure Data for the Ionescu-Shiley (25 mm) Bioprosthesis*

	Pressure (kPa)	Relative time** of occurrence in the cycle (ms)
Pulsatile Flow:		
ΔP_{max}	2.9 ± 0.2	173 ± 17
VP_{max}	20.5 ± 0.5 +	194 ± 16
P_{x1}	10.7 ± 0.6 +	0 ± 34
P_{x2}	10.9 ± 0.8 +	293 ± 16
$\left(\frac{dP}{dt}\right)_{max}$	219 ± 10 (kPa/s)	-17 ± 32
$\left(\frac{dP}{dt}\right)_{min}$	-356 ± 21 (kPa/s)	351 ± 16
$\overline{\Delta P}_{sys}$	0.8 ± 0.1	-
$\overline{\Delta P}_{dias}$	11.9 ± 0.4	-
$\overline{\Delta P}$	13.3 ± 0.6 +	-
Steady Flow:		
$\overline{\Delta P}$	1.3 ± 0.1	-

*Results given as mean ± standard deviation.

**Relative to the beginning of systolic ejection.

+Gauge pressure.

mean aortic pressure ($\overline{AP}$). These pulsatile-flow parameters are shown in Figure 12. For steady flow, only the mean pressure drop ($\overline{\Delta P}$) was calculated.

Time-integration was used to determine the values of $\overline{\Delta P}_{sys}$, $\overline{\Delta P}_{dias}$, $\overline{AP}$, and $\overline{\Delta P}$. No time of occurrence is given in Table 4 for these four parameters since they occurred over extended intervals of time.

The values reported in Table 4 are in the format of the mean ± the standard deviation. For each pulsatile-flow parameter, the arithmetic mean and the standard deviation of that parameter's value were calculated during each of the many cycles which constituted the pulsatile-flow experiment. The timing information was treated similarly. For the one steady-flow parameter, the time-integrated mean and standard deviation reported in Table 4 were simply those values computed from the steady-flow experiment.

For pulsatile flow, ΔP_{max} was 2.9 ± 0.2 kPa and occurred at t = 173 ± 17 milliseconds. VP_{max} was 20.5 ± 0.5 kPa (gauge) and occurred about 21 milliseconds later at t = 194 ± 16 milliseconds. $\left[\frac{dP}{dt}\right]_{max}$ had a value of 219 ± 10 kPa/s and occurred at t = -17 ± 32 milliseconds before systolic ejection. $\left[\frac{dP}{dt}\right]_{min}$ had a value of -356 ± 21 kPa/s and occurred at t = 351 ± 16 milliseconds. During the systolic interval, the pressure drop ($\overline{\Delta P}_{sys}$) was 0.8 ± 0.1 kPa. During the diastolic interval, defined as that part of the cycle between P_{x1} and P_{x2}, the pressure drop ($\overline{\Delta P}_{dias}$) was 11.9 ± 0.4 kPa. During the entire cycle, $\overline{AP}$ was 13.3 ± 0.1 kPa (gauge).

For steady flow, $\overline{\Delta P}$ was 1.3 ± 0.1 kPa.

Several parameters were also computed from the volumetric-flow data collected during each experiment. The value of each parameter and its time of occurrence in the cycle are presented in Table 5. For pulsatile flow, the

Table 5

Parameters Computed from the Volumetric-Flow Data for the Ionescu-Shiley (25 mm) Bioprosthesis*

	Flow (L/min)	Relative time** of occurrence in the cycle (ms)
Pulsatile Flow:		
Q_{max}	29.8 ± 0.3	190 ± 23
Q_{min}	-10.5 ± 0.4	328 ± 4
Q_{beg}	0.0 (by def.)	-5 ± 18
Q_{end}	0.0 (by def.)	298 ± 4
Q_F	5.50 ± 0.13	-
Q_C	-0.17 ± 0.04	-
Q_L	-0.11 ± 0.09	-
Q_{rms}	19.5 ± 0.1	-
Steady Flow:		
$\bar{Q}$	27 (rotameter)	-

*Results given as mean ± standard deviation.

**Relative to the beginning of systolic ejection.

parameters computed were the maximum and minimum flow rate (Q_{max} and Q_{min}), the flow rate at the beginning and end of the forward-flow phase (Q_{beg} and Q_{end}), the flow rate associated with the forward-flow phase (Q_F), the flow rate associated with the closure-flow phase (Q_C), the flow rate associated with the leakage-flow phase (Q_L), and the rms flow rate during the systolic interval (Q_{rms}). For steady flow, the mean flow rate ($\bar{Q}$) was determined using the Brooks rotameter placed in the steady-flow loop.

Time-integration was used to determine the values of Q_F, Q_C, Q_L, and Q_{rms}. No time of occurrence is given in Table 5 for these four parameters since they occurred over extended intervals of time.

The values reported in Table 5 are in the same format as that for Table 4. For each pulsatile-flow parameter, the arithmetic mean and the standard deviation of that parameter's value were again calculated during each of the many cycles which constituted the pulsatile-flow experiment. For the one steady-flow parameter, the value reported in Table 4 was that determined during the steady-flow experiment from the rotameter.

For pulsatile flow, Q_{max} was 29.8 ± 0.3 L/min and occurred essentially at the same time as VP_{max} at 190 ± 23 milliseconds. Q_{min} was -10.5 ± 0.4 L/min and occurred soon after the end of the systolic ejection interval at 328 ± 4 milliseconds. The flow rates for Q_{beg} and Q_{end} were zero by definition, as discussed in Chapter 2. The time of occurrence of Q_{beg} was -5 ± 18 milliseconds at essentially the beginning of the systolic ejection interval. The time of occurrence of Q_{end} was 298 ± 4 milliseconds at essentially the end of the systolic ejection interval.

During the forward-flow, closure-flow, and leakage-flow phases of the cycle the flow rates were 5.50 ± 0.13, -0.17 ± 0.04, and -0.11 ± 0.09 L/min, respectively.

Total regurgitant flow, the summation of closure and leakage flow, was therefore 0.28 L/min.

During systole, Q_{rms} was 19.5 ± 0.1 L/min. Q_{rms} was used to relate the pressure-drop results of steady flow to those of pulsatile flow. Studies of the four valve designs used in the present investigation have shown that Q_{rms} was about 69% of Q_{max}. For the Ionescu-Shiley valve, the ratio of Q_{rms} to Q_{max} was 70%.

$\bar{Q}$ was 27 L/min for steady flow and was measured using the rotameter. The electromagnetic flowmeter was used for the pulsatile-flow measurements.

3.3.3.2 Velocity Results

Velocity results for both steady and pulsatile flow were obtained. For steady flow, the flow rate used approximated the peak flow rate which was encountered for pulsatile flow at a mean flow rate of 5.4 L/min and a pulse rate of 70 beats per minute. For pulsatile flow the results represent those for a given interval of time (20-millisecond windows) relative to the time of the cycle. Figure 18 depicts the temporal location of the pulsatile-flow windows relative to an "idealized" volumetric-flow curve for the Ionescu-Shiley prosthesis.

Mean axial velocity results for pulsatile flow are presented in 3-D perspective in Figure 19. Data are shown for windows 6 through 23, 25, and 30. All 3-D plots were scaled equivalently. The value for the flow rate at each window was obtained by integrating the mean axial velocities using the two-dimensional Simpson's rule. The values are shown in parentheses adjacent to the corresponding window. For example, the mean axial velocities for window 6 integrated to a flow rate of 5 L/min. Windows 5 through 21 encompassed the systolic ejection interval. The diastolic interval extended from windows 22 through 43 and then up to window 4 of the next cycle.

IONESCU-SHILEY (25 mm)

KEY TO WINDOW LOCATIONS

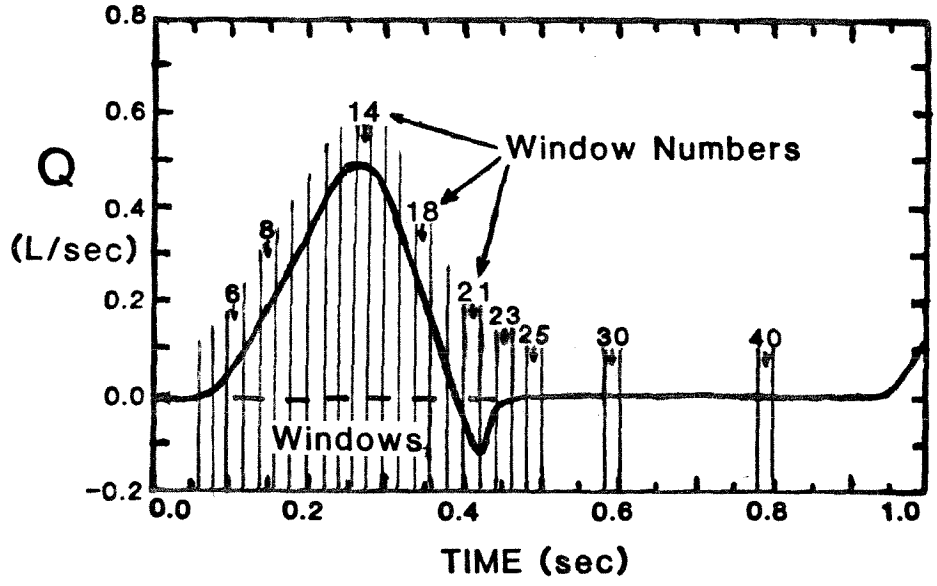

Figure 18. Idealized volumetric-flow curve showing temporal location of pulsatile-flow windows 6 through 25, 30, and 40 for the Ionescu-Shiley (25 mm) bioprosthesis.

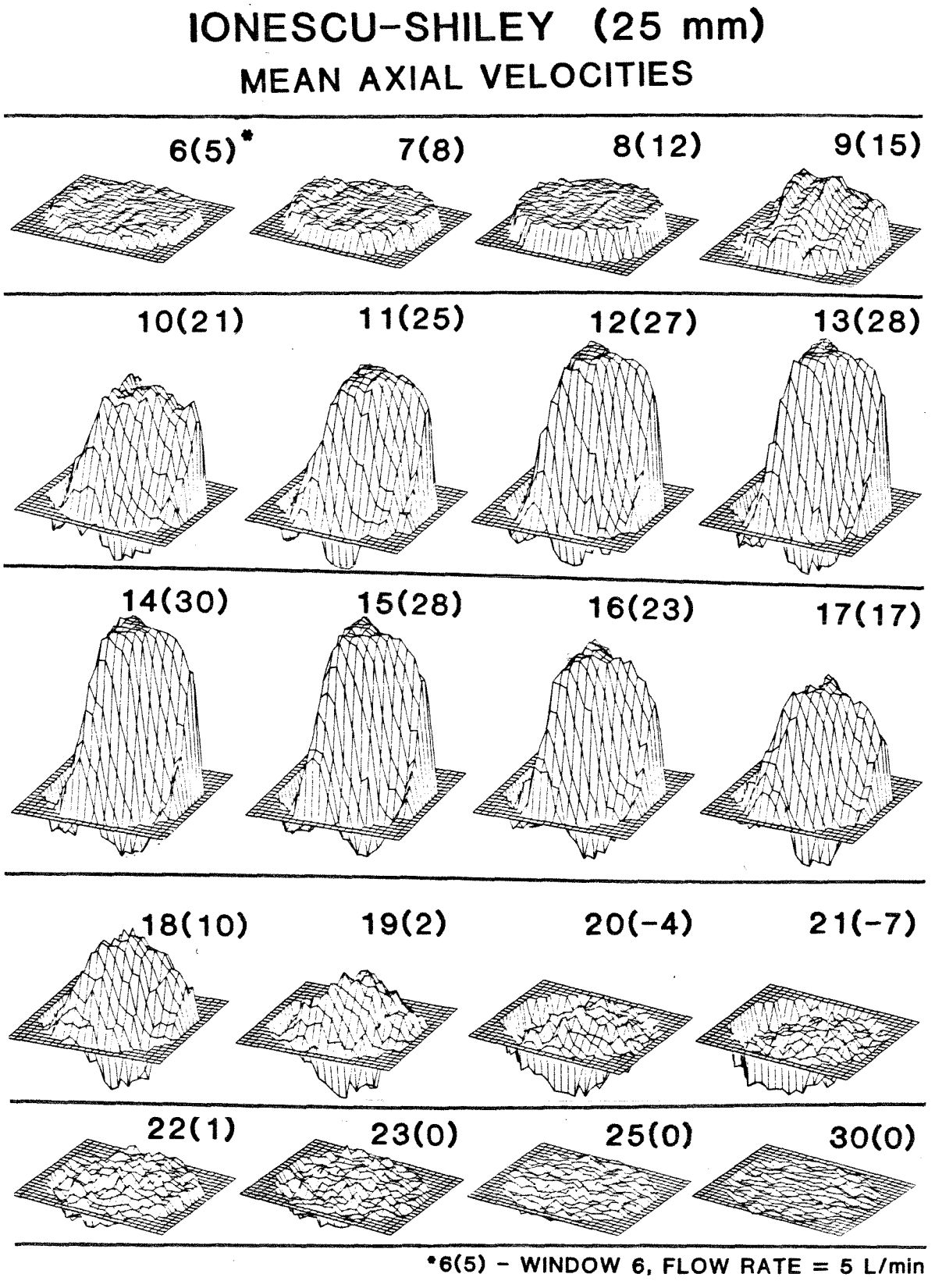

Figure 19. Mean axial velocities in 3-D perspective for pulsatile-flow windows 6 through 23, 25, and 30 downstream from the Ionescu-Shiley (25 mm) bioprosthesis at z = 31.8 mm.

A large, central jet can be seen in these plots during much of the systolic ejection interval. From Figure 19 it can be seen that this jet became significant by window 10 and persisted for at least 150 milliseconds until window 17. Reverse flow can also be seen adjacent to the jet indicating the presence of flow separation. Like the jet structure, flow separation also began by window 10. In contrast, however, flow separation persisted throughout the systolic ejection interval. As the systolic ejection interval ended, more reverse flow was apparent so that just before valve closure at windows 20 and 21 the net flow rate became negative. During diastole the axial velocities for windows 23, 25, and 30 progressively approached a flat plane indicating that the flow was "settling out." This diastolic settling of the flow resulted from the lack of an appreciable pressure gradient during diastole in the flow downstream from the closed valve.

Mean axial velocities are presented in Figure 20 for steady flow and for windows 8, 14, 18, and 21 of the pulsatile flow. The steady-flow results are presented along with the pulsatile-flow results for comparison. The steady-flow data have been presented elsewhere (Hanle, et al., 1983). The window key indicates the temporal location of the windows of the pulsatile flow in relation to the volumetric-flow curve. Window 8 corresponded to the time in early systole when the flow experienced maximum acceleration, window 14 to the time in the middle of systole when the maximum forward flow occurred, window 18 to the time in late systole when the flow experienced maximum deceleration, and window 21 to the time just before valve closure when the maximum reverse flow occurred. For steady flow the large jet structure was again evident. For pulsatile flow, the flow structure at window 14 during the middle of systole was similar to that for steady flow. Earlier in systole, at window 8, the flow had an almost flat velocity profile across the data plane. In particular, no jet structure or flow separation was apparent for the flow in window 8. Late in systole, at

IONESCU-SHILEY (25 mm)

MEAN AXIAL VELOCITIES

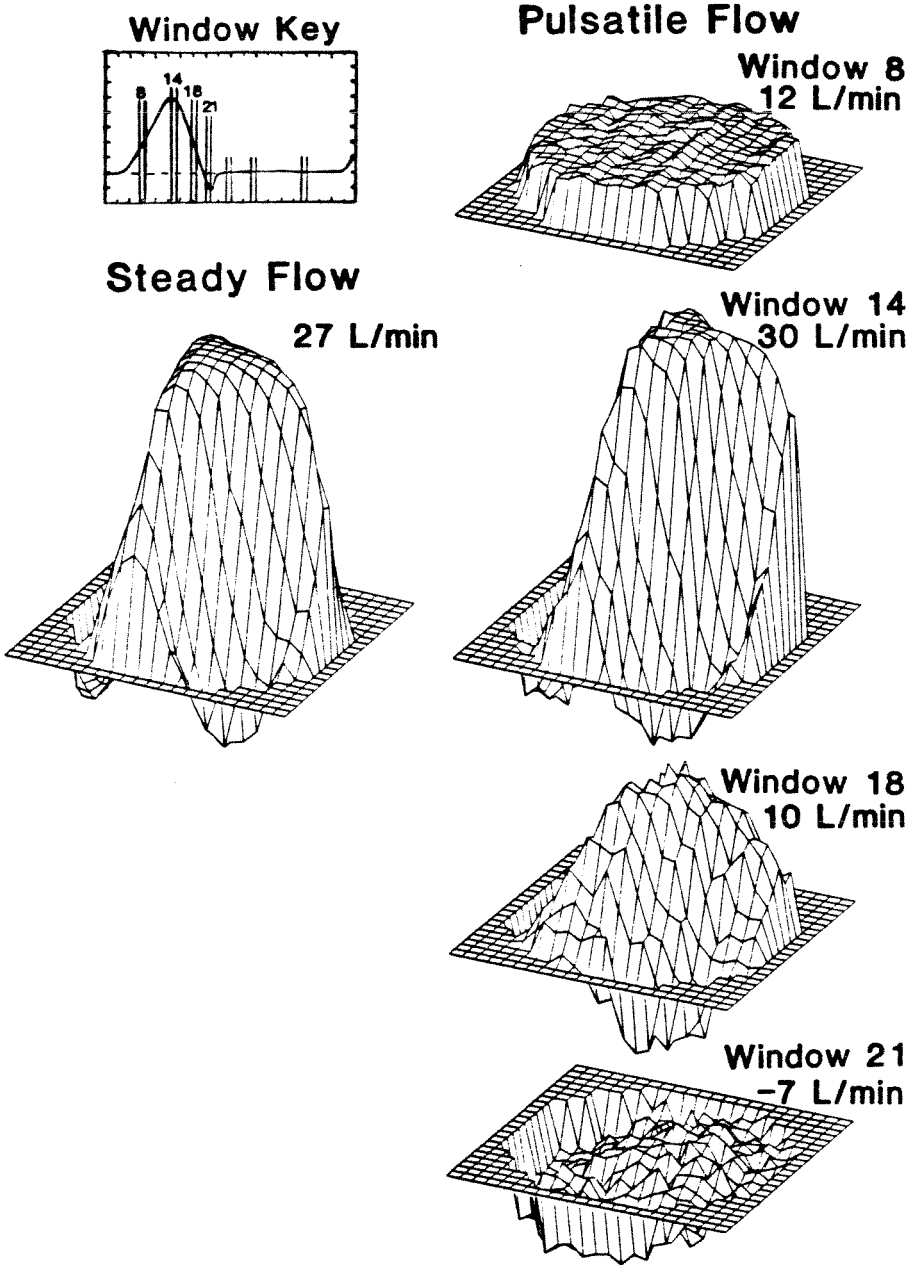

Figure 20. Mean axial velocities in 3-D perspective for steady flow and pulsatile-flow windows 8, 14, 18, and 21 downstream from the Ionescu-Shiley (25 mm) bioprosthesis at z = 31.8 mm.

window 18, a much diminished jet was still observed along with relatively large flow separation. Note that the flow rates for windows 8 and 18 were comparable. By window 21, immediately preceding valve closure, a remnant of the jet was still observable but generally the flow had reversed and hence the flow rate was negative.

Mean axial velocities are presented in Figure 21 for windows 25, 30, and 40 of the pulsatile flow. These diastolic results show more clearly the "settling out" behavior of the flow throughout diastole. Although finite mean velocities were measured at most grid points on the data plane, the flow rate obtained by integrating these mean velocities was zero.

The mean axial velocities shown in Figure 20 for steady flow and for windows 8, 14, 18 of the pulsatile flow are presented more quantitatively as contours in Figure 22. Dashed lines indicate the spatial limits of the results when the velocity near the wall of the tube was negative. The inset showing the valve orientation depicts the orientation of the valve superstructure relative to the structure of the velocity results. The gravitational vector is also indicated with respect to the valve orientation. The structure of the central jet can be more readily appreciated in Figure 22. A striking aspect of the jet generated by this valve is that at the data plane the jet was distinctly triangular in cross section. The triangular shape of the jet was most distinct for steady flow. The steady-flow results show definite 'sides' and 'apices' of the jet.

For both steady and pulsatile flow, the orientation of the triangularly shaped axial jet was such that the azimuthal location of the apices of the jet corresponded to that of the struts of the valve. Moreover, reorientation of the valve resulted in a similar reorientation of the results. The valve was rotated 60° with respect to the flow-section geometry and steady-flow axial velocities were obtained at selected data plane grid points (see Appendix A). This rotation

IONESCU-SHILEY (25 mm)

MEAN AXIAL VELOCITIES

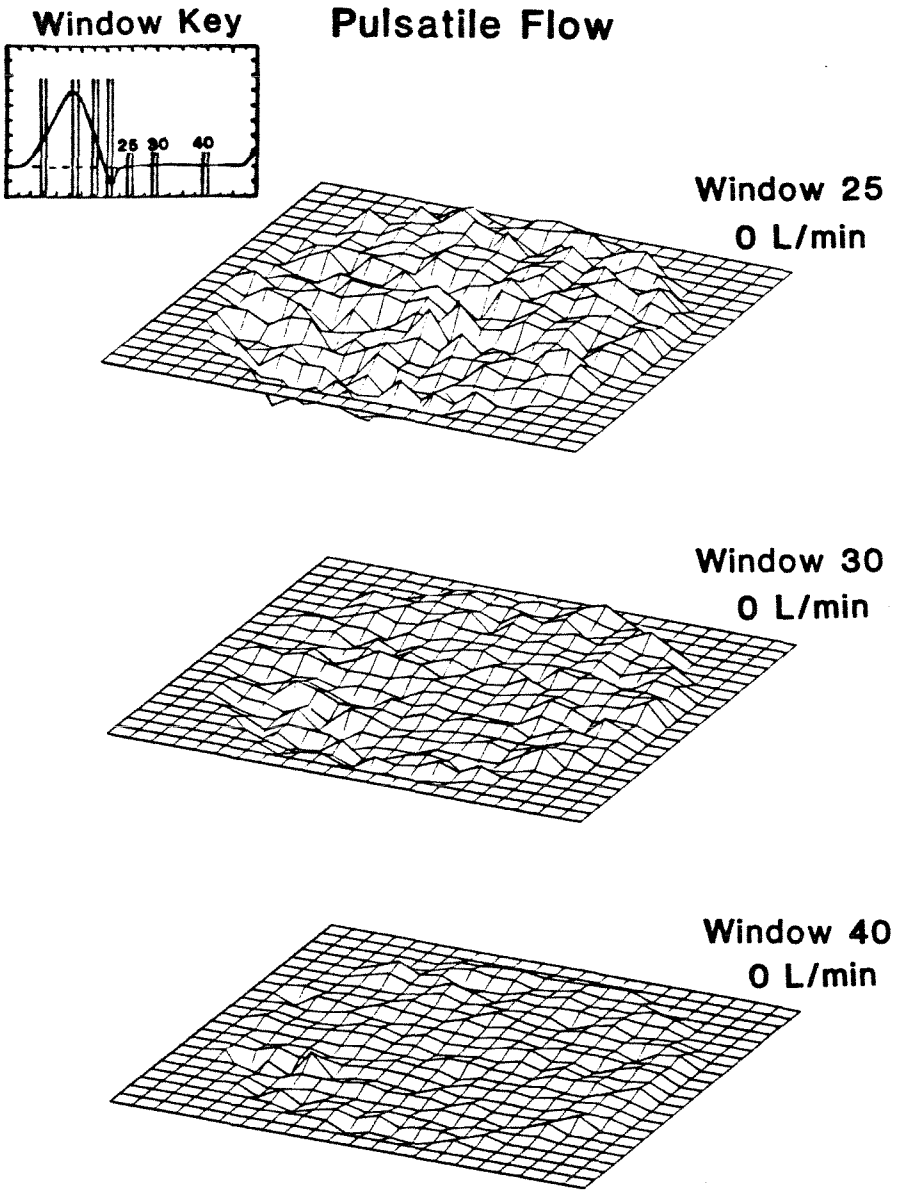

Figure 21. Mean axial velocities in 3-D perspective for pulsatile-flow windows 25, 30, and 40 downstream from the Ionescu-Shiley (25 mm) bioprosthesis at z = 31.8 mm.

IONESCU-SHILEY (25 mm)

MEAN AXIAL VELOCITIES

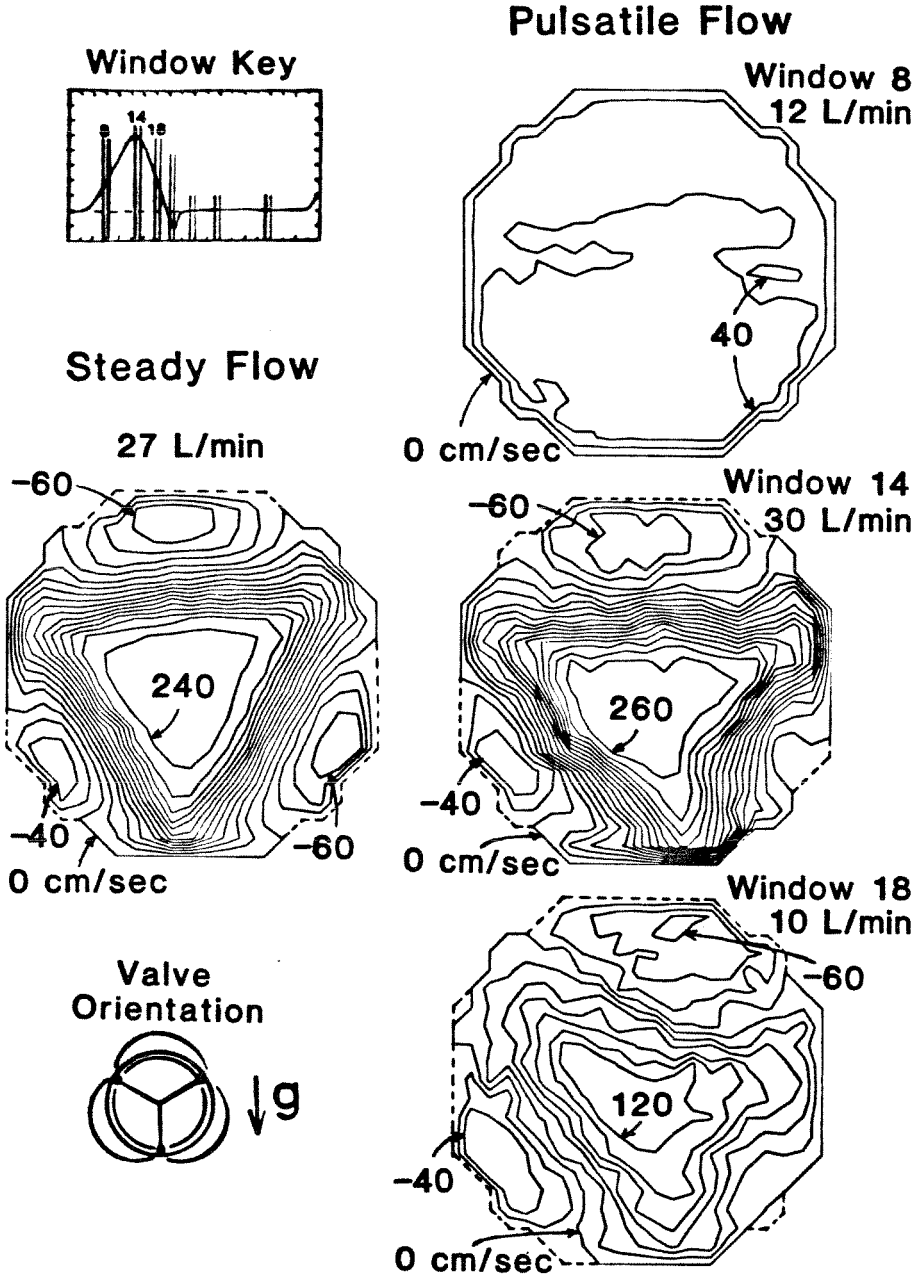

Figure 22. Mean axial velocities as contours for steady flow and pulsatile-flow windows 8, 14, and 18 downstream from the Ionescu-Shiley (25 mm) bioprosthesis at z = 31.8 mm. Contour interval: 20 cm/s.

was done to decouple the tri-symmetric aspect of the valve geometry with that of the flow section. As shown in Appendix A, high mean axial velocities were found near the wall downstream from the struts of the valve while negative velocities were found elsewhere along the wall. The azimuthal orientation of the 'apices' of the triangular jet were thus again determined to correspond to that of the struts of the valve. Therefore, the tri-symmetric structure of the flow downstream from this valve resulted from the tri-symmetric geometry of the valve and not from that of the flow section.

The magnitude of both the steady-flow and pulsatile-flow jets were such that very large flow acceleration and associated velocity gradients were present in the bulk flow. The jet attained maximum velocities of 240 and 260 cm/s, respectively, for steady and pulsatile flow. The fluid was therefore found to be accelerated by a factor of about 2.5 from the maximum velocity of 105 cm/s for the flow upstream from the mounted valve. For comparison, the flow through the empty flow section was accelerated by a factor less than 1.1. The maximum mean velocity gradient in the bulk flow was calculated to be approximately 800 s^{-1} over a radial distance of at least 2.5 mm and was found to occur along the 'sides' of the triangularly shaped jet. High velocity gradients also occurred where the 'apices' of the jet appear to impinge on the tube wall. Though *detailed* velocity measurements were not made near the wall, the maximum gradients at the wall appear to have been substantially larger than 800 s^{-1} where the jet impinged on the wall and substantially lower than 800 s^{-1} elsewhere.

For pulsatile flow, the triangular shape of the jet was less symmetrical than that for steady flow and was somewhat less distinct. At window 14, the jet was pronounced but its three 'apices' were not distributed azimuthally 120° apart. Early in systole at window 8 no jet was present. Only very small velocity gradients were found at window 8 and these were adjacent to the wall. Late in

systole at window 18 a diminished yet definite jet structure was present. The magnitude of the peak shown for window 18 had fallen to less than half its maximum value. The triangular aspect of the jet, though still apparent, had become even less distinct.

The structure of the separated-flow regions can also be more readily appreciated from Figure 22. For both steady and pulsatile flow, the flow separation was well established and relatively extensive. The flow separation for both flow regimes was divided into three individual flow-separation regions. These flow-separation regions were located adjacent to the wall and were interspersed azimuthally between the 'apices' of the jets. For steady flow, the size and magnitude of each flow-separation region were roughly comparable. For pulsatile flow, the flow-separation regions in the lower left and top of the plot for window 14 were roughly comparable but that in the lower right was almost non-existent. Early in systole at window 8 there was no flow separation. Late in systole at window 18 the separated-flow regions remained similar in magnitude to those for window 14 and had increased in area.

Mean axial velocities are presented in Figure 23 as contours for windows 25, 30, and 40 of the pulsatile flow. No mean axial velocities were measured greater than 20 cm/s in absolute value and hence only contours corresponding to zero velocity are plotted. Note that particularly for windows 25 and 30 the flow in the upper left half of the data plane was negative while that in the lower right half was positive. Apparently, during diastole there was a slowly rotating vortex with a length scale on the order of the tube diameter. The axis of the vortex was oriented about 45° clockwise from the gravitational vector and was located approximately 30 mm downstream from the valve mount in a plane perpendicular to the tube axis. The orientation and sense of the rotation of this vortex appear to have been influenced by the fact that the separated-flow region

IONESCU-SHILEY (25 mm)

MEAN AXIAL VELOCITIES

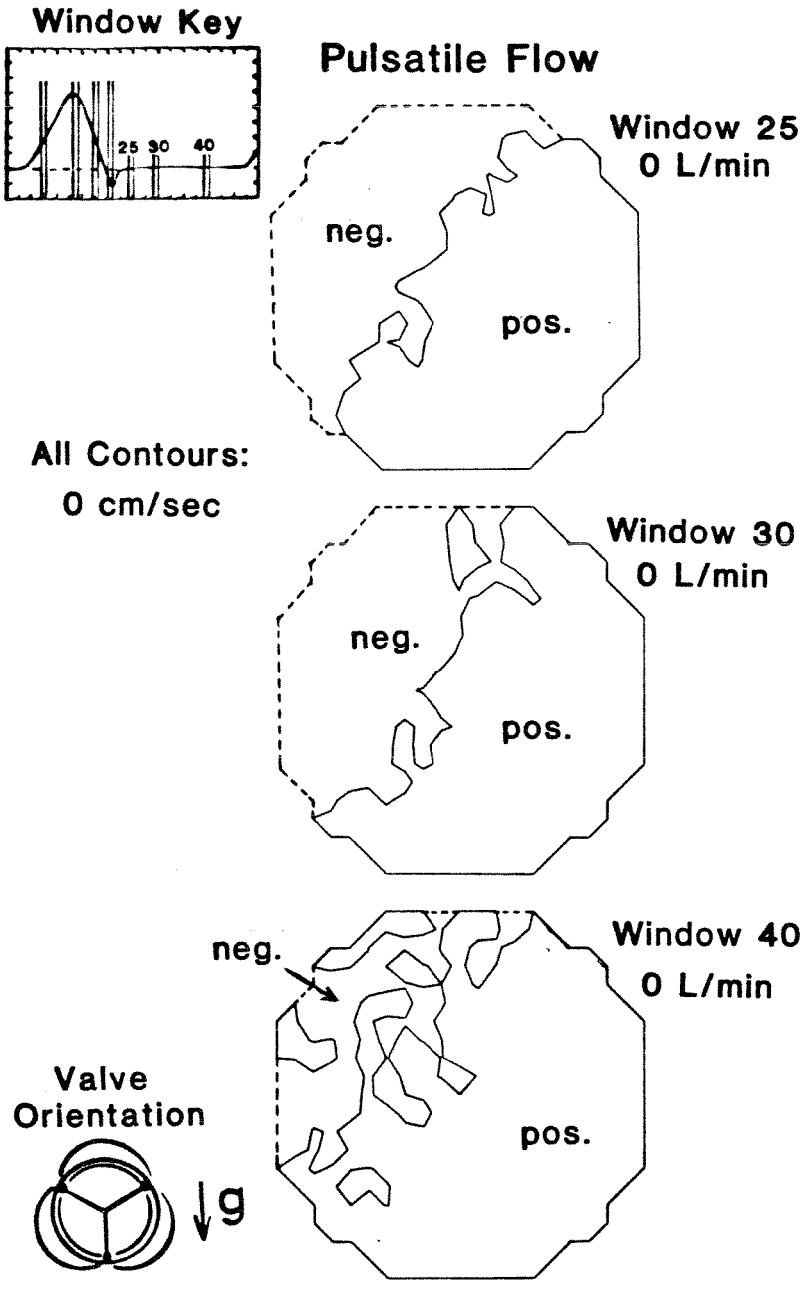

Figure 23. Mean axial velocities as contours for pulsatile-flow windows 25, 30, and 40 downstream from the Ionescu-Shiley (25 mm) bioprosthesis at z = 31.8 mm. Contour interval: 20 cm/s.

in the lower right of the plot for window 14 in Figure 22 was significantly smaller than the remaining two regions. This size difference of the negative-flow regions had been maintained at least into window 18. The vortex had largely disappeared by the time of window 40 in very late diastole.

Mean non-axial velocities are presented in Figure 24 for steady flow and for windows 8, 14, and 18 of the pulsatile flow as resultants of the mean velocities in the x- and y-directions. The magnitude of the non-axial velocities are represented by the lengths of the arrows scaled by the distance Δ as defined in Figure 8. No arrow was plotted if the magnitude of the non-axial velocity component was less than 2.0 cm/s. For both steady and pulsatile flow, the mean non-axial results showed large, wall-directed velocity components which corresponded spatially with the apices of the axial jet. These wall-directed velocities impinged on the wall creating a two-dimensional flow field like that of a stagnation-point flow. The "points" of these stagnation-point flow fields were not, however, true loci of flow stagnation because the axial velocity at each such point was non-zero. For ease of reference, these "points" will be referred to as pseudo-stagnation points. Three pseudo-stagnation points were generated which were each located azimuthally about 120° from the other two around the cross section of the tube. Smaller azimuthal velocity components near the wall were directed in both directions away from each of these pseudo-stagnation points and into the separated-flow regions shown for the axial results. Three additional pseudo-stagnation points were formed where the azimuthally directed velocity components met. From these latter three pseudo-stagnation points the flow was directed back towards the center of the tube. Thus, the fluid which was caught up in the secondary flow towards the wall was directed out of the axial jet and along the wall azimuthally into the separated-flow regions. Meanwhile the fluid in the separated-flow regions was moved away from the wall and was

IONESCU-SHILEY (25 mm)

MEAN NON-AXIAL VELOCITIES

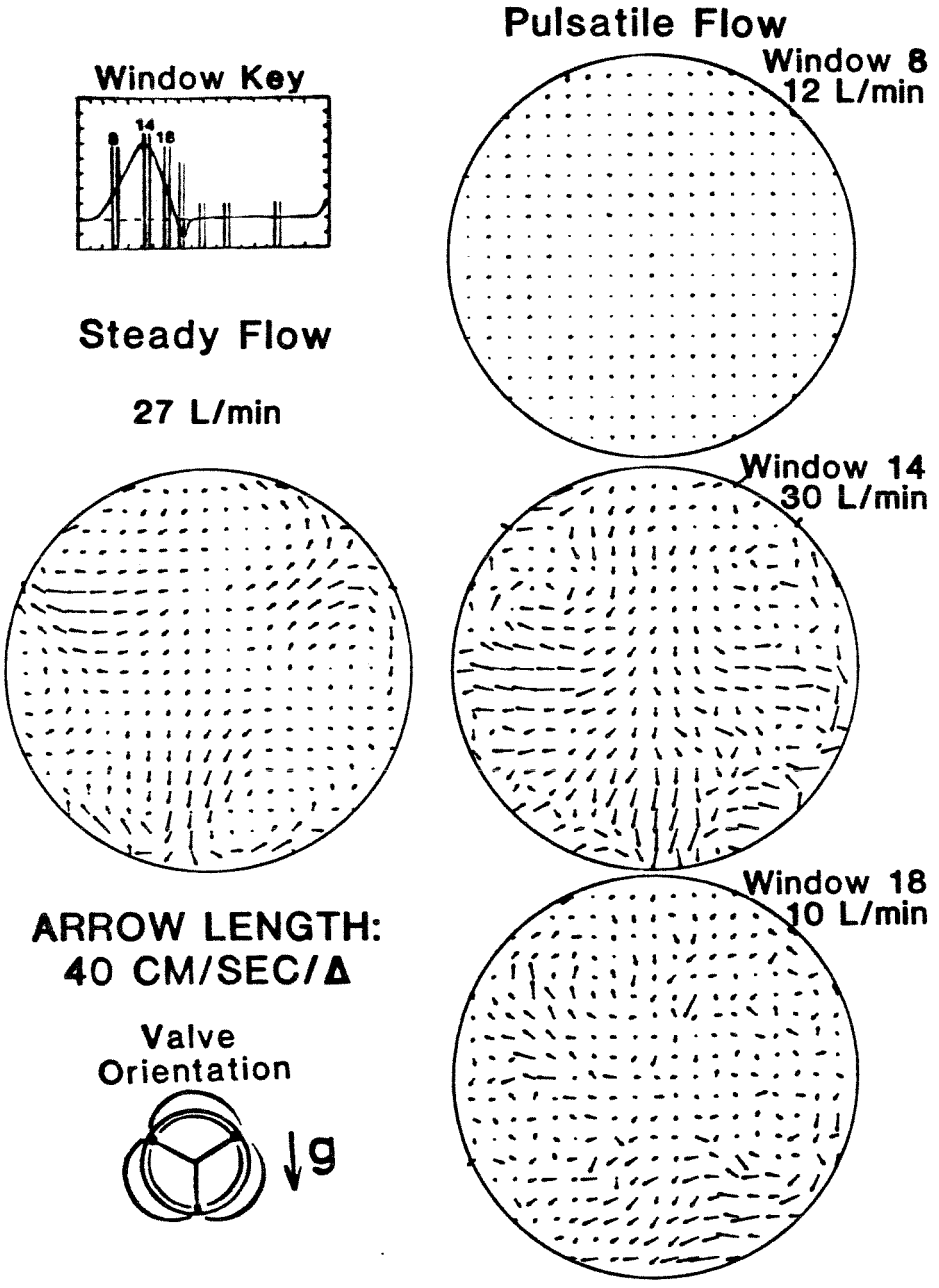

Figure 24. Mean non-axial velocities as resultants for steady flow and for pulsatile-flow windows 8, 14, and 18 downstream from the Ionescu-Shiley (25 mm) bioprosthesis at z = 31.8 mm.

caught up into the axial jet. For steady flow, the non-axial results were similar for each group of wall-directed velocities. The pulsatile-flow results for window 14 had a less symmetrical flow pattern which corresponded roughly with the less symmetrical structure of the axial flow results. Early in systole at window 8 very little mean non-axial velocities were present. Late in systole at window 18 the structure of the flow had degenerated considerably and limited structure of the flow pattern can be discerned. Some large, wall-directed velocity components were found which again corresponded to the azimuthal location of the 'apices' of the axial jet.

The maximum mean velocities in the radial and azimuthal directions were determined as resultants of the velocity components measured in the x- and y-directions. For steady flow, the maximum mean velocities in the radial and azimuthal directions were 42.0 ± 1.0 cm/s and 38.9 ± 1.0 cm/s, respectively. For pulsatile flow, these maximum velocities were 53.1 ± 1.0 cm/s and 43.1 ± 1.0 cm/s, respectively. These pulsatile-flow results were for window 14.

Mean non-axial velocities are presented as resultants in Figure 25 for windows 25, 30, and 40 of the pulsatile flow. Overall, only small velocity components were observed. As diastole proceeded, these small velocities generally became even smaller, as indicated by the increased number of grid points at which no arrow was plotted. No arrow was plotted, as mentioned above, when the magnitude of the velocity at that point was less than 2.0 cm/s. Moreover, there was no appreciable structure of the flow notable from these non-axial results. This lack of apparent flow structure was in spite of the finding from the axial results that during most of diastole there was a large, slowly rotating vortex downstream from the mounted valve. Apparently the data plane was located by chance very close to the plane of the axis of the vortex and hence only small non-axial velocity components were measured.

IONESCU-SHILEY (25 mm)

MEAN NON-AXIAL VELOCITIES

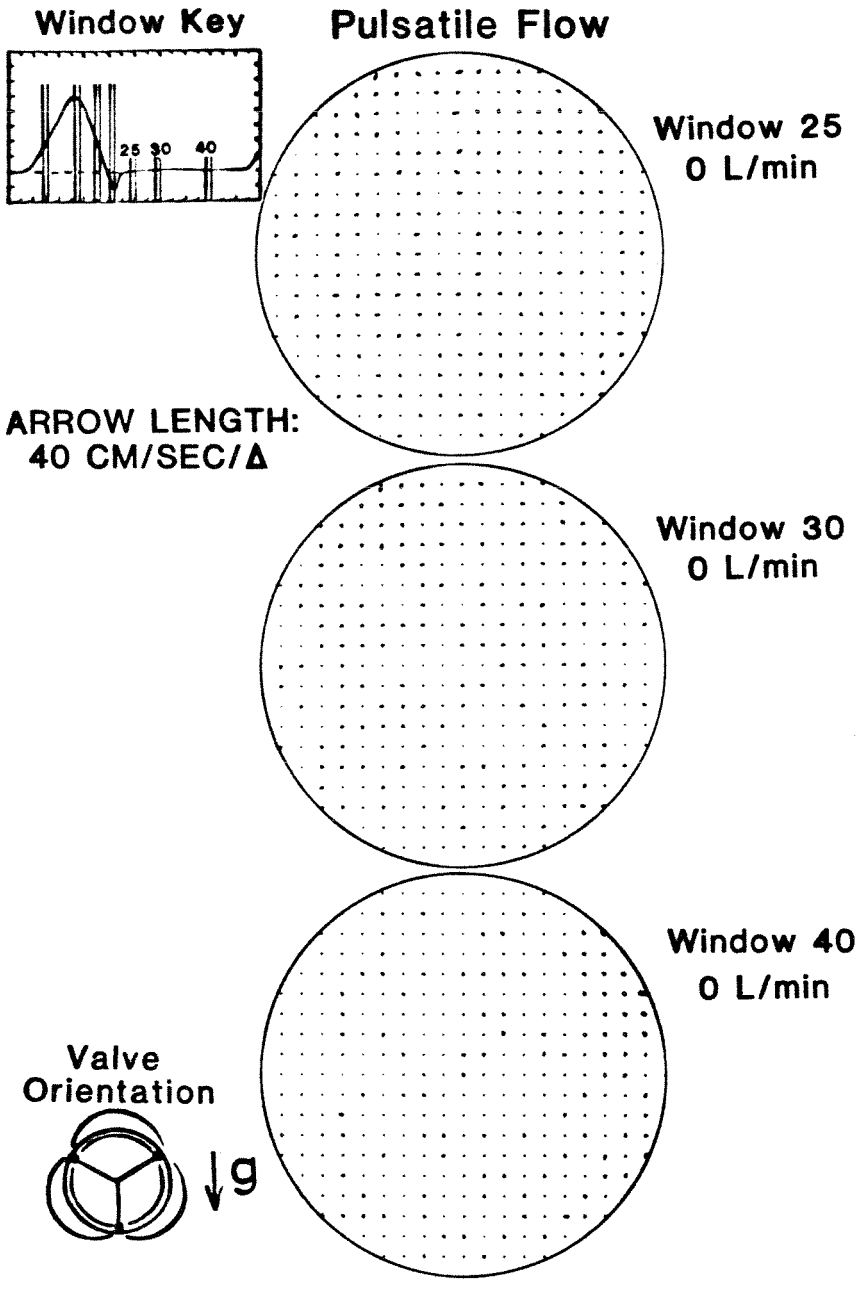

Figure 25. Mean non-axial velocities as resultants for pulsatile-flow windows 25, 30, and 40 downstream from the Ionescu-Shiley (25 mm) bioprosthesis at z = 31.8 mm.

The rms axial velocities are presented in Figure 26 for steady flow and for windows 8, 14, and 18 of the pulsatile flow. For both steady and pulsatile flow, the rms axial velocities reflect the triangular symmetry of the mean velocity results. Three ridges of high rms velocities are shown which correspond azimuthally to the 'sides' of the axial jets. The rms axial velocities for steady flow were generally greater than that for window 14 of the pulsatile flow. The maximum rms axial velocity for steady flow was 58.0 ± 1.0 cm/s while that for pulsatile flow was 52.5 ± 1.0 cm/s. The average rms axial velocity across the data plane for steady flow was 33.5 ± 1.0 cm/s while that for pulsatile flow was 29.3 ± 1.0 cm/s. The pulsatile-flow results are for window 14. The rms axial velocities corresponded to an average turbulence intensity across the data plane as high as 38% for steady flow and 29% for pulsatile-flow window 14. The maximum turbulence intensity at the data plane was 65% for steady flow and 55% for pulsatile-flow window 14. The axial rms results for the two flow regimes show a well-defined, triangular minimum which had both a cross-sectional shape and a location very similar to that of the respective axial jets. Early in systole at window 8 the rms axial velocities were by comparison very low. Late in systole at window 18 the rms axial velocities were still quite elevated, though generally smaller than those found at window 14.

The rms non-axial velocities in all three of the axial and non-axial directions are presented in Figure 27 for steady flow. The non-axial results were quite similar to the axial results except that the axial velocities were larger in magnitude. Thus the axial results represent an upper bound on the rms velocities. The non-axial results show that there were appreciable velocity fluctuations in the non-axial directions. For pulsatile flow, the difference between the rms velocities in the axial and those non-axial directions was even more substantial. Presenting the non-axial rms velocities as contours therefore

IONESCU-SHILEY (25 mm)

RMS AXIAL VELOCITIES

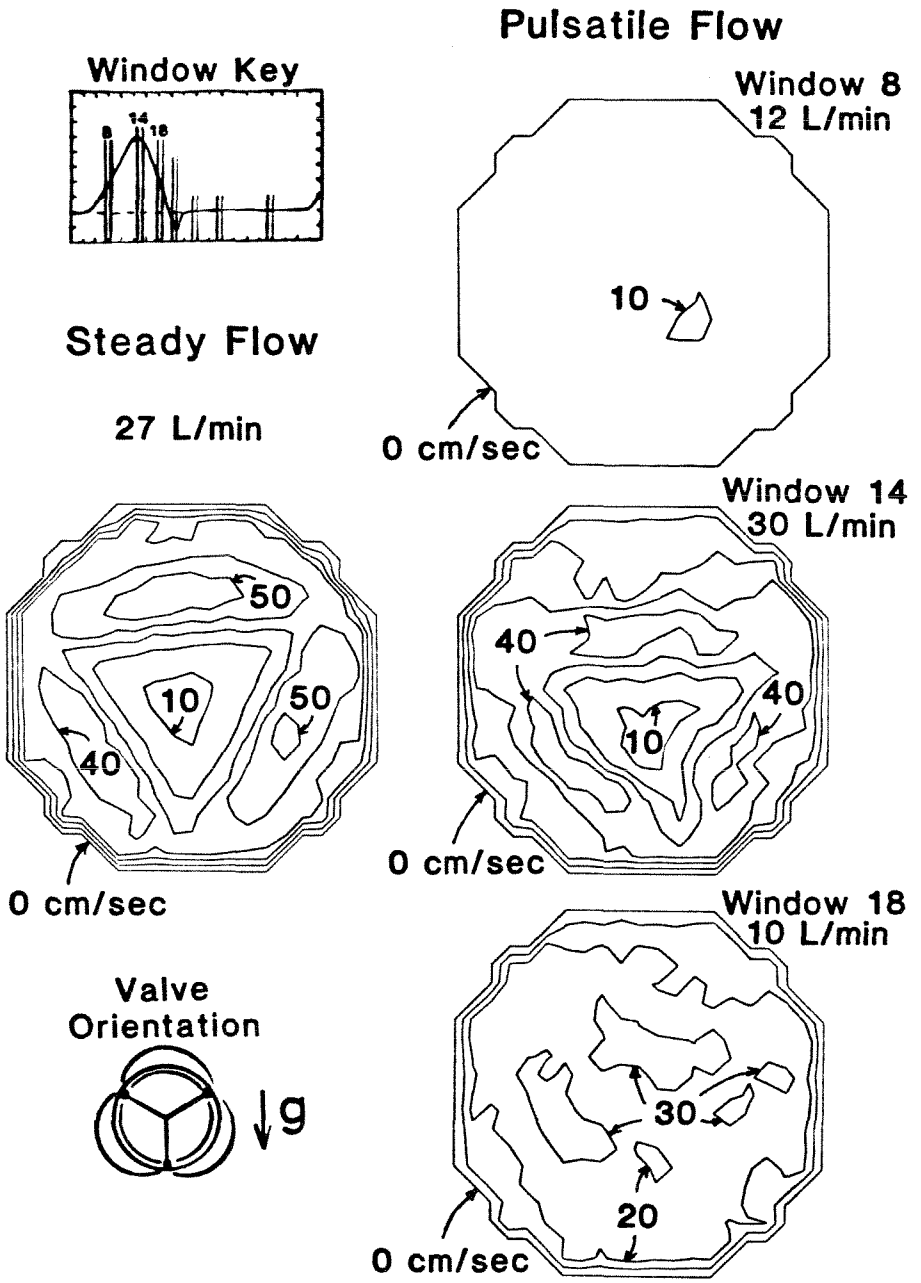

Figure 26. Root-mean-square (rms) axial velocities as contours for steady flow and pulsatile-flow windows 8, 14, and 18 downstream from the Ionescu-Shiley (25 mm) bioprosthesis at z = 31.8 mm. Contour interval: 10 cm/s.

IONESCU-SHILEY (25 mm)

RMS VELOCITIES

Steady Flow

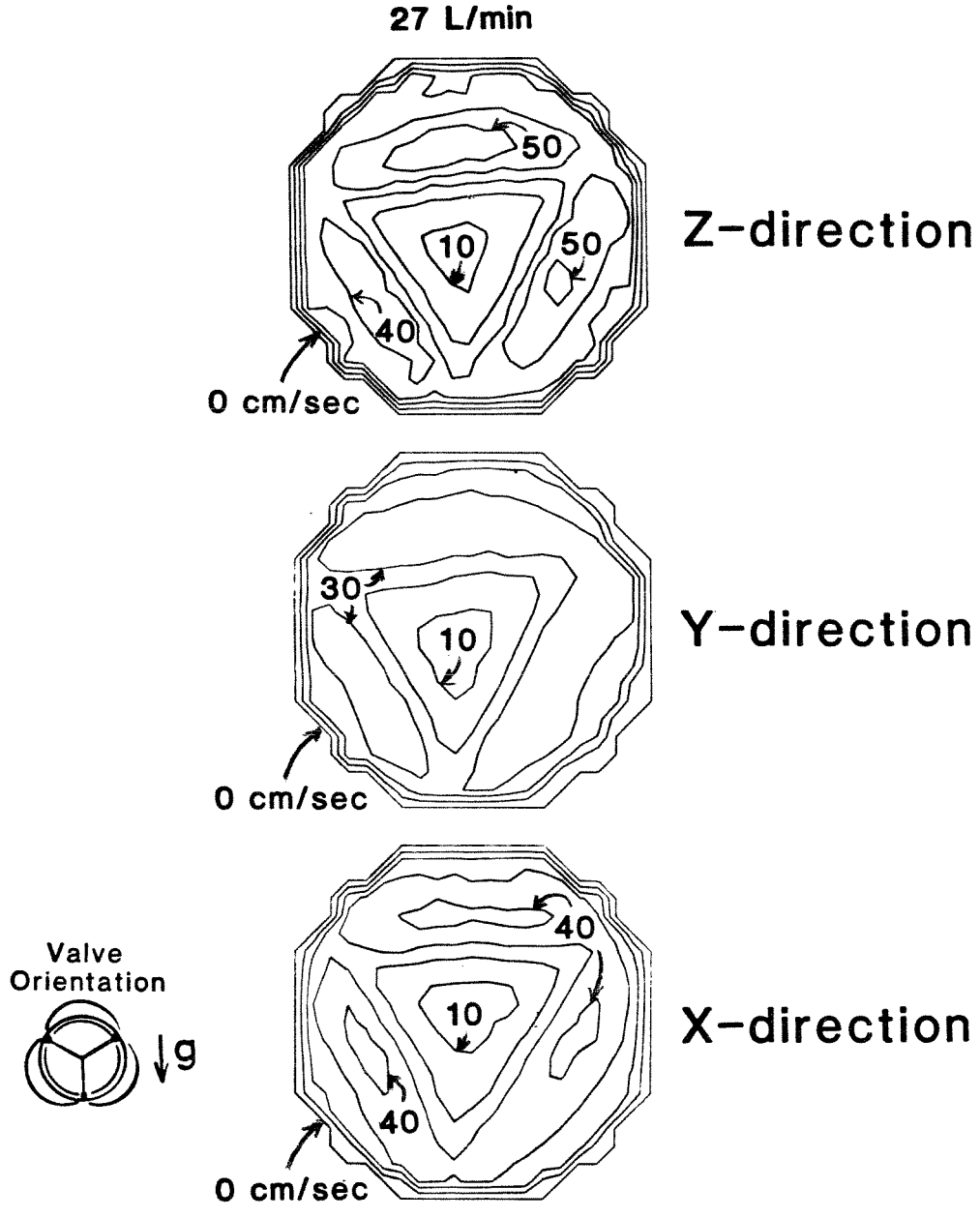

Figure 27. Root-mean-square (rms) velocities in the axial (z) direction and non-axial (y and x) directions as contours for steady flow downstream from the Ionescu-Shiley (25 mm) bioprosthesis at z = 31.8 mm. Contour interval: 10 cm/s.

did not add additional insight and hence they are not included here.

Because separated-flow regions were observed for the data plane location of z = 31.8 mm, velocity data were also collected farther downstream at the flow-reattachment point. It was desired to determine the extent of the flow separation. As the flow proceeded downstream, each of the three separated-flow regions remained distinct from the others and "reattached" at a different location downstream from the valve mount. The point of flow reattachment was taken as that location at which the last remaining separated-flow region attached. Using this criterion, flow reattachment was found to occur for steady flow at z = 55.9 mm. For pulsatile flow, however, variations of the location of the reattachment point from cycle to cycle made any reference to some "average" reattachment location to be rather arbitrary. The reattachment point would vary as much as 10 to 20 mm from cycle to cycle. Thus measurements of the velocities at the reattachment point were made for steady flow only.

Mean axial velocities for steady flow are presented in Figure 28 for both z = 31.8 mm and z = 55.9 mm. At z = 55.9 mm the jet was significantly changed in shape and somewhat diminished in magnitude. The apices were broader and the 'sides' of the jet were 'squeezed in'. The jet at z = 55.9 mm thus was less triangular in shape and instead was more 'tripodal' in shape. The resulting 'peak' of the jet at z = 55.9 mm was much narrower than that at z = 31.8 mm. Also, the mean velocity gradients in the bulk flow for the jet at z = 55.9 mm were considerably lower than those for the jet at z = 31.8 mm. Along the wall, the mean velocity gradients appeared to be higher over longer stretches of the wall for z = 55.9 mm than for z = 31.8 mm.

Mean non-axial velocities for steady flow are presented as resultants in the top of Figure 29 for both z = 31.8 mm and z = 55.9 mm. The tri-symmetric structure of the secondary flow for the results at z = 55.9 mm was similar to

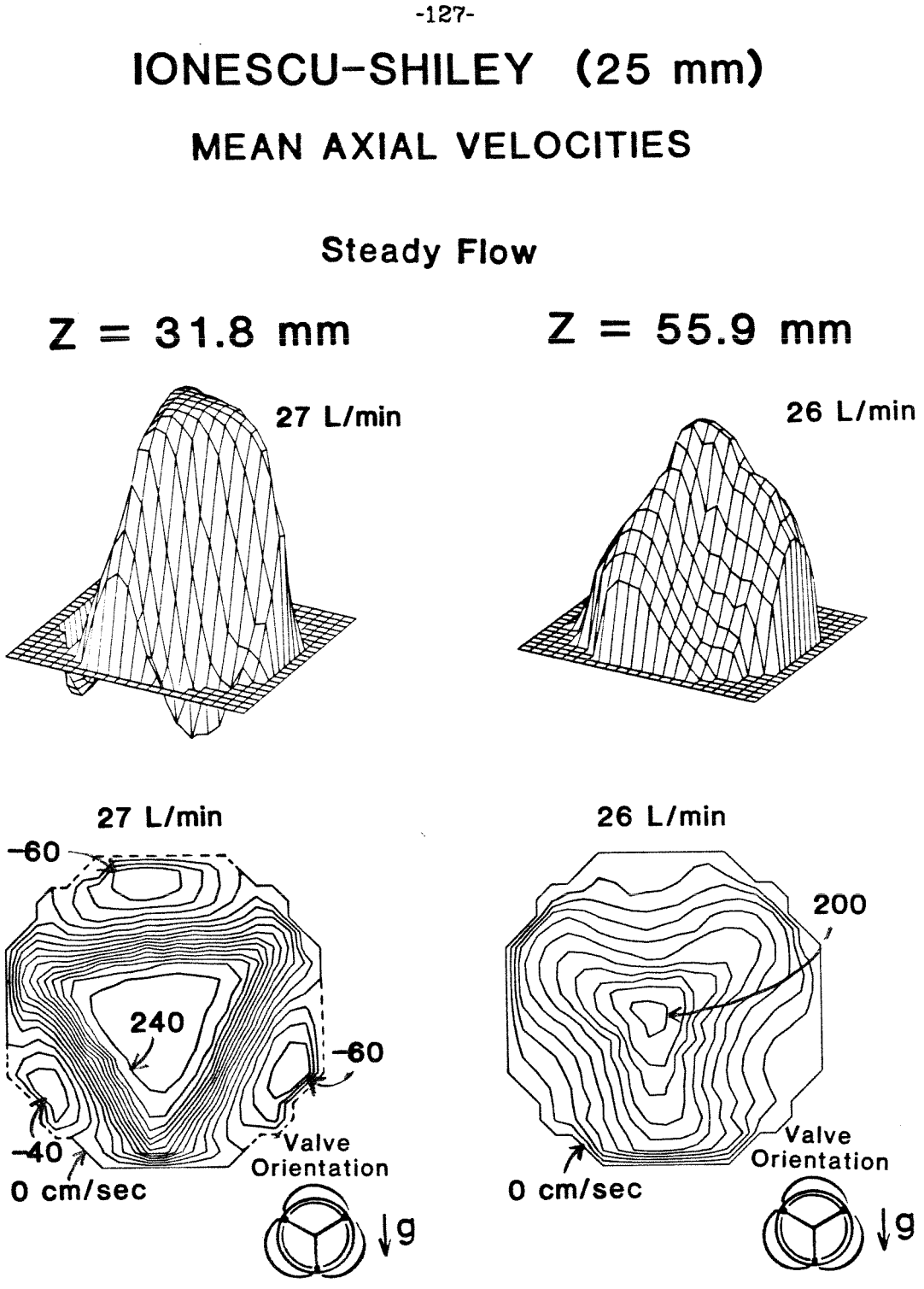

Figure 28. Comparison of mean axial velocities for data plane located at z = 31.8 mm with those for data plane located at z = 55.9 mm downstream from the Ionescu-Shiley (25 mm) bioprosthesis. Contour interval: 20 cm/s.

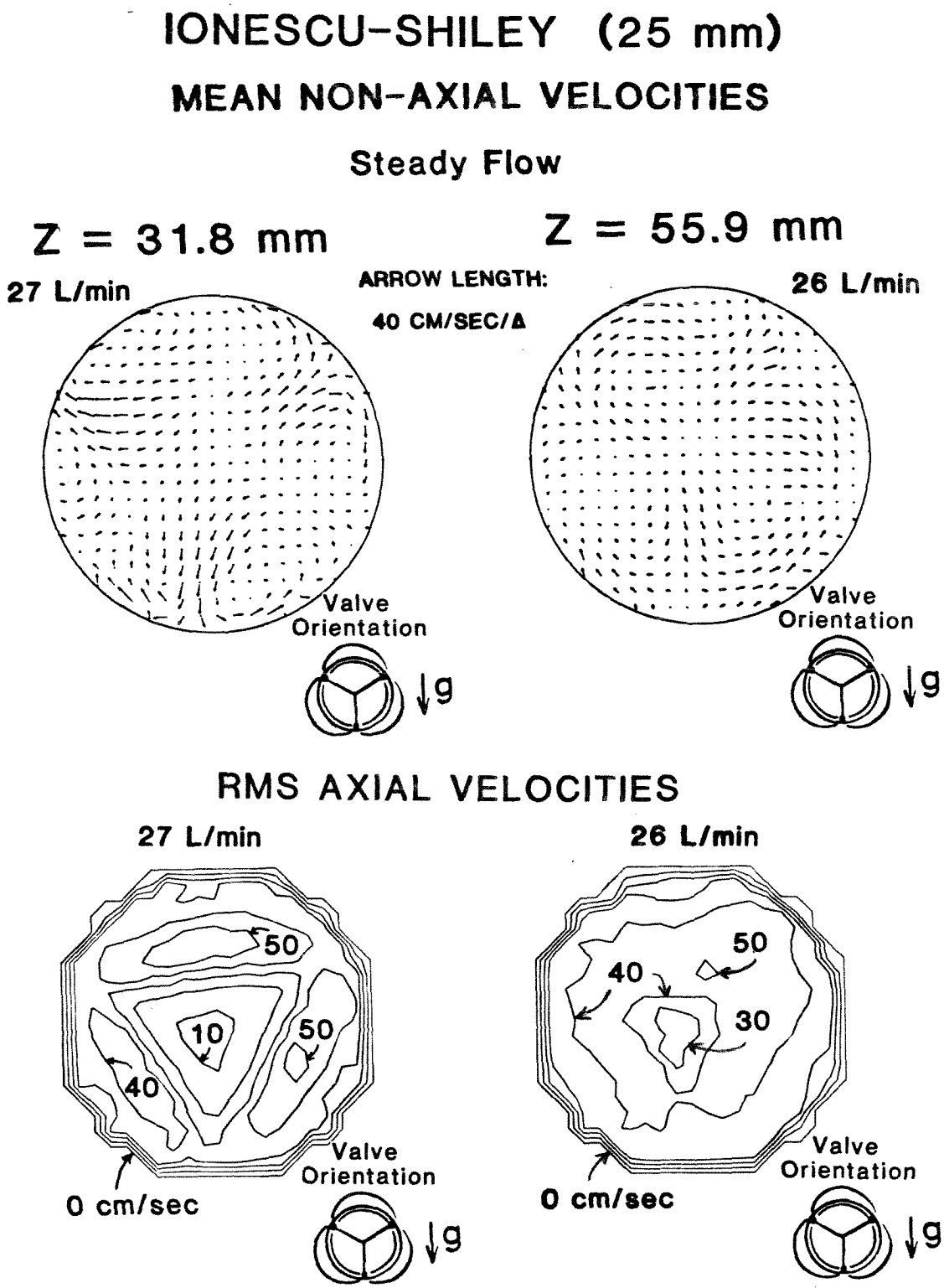

Figure 29. Comparison of the mean non-axial velocities (top) and rms axial velocities (bottom) for data plane located at z = 31.8 mm with those for data plane located at z = 55.9 mm downstream from the Ionescu-Shiley (25 mm) bioprosthesis. Contour interval for rms velocities: 10 cm/s.

that for the results at $z = 31.8$ mm. The highest non-axial velocities for $z = 55.9$ mm were, however, those oriented azimuthally whereas for $z = 31.8$ the highest velocities were those oriented radially.

The structure of the secondary flow seems to indicate the mechanism by which the axial jet was 'squeezed in'. The secondary flow at $z = 31.8$ mm, as discussed above, was noted as being structured in such a way that fluid was transferred out of the jet along its 'apices' and into the separated-flow regions along the wall. The relatively large axial momentum of the fluid being swept out of the jet into the separated-flow regions probably tended to shrink these regions. At the same time, this secondary flow was also noted as being structured in such a way that the fluid in the separated-flow regions was transferred into the jet at its 'sides'. The negative axial momentum of the fluid being swept into the jet thus simultaneously tended to diminish the mean axial velocities along the 'sides' of the jet. This negative axial momentum was, of course, smaller than the positive axial momentum of the jet. Thus the net effect of the secondary flow was to 'squeeze in' the 'sides' of the cross section of the jet while decreasing the cross-sectional area of the separated-flow regions.

The 'tripodal' cross-sectional shape of the jet at $z = 55.9$ mm appears to be the end result of this tri-symmetric, "squeezing-of-the-jet" phenomenon. By the time the flow has reached $z = 55.9$ mm the secondary-flow structure had transferred enough positive momentum into the separated-flow regions that flow reattachment had been completed. In the process, however, the axial jet lost some positive momentum overall and considerable positive momentum along its 'sides'. It should be mentioned that, overall, momentum was conserved as the flow proceeded from $z = 31.8$ mm to $z = 55.9$ mm. The average axial velocity across the tube, which was proportional to the axial momentum, was the same at both axial locations.

The shift in the sense of the velocities, and hence momentum, across the tube did result in a significant drop in the average kinetic energy ($\overline{KE}$) between the two data planes at z = 31.8 and 55.9 mm. $\overline{KE}$ dropped from 1.07 $kg \cdot m^2/s^2$ at z = 31.8 mm to 0.35 $kg \cdot m^2/s^2$ at z = 55.9 mm.

The rms axial velocities for both z = 31.8 mm and z = 55.9 mm are presented in the bottom of Figure 29 and show that the flow field was still highly disturbed near the reattachment point. The shape of the rms results at z = 55.9 mm was much less triangular than that for the rms results at z = 31.8 mm. The magnitude of the rms velocities at z = 55.9 mm, on the other hand, were not very much lower than those for z = 31.8 mm. In fact, because of the presence of very low rms velocities in the center of the results at z = 31.8 mm, the average of the rms velocities across the data plane was higher for z = 55.9 than for z = 31.8 mm. The average rms across the data plane at z = 31.8 mm was 33.5 cm/s while that at z = 55.9 mm was 38.2 cm/s. These average rms velocities correspond to average turbulence intensities of 38% and 46%, respectively.

Elevated rms, or fluctuating, velocities are of particular interest because from them an estimate of the magnitude of turbulent, or Reynolds, stresses can be obtained. These turbulent stresses are given by

$$\tau_{ij}^{turb} = \rho \ \overline{u' v'} \ , \tag{6}$$

where τ_{ij} is the Reynolds stress, ρ is the fluid density, and u' and v' are the orthogonal fluctuating velocity components in the i and j directions, respectively. Further, assuming an appropriate correlation coefficient can be found, $\overline{u' v'}$ can be estimated as

$$\overline{u' v'} = k_c \, (u_{rms} \, v_{rms}) \, , \tag{7}$$

where k_c is the correlation coefficient and u_{rms} and v_{rms} are the rms velocities in the i and j directions, respectively. Thus, as can be seen from Equation (7), if a correlation coefficient can be assumed across the data plane, then the magnitude of the turbulent stresses will be proportional to the product of two orthogonal rms velocities.

Given the above analysis, the total shear stress across the data plane can now be estimated. The laminar shear stress can be calculated from the mean velocity gradient of the axial velocity in the x-direction as

$$\tau_{zx}^{lam} = \mu \left| \frac{\partial v_z}{\partial x} \right| . \tag{8}$$

The absolute value is used here because the magnitude of the shear stresses is what was sought. Using the absolute value a maximum value for the total shear stress will be estimated. For calculating the turbulent shear, Tennekes and Lumely (1972) have suggested that for all turbulent shear flows k_c can be estimated as 0.4. It should be noted that this value of k_c is that for *steady* flow and hence can not strictly be used with pulsatile-flow results. The value of k_c for pulsatile flow would probably be lower than that for steady flow (Tennekes and Lumely, 1972) and hence the steady-flow value of 0.4 can be used to give upper-limit estimations of the pulsatile-flow turbulent shear stresses. Combining Equations (6) and (7), the turbulent shear can thus be estimated as

$$\tau_{zx}^{turb} \approx 0.4 \, \rho \, (u_{rms} \, v_{rms}) \, , \tag{9}$$

where $k_c = 0.4$ and u_{rms} and v_{rms} are the rms velocities in the z-direction and x-direction, respectively. Finally, the total shear stress τ_{zx}^{tot} is

$$\tau_{zx}^{tot} = \tau_{zx}^{lam} + \tau_{zx}^{turb} \,. \tag{10}$$

Therefore, substituting from Equations (8) and (9) into Equation (10), the total shear stress can be estimated as

$$\tau_{zx}^{tot} \approx \mu \left| \frac{\partial v_z}{\partial x} \right| + 0.4\, \rho\, (u_{rms}\, v_{rms}) \,. \tag{11}$$

The total shear stresses estimated from the velocity data using Equation (11) are presented as contours in Figure 30 for the axial velocity in the x-direction. Ridges of elevated shear stresses are apparent in Figure 30 at essentially the same spatial location as the ridges in the rms velocity results. These ridges of elevated shear stress also corresponded spatially to the high laminar shear stresses along the 'sides' of the jet structure. More elevated shear stresses are shown. Near the wall, the shear stresses near the wall corresponded spatially to the location of the 'apices' of the triangular jet. Low shear stresses are shown for locations which corresponded roughly to the locations of the separated-flow regions and also over the large central region corresponding to the peak of the triangular jet.

The maximum total shear stress was estimated which was present over at least 10% of the tube cross section. For steady flow, this maximum shear stress was estimated to be $128 \pm 5\ N/m^2$. For pulsatile flow, this maximum shear stress was estimated to be $112 \pm 5\ N/m^2$ at window 14.

Figure 31 shows the estimated total shear stresses for the three shear components of the stress tensor. As expected from the relative magnitudes of the rms velocities, the estimated shear stresses are largest for the stress components which include the rms axial velocities. Thus only a single shear stress component, τ_{zx}, is presented for the pulsatile-flow results.

Figure 32 shows the volumetric-flow rates and average rms velocities

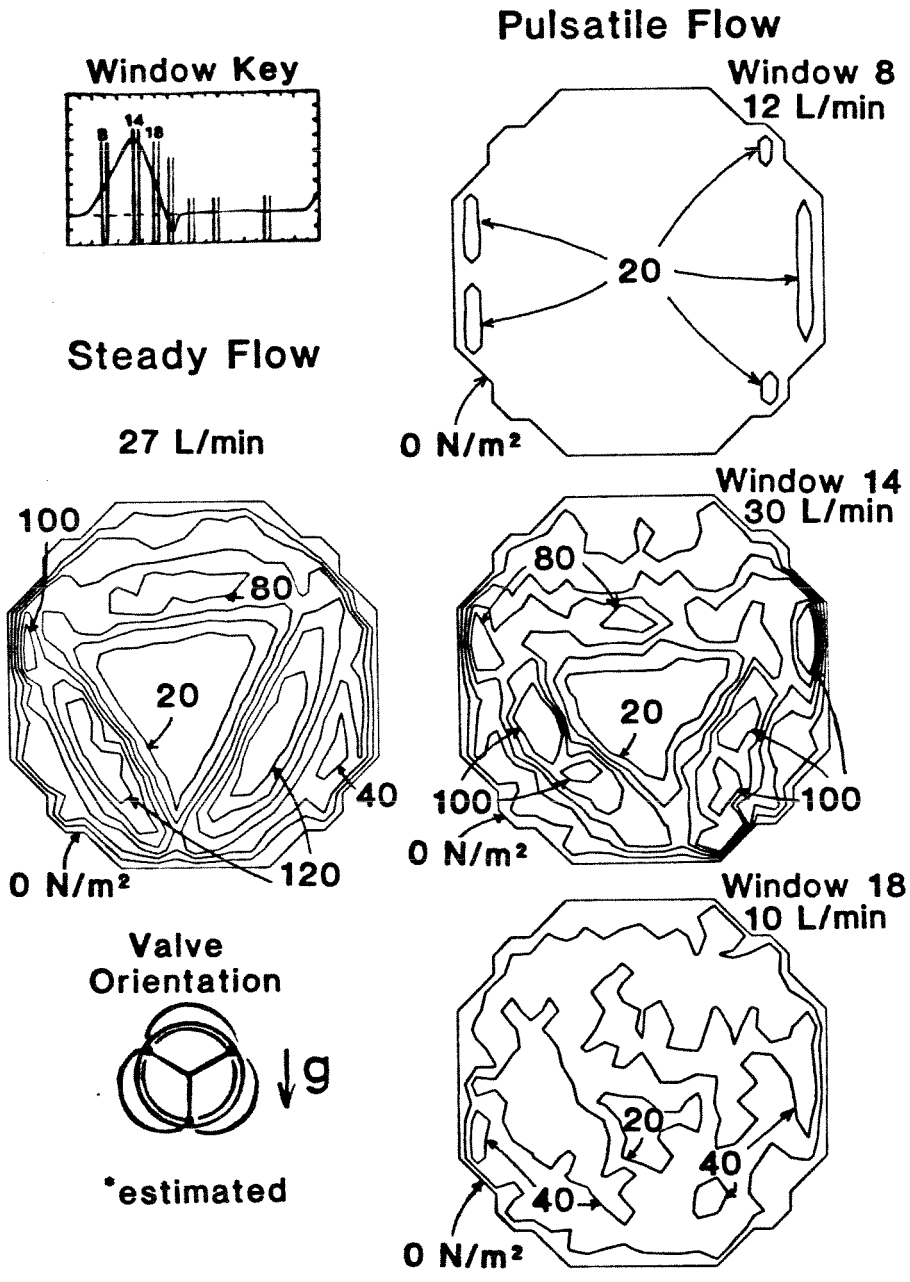

Figure 30. Total estimated shear stresses, τ_{zx}, as contours for steady flow and for pulsatile-flow windows 8, 14, and 18 downstream from the Ionescu-Shiley (25 mm) bioprosthesis at z = 31.8 mm. Contour interval: 20 N/m^2.

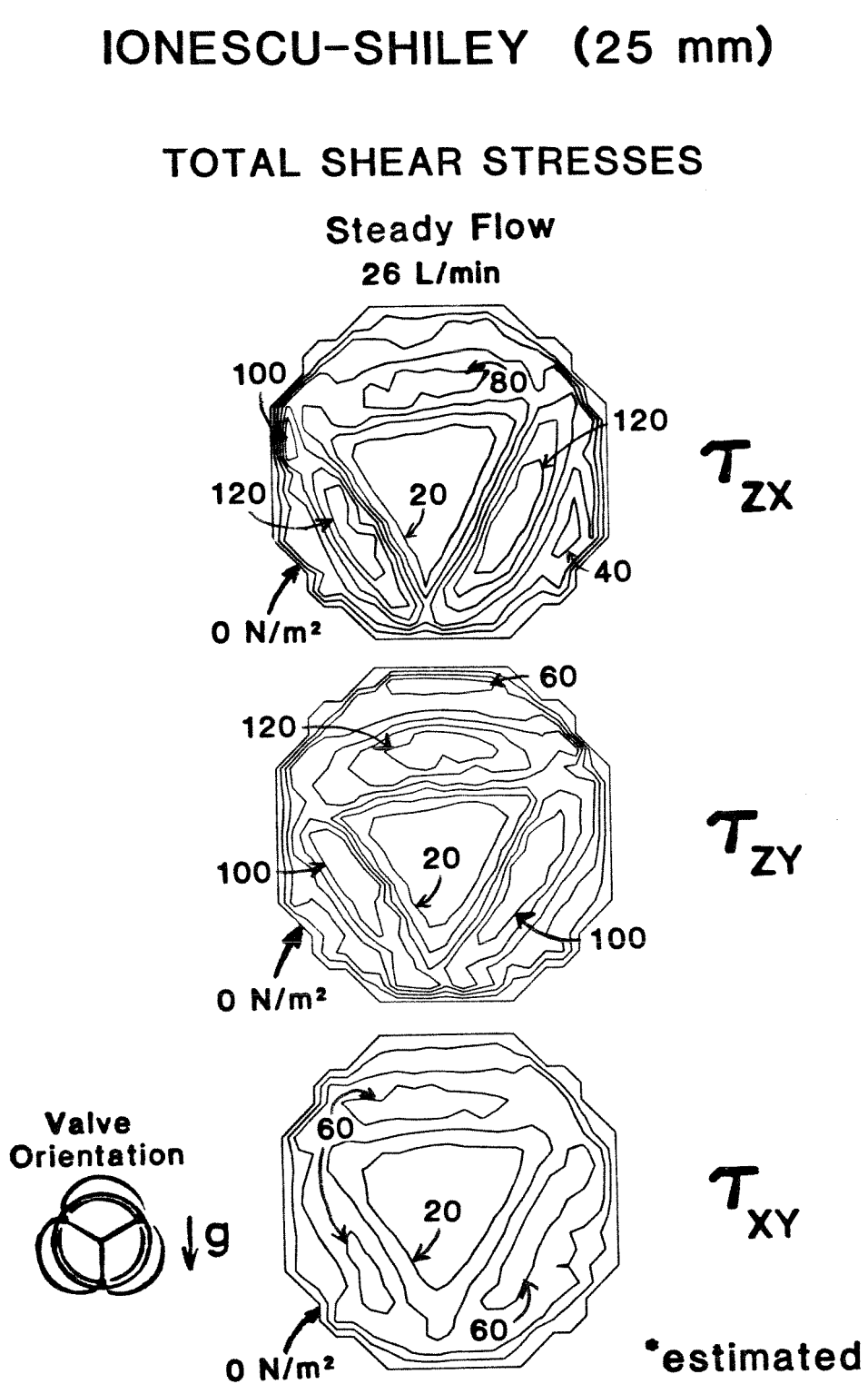

Figure 31. Total estimated shear stresses τ_{zx}, τ_{zy}, and τ_{xy}, for steady flow downstream from the Ionescu-Shiley (25 mm) bioprosthesis at z = 31.8 mm. Contour interval: 20 N/m^2.

IONESCU-SHILEY (25 mm)

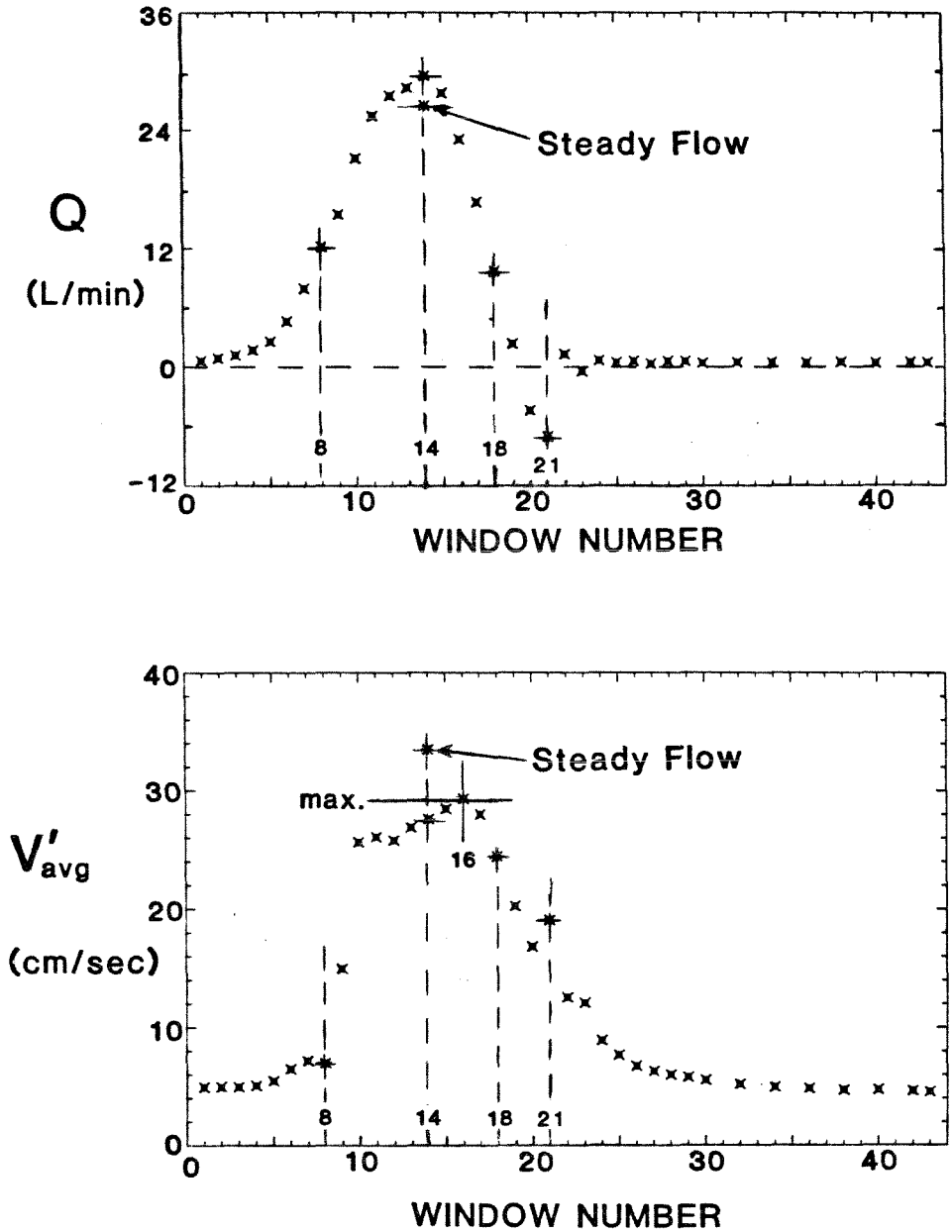

Figure 32. Volumetric-flow rate (top) and average rms velocity (bottom) calculated from the mean and rms velocities, respectively, at the data plane as a function of pulsatile-flow window number for the Ionescu-Shiley (25 mm) bioprosthesis.

calculated from the mean and rms velocities, respectively, at the data plane. The plots in Figure 32 allow an analysis and comparison of the steady-flow and pulsatile-flow results. In the top of Figure 32 the flow rate is plotted versus the pulsatile-flow window number. The flow rates plotted here were determined by averaging the mean axial velocities across the data plane. For pulsatile flow, the flow rate determined for each window is plotted to correspond with its respective window number along the abscissa. The flow rate for steady flow is plotted to correspond with window 14, which was the window encompassing the maximum flow rate for pulsatile flow. In the bottom of Figure 32 the average rms axial velocity is plotted versus the pulsatile-flow window number. The average rms axial velocities plotted here were determined by averaging the rms axial velocities across the data plane. For pulsatile flow the average rms axial velocity determined for each window is plotted to correspond with its respective window number along the abscissa. The average rms axial velocity for steady flow is plotted to correspond in time with the steady-flow result in the top of Figure 32.

The flow-rate results shown in Figure 32 generally agree with those in Table 5 which were obtained using the electromagnetic flowmeter. The maximum and minimum flow rates from the velocity data were 30 L/min and -8 L/min, respectively. The corresponding values from Table 5 are 29.8 L/min and -10.5 L/min. The smaller value for the minimum flow rate from the velocity data is a result of the "smoothing" effect of the finite width of the pulsatile-flow window. As discussed below, this smaller value may also result some from slight variability in the timing of the successive cycles from which these data were taken. Taking the beginning of the systolic ejection interval to be at window 5, the timing of the maximum and minimum flow rates also agree. The velocity data indicate that the maximum and minimum flow rates occurred about 180

and 320 milliseconds after the systolic ejection interval began, respectively. The corresponding values from Table 5 are 190 and 328 milliseconds, within the uncertainty of the width of the 20-millisecond windows.

There are some disagreements between the flow-rate results given in Figure 32 and those presented in Table 5. The forward-flow and leakage-flow rate calculated from the results plotted in Figure 32 are different from the respective rates presented in Table 5. The forward-flow rate obtained from Figure 32 is 5.8 L/min; that reported in Table 5 is 5.50 ± 0.13 L/min. The leakage-flow rate obtained from Figure 32 is -0.2 L/min; that reported in Table 5 is -0.11 ± 0.09 L/min The closure-flow rate agreed within experimental error with that obtained from Figure 32 being about -0.2 L/min and that reported in Table 5 being -0.17 ± 0.04 L/min. As stated earlier, the leakage-flow rate for the Ionescu-Shiley valve should be zero. The discrepancies in the forward-flow and leakage-flow rates were probably caused by the tendency for the electromagnetic flowmeter to drift. The negative value for the leakage-flow rate in Table 5 was discussed above as having been a result of the operating characteristics of the electromagnetic flowmeter. If the results in Table 5 are offset so that Q_L becomes zero, then Q_F becomes about 5.6 ± 0.1 L/min. The closure-flow rate would not be affected significantly. The high value of the leakage-flow rate from Figure 32 was probably a result of the tendency for the LDA to overestimate slightly the mean velocity in the probe volume. As discussed in Chapter 2 the LDA was subject to biasing. An analysis of the LDA used in single-burst mode, however, showed that this biasing could be substantially reduced by the use of time integrals for calculating the first and second moments of the data. This analysis showed that biasing, if any, would tend to overestimate the true mean. Thus it appears that experimentally some small biasing of the mean velocity results occurred. That the biasing was small

can be shown from the fact that all biasing was in the same direction, i.e., positive direction, for all grid points on the data plane. During diastole the average overestimation of the flow rate was about 0.45 L/min or about 7.5 cm^3/s. Dividing by the cross-sectional area of the tube, 5.1 cm^2, the average overestimation of the velocity was therefore less than 1.5 cm/s at each grid point on the data plane. In Chapter 2 it was shown that the resolution limit of the A/D converter was about 0.5 cm/s. Thus the effect of the biasing was on the order of the minimum resolving power of the experimental apparatus. If the results for the entire cycle are offset so that the flow rate during diastole shown in Figure 32 is equal to zero, then the forward-flow rate becomes 5.7 L/min. Again, the closure-flow rate would not be affected significantly. The remaining discrepancy of 0.1 L/min can be attributed to the experimental error.

Once the drift of the electromagnetic flowmeter and the biasing of the LDA had been compensated for, the closure-flow rate calculated to about 3% of the forward-flow rate. Since the leakage-flow rate for this prosthesis was zero, the total regurgitant-flow rate was 3% of the forward-flow rate.

Another difficulty with the results shown in the top of Figure 32 is that the flow rate at the end of diastole is shown to have risen before the apparent beginning of the systolic ejection phase. The end-diastolic flow rate at windows 3 and 4 was finite and positive and would not be entirely compensated for by the offsetting described above. The finite flow rates shown in Figure 32 for late diastole are probably a result of the averaging process by which the results were obtained. As can be seen from Tables 4 and 5, there was some variation of the time of the beginning of the systolic ejection interval. This variation was larger than the width of a window and thus some results were probably averaged into, for example, window 4 from windows 3 and 5. Since the flow rate during late diastole was zero and that during early systole was positive, this averaging

process skewed the results for the windows in late diastole towards higher values and the results before systolic ejection towards smaller values. As inferred earlier, the fact that the minimum flow rate shown in Figure 32 is somewhat smaller than that presented in Table 5 may also be a result of this averaging process.

3.3.4 Discussion

3.3.4.1 Discussion of the Pressure and Volumetric-Flow Results

The pressure and volumetric-flow results presented in Tables 4 and 5 indicate that the pressure and flow fields encountered by the mounted prosthesis in the pulse-duplicator were similar to those the valve might have encountered had it been implanted. The maximum rate of change of the ventricular pressure given in Table 4 of 219 ± 10 kPa/s compared well with that of a healthy human ventricle of about 197 ± 37 kPa/s (Yang, et al., 1978). Similarly, the minimum rate of change of the ventricular pressure given in Table 4 of -356 ± 21 kPa/s also compared well with that of a healthy human ventricle of about -355 ± 29 kPa/s (Yang, et al., 1978). For the volumetric-flow results, the forward, closure, and leakage flow given in Table 5 sum to a mean flow rate, or cardiac output (CO), of 5.22 L/min. This mean flow rate was only about 3% below the standard setting of the pulse-duplicator of 5.4 L/min given in Table 2. As was shown above, however, the flow-rate results in Table 5 were subject to adjustment to remove the effects of flowmeter drift. Once adjusted, the flow-rate results in Table 5 become 5.6 L/min, 0.0 L/min, and -0.2 L/min for the forward-flow, closure-flow, and leakage-flow rates, respectively. The sum of these adjusted flow rates is 5.4 L/min which agrees with the setting in Table 2. For a cardiac output of about 5.4 L/min, the maximum flow rate *in vivo* would be about 30 L/min (Yang, et al., 1978). Thus, the *in vitro* value of Q_{max} given in

Table 5 as 29.8 L/min was physiological in magnitude. Finally, the timing results given in Tables 4 and 5 show that the volumetric-flow and pressure events occurred at appropriate times in the cycle relative to one another and in the correct physiological sequence. The times of occurrence of P_{x1} and P_{x2} gave a systolic ejection interval which spanned 34% of the cycle. This percentage is similar to that found *in vivo* for a similar pulse rate and cardiac output. Also, the times of occurrence of Q_{beg} and Q_{end} gave a forward-flow phase with a beginning and ending that were not significantly different from those of the systolic ejection interval. During systole, ΔP_{max} preceded both Q_{max} and VP_{max} by about 20 milliseconds. Though this difference was not significant, the order of events was that observed *in vivo*. The time of occurrence of $\left(\frac{dP}{dt}\right)_{max}$ was appropriately located in time during the iso-volumetric contraction phase. The iso-volumetric compression phase is the short time period after the onset of ventricular contraction but before the ventricular pressure rises sufficiently to allow the aortic valve to open. Similarly, the time of occurrence of $\left(\frac{dP}{dt}\right)_{min}$ was appropriately located in time during the iso-volumetric ***relaxation*** phase. The iso-volumetric relaxation phase is the short time period after the aortic valve closes but before the ventricular pressure falls sufficiently to allow the mitral valve to open. Q_{min} signaled valve closure appropriately by occurring after the end of the systolic ejection interval but before the occurrence of $\left(\frac{dP}{dt}\right)_{min}$ in the iso-volumetric relaxation phase.

The pressure drop across the valve resulting from these pulsatile pressure and flow fields was moderate in magnitude. Of the four valves studied in the present investigation, only the Smeloff prosthesis had a higher ΔP_{max} and $\overline{\Delta P}_{sys}$. Yoganathan, et al. (1983b) have reported the mean systolic pressure drop for

the Ionescu-Shiley prosthesis for similar flow-section geometries and pulsatile-flow parameters. They found a higher $\overline{\Delta P}_{sys}$ of 1.3 kPa for an Ionescu-Shiley valve with a TAD of 25 mm. Only this limited amount of *in vitro* pressure-drop results for pulsatile flow, however, have been found in the literature and additional directly comparable data were not available.

The systolic pressure-drop results that have been reported for *in vivo* investigations have been generally similar to those given in Table 4. Ionescu and coworkers (Ionescu, et al., 1977; Ionescu, et al., 1982; Tandon, et al., 1977) have reported mean systolic pressure drops of 1.0 ± 0.1 kPa for various sizes and for various values of the cardiac index (CI). The cardiac index is defined as the cardiac output in liters per minute divided by the body surface area in square meters.

For pulsatile flow, $\overline{\Delta P}_{dias}$ and $\overline{AP}$ were related to the regurgitant-flow characteristics of this valve during diastole. $\overline{\Delta P}_{dias}$ was a measure of the driving force for regurgitant flow through the closed valve. For the Ionescu-Shiley prosthesis, the leaflets supported this diastolic pressure without allowing any regurgitant flow. $\overline{AP}$ was an indicator of the extent of regurgitating flow during diastole. If a significant amount of regurgitant flow occurred through the valve during diastole, the aortic pressure would drop. The average aortic pressure over the entire cycle would therefore also drop. The average aortic pressure for the Ionescu-Shiley prosthesis study was high relative to the other valves studied. This was explained by the lack of regurgitant flow during diastole for this valve design.

The small amount of leakage flow reported in Table 5 for this valve design probably resulted from flowmeter drift. The leakage flow given in Table 5 needs explanation since leakage flow for the Ionescu-Shiley valve should be so low as to not be measurable. Experimentally, it was found that because of the relatively

long diastolic interval, leakage-flow results for all four valve designs studied were somewhat sensitive to the zero setting of the volumetric flowmeter. Electromagnetic flowmeters are known to have a strong tendency to drift (Wyatt, 1977) and the small, non-zero leakage flow reflects the difficulty of maintaining a precise zero for the flowmeter during three experiments of thirty-hour duration. The flowmeter had a tendency to drift toward lower voltages and thus the leakage flow was determined to be slightly low. Even without correcting for flowmeter drift, the total regurgitant flow of 0.28 L/min was quite small, representing only 5% of the forward flow. The occluding mechanism of the Ionescu-Shiley prosthesis studied thus did not allow significant regurgitant flow during diastole. Further analysis of the regurgitant-flow characteristics of this valve is given below in the section comparing steady-flow and pulsatile-flow results.

For steady flow, $\bar{Q}$ indicates that the steady-flow velocity results were comparable in magnitude to those for pulsatile flow. $\bar{Q}$ at 27 L/min was about 9% smaller than Q_{max} for pulsatile flow. Thus the average velocity at the data plane for both cases was similar. Significantly larger velocities at a given location for pulsatile flow than for steady flow would thus be a result of the flow dynamic and would not simply reflect the higher flow rate.

The steady-flow pressure drop $\overline{\Delta P}$ across the valve resulting from $\bar{Q}$ was also significant, as ΔP_{max} and $\overline{\Delta P}_{sys}$ were for pulsatile flow. Of the four valves studied in the present investigation only the Smeloff prosthesis had a significantly higher pressure drop. $\overline{\Delta P}$ was essentially the same for the Björk-Shiley prosthesis.

There have been more pressure-drop results for steady flow reported in the literature for the Ionescu-Shiley valve than for pulsatile flow. For prostheses with a TAD of 25 mm, Schramm, et al. (1982) reported a mean pressure drop of

0.9 kPa at a flow rate of 18 L/min and Yoganathan, et al. (1983b) reported a mean pressure drop of 2.4 kPa at a flow rate of 25 L/min. For a prosthesis with a TAD of 21 mm, Martin and coworkers (Martin, et al., 1981; Tindale, et al., 1982) reported a mean pressure drop of 1.6 kPa at a flow rate of 20 L/min.

Pressure-drop results for steady flow can be compared for the same TAD at different flow rates. Peskin (1982) has shown that theoretically for steady flow

$$\Delta P = C\, Q^2 , \tag{12}$$

where ΔP is the steady-flow pressure drop, C is a constant and in particular $C \neq C(Q)$, and Q is the volumetric flow. In deriving Equation (12), Peskin assumed i) that the energy was conserved in the inflow region upstream from the valve, ii) that momentum was conserved in the outflow region downstream from the valve, iii) that the pressure was equal across all planes perpendicular to the flow direction, iv) that the velocity profile was flat both up and downstream from the valve, and v) that the geometry of the flow path was independent of time. Using Equation (12), a pressure drop ΔP_1 for a flow rate Q_1 can be used to determine the pressure drop ΔP_2 for a known flow rate Q_2. Thus,

$$\Delta P_2 = \left[\frac{Q_2}{Q_1}\right]^2 \Delta P_1 . \tag{13}$$

Note that the constant C has canceled out. Several investigators (Forrester, et al., 1969; Yoganathan, 1978; Yoganathan, et al., 1983b; Emery and Nicoloff, 1979; Gombrich, et al., 1979; Gabbay, et al., 1980; Bruss, et al., 1983) have presented pressure-drop results which show that the exponent in Equations (12) and (13) indeed ranged from 1.9 to 2.0 for most currently available mechanical prostheses. For the Ionescu-Shiley valve, however, the results presented in the literature have indicated an exponent closer to 1.6 (Tindale, et al., 1982; Yoganathan, et al., 1983b).

When corrected to a flow rate of 27 L/min using the exponent of 1.6 in Equation (13), the reported steady-flow pressure drops have been generally higher than that found in the present investigation. When corrected to 27 L/min, the pressure drop found by Yoganathan, et al. (1983b) was 2.9 kPa; that found by Schramm, et al. (1982) was 1.7 kPa; and that found by Martin and coworkers (Martin, et al., 1981; Tindale, et al., 1982) was 2.6 kPa.

The results of Martin and coworkers were, however, for a prosthesis with a TAD of 21 mm. For a TAD of 25 mm, the pressure drop would be less than 2.6 kPa. How much less is difficult to determine. Yoganathan (1978) has attempted to estimate the pressure drop across a prosthesis of one size from the known pressure drop of another size. To make his estimations he assumed that the pressure drop across the valve was due entirely to the valve orifice. The pressure drop he estimated, however, varied from that he measured by as much as 100% of the measured value. The lack of success of this approach was probably based on the fact that the pressure drop was *not* due entirely to the valve orifice. Rather the valve orifice, occluder, and superstructure each caused some flow obstruction and contributed in an unknown way to the total pressure drop. The assumption above thus was invalid and estimating pressure drops for different sized valves was not reliable.

The agreement among the pressure results for steady flow has been generally poor. As given above, a difference between results of more than a factor of two exists. This disagreement may stem from the fact that the Ionescu-Shiley prosthesis has been shown to require a pressure-recovery length greater than 100 mm (Martin, et al., 1981; Schramm, et al., 1982). These investigations of the pressure-recovery characteristics of the Ionescu-Shiley valve have shown that the maximum pressure drop is about 50% greater than the fully recovered pressure drop and occurs between 30 mm and 40 mm downstream from the

valve. The pressure-drop results of Yoganathan, et al. (1983b), the highest quoted above, were for a downstream pressure tap location of z = 40.5 mm. For the present investigation, as mentioned in Chapter 2, the downstream pressure tap was located at z = 150 mm. Also, as Martin, et al. (1981) have observed, a slight off-axis mounting of this prosthesis can notably affect its pressure-recovery characteristics and hence the pressure drop measured at a given location. Some disagreement is therefore also possible if adequate attention is not given to the precise mounting of this valve.

The pressure-drop characteristics for pulsatile flow can be estimated from that found for steady flow. Yoganathan (1978) found that $\overline{\Delta P}$ for several mechanical valves was related to $\overline{\Delta P}_{sys}$ such that

$$\frac{\overline{\Delta P}}{\overline{Q^2}} = \frac{\overline{\Delta P}_{sys}}{\overline{Q^2}}, \tag{14}$$

where

$$\overline{Q^2} = (Q_{rms})^2 .$$

Yoganathan also found that ΔP_{max} is related to $\overline{\Delta P}$ such that

$$\Delta P_{max} = \overline{\Delta P} + \frac{\rho L}{A}\left(\frac{dQ}{dt}\right), \tag{15}$$

where L is the distance between the pressure taps in meters and A is the cross-sectional area of the tube in square meters. In deriving Equations (14) and (15) it was assumed that the drag coefficient for steady flow was equal to that for pulsatile flow, the velocity profile was flat, and the inductive pressure drop for pulsatile flow was due primarily to the acceleration of the fluid through the flow section. Experimentally, Yoganathan (1978) determined that $\frac{dQ}{dt}$ could be closely approximated by $\frac{2\,Q_{max}}{\Delta t_{sys}}$ where Δt_{sys} is the systolic ejection time interval.

Equation (15) becomes

$$\Delta P_{max} = \overline{\Delta P} + \frac{\rho L}{A}\left[\frac{2\,Q_{max}}{\Delta t_{sys}}\right]. \qquad (16)$$

Thus estimations of the pressure-drop characteristics for pulsatile flow were possible from steady-flow results when $\overline{Q}$, Q_{rms}, Q_{max}, and Δt_{sys} were known.

For the pressure-drop results of the present investigation, Equations (14) and (16) gave estimated values somewhat smaller than that measured for the Ionescu-Shiley valve. Substituting into Equation (14) the values for $\overline{\Delta P}$, $\overline{Q}$, and Q_{rms} from Tables 4 and 5, the $\overline{\Delta P}_{sys}$ calculated was 0.68 kPa. $\overline{\Delta P}_{sys}$ in Table 4 was 0.8 ± 0.1 kPa. Substituting into Equation (16) the values of $\overline{\Delta P}$, Q_{max}, and Δt_{sys} yields a value of ΔP_{max} of 2.4 kPa. ΔP_{max} in Table 4 was 2.9 ± 0.2 kPa. These differences are probably because the flow generated by this prosthesis was dramatically different from the flow generated by the mechanical valves studied by Yoganathan (1978). As was shown above, the Ionescu-Shiley valve generated a large central jet of fluid which caused higher flow accelerations and more extensive flow separation than has generally been seen for the mechanical valves. The large jet structure of the flow thus draws into increased suspicion the assumption used to derive Equations (14) and (15) that the velocity profile was flat. Moreover, the extensive flow separation draws into suspicion the assumption that the inductive pressure drop was due primarily to flow acceleration. Schramm, et al. (1982) have suggested that dissipation losses in this large flow separation contribute significantly to the total pressure loss of the Ionescu-Shiley valve. It should be mentioned that for the three mechanical prostheses also studied in the present investigation, the estimation of the pulsatile-flow pressure drop from the steady-flow results was accurate within experimental error. Therefore, the underestimation of the measured values by

using the steady-flow data in Equations (14) and (16) probably resulted from the greatly disturbed flow field associated with the Ionescu-Shiley valve.

3.3.4.2 Discussion of the Velocity Results

For both steady and pulsatile flow, the structure of the flow downstream from the Ionescu-Shiley valve was found to be greatly constricted, had definite secondary-flow structure, and was highly disturbed. Thus, the flow through this valve was dramatically different from the flow through the empty aortic-valve flow section.

In particular, the structure of the flow downstream from the Ionescu-Shiley valve included a large, centrally-located jet of fluid surrounded by extensive regions of flow separation. The jet was, somewhat surprisingly, non-circular in cross section at the data plane at z = 31.8 mm. The shape of the jet cross section was particularly surprising because the jet emerged from the approximately circular orifice of the opened valve. Several investigators have shown that the orifice of the fully opened Ionescu-Shiley prosthesis is very nearly circular (Ionescu, et al., 1977; Ionescu, et al., 1982; Wright, 1978; Frater, et al., 1979; Tindale, et al., 1982).

The results obtained at z = 55.9 mm when compared with those at z = 31.8 mm indicate that the non-circular shape of the jet was a result of the secondary-flow structure of the flow. The fact that in Figure 28 the jet appears to have been 'squeezed in' at its 'sides' as it progressed downstream from z = 31.8 mm to z = 55.9 mm, suggests that that 'squeezing' process may have been the mechanism by which the jet obtained its triangular cross section at z = 31.8 mm. The opened valve assumed a geometry not unlike a flow nozzle. Thus, it is reasonable to expect that the jet leaving the nearly circular orifice was also nearly circular in cross section. The cross section found at

z = 31.8 mm was probably, therefore, the result of a circular jet having been 'squeezed' tri-symmetrically to form the triangular shape. Hence, the jet emerging from this valve seems to have diverged *tri-symmetrically* as it proceeded downstream. This tri-symmetric divergence quickly divided the flow separation into three separated-flow regions. Each separated-flow region then reattached by being constantly fed fluid with positive axial momentum.

In addition, the flow was found to be highly disturbed over an extended axial distance. At z = 31.8 mm the rms velocities were found to be elevated over the tube cross section. At z = 55.9 mm the average rms velocity across the tube was even higher than that found upstream. The reattachment process probably accounted for this increase in the average rms velocity by feeding into the energy of the fluctuating velocities some of the 0.72 $kg \cdot m^2/s^3$ loss of $\overline{KE}$ between z = 31.8 mm and z = 55.9 mm noted above. Having completed reattachment, the flow downstream from z = 55.9 mm was free to redevelop letting the energy in the fluctuating velocities diminish. The elevated rms velocities, in turn, implied large turbulent shear stresses in the bulk which were potentially hemolytic.

The mean velocity results downstream from the Ionescu-Shiley valve indicate i) that the flow was more constricted than expected by the near-circular valve orifice and ii) that this flow constriction was probably the reason this valve's pressure drop was not significantly different from the totally mechanical Björk-Shiley convexo-concave valve of a tilting disc design with a semi-central flow.

The shape and orientation of the cross section of the flow at z = 31.8 mm indicate that the constriction of the flow through the Ionescu-Shiley valve was generated by the valve's leaflets. As noted earlier, the azimuthal orientation of the 'apices' of the triangularly shaped cross section of the axial jet corresponded with that of the struts of the valve. The 'sides' of the triangular cross section thus corresponded with the azimuthal orientation of the free

edges of the valve leaflets. Observations in our laboratory have shown that the leaflets of this valve "billowed" out in response to the forward flow with their free edges stretched taut. Other investigators have also reported this phenomenon (Martin, et al., 1981; Schramm, et al., 1982; Tindale, et al., 1982). The leaflet's "billowed" form imparted significant radial velocity components directed toward the center of the tube to the flow past the leaflets. The flow passing through the valve along the struts, on the other hand, suffered much less diversion from its axial sense. The emerging jet, therefore, seems to have developed its significant secondary-flow structure and hence its characteristic cross-sectional shape as a result of the unequal constriction of the flow by the valve leaflets.

The relative magnitude of the flow constriction generated by the valve leaflets can be seen from the magnitude of the average kinetic energy ($\overline{KE}$). For a given flow rate of an incompressible fluid, the greater the flow constriction the greater $\overline{KE}$ becomes. $\overline{KE}$ was 0.18 $kg \cdot m^2/s^2$ for the fully developed turbulent pipe flow. For steady flow, this fully developed flow was the entrance flow to the aortic-valve flow section. $\overline{KE}$ was 0.20 $kg \cdot m^2/s^2$ at z = 31.8 mm for the flow through the empty flow section where there was little or no constriction of the flow. For the Ionescu-Shiley valve, the value of $\overline{KE}$ at z = 31.8 mm of 1.07 $kg \cdot m^2/s^2$ given above was more than five times that of both the entrance flow and the flow through the empty flow section. Moreover, this high ratio of between five and six was probably not the maximum. The maximum flow constriction and thereby the maximum of $\overline{KE}$ probably occurred at the orifice generated by the free edges of the valve leaflets. At z = 55.9 mm, the value of $\overline{KE}$ had dropped by two-thirds to 0.35 $kg \cdot m^2/s^2$ but was still about two times that of the entrance flow. In comparison, the ratios at z = 31.8 mm for the other valves studied in the present investigation ranged from 0.20 to 0.33. Thus, the high values of $\overline{KE}$ for the Ionescu-Shiley valve at both z = 31.8 mm and z = 55.9 mm indicate that the

constriction of the flow by the occluding mechanism of the Ionescu-Shiley valve was relatively large.

The large constriction of the flow by this valve's occluding mechanism generated extensive flow separation which possibly correlated with the relatively large pressure drop found for this valve. Schramm, et al. (1982), studying the pressure-recovery characteristics of this valve, observed an extended distance over which the maximum pressure drop occurred. This extended distance, they reported, corresponded 'to the length of the jet" or, inversely, the length of the extensive flow separation. Tindale, et al. (1982) also investigated the phenomenon of pressure recovery. In their investigation, they found that the distance required for maximum pressure recovery correlated with the distance required for flow reattachment. Thus, the extent of flow separation generated downstream from this valve appeared to be directly related to the valve's pressure recovery characteristics.

An energy balance further suggests that the flow constriction caused by this valve was responsible for its high pressure drop characteristics. For an incompressible fluid in an isothermal flow the steady-state macroscopic mechanical energy balance (extended Bernoulli equation) is

$$\frac{1}{2}(\bar{v}_2^2 - \bar{v}_1^2) + g\,(h_2 - h_1) + \frac{1}{\rho}(p_2 - p_1) + E_f = 0\,. \qquad (17)$$

where $\bar{v}_i$ is the average velocity across the tube at station i, g is the gravitational constant, h_i is the height of the flow section at station i, ρ is the (constant) fluid density, p_i is the fluid pressure at station i, and E_f is the rate at which mechanical energy is irreversibly converted to thermal energy ("friction" loss). The first three terms in Equation (17) are, respectively, the kinetic energy per unit mass, the potential energy per unit mass, and the Gibbs free energy per unit mass in an isothermal flowing system. Equation (17) is strictly valid only

for v_1 and v_2 being the velocity at stations 1 and 2 along the same streamline. Taking $\bar{v}_i$ to be the average velocity across the tube, however, is a good approximation for turbulent flow where the velocity profile across the tube is approximately flat. For Equation (17) it has also been assumed that the system performs no work on its surroundings and vice versa. For the present investigation h_2 was equal to h_1. Hence, Equation (17) becomes

$$\frac{1}{2}(\bar{v}_2^2 - \bar{v}_1^2) + \frac{1}{\rho}(p_2 - p_1) = -E_f . \tag{18}$$

It can be seen from Equation (18) that if the kinetic energy at station 1 is equal to that at station 2, then any pressure drop between the two stations would be due solely to the friction losses. If stations 1 and 2 were located upstream and downstream from the mounted valve, respectively, then the kinetic energy across the tube at these two stations would be equal when pressure recovery was complete. For the Ionescu-Shiley valve, friction, or dissipative, forces were relatively large because of the extensive flow separation in which such dissipative processes as vortex formation were present. This extensive flow separation was in turn generated by the constriction of the flow by the valve leaflets. Therefore, the relatively large pressure drop of this valve after recovery was probably a result of the flow constriction generated by the valve leaflets.

The rms velocity results downstream from the Ionescu-Shiley valve also indicate that the flow was greatly constricted and that this constriction may have generated shear stresses in the bulk flow which were of such a magnitude as to have been potentially hemolytic.

The large extent to which the flow was constricted by the leaflets was attested to by the highly elevated rms velocities generated downstream from this valve. The rms velocity was elevated in the bulk flow along ridges which aligned with the free edges of the opened leaflets of the valve. At the flow-reattachment

point at z = 55.9 mm the rms axial velocities remained elevated. Thus high rms velocities in the axial direction were sustained for a significant distance downstream.

The magnitudes of the total shear stresses estimated from the rms velocities were large enough to activate platelets causing a chemical release reaction. Total shear stresses were estimated to be over 100 N/m^2 in the bulk flow. As shown in Table 1 of Chapter 1, platelets were shown to undergo chemical release reactions at shear stresses around 20 N/m^2. The total shear stresses estimated in the present investigation were probably *not* sufficient to cause lethal damage to platelets.

The magnitudes of the estimated total shear stresses were large enough to possibly damage red blood cells. As discussed in Chapter 1 and shown in Table 1, shear stresses on the order of 150 N/m^2 to 300 N/m^2 were found to be sufficient to cause hemolysis. As such it is interesting to note that, though earlier investigators found little hemolysis associated with this valve (Ionescu, et al., 1977), more recently Febres-Roman, et al. (1980) have reported a hemolysis rate for this valve greater than that for the Björk-Shiley prosthesis *in vivo*. Febres-Roman, et al. (1980) studied ten patients with Ionescu-Shiley valves in the aortic position which ranged in their tissue annulus diameters from 19 to 27 mm. They reported significantly elevated serum LDH levels and reticulocyte counts along with significantly reduced serum haptoglobin concentrations. The degree of hemolysis that they found "had no direct relation to valve size." A higher hemolysis rate was found in spite of the fact that the Ionescu-Shiley valve has been shown to generate relatively small shear stresses along most of the wall of the flow section. Thus some RBC destruction may be taking place via the high shear stresses found in the bulk flow in the present investigation.

The findings discussed above suggest that the tri-leaflet design of the Ionescu-Shiley valve will need to be improved if the hemodynamical advantages of the tri-leaflet design of the natural valve are to be more fully realized. The large regions of flow separation, the large mean velocity gradients in the bulk flow, and the elevated rms velocities in the bulk flow all attest to the large extent to which the valve leaflets constricted the flow through this valve. The flow characteristics of this valve, therefore, were quite different from those of the natural valve even though the tri-leaflet design of the prosthesis was modeled after that of the natural valve. Thus it would seem clear that a redesigning of the Ionescu-Shiley valve to generate less flow constriction would result in a significantly improved prosthesis. Some such improvement of this design may be incorporated in the new "low-profile" valve of this design. This newer prosthesis was not studied in the present investigation.

The velocity results of the present investigation are consistent with the limited results presented in previous investigations. The large jet structure and the extensive flow separation generated by the Ionescu-Shiley valve have both been previously reported (Schramm, et al., 1982; Tindale, et al., 1982; Yoganathan, et al., 1983b).

Previous investigators (Schramm, et al., 1982; Tindale, et al., 1982; Yoganathan, et al., 1983b) have reported that this valve generated a large jet of fluid but failed to recognize its shape and hence its true dimensions. This failure to determine the shape of the jet was because of limitations in the methods by which the results were obtained. Schramm, et al. (1982), Tindale, et al. (1982), and Yoganathan, et al. (1983b) reported results from flow-visualization studies but only did so for a single 'slice' of the flow. Yoganathan, et al. (1983b) also reported velocity measurements obtained using LDA but, again, only for a single 'slice', or 'profile', of the flow. No information has been

presented previously, therefore, which would allow an analysis of the three-dimensional aspect of the central jet. It should be mentioned that non-axial results like those obtained in the present investigation would be difficult to obtain using standard flow-visualization techniques.

Tindale, et al. (1982) used flow visualization to investigate the flow field and reported that a "central high velocity jet of fluid" emerged from the valve that was "well defined" and "slow to reattach" to the wall. These investigators studied this prosthesis with a TAD of 21 mm in steady flow at a flow rate of 20 L/min using a 0.9% saline solution as the test fluid. Schramm, et al. (1982), using laser ultramicroscope anemometry and flow visualization, reported that the flow was "constricted to a jet of nearly circular cross section" and that this jet was "almost non-divergent" over a length of 60 mm downstream from the valve. They studied this prosthesis with a TAD of 25 mm in steady flow at a flow rate of 18 L/min using both water and a 0.14% polyacrylamide (PAA) solution as test fluids. Yoganathan, et al. (1983b), using laser-Doppler anemometry and flow visualization, also reported a "well-defined central jet." These latter investigators reported their results for this prosthesis with a TAD of 27 mm in steady and pulsatile flow using a 0.9% saline solution as the test fluid. Their LDA velocity measurements were made in steady flow at flow rates varying from 10 to 25 L/min. Their flow-visualization results were obtained for pulsatile flow. They operated their pulse-duplicator at a rate of 70 beats/min with a systolic interval of 300 milliseconds, a mean aortic pressure of about 13.33 kPa (gauge) and mean flow rates of 2.5 to 6.5 L/min.

The results that are presented from previous investigations show some evidence of the shape of the jet. Comparisons are possible between the results of others and those of the present work because many of the results from these earlier investigations have been presented for one of two mutually orthogonal

'slices' of the flow. Each 'slice' presented was on a plane which contained the axis of the tube. For some 'slices' the azimuthal orientation of the plane was such that the plane intersected one of the valve struts. This azimuthal orientation corresponds to the direction in Figure 22 parallel with the gravity vector shown in the "valve orientation" inset. For the remaining 'slices' the azimuthal orientation of the plane was orthogonal to that of the others and corresponds to the direction in Figure 22 normal to the gravity vector shown in the "valve orientation" inset.

Yoganathan, et al. (1983b) presented flow-visualization results for the parallel orientation and velocity results for the normal orientation. Schramm, et al. (1982) and Tindale, et al. (1982) presented flow-visualization results for the parallel and normal orientations, respectively. The results presented for these two orientations of the results can thus be compared here both among themselves and with the results of the present investigation. From these comparisons, it has become apparent that the jets studied in previous investigations have been at least non-circular in cross section.

The results of Yoganathan, et al. (1983b) for the two mutually orthogonal directions showed that the jet was probably non-circular. The width of the jet determined from their flow-visualization results for the parallel orientation was significantly smaller than that determined from the LDA velocity measurements in the normal orientation. From their flow-visualization results, obtained for pulsatile flow, the width of the jet emerging from this prosthesis with a TAD of 27 mm was determined "by eye" to be about 15 mm at $z \approx 34$ mm. From their velocity results, measured in steady flow at 25 L/min, the width of the jet was determined to be about 23 mm at $z = 33.99$ mm. The width of the jet determined from the velocity data was defined as the distance across the tube diameter for which the mean velocity was greater than 10% of the maximum.

This difference between the two calculations of the width of the jet may simply reflect differences in experimental apparatus and methodology and any differences in studying steady or pulsatile flow. Another explanation, however, might be that two different aspects of a non-circular (e.g., triangular) jet were measured using the two data-collection techniques. The jet shown in Figure 22, being substantially non-circular in shape, had a greater "width" in the direction parallel to the gravitational vector than in the normal direction. Hence, the triangular shape of the jet may explain why a smaller width of the jet was determined from the velocity measurements of Yoganathan, et al. (1983b) at $z = 33.99$ mm than from their flow-visualization results at $z \approx 34$ mm.

The flow-visualization results of Yoganathan, et al. (1983b) themselves may also indicate in another way that the jet was non-circular. These investigators note that the jet shown in their flow-visualization results is "skewed" towards the wall. Note, however, that a 'side view' of the jet shown in Figure 22 from the direction normal to the gravitational vector would show a jet which would not appear to diverge much towards, say, the upper wall but which extended all the way down to the lower wall. Thus some of the "skewness" of the jet reported by Yoganathan, et al. (1983b) may be simply a result of the unorthodox way in which the jet diverges.

The flow-visualization results of Schramm, et al. (1982) also indicate that the jet had a non-circular cross section at $z = 34$ mm. The results they presented were for this prosthesis with a TAD of 25 mm in a steady flow of 18 L/min. From their results, the width of the jet was determined to be 21 mm at $z = 34$ mm. The plane of their 'slice' of the flow was in the same direction as the velocity results presented by Yoganathan, et al. (1983b). Thus the width of the jet determined from the flow-visualization results of Schramm, et al. (1982) tends to agree with that determined from the velocity results of Yoganathan,

et al. (1983b) as opposed to that determined from these latter investigators' flow-visualization results. Had they studied this prosthesis with a TAD of 27 mm, Schramm, et al. (1982) probably would have found an even larger width of the jet and thus their flow-visualization results differed significantly in this respect with the flow-visualization results of Yoganathan, et al. (1983b). The inner diameter of the downstream tube used by Schramm, et al. (1982) was, however, almost 10 mm larger than that for Yoganathan, et al. (1983b). The inner diameters were 35 mm and 25.4 mm, respectively. Thus there was an additional annulus of deadwater around the periphery of the emerging jet for the work of Schramm, et al. (1982) that was not there for either the present work or that of Yoganathan, et al. (1983b). Also, as mentioned in Chapter 2, Schramm, et al. (1982) used polyacrylamide (PAA) as the test fluid for their investigation. These differences in experimental apparatus did not grossly affect the shape and magnitude of the emerging jet of fluid near the valve because i) the additional deadwater region would only affect the jet farther downstream after it had diverged considerably, and ii) the use of PAA as the test fluid, as discussed in Chapter 2, had only a small effect on the overall dimensions of the large and well-defined jet generated by this valve.

The flow-visualization results of Tindale, et al. (1982) may also imply that the jet was non-circular. From their reported results for the Ionescu-Shiley valve with a TAD of 21 mm, however, it is not clear what the test-chamber diameter, the flow rate, and the valve orientation were. Thus no quantitative analysis was possible from their results. It would appear from their results that their 'slice' of the flow was in the same direction as that for the flow-visualization work of Yoganathan, et al. (1983b). If this supposed direction is correct then the emerging jet they show has the same "skewed" aspect as that of Yoganathan, et al. (1983b) and, hence, implies again that the jet was not circular in cross

section.

Thus, the jet structures studied by these previous investigators show definite signs of being triangular in shape as found in the present investigation. This non-circular shape, however, apparently went unnoticed.

Previous investigators also observed extensive flow separation in the flow but again the techniques they used failed to determine the true extent of the flow separation. In evaluating their results, these investigators generally assumed that the flow separation generated at the valve by the emergent jet remained essentially "annular" as the flow moved downstream. The extent of flow separation was assumed to be the extent to which flow separation was observed in their 'slice' of the flow. The presence of more than one flow-separation region, as found in the present investigation, thus brings up the possibility that the full extent of flow separation was not obtainable from the results of these earlier investigations. Furthermore, being divided from the others, each of the three separated-flow regions established its own reattachment location. The locations of flow reattachment of the three regions would generally differ. In the previous investigations, the location of flow reattachment was assumed to occur at the axial location in the 'slice' of the flow beyond which no separated flow was observable. Therefore, the extent of the flow separation could not be determined reliably using the methodological approach of earlier investigations.

Tindale, et al. (1982) reported from their flow-visualization studies that the jet generated by this valve was "slow to reattach" downstream. Schramm, et al. (1982) observed an "axisymmetric deadwater" region approximately 9 mm in thickness which surrounded the emergent jet and extended over a length of 60 mm downstream from the sewing ring. Yoganathan, et al. (1983b) reported a "flow-separation region" that extended as far as 120 mm downstream.

The results presented by Yoganathan, et al. (1983b) indicate that the relative sizes of the flow-separation regions are consistent with the findings of the present investigation. They present flow-visualization results which show a large flow-separation region on one side of the emerging jet but almost no flow-separation region on the other side for $z > 30$ mm. This absence of flow separation can be considered a result of the emerging jet being "skewed" towards the wall such that the jet impinges on the wall near $z = 25$ mm. On the other hand, this lack of flow separation could be simply a result of one of the 'apices' of the tri-symmetrically diverging jet impinging on the wall. As mentioned above, Yoganathan, et al. (1983b) presented their flow-visualization results for a 'slice' of the flow in the direction parallel to the gravitational vector shown in Figure 22. As can be seen from Figure 22, the flow-separation region on one side of the jet in such a 'slice' would appear quite large while on the other side there would be no separation but rather high axial velocities very near the wall. The velocity results presented by Yoganathan, et al. (1983b) are also consistent with there being three individual flow-separation regions. They presented their velocity results for a profile of the flow across the tube in the direction normal to the gravitational vector of Figure 22. Small flow-separation zones were observable on either side of their velocity results very similar to what would be observed by taking a 'slice' of the results shown in Figure 22 through the center of the plot and in the direction normal to the gravitational vector.

The results of Schramm, et al. (1982) are also consistent with the findings of the present investigation. The plane of their 'slice' of the flow was, as stated before, in the same direction as the velocity results presented by Yoganathan, et al. (1983b). The flow-separation regions were distributed fairly evenly on each side of the emerging jet. This even distribution is what was found for the results of Figure 22 when a 'slice' of the flow considered along a line through the middle

of the plot and parallel to the gravitational vector. The differences discussed earlier regarding the experimental apparatus used by Schramm, et al. (1982) again make little difference in the overall interpretation of the results.

The results of Tindale, et al. (1982) may also be consistent with the flow-separation findings of the present investigation. The uncertainties in these investigators' experimental method, as discussed above, again make definite statements difficult. If, as assumed above, their results are for a 'slice' of the flow in the same direction as that for the flow-visualization work of Yoganathan, et al. (1983b), then Tindale, et al. (1982) also show the large flow-separation region on one side of the flow and none on the other side. Tindale, et al. (1982) attribute the "skewness" of their jet to the valve being "obliquely mounted." As discussed, however, some of this "obliqueness" may simply be a result of one "apex" of the triangularly shaped jet impinging on the wall.

Therefore, the flow separation observed by previous investigators was probably also divided into three regions as found in the present investigation. Like the shape of the jet, however, this division of the flow separation by the jet apparently went unnoticed.

Only very limited results from other investigations are available with which to compare the estimations of the total shear stresses of the present investigation. To the author's knowledge the only reported measurements of shear stress downstream from the Ionescu-Shiley valve have been reported by Yoganathan, et al. (1983b). They report initial results indicating turbulent shear stresses on the order of 100 to 300 N/m^2 for a flow rate of 25 L/min. They further reported that the maximum turbulent shears occurred along the 'side' of the axial jet. Thus in both magnitude and location the results of Yoganathan, et al. (1983b) seem to agree with the estimated shear stress results of the present investigation.

The agreement found with the work of Yoganathan, et al. (1983b) seems to indicate that the assumption of a correlation coefficient, k_c, in Equation (7) for the cross section of the tube was not in gross error. Moreover, the *value* of k_c of 0.4 was apparently not in gross error either.

3.3.4.3 Steady Versus Pulsatile Flow

The velocity results presented in Figures 19 through 27 for both steady and pulsatile flow allow an evaluation of the applicability of steady-flow velocity results to the pulsatile-flow regime found *in vivo*. For *pressure-drop* results Yoganathan and coworkers (Yoganathan 1978, 1979b) have shown that steady-flow measurements can be used to estimate a valve's pressure drop characteristics in pulsatile flow. It has not been at all clear, however, how relevant *velocity* results for steady flow are to those results found in pulsatile flow. Recently, Tindale, et al. (1982) concluded from their steady-flow analysis that "the clinical significance of *in vitro* testing of artificial heart valves is, at present, questionable." They continued by noting that steady-flow analyses should "be treated with particular caution." Martin, et al. (1981) had earlier come to a similar conclusion citing variability in the experimental techniques used by different investigators as a possible source of artifactual and non-comparable results. To date, only very limited velocity results have been reported for pulsatile-flow and even less have been reported along with steady-flow results from the same experimental rig. Thus there is a paucity of data available in the literature from which an analysis can be made of the applicability of steady-flow results.

Theoretical approaches to the problem have been limited. The presence of non-isotropic, inhomogeneous turbulent flow along with a spectrum of length and time scales, has hindered theoretical determinations of the flows generated

downstream from prosthetic valves. Hussain (1977), using the phase-averaging decomposition discussed in Chapter 2, developed the momentum balance and kinetic energy balance equations for pulsating flows. He determined that these pulsating flows were made up of a superposition of the mean flow field, the pulsating flow field, and the turbulent flow field. Though a general solution does not exist for the equations, by comparing terms in the equations Hussain was able to show that for pulsating flows there is a "hierarchy" of momentum transport. Pulsation-induced momentum contributes to the pulsating momentum field and the mean momentum field but not to the turbulent field; the background turbulence contributes to all three momentum fields. He also found a "hierarchy" of kinetic energy production: the mean field loses energy to the pulsating and turbulence fields while the pulsating field receives energy from the mean field and loses energy to the turbulent field. The mean, pulsating, and turbulent fields all lose energy to direct viscous dissipation. A major implication of this work was that the pulsation can be strengthened by the mean field. Thus there is a mechanism by which pulsatile flows may evolve such that they become quite unlike steady flows in the same flow section at comparable flow rates. As Hussain notes, however, the above analysis is "more relevant" for a traveling pulsation disturbance or for small-amplitude pulsations compared to the mean velocity. Therefore, for the present investigation, where the pulsations were not a traveling disturbance and were relatively large, the relevance of steady-flow velocity measurements is difficult to determined *a priori*.

It can be assumed *a priori* that the flow structure at peak flow would be similar to that for steady flow at a comparable flow rate. Generally for pulsatile flow the mechanical energy balance given in Equation (18) would include time-dependent terms, such that

$$\frac{d}{dt}(K_{tot} + \Phi_{tot}) = \frac{1}{2}(\bar{v}_2^2 - \bar{v}_1^2) + \frac{1}{\rho}(p_2 - p_1) + E_f , \tag{19}$$

where K_{tot} and Φ_{tot} are the total kinetic energy and the total potential energy, respectively. K_{tot} is given by

$$K_{tot} = \frac{\rho}{2}\int_v (\bar{v}^2 + \overline{v'^2})\, dV , \tag{20}$$

and Φ_{tot} is given by

$$\Phi_{tot} = \rho \int_v gh\, dV . \tag{21}$$

Substituting Equations (20) and (21) into (19) the latter becomes

$$\rho \frac{d}{dt}\left[\frac{1}{2}\int_v (\bar{v}^2 + \overline{v'^2})\, dV + \int_v gh\, dV\right] = \frac{1}{2}(\bar{v}_2^2 - \bar{v}_1^2) + \frac{1}{\rho}(p_2 - p_1) + E_f . \tag{22}$$

For the present investigation, h was constant, so the second integral becomes invariant in time and Equation (22) becomes

$$\rho \frac{d}{dt}\left[\frac{1}{2}\int_v (\bar{v}^2 + \overline{v'^2})\, dV\right] = \frac{1}{2}(\bar{v}_2^2 - \bar{v}_1^2) + \frac{1}{\rho}(p_2 - p_1) + E_f . \tag{23}$$

During systole the flow first accelerated to a maximum flow rate, then decelerated back to flow rate of zero. Near the maximum flow rate the accelerative forces were small or non-existent and hence the accelerative, time-dependent terms of Equation (23) vanished. Hence, for the flow near the maximum flow rate,

$$0 = \frac{1}{2}(\bar{v}_2^2 - \bar{v}_1^2) + \frac{1}{\rho}(p_2 - p_1) + E_f , \tag{24}$$

which is the same as Equation (18). It was expected then that the flow at the maximum flow rate would be similar to that or steady flow at a comparable flow rate.

A comparison of the steady-flow results to those for pulsatile flow at the maximum flow rate must take into account the time required for flow

disturbance generated by the valve to reach the axial location of the data plane. The maximum flow rate for the Ionescu-Shiley valve occurred about two-thirds of the way (64.8%) through the systolic ejection interval. By the time of peak flow, about 50 cm^3 had passed through the opened valve. It was assumed (conservatively) that the fluid passing through the valve displaced *all* of the fluid downstream from the valve in a plug-flow manner. If so, then at the time of peak flow some 20 cm^3 of the ejected volume had not yet reached the data plane at z = 31.8 mm. That is, the total volume of the flow section between z = 0 and z = 31.8 mm minus the volume of the valve superstructure was about 20 cm^3. The volume contained by the Lucite® sinus section was 19 cm^3 and that contained by the short tube section from the end of the sinuses at z = 25.4 mm to the data plane at z = 31.8 mm was 3.2 cm^3. The volume occupied by the superstructure of the valve was about 2 cm^3. Hence, at the time of peak flow, 30 cm^3 of the 50 cm^3 ejected had passed the location of the data plane. An integration of this valve's flow curve from the beginning of the systolic ejection interval showed that 30 cm^3 had been ejected by t = 145 milliseconds. The time of the maximum flow rate was t = 190 milliseconds. Thus at the time when the peak flow was passing through the valve base ring, the flow arriving at the data plane was that which had passed through the base ring at most 45 milliseconds earlier.

This "delay" time of 45 milliseconds is probably somewhat overestimated because of the assumptions included in its calculation. In reality not *all* of the fluid was displaced from the modeled aorta by the newly ejected fluid. The fluid in the sinuses, for instance, may have been "trapped" inside flow separation regions removing that volume from the calculation.

The flow disturbance corresponding to the maximum flow thus arrived at the data plane about two pulsatile-flow windows after peak flow. The 45-millisecond

delay time corresponded to about a delay of about two 20-millisecond windows. The two-window delay appears to be verified from Figure 32. In the plot on the bottom of Figure 32, the maximum average rms velocity occurs two windows after the peak flow. In Figure 32 the peak flow is indicated temporally by the steady-flow result which has been plotted to correspond with the pulsatile-flow window of maximum flow (window 14). Moreover, for the other valves studied in the present investigation, this two-window delay between the maximum flow and the maximum average rms velocity was also observed.

The maximum average rms velocity corresponded in time to the peak flow since the maximum energy was input into the flow at that time. From the analysis of Hussain it was found that the hierarchy of the energy "cascade" was from the mean and pulsating flow fields to the fluctuating flow field. At peak flow the kinetic energy of the mean and pulsating flow fields was maximized. Therefore, it is to be expected that the fluctuating flow field, from which the rms velocities were measured, was also at or quite near its maximum.

Thus it can be assumed *a priori* that the flow structure at peak flow would be similar to that for steady flow, once the delay caused by the finite distance from the valve to the data plane is taken into consideration. A tougher issue to settle *a priori* is how long during systole the pulsatile flow is similar to the steady flow. Related questions are: What happens before the pulsatile flow becomes similar to the steady flow and what happens after? Also, can any sort of quasi-steadiness assumption be applied so that the pulsatile-flow dynamics during all of systole can be inferred from steady-flow results?

In analyzing the pulsatile-flow results shown in Figures 19 through 27, it became apparent that the systolic ejection interval could be divided into three phases. The flow at the data plane during each of these phases was quite distinct from each other as evidenced by the mean axial velocity plots of

Figure 19. The first phase, termed "early systole", included windows 5 through 9. The second phase, termed 'mid-systole", included windows 10 through 17. The third phase, termed 'late systole," included windows 18 through 21.

Early systole began at the beginning of the systolic ejection interval and ended when the first flow disturbance arrived at the data plane after having been generated at the valve. During this first phase of systole, the flow had generally not yet been affected, this cycle, by the flow dynamics of the valve. The flow field at the data plane erupted quickly into the jet structure after earlier exhibiting the flat velocity profile of accelerating flow. Window 8 of Figures 20 and 22 show typical results for early systole. A calculation of the average flow acceleration from the beginning of the systolic ejection interval indicated that the vorticity generated at the valve orifice and convected to the data plane arrived during window 9. Thus it is not surprising that window 9 appears to be a transition between the flow in early systole and that in mid-systole.

Mid-systole began at the end of early systole and ended when the decelerating flow had significantly diminished the jet structure. During this middle phase of systole, the flow was similar to that found for steady flow. By window 10 the jet was fairly well established and had begun to resemble that found for steady flow, as shown in Figure 19. Window 14 of Figures 20 and 22 show typical results for mid-systole. In Figure 19 it can be seen that this resemblance persisted until about window 17 at which time the magnitude of the jet was becoming significantly smaller than that found for steady flow. Mid-systole thus lasted about 160 milliseconds with the maximum flow rate occurring roughly half-way through.

Late systole began at the end of mid-systole and ended at the end of the systolic ejection interval. During this last phase of systole, the flow decelerated rapidly and reversed. At window 17 the shape of the jet was still similar to that

at window 14 but the mean velocity gradients had dropped dramatically and the regions of reverse flow had increased in area. Window 18 of Figures 20 and 22 show typical results for late systole. The regions of reverse flow grew until at window 21 the maximum reverse flow rate occurred.

The mean non-axial results of Figure 24 show that the secondary-flow structure of each phase of systole was different. Early systole was characterized by the lack of appreciable non-axial velocities, as shown for window 8 of Figure 24. Thus flow during early systole was a "plug flow" type having flat axial velocity profiles with only small non-axial components. Mid-systole was again characterized by flow structure similar to that seen for steady flow, as shown for window 14 of Figure 24. Late systole was characterized by the presence of appreciable non-axial velocities but a general *lack* of discernible flow structure, as shown for window 18 of Figure 24.

The rms axial results of Figure 26 show that the magnitude of the fluctuating velocities was also dependent on the systolic phase. Early systole was characterized by flow with very low rms velocities. These low rms velocities, shown for window 8 of Figure 26, reflect the laminar structure of the flow at the data plane at this time in systole. Flow-visualization studies in our laboratory have indicated that laminar flow was indeed the case during early systole. Once again, mid-systole was characterized by flow structure similar to that seen for steady flow. The rms axial results for pulsatile flow, however, were notably smaller than that for steady flow, as shown for window 14 of Figure 26. Late systole was characterized by elevated velocity fluctuations. Though the flow rate at window 18 had dropped to one-third of its maximum value, the axial rms velocities at window 18 were still more than three-quarters of their maximum value.

The results thus indicate that of the three phases of systole, the results for two of the phases, early and mid-systole, can be approximated *a priori*. Early systole can be approximated *a priori* as plug flow. This approximation is dependent upon the time elapsed since the beginning of the systolic ejection interval and the axial location at which data are taken. At a given axial location, as shown above, the time span of early systole could be estimated from the mean velocity at which the flow structure was being convected downstream. Mid-systole can be approximated *a priori* by appropriately scaling steady-flow results. In this way, mid-systole could be considered as quasi-steady for analysis purposes. The time span of mid-systole must be determined experimentally but was shown to encompass about half of the systolic ejection interval starting at the end of early systole. Late systole, however, would be difficult to approximate *a priori*. The effect on the flow of its rapid deceleration would be hard to predict without experimental results. Thus at most only about half of the systolic ejection interval could be considered as quasi-steady and estimated from steady-flow results.

Overall, the pulsatile-flow results shown for maximum flow in Figures 20, 22, 24, and 26 were less distinct than those shown for steady flow. The 3-D and contour plots of the mean and rms axial results for pulsatile flow generally appear more "ragged" than that for steady flow. Also, the resultant plots for the mean non-axial results appear to reflect more "scatter" in the data. These differences can be attributed to the relative amount of data available from the pulsatile-flow experiments and the reproducibility of the flow from one cycle to the next. As discussed in Chapter 2, because of the finite size of the windows each mean and rms velocity result for pulsatile flow was calculated from about one-tenth the raw data available for the steady-flow calculations. The probability of obtaining a spurious result was therefore much higher for

pulsatile flow. Thus some differences in "raggedness" or "scatter" probably reflected the smaller data base (per result) from the pulsatile-flow experiments. The reproducibility of the pulse-duplicator also may have contributed to the "raggedness" and "scatter" of the pulsatile flow results. The reproducibility of the flow from cycle to cycle was generally good but details of the larger flow structures tended to reproduce less well. This intermittent pulse-to-pulse non-reproducibility was noted from flow-visualization studies. For example, as mentioned earlier, the location of flow reattachment varied considerably from cycle to cycle. Also, during flow deceleration in late systole the extent and growth of the separated-flow regions varied between cycles.

During diastole the flow structure strongly reflected the fact that there was no appreciable diastolic pressure drop. Without an energy input, the flow was left to "relax" towards a quiescent state. The 3-D plots in Figures 19 and 21 for windows 22, 23, 25, 30, and 40 clearly show that after valve closure the kinetic energy of the mean flow decreased rapidly, as indicated by the progressively diminished mean velocities. The diastolic vortex implied by the results from Figure 23 also seems to follow this pattern of decreasing kinetic energy. By window 40 of Figure 23 this large-scale vortex, present during early diastole, had almost disappeared. The mean non-axial velocities of Figure 25 also show progressively diminishing values overall as diastole proceeds.

The flow at the beginning of each cycle was not, however, entirely quiescent. As will be shown below, the axial rms velocities during diastole did not quite settle out before the beginning of the next cycle. Thus the flow approached but did not quite achieve a quiescent state by the end of each cycle. Hence, during a pulsatile-flow experiment, the results for a given cycle were based on the flow generated by the previous cycle at the end of diastole and not on a perfectly quiescent fluid. Therefore, an experiment not designed to provide for a

physiologically pertinent diastolic phase may give questionable results.

A further comparison of the results for steady flow with those for pulsatile flow can be made from the results shown in Figure 32. The flow-rate results in Figure 32 show that the flow rate during the middle of systole was comparable to that for steady flow. The pulsatile-flow results were within 10% of the steady-flow result over much of mid-systole. This finding is accented by the fact that about 78% of the flow ejected during systole was ejected during mid-systole. For comparison, 17% of the flow ejected during systole was ejected during early systole while only 5% was ejected during late systole.

The small positive flow indicated during diastole in Figure 32 was discussed above as having been artifactual. The Ionescu-Shiley valve required only 3% of the forward flow for closure. Once closed, the Ionescu-Shiley valve allowed no further regurgitant flow.

The average rms axial velocities plotted in the bottom of Figure 32 clearly show that the magnitude of the fluctuating velocities was dependent upon the systolic phase. This dependency had been inferred by the results from Figure 26 discussed above. The average rms axial velocities for windows during early systole were not very different from that for windows during diastole. Note that here again window 9 appears to be a transition from early systole to mid-systole. The average rms axial velocities for windows 10 through 17 were relatively similar in magnitude, yet were all significantly less than that for steady flow. This similarity of magnitude may result from some given amount of velocity fluctuations associated with the confined jet downstream from this valve. This "flattening off" phenomenon was not seen for the other valve designs studied in the present investigation. It can be seen from Figure 32 that during late systole the rms axial velocities were indeed elevated with respect to early systole. As late systole progressed the average rms axial velocity dropped gradually until

maximum flow reversal where this value rose again. This rise at the end of the systolic ejection interval was apparently in response to the significantly increased flow rate (in absolute value) just prior to valve closure. In fact a second, smaller "shoulder" in the average rms axial velocity can be seen for window 23 early in diastole. Comparing with the flow rate results in the top of Figure 32, this small shoulder correlated in time with a small "reflection" in the flow rate at window 23.

The average rms axial velocities shown in Figure 32 also indicate that rms velocities measured in steady flow tend to be an upper bound on those found in pulsatile flow. An analysis of the experimental technique and the kinetic energy considerations discussed above further indicate that rms results for steady flow will be an upper bound to those for pulsatile flow. First, as is readily noted from Figure 32, the experimental results show that the axial rms velocities measured in steady flow were higher than those measured for pulsatile flow. This same "bounding" tendency of the steady-flow results was also seen for the non-axial rms velocities. Second, the velocity measurement technique probably also tended to give rms results which were higher for steady flow than for pulsatile flow. As discussed earlier, no provision was made in the data-collection technique for natural frequencies in the flow. Shedding vortices and the like were "averaged out" and ultimately contributed to the magnitude of the rms velocities calculated from the raw data. This omission was probably more serious for steady flow because for pulsatile flow a period of about one second was imposed on the system and data were collected in phase with that period. Third, the cascade of kinetic energy described earlier may provide a mechanism by which, all else being equal, more of the energy input into a steady flow would reside at a given time in the fluctuating flow field than for pulsatile flow. By assuming a correlation coefficient similar to that of Equations (7) and (9) the

square of the rms results shown in Figure 32 can be taken as proportional to the kinetic energy of the fluctuating field (KE'). Thus,

$$KE' \approx 0.4\,\rho\,(u_{rms}\,u_{rms})\,, \tag{25}$$

where u_{rms} is the rms velocity in the z-direction. The relative kinetic energy of the fluctuating flow field can thus be inferred from the results plotted in the bottom of Figure 32. The kinetic energy was earlier said to cascade from the mean field to the pulsating and fluctuating fields for pulsating flows. For steady flow the energy cascades from the mean field to the fluctuating field. Kinetic energy is lost to viscous dissipation from all fields. Thus it seems that a pulsating flow has one more flow field than steady flow which draws from the kinetic energy of the mean field and in this way competes with the fluctuating field for that energy. For a pulsating flow, therefore, some of the kinetic energy from the mean field ends up in the pulsating field, causing the kinetic energy of the fluctuating field to be that much less than it would be if there was no pulsation. In Chapter 2 the mean velocity in the present investigation was taken as zero for the pulsatile-flow experiments to simplify the data reduction requirements. A zero mean velocity would imply a non-existent mean flow field. There was, however, a finite mean flow rate through the pulse-duplicator indicating that there was a mean flow field present. Ignoring that mean field in the data reduction caused no problem because the mean velocity determined by phase-averaging picked up the contribution of the mean velocity. Therefore, it can be concluded that rms velocity results measured in steady flow will probably provide an upper bound on those which would be found for physiologic pulsatile flow.

The concept of cascading energy may also explain the apparent 'base-line' of the average rms axial velocities during diastole. The results plotted in the bottom of Figure 32 appear to approach a minimum value of about 5 cm/s. At

this level of rms velocities, the measuring equipment was capable of faithfully eliciting the second moment of the velocity in the probe volume of the LDA. Thus a "background" velocity fluctuation is implied which is hard to explain in the presence of viscosity. The large-scale diastolic vortex implied in the mean axial data may provide the source of the energy necessary to maintain the elevated energy level in the fluctuating flow field. This vortex was seen in Figure 23 to have diminished over the course of diastole. Its energy was probably spent in generating smaller vortices as well as being lost to viscous dissipation. These smaller vortices may then have been interpreted by the measuring technique as "background" velocity fluctuations. Thus as the energy in the fluctuating flow field was lost to viscous dissipation on the one hand, these small vortices were being generated on the other hand which apparently compensated somewhat in the *measured* rms velocities.

3.3.5 Conclusions

The flow structure generated by this valve was dramatically different from that found for the empty flow section. The findings from the measurement of the velocities suggest that the central-flow aspect of the occluding mechanism of this valve caused flow that was markedly different from the flow downstream from a natural aortic valve. Somewhat surprisingly, the nearly circular orifice for flow generated by the valve leaflets did not result in a circular flow structure downstream from the valve. It was determined that the pronounced, jet-like structure emerging from this valve had a shape and orientation which suggested that the valve leaflets greatly constricted the forward flow. Significant, well-defined secondary-flow structures were also found and may have played a role in generating the non-circular, jet-like flow. The shape and magnitude of this jet indicated that the flow was greatly constricted by the superstructure of the

valve. Further analysis showed that this constriction was probably caused by the valve leaflets.

This flow constriction was shown to give rise to large regions of flow separation and high mean velocity gradients in the bulk flow. The extensive flow separation was implicated as the cause of the moderate pressure drop found for this valve. Although the pressure-drop results in steady and pulsatile flow were consistent with one another, there was general disagreement with the results reported by others *in vitro*. The pressure drop results reported herein for pulsatile flow, however, were not very different from that reported by others *in vivo*.

Results from farther downstream in steady flow provided insight into the structure of the forward flow. The large axial jet was found to have diverged tri-symmetrically thus generating three individual regions of separated flow. This finding resolved the otherwise seemingly contradictory findings of other investigators.

High mean velocity gradients and elevated rms velocities in the bulk flow were shown to contribute to significant shear stresses in the bulk flow. The estimated total shear stresses were on the order of those considered to be potentially hemolytic. These shear stresses, in turn, seemed to correlate with the findings of others that this valve may generate significant intravascular hemolysis. The estimated total shear stresses were also sufficient to activate platelets and cause a chemical release reaction. The presence in the flow of activated platelets increases the possibility of thrombus formation and hence valve thrombosis and thromboembolic events.

The analysis of the results obtained downstream from the Ionescu-Shiley prosthesis, allowed some comments to be made regarding the design of this

valve. It was concluded that the tri-leaflet design of this valve needs further improvement before the hemodynamical advantages attributed to the tri-leaflet design of the natural valve will be realized. Some improvement of this design may be incorporated in the new "low-profile" valve and it should be studied in similar fashion.

A comparison of steady-flow and pulsatile-flow results showed that i) the steady-flow results approximated those for pulsatile flow only during the middle of systole and ii) the rms velocities for steady flow provided an upper bound to those found in pulsatile flow. The results indicated that the systolic ejection interval could be divided into three phases: early systole, mid-systole, and late systole. For each phase of systole the flow structure was significantly different. The flow structure of mid-systole was most similar to that for steady flow. The steady-flow results were quite different from those for pulsatile flow during early and late systole. It was found that early systole could be estimated *a priori* as plug flow. Late systole would be difficult to predict *a priori*. Pulsatile-flow results in diastole were found to have structure which were not predictable from the steady-flow results. The results from the steady-flow experiments, therefore, were limited in their ability to provide an understanding of the pulsatile flow. It was concluded that steady-flow results can provide some knowledge of the flow fields downstream from the Ionescu-Shiley valve but only for a relatively small portion of systole.

3.4 BJORK-SHILEY CONVEXO-CONCAVE PROSTHESIS

3.4.1 Introduction

The Björk-Shiley prosthesis was first used clinically in 1969. This semi-central flow tilting-disc valve has now become the most commonly used mechanical prosthesis worldwide (Bonchek, 1981). When introduced, the semi-central flow design of this valve combined a lower pressure drop than the other prostheses then available with adequate durability. The valve is shown in the bottom of Figure 5a. In Figure 5a the major and minor outflow regions of the valve can be seen. Because of its semi-central flow design, the occluder of this valve divides the base-ring orifice into two unequal regions. The larger region has been called the major outflow region because, as Yoganathan, et al. (1980) have shown, the larger portion of the forward flow passes through this larger region. The smaller region has been called the minor outflow region because the smaller portion of the forward flow passes through that region.

This prosthesis has undergone several modifications aimed at improving its performance as a substitute heart valve (Björk, 1978; Björk and Henze, 1979). In 1971 the material used for the disc occluder was changed from Delrin® to pyrolytic carbon which improved the durability of the valve even further. In 1975 a radiopaque marker was incorporated into the pyrolytic-carbon occluder to allow non-invasive, cineradiographic assessment of valve function. In 1976 this valve was redesigned in an effort to increase flow through the minor outflow region and thereby reduce valve thrombosis and thromboembolic complications. This redesigned prosthesis is called the Björk-Shiley *convexo-concave* prosthesis with reference to the cross-sectional shape of the redesigned occluder of the valve. Preliminary results (Björk and Henze, 1979) suggest that the redesigning of this prosthesis may have improved the associated thromboembolic rate, but may also have compromised the favorable hydrodynamic performance of the

valve (Gabbay, et al., 1980).

In the present investigation, a Björk-Shiley convexo-concave prosthesis with a TAD of 25 mm was studied *in vitro* in both steady and pulsatile flow regimes. Pressure and volumetric-flow data were collected to insure that the pressure and flow fields encountered by the valve in the experimental rig were similar to that which the valve might encounter when implanted in a patient. For pulsatile flow, the pulse-duplicator was operated at pressures and flows found *in vivo* in a resting state, i.e., as might be measured in the catheterization laboratory. After establishing these pressure and flow fields, the assessment of the *in vitro* states was extended to i) an extensive evaluation of the mean and rms velocities in the axial and non-axial directions across a data plane downstream from the mounted prosthesis, ii) the estimation of the total shear stresses at the data plane from the rms velocity results, iii) the estimation of the total regurgitant flow associated with this prosthesis to be used in comparison with other valves studied, and iv) the comparison of steady and pulsatile flow results to give insights into the relevance of steady-flow analyses of flow fields downstream from prosthetic valves.

This extensive analysis was primarily undertaken to gain a better insight into the structure of the flow downstream from the Björk-Shiley convexo-concave prosthesis. It was expected that this extensive analysis would allow more definitive comments regarding the hydrodynamic performance of this improved, semi-central flow valve prosthesis. In particular, the acentric flow generated by this valve was to be analyzed and interpreted in light of the results found by other investigators for both the convexo-concave design and the previous standard design. Detailed estimations of shear stresses was undertaken in the hope that better correlation between *in vitro* results and *in vivo* levels of hemolysis could be achieved.

3.4.2 Methodology and Apparatus

The experimental methodology and apparatus used to obtain the results for the Björk-Shiley convexo-concave valve were those discussed in detail in Chapter 2.

3.4.3 Results

3.4.3.1 Pressure and Volumetric-Flow Results

The pressure and volumetric-flow results for the Björk-Shiley convexo-concave valve were computed during each experiment in the same fashion as for the Ionescu-Shiley valve. These two sets of results are presented in Tables 6 and 7, respectively.

3.4.3.2 Velocity Results

The velocity results are presented for steady and pulsatile flow in the same fashion as for the Ionescu-Shiley valve. No data were collected for the Björk-Shiley convexo-concave valve at data-plane locations other than at z = 31.8 mm. The temporal locations of the pulsatile-flow windows for the Björk-Shiley convexo-concave valve are shown in Figure 33. For the Björk-Shiley convexo-concave valve, pulsatile-flow windows 4 through 20 encompassed the systolic ejection interval. The diastolic interval thus extended from windows 20 through 43 and then up to window 3 of the next cycle. Window 8 corresponded to the time when the flow experienced maximum acceleration, window 13 corresponded to the time of maximum forward flow, window 17 to the time when the flow experienced maximum deceleration, and window 20 to the time of maximum reverse flow.

Mean axial velocity results for pulsatile flow are presented in 3-D perspective in Figure 34. Results are shown for windows 6 through 23, 25, and 30.

Table 6

Parameters Computed from the Pressure Data
for the Björk-Shiley Convexo-Concave (25 mm) Prosthesis*

	Pressure (kPa)	Relative time** of occurrence in the cycle (ms)
Pulsatile Flow:		
ΔP_{max}	2.6 ± 0.2	169 ± 27
VP_{max}	19.7 ± 0.5 +	195 ± 13
P_{x1}	12.3 ± 0.8 +	0 ± 24
P_{x2}	10.8 ± 0.9 +	289 ± 14
$\left(\frac{dP}{dt}\right)_{max}$	192 ± 12 (kPa/s)	-28 ± 25
$\left(\frac{dP}{dt}\right)_{min}$	-293 ± 26 (kPa/s)	343 ± 12
$\overline{\Delta P}_{sys}$	0.8 ± 0.2	-
$\overline{\Delta P}_{dias}$	10.2 ± 0.3	-
$\overline{AP}$	12.1 ± 0.4 +	-
Steady Flow:		
$\overline{\Delta P}$	1.4 ± 0.1	-

*Results given as mean ± standard deviation.

**Relative to the beginning of systolic ejection.

+Gauge pressure.

Table 7

Parameters Computed from the Volumetric-Flow Data for the Björk-Shiley Convexo-Concave (25 mm) Prosthesis*

	Flow (L/min)	Relative time** of occurrence in the cycle (ms)
Pulsatile Flow:		
Q_{max}	31.2 ± 0.6	191 ± 8
Q_{min}	-8.2 ± 0.7	326 ± 5
Q_{beg}	0.0 (by def.)	-15 ± 8
Q_{end}	0.0 (by def.)	304 ± 5
Q_F	6.43 ± 0.13	-
Q_C	-0.10 ± 0.03	-
Q_L	-1.25 ± 0.14	-
Q_{rms}	20.6 ± 0.1	-
Steady Flow:		
$\bar{Q}$	27 (rotameter)	-

*Results given as mean ± standard deviation.

**Relative to the beginning of systolic ejection.

BJÖRK-SHILEY CC (25 mm)

KEY TO WINDOW LOCATIONS

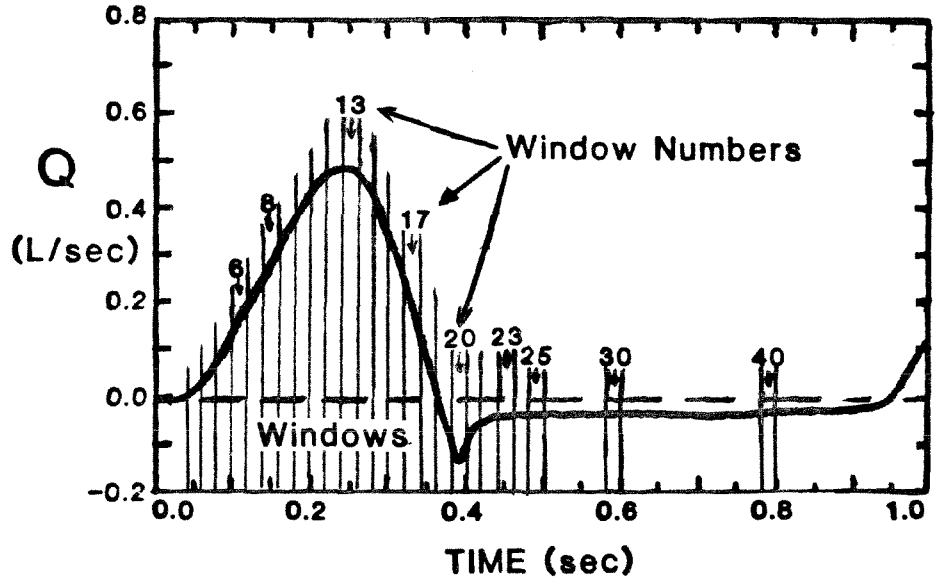

Figure 33. Idealized volumetric-flow curve showing temporal location of pulsatile-flow windows 6 through 25, 30, and 40 for the Björk-Shiley convexo-concave (25 mm) prosthesis.

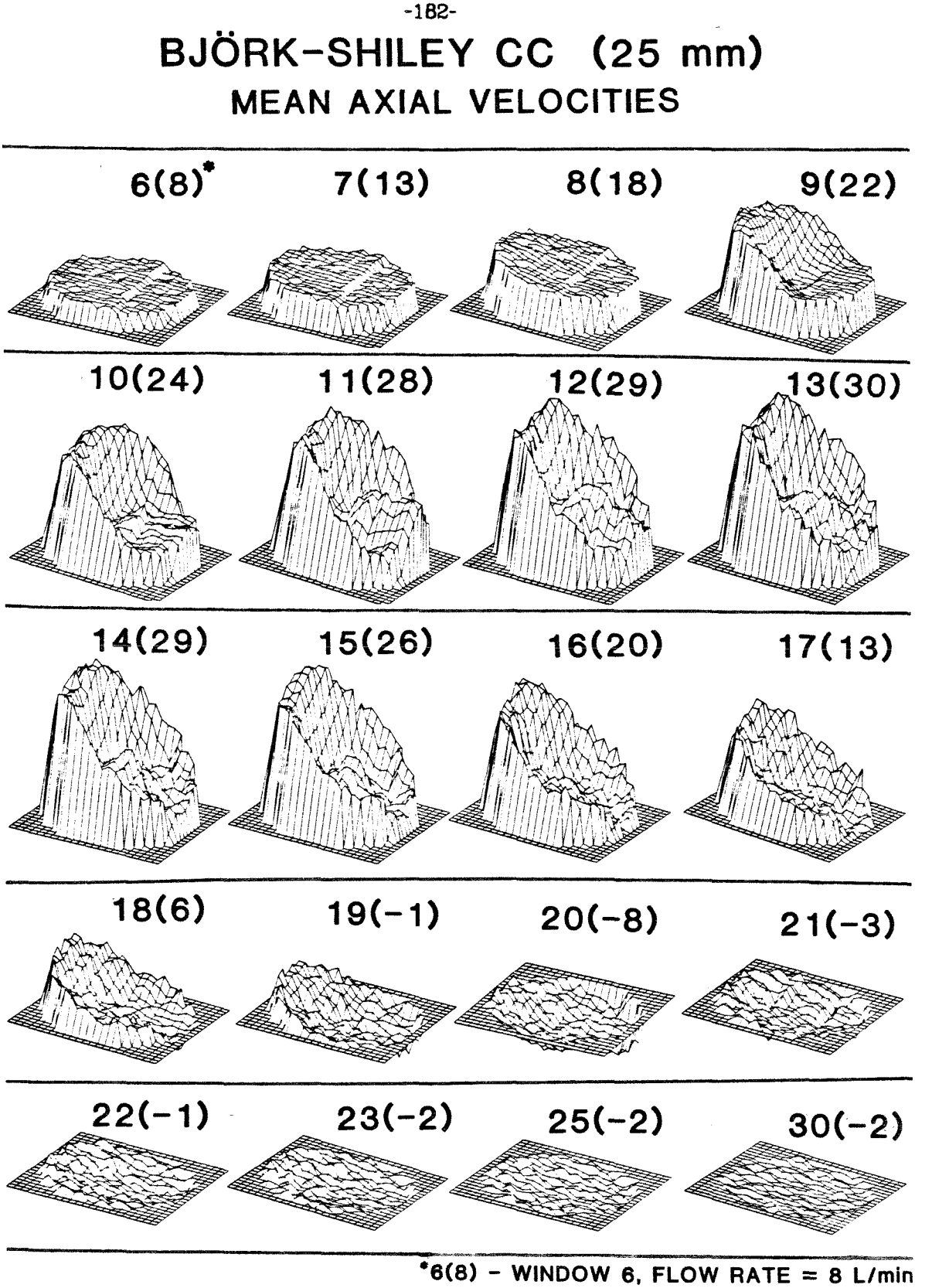

Figure 34. Mean axial velocities in 3-D perspective for pulsatile-flow windows 6 through 23, 25, and 30 downstream from the Björk-Shiley convexo-concave (25 mm) prosthesis at z = 31.8 mm.

A large "armchair"-shaped jet of fluid is readily seen in Figure 34. This jet was noticeable by window 9 and was almost full-sized by window 10 persisting for at least 150 milliseconds until window 17. The jet was largely skewed toward the wall of the tube. A smaller local maximum of the flow can be seen for windows 10 through 16 near the centerline of the tube. As will be discussed further in the next sections, this smaller flow structure was probably made up of the flow emerging from the minor outflow region. Similarly the larger jet was probably made up of the flow emerging from the major outflow region. Thus these two larger and smaller flow structures will be referred to herein as the large and small jets, respectively. No regions of flow separation are notable in Figure 34 during systole until the flow begins to reverse to close the valve. During diastole the axial velocities settled out as they had for the Ionescu-Shiley valve.

Mean axial velocities are presented in Figure 35 for steady flow and for windows 8, 13, 17, and 20 of the pulsatile flow. For steady flow both the large and small jet structures were again evident. For pulsatile flow the flow structure at window 13 was similar to that for steady flow. Early in systole at window 8 the flow had an almost flat velocity profile; however, a slight slope upward is noticeable where the large jet appeared during the next window (see Figure 34). Late in systole at window 17 the large jet had diminished significantly and the small, central jet had disappeared altogether. At window 17 the first indication of flow reversal was observable. By window 21, immediately preceding valve closure the flow had fully reversed but still showed a "sloping" effect. The maximum reversed velocities occurred opposite from the side of the tube where the large jet had occurred during the middle of systole. The position of the maximum reverse velocities corresponded to the area of the lesser flow orifice.

BJÖRK-SHILEY CC (25 mm)

MEAN AXIAL VELOCITIES

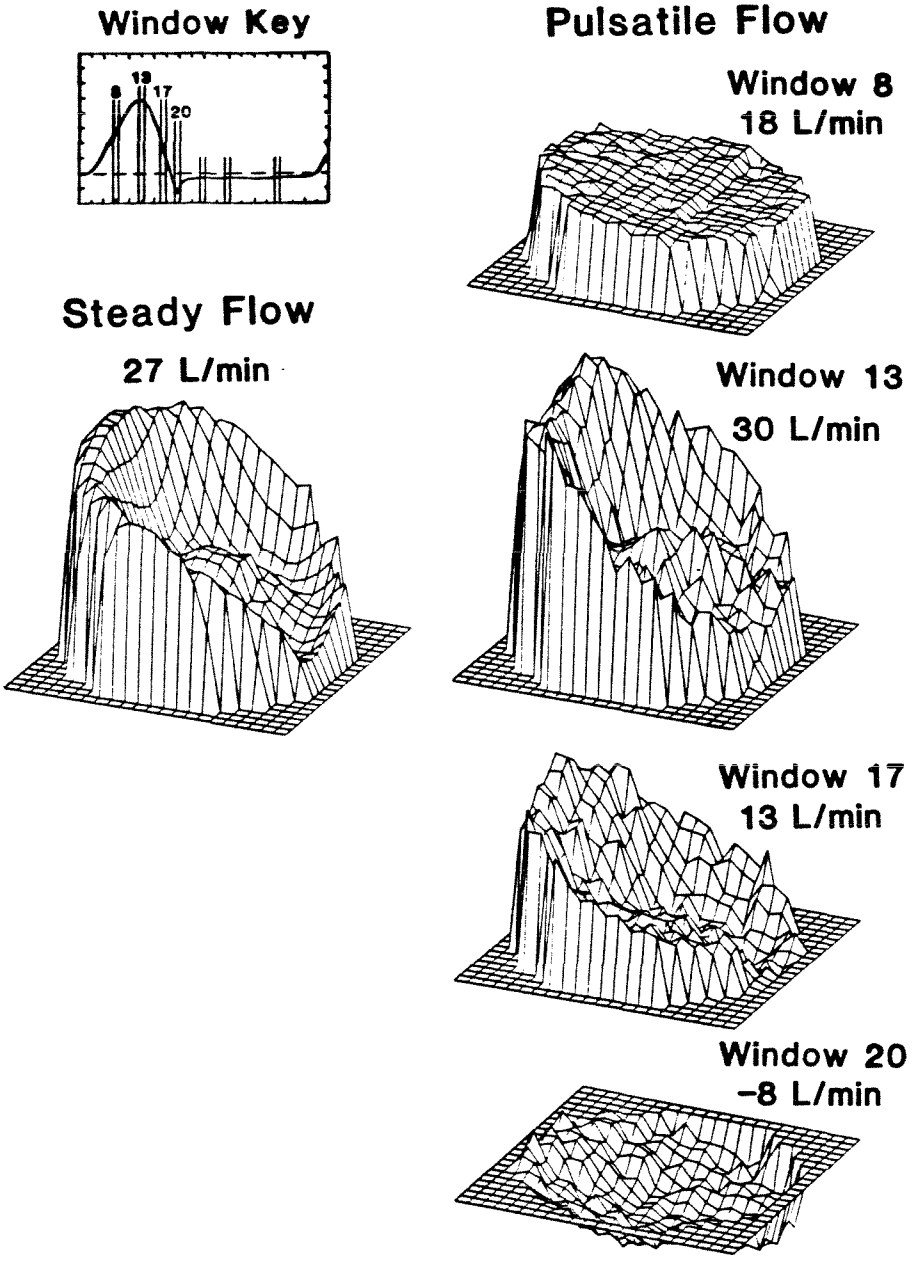

Figure 35. Mean axial velocities in 3-D perspective for steady flow and pulsatile-flow windows 8, 13, 17, and 20 downstream from the Björk-Shiley convexo-concave (25 mm) prosthesis at z = 31.8 mm.

Mean axial velocities for windows 25, 30, and 40 of the pulsatile flow are presented in Figure 36. These velocities show the settling out of the flow during diastole. Note that though both positive and negative velocities are shown in this figure, the integrated flow rate was negative. By window 40 the negative flow rate had dropped some in magnitude from -2 L/min to -1 L/min.

The mean axial velocities shown in Figure 35 for steady flow and for windows 8, 13, 17 of the pulsatile flow are presented more quantitatively as contours in Figure 37. The inset showing the valve orientation depicts the orientation of the valve superstructure relative to the structure of the velocity results. From Figure 37 the structure of the large and small jets can be more readily appreciated. The large jet of fluid appears to have been lenticular in cross section and significantly skewed towards the wall of the tube. The small jet appears to have been roughly circular in cross section and located almost on the centerline of the tube. Also notable in this figure is a region of low velocities which was located on the opposite side of the tube from the maximum of the large jet. At window 13 of the pulsatile-flow results, the low-velocity region was not quite as extensive as that for steady flow but was also located opposite from the maximum of the large jet. For these pulsatile-flow results, a second shallow minimum was found which lay essentially between the peaks of the large and small jets.

The orientation of the results for steady and pulsatile flow corresponded with that of the major and minor outflow regions delineated by the opened tilting-disc occluder of this valve design. The large jet corresponded in orientation to the major outflow region of this valve The corresponding flow structure to the minor outflow region was the low-velocity region. Accordingly, the flow structure as shown in Figure 37 was notably bi-symmetric having a plane of symmetry generally parallel with the gravitational vector.

BJÖRK-SHILEY CC (25 mm)

MEAN AXIAL VELOCITIES

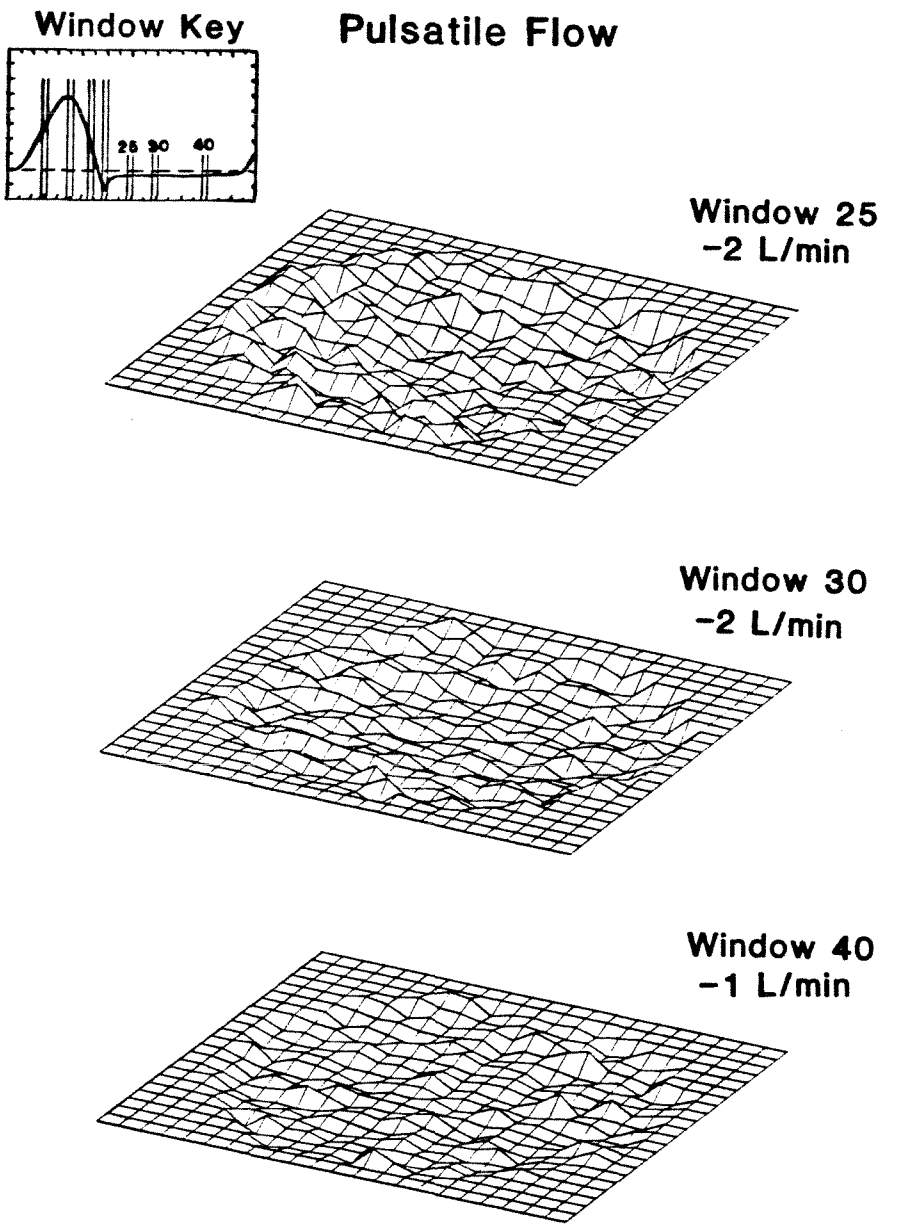

Figure 36. Mean axial velocities in 3-D perspective for pulsatile-flow windows 25, 30, and 40 downstream from the Björk-Shiley convexo-concave (25 mm) prosthesis at z = 31.8 mm.

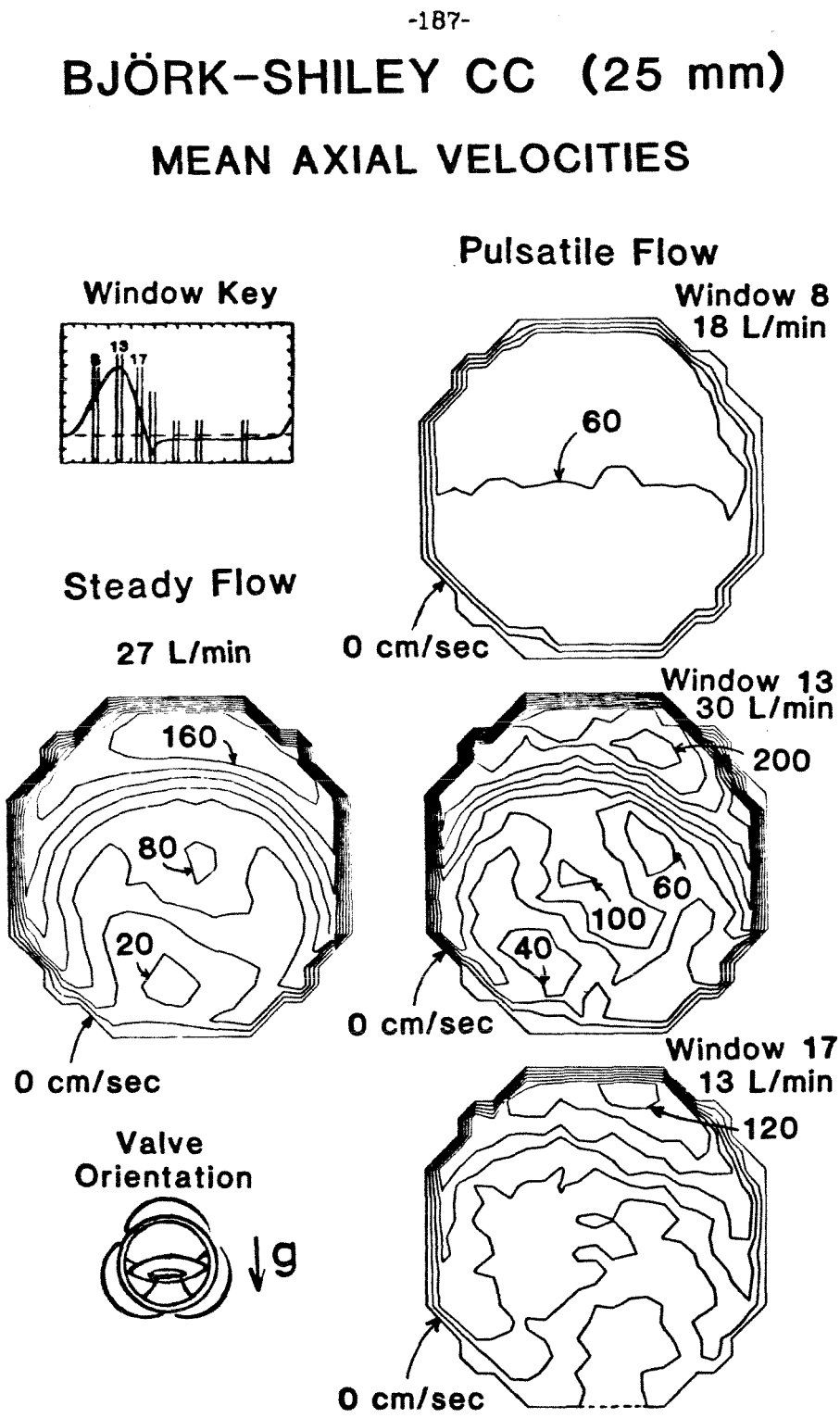

Figure 37. Mean axial velocities as contours for steady flow and pulsatile-flow windows 8, 13, and 17 downstream from the Björk-Shiley convexo-concave (25 mm) prosthesis at z = 31.8 mm. Contour interval: 20 cm/s.

The magnitude of the large jets in steady and pulsatile flow were such that very large flow acceleration and associated velocity gradients were present near the wall. The mean velocity gradient at the tube wall appears to have been significantly elevated over an azimuthal range of more than 180° for both the steady and pulsatile flow. The maximum velocity for the large jets was more than 160 cm/s and 200 cm/s for the steady-flow and pulsatile-flow results, respectively. The fluid was therefore found to be accelerated by a factor of about 1.6 to 2.0 from the maximum velocity of 105 cm/s for the flow upstream from the mounted valve. This factor was less than 1.1 for the flow through the empty flow section. For the small jet, the factor was about 0.8 for steady flow and 1.0 for pulsatile flow. The maximum mean velocity gradient in the bulk flow was calculated to have been approximately 500 s^{-1} over a radial distance of at least 2.5 mm and was found to occur along the inner aspect of the large, lenticularly-shaped jet. High velocity gradients also occurred at the wall of the tube along the outer aspect of the large jet. Detailed velocity measurements were not made near the wall but the maximum gradients at the wall appear to have been substantially larger than 1000 s^{-1} where the outer aspect of the jet was near the wall of the tube and lower than 250 s^{-1} elsewhere.

The pulsatile-flow results showed less symmetry and were less distinct than those for steady flow. The maximum of the large jet shown in window 13 was skewed off to the right of the plot as compared with the steady-flow results. Also, the small jet was less circular in cross section for pulsatile flow. The low-velocity regions for pulsatile flow were less symmetrically located for window 13 than that for steady flow. Early in systole at window 8 little flow structure was present. Only very small velocity gradients were found at window 8 and these were adjacent to the wall. The somewhat higher velocities at the top of the plot for window 8 corresponded to the location of the large jet later in systole. Late

in systole at window 17 a diminished yet definite large jet structure was present. At window 17 little remnant can be seen of the small jet and the low velocities were found in a single locus next to the tube wall. The magnitude of the peak shown for window 17 had fallen to a little more than half its maximum value at window 13. The lenticular shape of the jet, though still apparent, had become even less pronounced.

Mean axial velocities are presented in Figure 38 as contours for windows 25, 30, and 40 of the pulsatile flow. No mean axial velocities were measured greater than 20 cm/s in absolute value and hence only contours corresponding to zero velocity are plotted. For window 25 a significant portion of the tube cross section still showed positive flow even though the mean flow rate across the tube was negative. The location in the cross section of this positive flow corresponded to the location of the large jet during the systolic ejection interval. Later in diastole, by window 30 much of this positive flow had disappeared. By window 40 almost no positive flow was found. Early in diastole the positive flow may have been the result of a slowly rotating vortex as was seen for the Ionescu-Shiley valve during diastole. The vortex for the Björk-Shiley convexo-concave valve, if present, was relatively short-lived and not as large in diameter as that found for the Ionescu-Shiley valve.

Mean non-axial velocities are presented in Figure 39 for steady flow and for windows 8, 13, and 17 of the pulsatile flow as resultants of the mean velocities in the x- and y-directions. For both steady and pulsatile flow, the mean non-axial results showed large velocity components near the wall of the tube. For steady flow these velocity components were directed along the wall in such a way as to form a pseudo-stagnation point like those found for the Ionescu-Shiley valve. This pseudo-stagnation point corresponded in location with the low-velocity region shown for steady flow in Figure 38. Radially directed velocities were

BJÖRK-SHILEY CC (25 mm)

MEAN AXIAL VELOCITIES

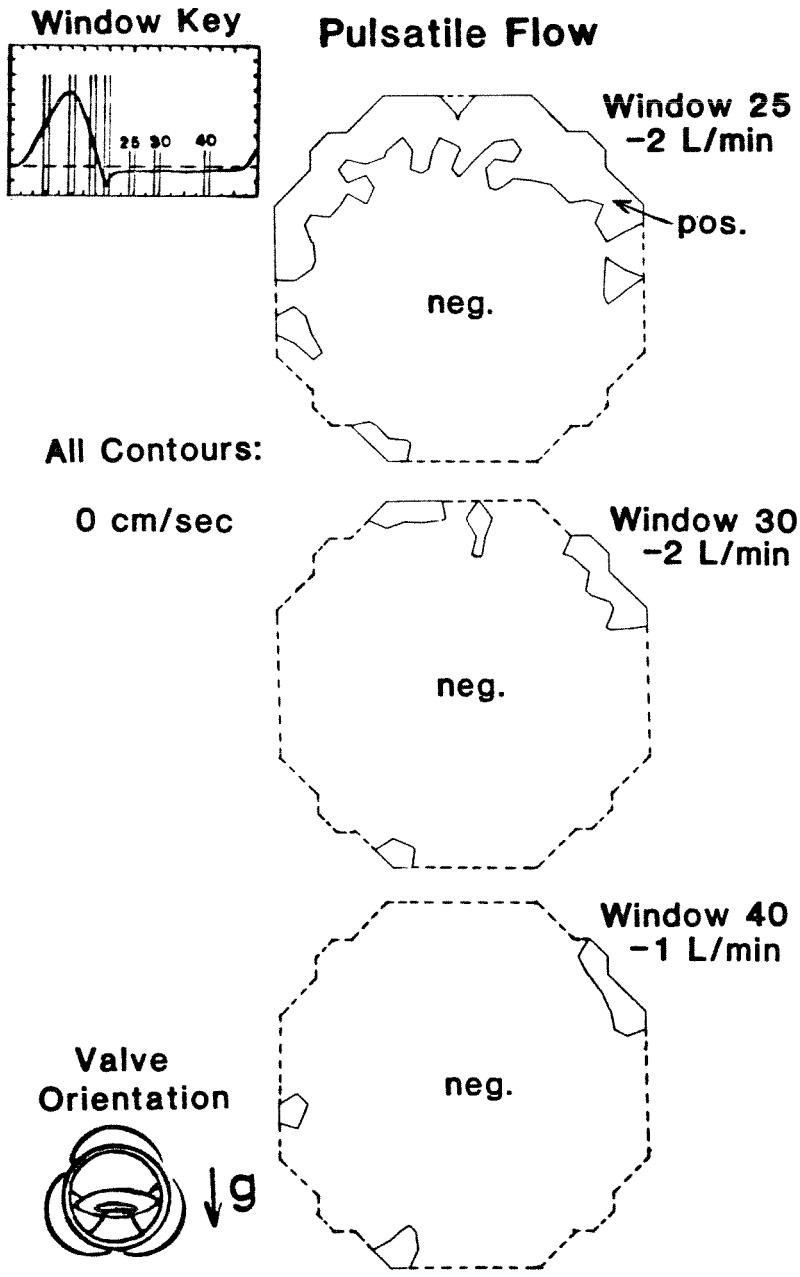

Figure 38. Mean axial velocities as contours for pulsatile-flow windows 25, 30, and 40 downstream from the Björk-Shiley convexo-concave (25 mm) prosthesis at z = 31.8 mm. Contour interval: 20 cm/s.

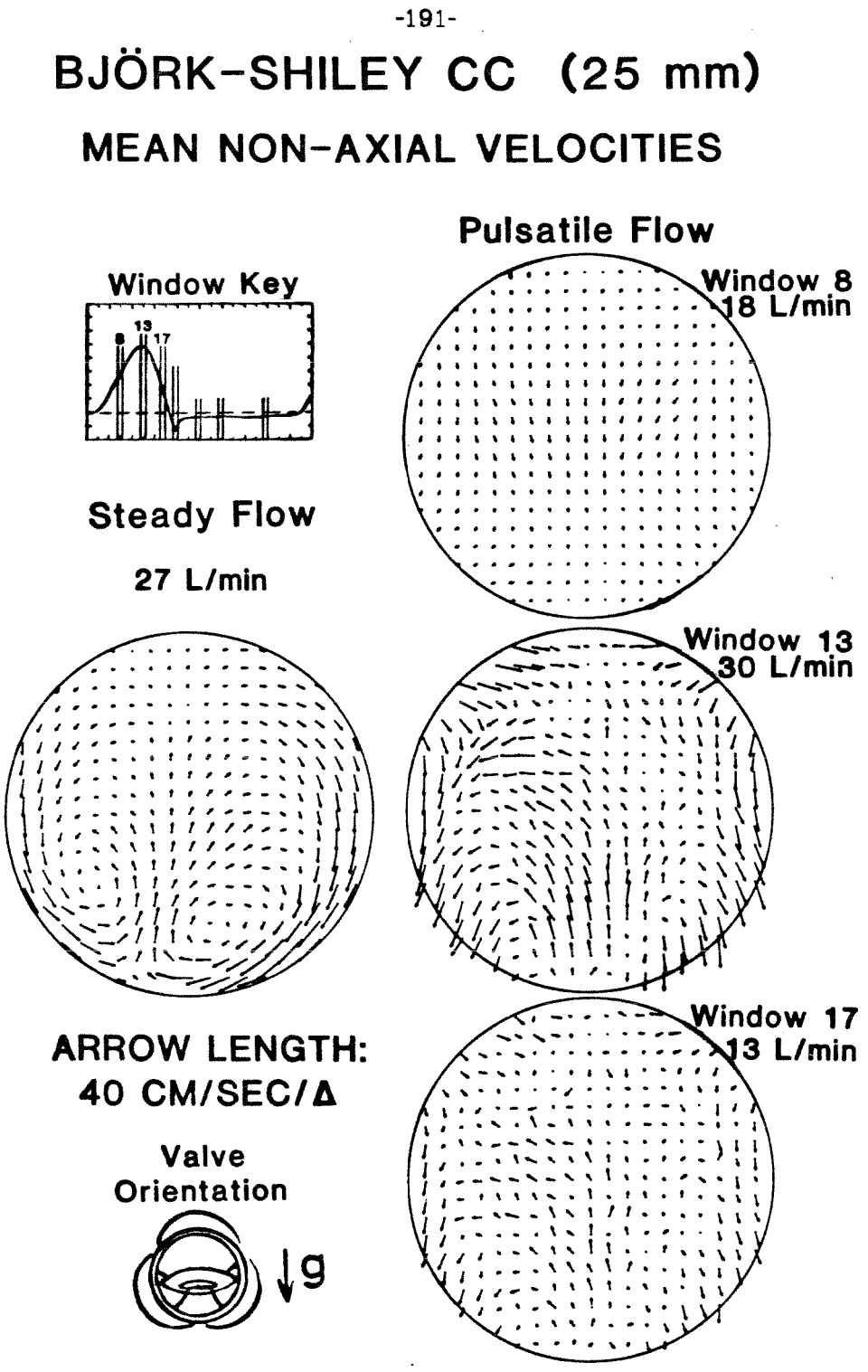

Figure 39. Mean non-axial velocities as resultants for steady flow and for pulsatile-flow windows 8, 13, and 17 downstream from the Björk-Shiley convexo-concave (25 mm) prosthesis at z = 31.8 mm.

found directed away from the pseudo-stagnation point at the wall and towards the centerline of the tube. Two well-defined vortices were thus formed which moved the flow in a fashion reminiscent of a two-roller mill. Flow was drawn along the wall, between the centers of the two vortices, and out into the bulk of the flow. The flow in the large jet was thus being pulled along the tube wall from regions of higher axial velocity into regions of lower axial velocity. The flow in the low-velocity region was being fed into the region of the small axial jet. The pulsatile-flow results were quite different from the steady-flow results. At window 13 the non-axial velocity components were generally larger for pulsatile flow than those for steady flow. At the wall of the tube significant velocity components were measured that were radially oriented. Near the top of the plot for window 13 in Figure 39 these radially oriented velocity components were directed away from the wall of the tube. Near the bottom of the plot for window 13 the radially oriented velocities were directed towards the wall. Two vortices were noticeable near the bottom of the plot for window 13 but these were much less distinct than those for steady flow. For pulsatile flow an apparent pseudo-stagnation point was also formed which was similar in location and form to that found for steady flow. Early in systole at window 8 small non-axial velocities were present in the middle of the tube which were directed towards the bottom of the plot. The secondary-flow structure shown in window 8 was very orderly. Late in systole at window 17 the structure of the flow had degenerated considerably from that at window 13 but some remnants of the earlier flow structure were noticeable. In particular, the two vortices appear to have still been present with their associated non-axial velocities.

The maximum mean velocities in the radial and azimuthal directions were determined as resultants of the velocity components measured in the x- and y-directions. For steady flow, the maximum mean velocities in the radial and

azimuthal directions were 59.8 ± 1.0 cm/s and 40.1 ± 1.0 cm/s, respectively. For pulsatile flow, these maximum velocities were 62.0 ± 1.0 cm/s and 45.2 ± 1.0 cm/s, respectively. These pulsatile-flow results were for window 13.

Mean non-axial velocities are presented as resultants in Figure 40 for windows 25, 30, and 40 of the pulsatile flow. Overall, only very small velocity components were observed throughout diastole. There was no appreciable structure of the flow notable from these diastolic results.

The rms axial velocities are presented in Figure 41 for steady flow and for windows 8, 13, and 17 of the pulsatile flow. For both steady and pulsatile flow, the rms axial velocities reflect the flow structure observed from the mean velocities. The highest rms axial velocities for steady flow and for window 13 of pulsatile flow were found in a lenticular region corresponding spatially to the cross section of the large axial jet and also near the centerline of the tube corresponding spatially to the cross section of the small axial jet. The lowest rms axial velocities for steady flow and for window 13 of pulsatile flow were found to correspond spatially to the locations of the low-velocity regions of the mean axial velocity results. Generally, the rms axial velocities for steady flow were larger than those for window 13 of the pulsatile flow. The maximum rms axial velocities for steady and pulsatile flow were, however, both the same at 44.8 ± 1.0 cm/s. The average rms axial velocity across the data plane for steady flow was 32.5 ± 1.0 cm/s while that for pulsatile flow was 30.7 ± 1.0 cm/s. The pulsatile-flow results are for window 13. The rms axial velocities corresponded to an average turbulence intensity across the data plane of 31% for window 13 of pulsatile flow and 37% for steady flow. The maximum turbulence intensity at the data plane was 42% for window 13 of pulsatile flow and 50% for steady flow. Early in systole at window 8 the rms axial velocities were in comparison very low. The rms axial velocities were elevated somewhat in

BJÖRK-SHILEY CC (25 mm)

MEAN NON-AXIAL VELOCITIES

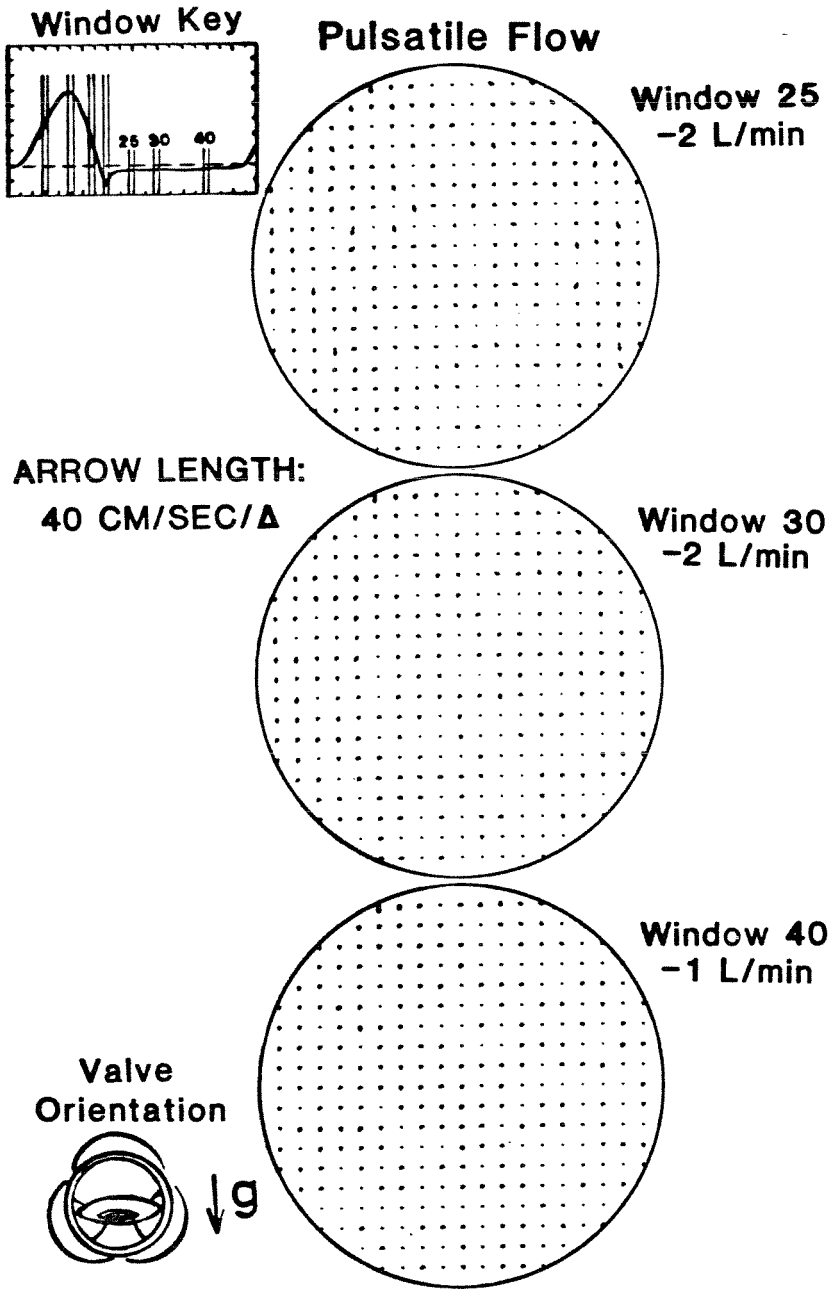

Figure 40. Mean non-axial velocities as resultants for pulsatile-flow windows 25, 30, and 40 downstream from the Björk-Shiley convexo-concave (25 mm) prosthesis at z = 31.8 mm.

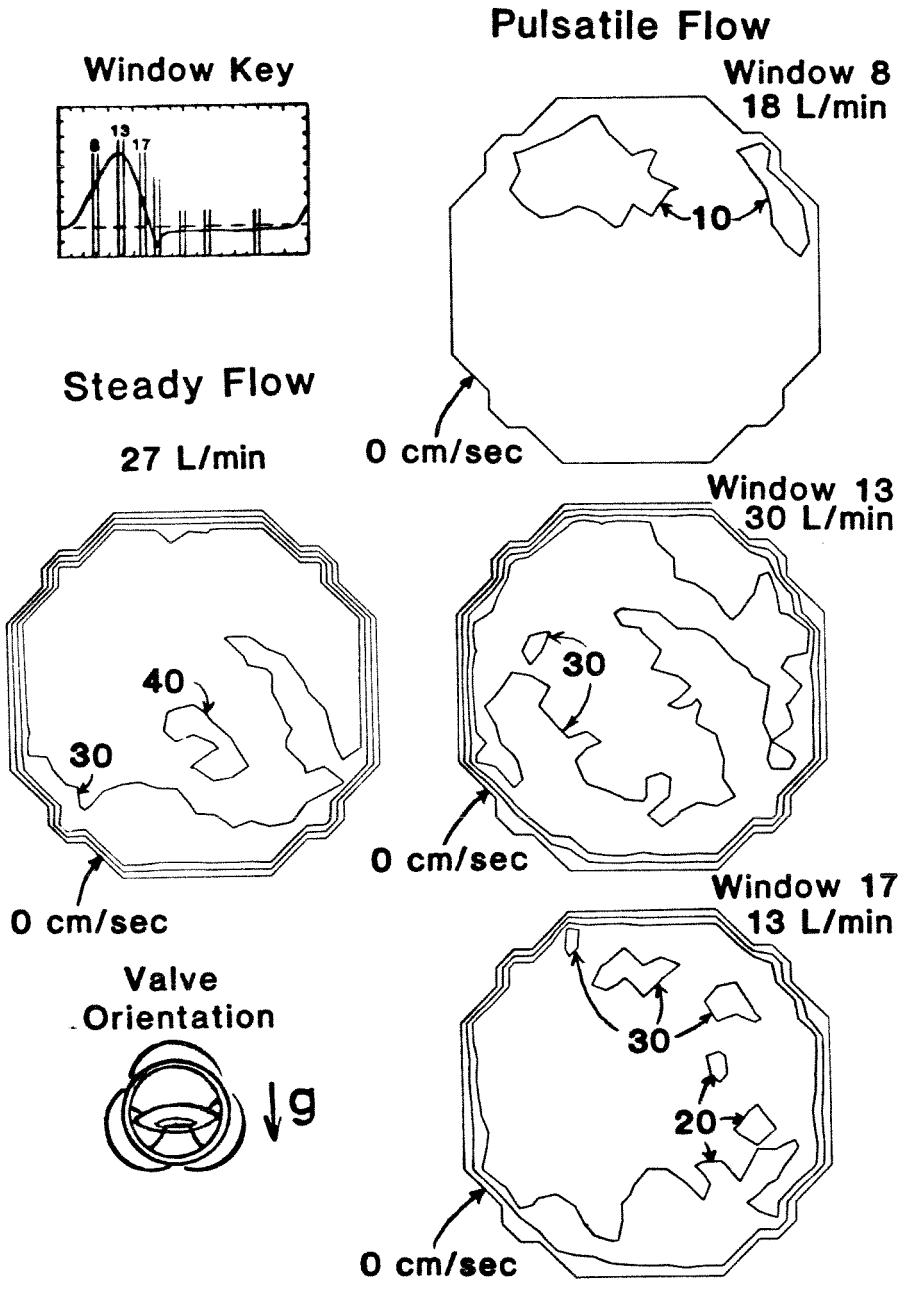

Figure 41. Root-mean-square (rms) axial velocities as contours for steady flow and pulsatile-flow windows 8, 13, and 17 downstream from the Björk-Shiley convexo-concave (25 mm) prosthesis at z = 31.8 mm. Contour interval: 10 cm/s.

the top of the plot for window 8. These elevated rms velocities corresponded in their location with the higher mean axial velocities shown in the top of the plot for window 8 in Figure 37. Late in systole at window 17 the rms axial velocities still remained elevated but were generally smaller than those found at window 13. Notably, the highest rms axial velocities shown in window 17 were located at the top of the plot corresponding to the location of the remnant of the large axial jet as shown for window 17 in Figure 37.

The total shear stresses estimated from the velocity data using Equation (11) are presented as contours in Figure 42 for the axial velocity in the x-direction. The total shear stresses for the axial velocity in the y-direction are presented as contours in Figure 43. Steep ridges of elevated shear stresses are apparent in Figures 42 and 43 along the wall of the tube. In Figure 42 the elevated stresses are shown to be greater than 100 N/m^2 near the wall of the tube to the left and right of the plots for window 13 and for steady flow. In Figure 43 the elevated stresses are shown to be greater than 100 N/m^2 near the wall of the tube at the top of the plots for window 13 and for steady flow. For window 13 of the pulsatile flow, the elevated stresses are shown in Figure 43 to rise up beyond 140 N/m^2. Figures 42 and 43 show the very low shear stresses near the wall of the tube at the bottom of the plots for window 13 of pulsatile flow and for steady flow. In the bulk flow, i.e., in the flow farther than a millimeter or so from the the tube wall, the estimated total shear stresses were generally low. The stresses in the bulk were, however, higher than the lowest stresses found at the tube wall. The stresses in the bulk show slight structure which corresponded spatially to the large and small axial jets which corresponded, respectively, to the flow through the major and minor outflow regions. Somewhat higher stresses were grouped into a lenticularly shaped region which corresponded in orientation to that for the large axial jet. This was most pronounced in the

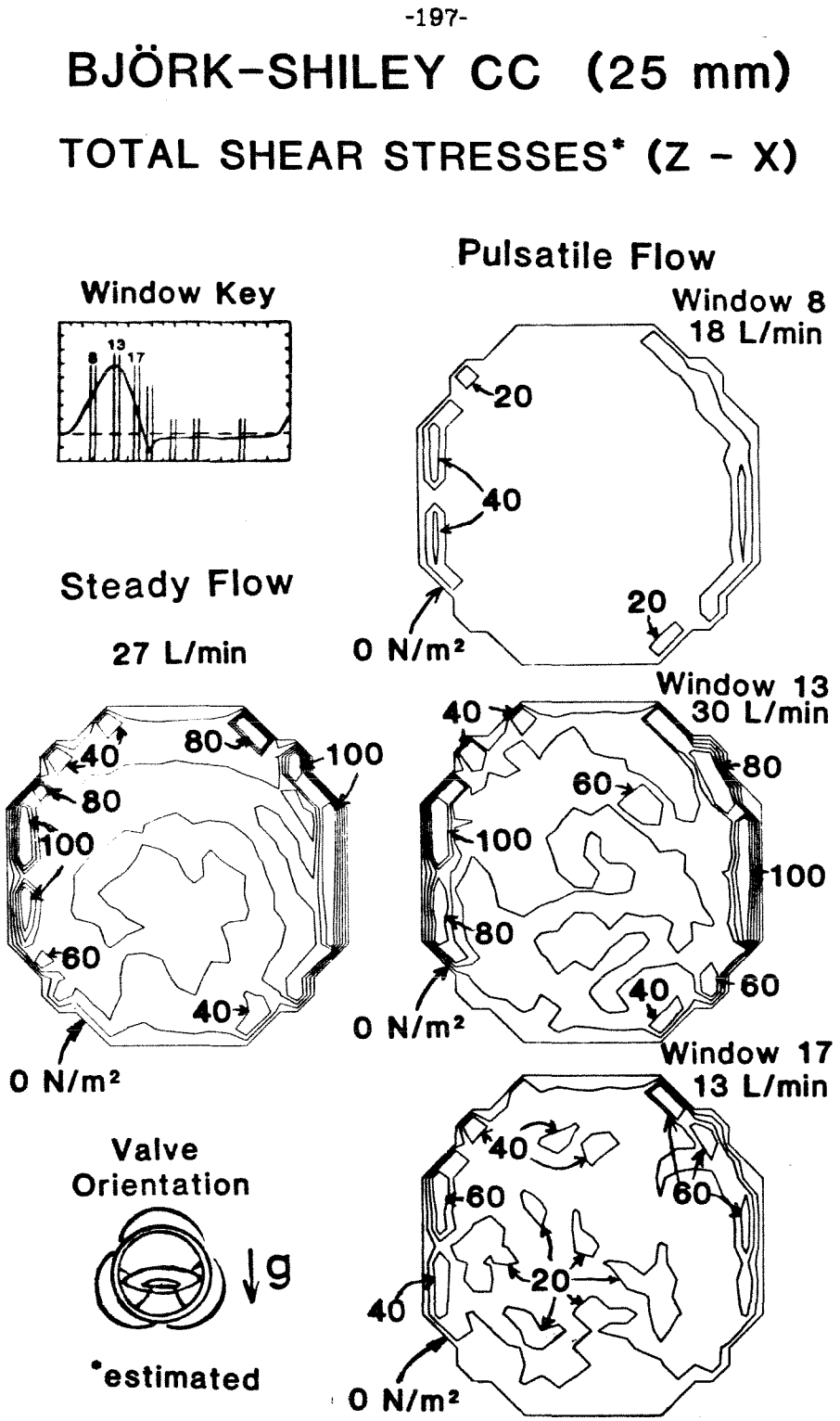

Figure 42. Total estimated shear stresses, τ_{zx}, as contours for steady flow and for pulsatile-flow windows 8, 13, and 17 downstream from the Björk-Shiley convexo-concave (25 mm) prosthesis at z = 31.8 mm. Contour interval: 20 N/m^2.

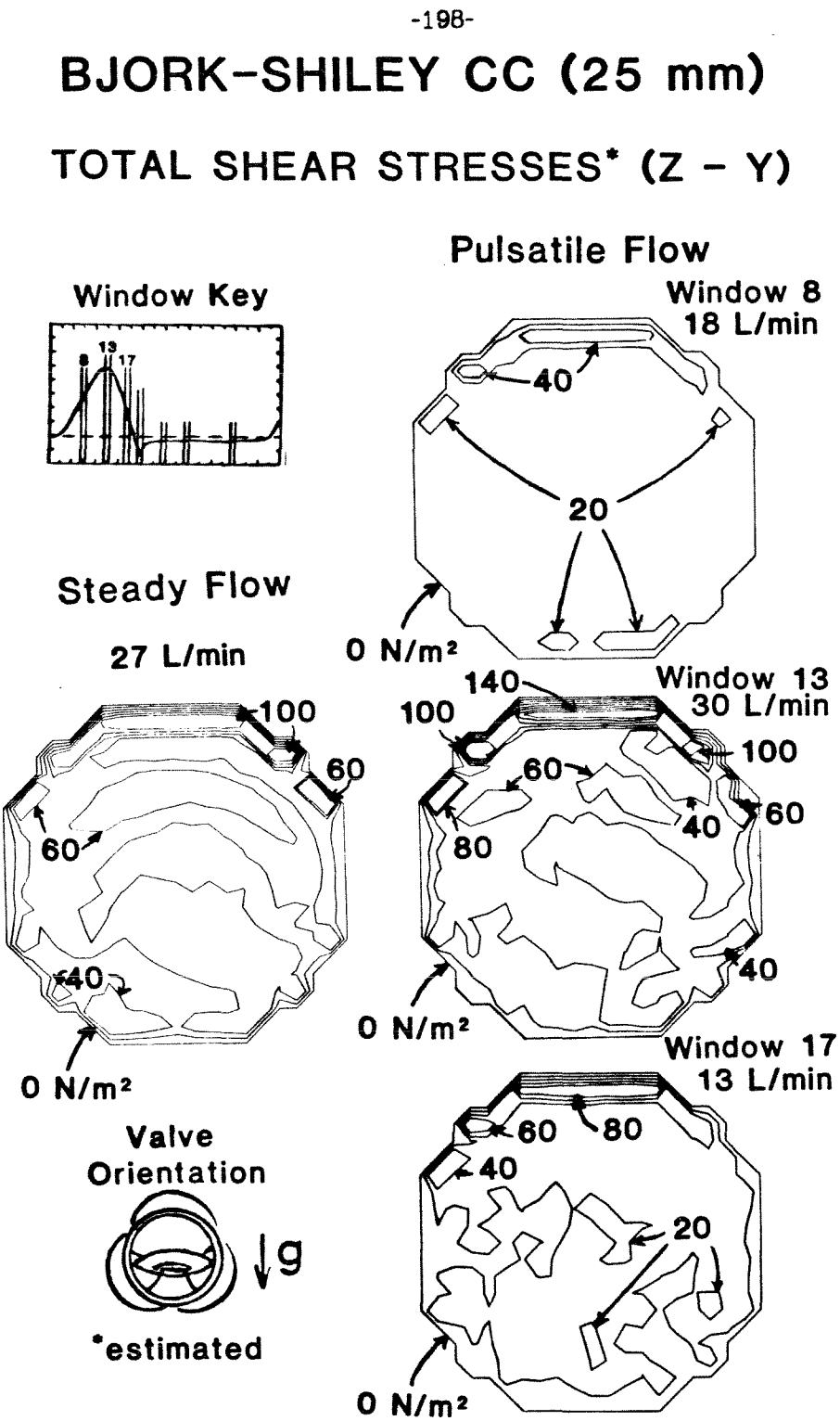

Figure 43. Total estimated shear stresses, τ_{zy}, as contours for steady flow and for pulsatile-flow windows 8, 13, and 17 downstream from the Björk-Shiley convexo-concave (25 mm) prosthesis at z = 31.8 mm. Contour interval: 20 N/m^2.

steady-flow results. Also, the steady-flow results show a weak maximum near the center of the tube which corresponded roughly to the location of the small axial jet. Early in systole at window 8, some small shear stresses are shown in Figures 42 and 43 near the wall of the tube. As was found for window 13, the estimated total shear stresses were lower near the wall of the tube at the bottom of the plot for window 8. Late in systole at window 17, the shear stresses at the wall are shown in Figure 42 and 43 to remain elevated as they were at window 13. The maximum shear stress shown for window 17 for Figures 42 and 43 were greater than 60 N/m^2 and 80 N/m^2, respectively.

The maximum total shear stress was estimated which was present over at least 10% of the tube cross section. For steady flow, this maximum shear stress was estimated to be 112 ± 5 N/m^2. For pulsatile flow, this maximum shear stress was estimated to be 106 ± 5 N/m^2 at window 13.

Figure 44 shows the volumetric-flow rates and average rms velocities calculated from the mean and rms velocities, respectively, at the data plane. The plots in Figure 44 allow an analysis and comparison of the steady-flow and pulsatile-flow results. In the top of Figure 44 the flow rate is plotted versus the pulsatile-flow window number. The flow rates plotted here were determined by averaging the mean axial velocities across the data plane. For pulsatile flow, the flow rate determined for each window is plotted to correspond with its respective window number along the abscissa. The flow rate for steady flow is plotted to correspond with window 14, which was the window encompassing the maximum flow rate for pulsatile flow. In the bottom of Figure 44 the average rms axial velocity is plotted versus the pulsatile-flow window number. The average rms axial velocities plotted here were determined by averaging the rms axial velocities across the data plane. For pulsatile flow the average rms axial velocity determined for each window is plotted to correspond with its respective

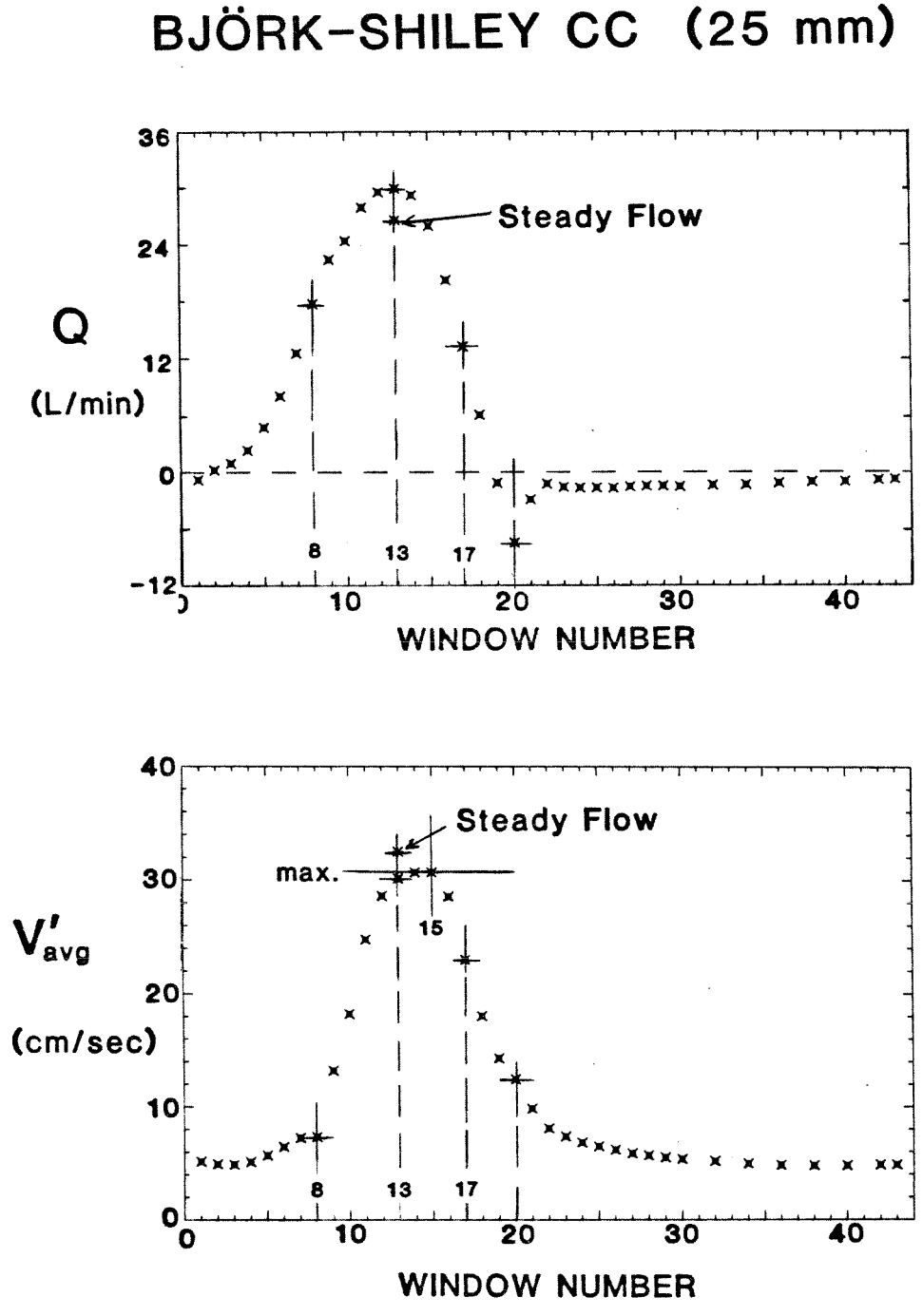

Figure 44. Volumetric-flow rate (top) and average rms velocity (bottom) calculated from the mean and rms velocities, respectively, at the data plane as a function of pulsatile-flow window number for the Björk-Shiley convexo-concave (25 mm) prosthesis.

window number along the abscissa. The average rms axial velocity for steady flow is plotted to correspond in time with the steady-flow result in the top of Figure 44.

The flow-rate results in Figure 44 generally agree with those presented in Table 7. The maximum and minimum flow rates from the velocity data were 30 L/min and -8 L/min, respectively. The corresponding values from Table 7 are 31.2 L/min and -8.2 L/min. The effect of the finite width of the pulsatile-flow window and variability in the timing from one cycle to another probably account for the small differences between these two sets of the maximum and minimum flow rates. Taking the beginning of the systolic ejection interval to be at window 4, the timing of the maximum and minimum flow rates also agree. The velocity data indicate that the maximum and minimum flow rates occurred about 180 and 320 milliseconds after the systolic ejection interval began, respectively. The corresponding values from Table 7 are 191 and 326 milliseconds, within the uncertainty of the width of the 20-millisecond windows.

The forward-flow and leakage-flow rates calculated from the results in Figure 44 differ significantly from the those given in Table 7. From the results plotted in Figure 44, the forward-flow and leakage-flow rates were calculated as 6.6 L/min and -0.7 L/min, respectively. The forward-flow and leakage-flow rates given in Table 7 are 6.43 ± 0.13 L/min and -1.25 ± 0.14 L/min, respectively. The closure-flow rate obtained from Figure 44 agrees within experimental uncertainty with that reported in Table 7. The closure-flow rate obtained from Figure 44 is -0.1 L/min; that reported in Table 7 is -0.10 ± 0.03 L/min.

The discrepancy between the leakage-flow rate obtained from Figure 44 and that given in Table 7 probably was caused by drift of the electromagnetic flowmeter and biasing of the mean velocity results from the LDA. For the

Ionescu-Shiley valve it was shown that during data collection the flowmeter drifted sufficiently to give a value of the leakage-flow rate that was low by about 0.1 L/min. For the Björk-Shiley convexo-concave valve this drift may have been as much as 0.2 L/min. For the Ionescu-Shiley valve it was also shown that the bias in the mean velocity results obtained using the LDA was 0.2 L/min for the leakage-flow rate. The bias encountered with both valves would most probably be similar. In Chapter 2 it was noted that bias in the mean velocity results was worse for locations where there were larger rms velocities, and vice versa. The average rms axial velocities shown in Figures 32 and 44 are roughly equal in magnitude. Thus it is reasonable to expect that any biasing of the mean axial velocities averaged for the flow-rate results shown in these two figures would be roughly equal. Subtracting out the bias of 0.2 L/min from the results for the Björk-Shiley convexo-concave valve would give a forward-flow rate of 6.4 L/min and a leakage-flow rate of about -0.9 L/min. With the flowmeter drift and LDA biasing compensated for, the leakage-flow rates become -1.0 ± 0.1 L/min and -0.9 L/min from Table 7 and Figure 44, respectively. The forward-flow rates become 6.5 ± 0.1 L/min and 6.4 L/min, respectively. The closure-flow rates were not affected significantly. Using the forward-flow rate of 6.4 L/min, the closure-flow rate of -0.1 L/min, and the leakage-flow rate of -0.9 L/min, the percentage of regurgitant flow relative to the forward flow was about 16%.

Another difficulty with the results shown in the top of Figure 44 is that the flow rate at the end of diastole is shown to have risen up before the apparent beginning of the systolic ejection phase. The finite flow rates shown in Figure 44 for late diastole are probably a result of the averaging process by which the results were obtained. This phenomenon was seen in the results for Ionescu-Shiley valve and was again caused here by variations in the time the systolic ejection interval began.

3.4.4 Discussion

3.4.4.1 Discussion of the Pressure and Volumetric-Flow Results

The pressure and volumetric-flow results presented in Tables 6 and 7 indicate that the pressure and flow fields encountered by the mounted prosthesis in the pulse-duplicator were similar to those the valve might have encountered had it been implanted. The maximum rate of change of the ventricular pressure given in Table 6 of 192 ± 12 kPa/s compared well with that of a healthy human ventricle of about 197 ± 37 kPa/s (Yang, et al., 1978). Similarly, the minimum rate of change of the ventricular pressure given in Table 6 of -293 ± 26 kPa/s was not too different from that of a healthy human ventricle of about -355 ± 29 kPa/s (Yang, et al., 1978). For the volumetric-flow results, the forward flow, closure flow, and leakage flow given in Table 7 sum to a mean flow rate, or cardiac output (CO), of 5.08 L/min. This mean flow rate was about 6% below the standard setting of the pulse-duplicator of 5.4 L/min given in Table 2. As was shown above, however, the flow-rate results in Table 7 were subject to adjustment to remove the effects of flowmeter drift. Once adjusted, the flow-rate results in Table 7 become 6.5 L/min, -0.1 L/min, and -1.0 L/min for the forward-flow, closure-flow, and leakage-flow rates, respectively. The sum of these adjusted flow rates is 5.4 L/min which agrees with the setting in Table 2. Q_{max} given in Table 7 as 31.2 L/min was physiological in magnitude. The timing results given in Tables 6 and 7 were physiologically appropriate. The systolic ejection interval spanned 34% of the cycle which is similar to that percentage found *in vivo* for a similar pulse rate and cardiac output. The forward-flow phase began and ended at times not significantly different from those of the systolic ejection interval. During systole, ΔP_{max} preceded both Q_{max} and VP_{max} by about 24 milliseconds. Though this difference was not significant, the order of the events was that observed *in vivo*. The time of occurrence of $\left[\frac{dP}{dt}\right]_{max}$ was

appropriately located in time during the iso-volumetric contraction phase and the time of occurrence of $\left[\frac{dP}{dt}\right]_{min}$ was appropriately located in time during the iso-volumetric relaxation phase. Q_{min} signaled valve closure appropriately by occurring after the end of the systolic ejection interval but before the occurrence of $\left[\frac{dP}{dt}\right]_{min}$ in the iso-volumetric relaxation phase.

The pressure-drop results across the valve resulting from these pulsatile pressure and flow fields compared well with the limited pulsatile-flow results presented in the literature. For the Björk-Shiley convexo-concave valve, Gombrich, et al. (1979) have reported pressure-drop results for pulsatile flow *in vitro*. They operated their pulse-duplicator at 72 beats per minute at a mean flow rate of 5.25 L/min using a blood-analog fluid of 37% glycerine and 63% saline. With a maximum ventricular pressure of 16.0 kPa (gauge) and a systemic resistance of 10.7 kPa (gauge), they found a mean systolic pressure drop of 0.7 kPa for a Björk-Shiley convexo-concave valve with a TAD of 27 mm. Their finding was not significantly different from $\overline{\Delta P}_{sys}$ reported in Table 6 of 0.8 ± 0.2 kPa. No pressure-drop results were found in the literature to compare with the value of ΔP_{max} of 2.6 ± 0.2 kPa.

Although numerous *in vivo* investigations of the standard model of the Björk-Shiley valve have been reported, very little *in vivo* results have been reported to date for the convexo-concave model. In particular, no *in vivo* pressure-drop data have been found in the literature to compare with the pulsatile-flow results *in vitro*.

Regurgitant flow for the Björk-Shiley convexo-concave valve was significant. The total regurgitant flow rate for this valve of 1.35 L/min was about 21% of the forward-flow rate of 6.43 L/min. Leakage flow accounted for 93% of the

regurgitant flow. The magnitude of the total regurgitant flow, however, was probably less than that shown in Table 7. The electromagnetic flowmeter may have suffered significant drift during data collection. This drift tended to be towards lower flow rates and hence the actual regurgitant-flow rate may have been somewhat smaller, and the forward-flow rate somewhat larger, than that shown in Table 7. The effect of the performance of the electromagnetic flowmeter on the measured regurgitant-flow rate is discussed in more detail below. $\overline{\Delta P}_{dias}$ and $\overline{AP}$ were consistent with a moderate level of regurgitation. The aortic pressure drops during diastole when there is regurgitant flow and hence $\overline{\Delta P}_{dias}$ and $\overline{AP}$ also drop. Of the four valves studied in the present investigation, only the Smeloff valve had values of $\overline{\Delta P}_{dias}$ and $\overline{AP}$ which were lower than those for the Björk-Shiley convexo-concave valve.

For steady flow, $\overline{Q}$ in Table 7 indicates that the steady-flow velocity results were comparable in magnitude to those for pulsatile flow. $\overline{Q}$ at 27 L/min was about 13% smaller than Q_{max}.

The steady-flow pressure drop found in the present investigation was lower than those reported in the literature. More pressure-drop results for the Björk-Shiley convexo-concave valve have been reported in the literature for steady flow than for pulsatile flow. Åberg and Henze (1979) reported a steady-flow pressure drop of 2.5 kPa for a Björk-Shiley convexo-concave prosthesis with a TAD of 25 mm at a flow rate of 27 L/min. Björk and Henze (1979) reported a steady-flow pressure drop of 2.7 kPa for this valve with a TAD of 25 mm at a flow rate of 27 L/min. Schramm, et al. (1980) reported a steady-flow pressure drop of 0.8 kPa for this valve with a TAD of 25 mm at a flow rate of 18 L/min. Using Equation (13) with an exponent of 2.0, the results of Schramm, et al. (1980) predict a steady-flow pressure drop of 1.7 kPa at a flow rate of 27 L/min. An exponent of 1.9 to 2.0 in Equation (13) is consistent with the pressure-drop

results presented for the Björk-Shiley convexo-concave valve by several investigators (Gombrich, et al., 1979; Gabbay, et al., 1980; Tindale, et al., 1982; Bruss, et al., 1983; Yoganathan, et al., 1983a). $\overline{\Delta P}$ is reported in Table 6 as 1.4 ± 0.1 kPa.

The higher steady-flow pressure drops reported by other investigators are probably related to the location at which the measurements were made and to the differences in the experimental rigs. Schramm, et al. (1980) have shown that the Björk-Shiley convexo-concave valve may require up to 100 mm for pressure recovery. Åberg and Henze (1979) and Björk and Henze (1979) both measured their downstream pressures at about z = 42 mm. For the present investigation the pressure tap was located at z = 150 mm. Thus the higher values for the pressure drop that these investigators reported may be explained as a result of this valves pressure-recovery characteristics. The discrepancy with the results of Schramm, et al. (1980) may stem from the fact that the inner diameter of their model of the ascending aorta was 9.6 mm larger than that for the present investigation. Their flow section thus had about 53% more area for flow than that of the present investigation. The flow through the mounted valve in the work of Schramm, et al. (1980), therefore, experienced a more pronounced "sudden expansion" upon emerging from the valve. For a sudden expansion in a pipe, the losses are a function of the ratio of the upstream and downstream areas available for flow and the upstream mean velocity across the pipe (Streeter and Wiley, 1975):

$$E_{f,ex} = \frac{1}{2} u_1^2 \left(1 - \frac{A_1}{A_2}\right)^2 \qquad (26)$$

where $E_{f,ex}$ is the rate at which mechanical energy is irreversibly converted to thermal energy at a sudden expansion in the pipe, u_1 is the mean velocity across the pipe upstream from the expansion, A_1 is the area available for flow upstream

from the expansion, and A_2 is the area available for flow downstream from the expansion. The inner diameter of the base-ring of the Björk-Shiley convexo-concave prosthesis with a TAD of 25 mm is 20 mm. Disregarding the occluding mechanism of the valve and assuming that for the present investigation the sinuses can be ignored in the calculation, the "sudden expansion" for the flow through the valve would cause a pressure loss which was about 2 kPa greater for the flow-section geometry of Schramm, et al. (1980). Subtracting this pressure difference from the pressure drop of 1.7 kPa calculated above for 27 L/min, the results of Schramm, et al. (1980) agree with the results from the present investigation within the experimental uncertainty.

The pulsatile-flow pressure drops estimated from the pressure-drop results for steady flow in the present investigation compare well with the pulsatile-flow results presented in Table 6. The pulsatile-flow pressure drops can be estimated using Equations (14) and (16). Substituting into Equation (14) the values for $\overline{\Delta P}$, $\overline{Q}$, and Q_{rms} from Tables 6 and 7, the $\overline{\Delta P}_{sys}$ calculated was 0.81 kPa. $\overline{\Delta P}_{sys}$ in Table 6 was 0.8 ± 0.2 kPa. Substituting into Equation (16) the values of $\overline{\Delta P}$, Q_{max}, and Δt_{sys} yields a value of ΔP_{max} of 2.6 kPa. ΔP_{max} in Table 6 was 2.6 ± 0.2 kPa. Thus the pressure-drop results obtained from the steady-flow and pulsatile-flow experiments in the same flow section were consistent with one another.

3.4.4.2 Discussion of the Velocity Results

The most recent redesigning of the Björk-Shiley prosthesis was aimed mainly at reducing its associated incidence of thromboembolic complications. Early investigations had found little or no thromboembolic complications associated with the standard model (Björk, et al., 1971; Björk, et al., 1972). Later, however, massive thrombosis of the standard model was reported on a frequent basis

(Bozer and Karamehmetoglu, 1972; Ben-Zvi, et al., 1974; Björk and Henze, 1975; Fernandez, et al., 1976; Yoganathan, et al., 1978b). Subsequent studies have found significant thromboembolic incidence rates associated with the standard model (Dale, et al., 1980; Karp, et al., 1981) and have continued to report problems of massive thrombus formation (Dale, 1977; Venkataraman, et al., 1980).

The disc-occluding mechanism was redesigned so as to minimize stagnant zones in the flow in the near vicinity of the implanted prosthesis (Björk, 1978). Regions of stagnant and low flow behind the disc occluder in the area of the minor outflow region had previously been implicated as a primary cause of the massive thrombosis encountered with the standard model (Björk and Henze, 1975; Yoganathan, et al., 1978b). From studies of recovered standard models, Björk and coworkers (Björk and Henze, 1975; Björk and Henze, 1979) concluded that the formation of thrombus on this valve probably starts downstream from the two pivot points between the disc and base-ring. By correlating *in vitro* velocity results with clinical findings, Yoganathan, et al. (1978b) were able to suggest further that the large stagnant zone immediately downstream from the disc occluder contributed to thrombus formation. Therefore, to minimize or eliminate these stagnant zones, a convexo-concave occluding disc was introduced with its pivoting point moved 2.5 mm downstream.

Preliminary results with this new occluder configuration have indicated that the incidence of thromboembolic problems has decreased by 50% (Björk and Henze, 1979). Yoganathan, et al. (1980), studying the two models of this prosthesis in the same experimental rig, have reported that the design changes were indeed successful in decreasing the size of the stagnant zone immediately downstream from the disc occluder. Thus it appears that the redesign of the

valve has been beneficial with respect to further reducing associated thromboembolic events, but, as Björk concludes, longer follow-up periods are necessary before any definite conclusions can be made.

The redesigned occluding mechanism also divides forward flow more evenly. Åberg and Henze (1979) found that in the former model only about 23% of the forward flow passed through the smaller (minor) outflow region whereas, for the convexo-concave model, about 30% of the flow passed through the minor outflow region. Measured velocities in the two outflow regions also indicate that a larger portion of the flow passes through the minor region for the convexo-concave model as compared to the standard model (Yoganathan, et al., 1980; Schramm, et al., 1980; Schramm, et al., 1982). The maximum velocity in the minor outflow region has increased for the new model while that in the major outflow region has decreased.

The latest modifications of this prosthesis, however, may have compromised its favorable hydrodynamic performance. First, the convexo-concave model has been reported to allow significantly more flow regurgitation than the standard model. Though Åberg and Henze (1979) reported that regurgitation through the *closed* convexo-concave model was "slightly but definitely lower" than that through the standard model, Gabbay, et al. (1980) found that the convexo-concave model allowed more flow regurgitation for *pulsatile-flow* tests wherein closure flow was included. Second, the structure of the flow generated by the prosthesis also appears to have been adversely affected by the changes to this valve. Using LDA, Bruss, et al. (1983) measured velocities in the near vicinity of the two models and concluded that the curvature of the convexo-concave disc caused a larger deflection of the forward flow and therefore generated an enlarged wake. Yoganathan, et al. (1980) had earlier made note of this large deflection of the flow towards the wall of the ascending aorta. They reported

high wall shear stresses where the deflected flow impinged on the aortic wall and therefore recommended that the valve be implanted so that the deflected flow is directed towards the non-coronary sinus. Finally, the pressure drops across the two models have been reported as similar for similar valve sizes (Björk and Henze, 1979; Gabbay, et al., 1980; Schramm, et al., 1980; Yoganathan, et al., 1980). Thus, compared to the standard model, the new model may allow larger flow regurgitation and may generate larger flow disturbances and shear stresses at the wall of the aorta without providing a significant improvement in pressure drop characteristics. As Gabbay, et al. (1980) concluded, the redesign of this valve may have degraded its hydrodynamic performance somewhat to achieve a reduction in the "relatively rare complication" of thromboembolism.

In the present investigation, the flow structure downstream for the Björk-Shiley convexo-concave valve was found to be very acentric. The axial flow structure was comprised of a large axial jet with a lenticularly shaped cross section, a small axial jet with a roughly circular cross section, and one or more low-velocity regions interspersed among the two jets. The secondary-flow structure was comprised of two vortices. These vortices were positioned and oriented such that the large jet was shown to be "spreading out" along the tube wall and the small jet was shown to be moving towards the centerline of the tube.

The pressure-drop characteristics of this valve were adversely affected by the wake generated downstream from the disc occluder. The acentricity of the flow indicates that the disc occluder of this valve significantly redirected the forward flow so that a relatively large wake was generated behind the occluder. It was this wake which was responsible for the region of low velocity found between the large and small jets. In a wake pressure losses are not recovered (Streeter and Wiley, 1975). Hence the presence and extent of the wake downstream from the

Björk-Shiley convexo-concave valve contributed to this valve's pressure drop. Efforts to improve the pressure-drop characteristics of this valve therefore should minimize the extent of the wake generated by the occluding mechanism, a criterion which was not entirely adhered to when the convexo-concave disc was designed.

The acentricity of the flow generated very large shear stresses at the tube wall. These large stresses were found to be present over more than half of the circumference of the tube cross section. The major source of the large shear stresses was the very high mean velocity gradients generated by the large axial jet. Total shear stresses were estimated to be greater than 100 N/m^2 along much of the tube wall.

The magnitudes of the estimated total shear stresses were large enough to activate platelets, causing a chemical release reaction. As shown in Table 1 of Chapter 1, platelets were shown to undergo chemical release reactions at shear stresses around 20 N/m^2. The total shear stresses estimated in the present investigation were probably *not* sufficient to cause damage to platelets.

The magnitudes of the estimated total shear stresses were large enough to possibly damage red blood cells. As discussed in Chapter 1 and shown in Table 1, shear stresses on the order of 150 N/m^2 to 300 N/m^2 were found to be sufficient to cause hemolysis. The acentricity of the flow, thus, may cause elevated levels of hemolysis to be associated with this valve *in vivo*.

Very little information is available, however, on the hemolytic characteristics of the convexo-concave model of the Björk-Shiley prosthesis. The standard model has been shown by several investigators (Slater, et al., 1974; Sallam, et al., 1976; Santinga, et al., 1976; Falk, et al., 1979; Dale, et al., 1980; Febres-Roman, et al., 1980) to have the desirable trait of causing only slight amounts of

intravascular hemolysis. The convexo-concave model, however, has been shown (Alchas, et al., 1980; Phillips, et al., 1980; Schramm, et al., 1980; Yoganathan, et al., 1980; Bruss, et al., 1983) to generate larger mean velocity gradients at the wall of the tube modeling the ascending aorta than the standard model. In the present investigation, these high mean velocity gradients have been shown to be present over more than half of the circumference of the tube cross section. Thus intravascular hemolysis associated with the convexo-concave model may be greater than that associated with the standard model.

The moderate rms axial velocities across the tube cross section found in the present investigation indicate that relatively little hemolysis would be generated by this valve in the bulk flow from turbulent shear stresses. The total shear stresses estimated in the bulk flow away from the tube wall were generally below about 50 N/m^2. This level of shear stress would probably not be sufficient to cause significant hemolysis. Sub-lethal damage to the RBC may occur at these shear stress levels but the effect of such damage is difficult to quantitate *a priori*.

The acentricity of the flow also generated a region of low velocities near the tube wall. This low-velocity region was oriented azimuthally to correspond roughly with that orientation of the minor outflow region. The mean velocity gradient at the wall near this region was relatively small. Thus the shear stress at the wall near this region was also relatively small and the region was not "flushed out" as much as it would have been otherwise. The flow in this region was, therefore, potentially thrombogenetic in nature.

The velocity results of the present investigation are more extensive yet consistent with the results presented in previous investigations. The large and small jet structures and the low-velocity regions generated by the Björk-Shiley convexo-concave valve have both been previously reported.

Previous investigators (Alchas, et al., 1980; Phillips, et al., 1980; Schramm, et al., 1980; Yoganathan, et al., 1980; Bruss, et al., 1983) have measured velocities at axial locations near that used in the present investigation and also nearer to the valve. These investigators measured velocities at one or two profiles across their flow sections and have all reported acentric flow structure downstream from this valve. For velocities measured close to the valve superstructure at $z \approx 15$ mm two distinct maxima in the velocity profiles have been reported (Alchas, et al., 1980; Phillips, et al., 1980; Yoganathan, et al., 1980; Bruss, et al., 1983). The locations of these maxima have corresponded well with one of the two outflow regions of this valve which was immediately upstream from where the data were taken. The maximum corresponding to the location of the major outflow region was generally somewhat larger in magnitude than that corresponding to the minor outflow region. The maxima reported by Bruss, et al. (1980) at $z = 17.5$ mm were similar in magnitude. Very close to the valve structure at $z = 3$ mm, Yoganathan, et al. (1980) reported a greater maximum corresponding to the minor outflow region than that corresponding to the major outflow region. Farther from the valve at $z \approx 30$ mm, the maximum in the velocity profile corresponding to the major outflow region was much larger than that corresponding to the minor outflow region (Alchas, et al., 1980; Phillips, et al., 1980). Also, the maximum which corresponded to the minor outflow region was found to be closer to the centerline of the flow channel at $z \approx 30$ mm than at $z \approx 15$ mm.

The flow-visualization studies of Alchas, et al. (1980) and Schramm, et al. (1980) agree qualitatively with the measured-velocity results discussed above. In these flow-visualization studies, a large axial jet of fluid can be seen to emerge from the major outflow region of the valve and persist for more than 40 mm downstream. A small axial jet of fluid can be seen emerging from the

minor outflow region. The smaller jet was directed towards the centerline of the tube and was largely attenuated before it reached a downstream distance of about 20 mm.

Previous investigations have failed to find that such a large azimuthal extent of the tube wall was exposed to highly elevated shear stresses. This failure to determine the shape of the jet was because of limitations in the methods by which the results were obtained. In particular, there has been a lack of a systematic, data-plane type approaches to the data collection. No information has been presented previously, therefore, which would allow an analysis of the three-dimensional aspects and extent of the large and small axial jets and the low-velocity regions.

No direct measurements of the turbulent shear stresses downstream from the Björk-Shiley convexo-concave valve have been reported in the literature. Thus comparisons can not be made of the turbulent shear stresses estimated in the present investigation with directly measured values. Comparisons made for other valve designs studied in the present investigation, however, show that the estimated turbulent shear stresses of the present investigation are comparable with those measured directly by other investigators. The other valve designs for which comparative results have been available include the Ionescu-Shiley and St. Jude valves. For these two valves, the average rms axial velocities measured in the present investigation were higher and lower, respectively, than that for the Björk-Shiley convexo-concave valve. Therefore, since the estimated turbulent shear stresses for the Ionescu-Shiley and St. Jude valves were comparable to directly measured turbulent shear stresses, the same can be expected for the Björk-Shiley convexo-concave valve.

3.4.4.3 Steady Versus Pulsatile Flow

The pulsatile-flow results presented in Figures 34 through 41 show that the systolic ejection interval could be divided into three phases. Windows 4 through 9 were taken as encompassing early systole, windows 10 through 16 were taken as encompassing mid-systole, and windows 17 through 20 were taken as encompassing late systole. The flow during early systole was characterized by flat axial velocity profiles, small non-axial velocities, and relatively low rms axial velocities. The flow during mid-systole was similar to that found for steady flow. The flow during late systole was characterized by rapidly deceleration and eventual flow reversal, a general lack of secondary-flow structure, and elevated rms axial velocities. The results thus indicate again, as for the case of the Ionescu-Shiley valve, that the results for early and mid-systole can be approximated *a priori*. Late systole would be difficult to approximate *a priori*.

The pulsatile-flow results were less distinct than the steady-flow results. These differences can be attributed to the relative amount of data available from the pulsatile-flow experiments and the reproducibility of the flow from one cycle to the next. The reproducibility of the pulse-duplicator may have also contributed to the "raggedness" and "scatter" of the pulsatile flow results.

During diastole the flow structure was affected by the fact that the occluding mechanism of the Björk-Shiley convexo-concave valve allowed a controlled amount of flow regurgitation. As shown in Figures 34, 36, and 38, the mean velocities in the flow after valve closure decreased rapidly but did not vanish entirely. Small, negative mean velocities were present throughout diastole. The mean non-axial velocities shown in Figure 40 did not show a tendency to vanish during diastole either. These finite velocities resulted from the small area available for reverse flow through the fully closed valve and the diastolic pressure gradient which provided the driving force for flow.

The flow at the beginning of each cycle thus was not entirely quiescent. During a pulsatile-flow experiment, therefore, the results for a given cycle were based on the flow generated by the previous cycle at the end of diastole and not on a perfectly quiescent fluid.

The amount of regurgitant flow during diastole was determined both with the electromagnetic flowmeter and using the mean axial velocity results. The regurgitant-flow rate results from the flowmeter were given in Table 7. The regurgitant-flow rate results from the mean axial velocity results were given in Figure 44. As discussed earlier, however, the results in Table 7 and Figure 44 required adjustment to remove the effects of flowmeter drift and data biasing. Once these effects had been removed, the closure-flow and leakage-flow rates were calculated to be 2% and 15%, respectively, of the forward-flow rate. The total regurgitant-flow rate was 16% of the forward flow. The closure-flow and leakage-flow rate percentages do not sum to the total regurgitant flow rate because of round-off errors.

The percentage of regurgitant flow found for the present investigation was in the range of the percentages found in previous pulsatile-flow investigations (Gombrich, et al. 1979; Dellsperger, et al. 1983). Gombrich, et al. (1979) measured flow regurgitation for a Björk-Shiley convexo-concave valve with a TAD of 27 mm. For a pulse rate of 72 beats per minute, a mean flow rate of 5.25 liters per minute, a ventricular pressure of 16.0 kPa, and a systemic resistance of 10.7 kPa, they found the total regurgitant flow to be 18% of the forward flow. Dellsperger, et al. (1983) also measured flow regurgitation for a Björk-Shiley convexo-concave valve with a TAD of 27 mm. For a pulse rate of 80 beats per minute, a mean flow rate of 6 liters per minute, and an average aortic pressure of 13.3 kPa, they found the total regurgitant flow to be 12.0% of the forward flow. The area available for flow back through the closed valve

would in general be smaller for a Björk-Shiley convexo-concave valve with a TAD of 25 mm than for a TAD of 27 mm. The orifice diameters of this prosthesis with a TAD of 25 mm and 27 mm are 20.0 mm and 22.0 mm, respectively. Assuming the same clearance between the edge of the disc occluder and the inside aspect of the valve base-ring for the two sizes of valves, and assuming the clearance distance small relative to the base-ring radius, the ratio of the areas would be approximately the ratio of the base-ring radii (or diameters). These two assumptions were valid for the size 25 and 27 prostheses considered here. The area available for regurgitant flow for the size 25 prosthesis was thus only about 10% less than that for the size 27 prosthesis. The regurgitant flow for the size 25 prosthesis would probably not be significantly less than that for the size 27 prosthesis. Åberg, et al. (1979) compared the amount of steady flow through different sizes of closed Björk-Shiley convexo-concave valves as a function of the pressure-drop driving force. They found that for the range of diastolic pressure drops found *in vivo*, the amount of flow through a closed size 27 prosthesis was about 5% of that through a closed size 25 prosthesis. Therefore, the regurgitant flow found for the size 25 prosthesis of the present investigation was consistent with that found by previous investigators for the size 27 prosthesis.

A further comparison of the results for steady flow with those for pulsatile flow can be made from the results shown in Figure 44. The flow-rate results in Figure 44 show that the flow rate during the middle of systole was comparable to that for steady flow. The pulsatile-flow results were within 10% of the steady-flow result over much of mid-systole.

The average rms axial velocities plotted in the bottom of Figure 44 clearly show that the magnitude of the fluctuating velocities was dependent upon the systolic phase. During early systole, the average rms axial velocities were not very different from that for windows during diastole. During mid-systole, the

average rms axial velocities went through a well-defined maximum and began to decrease before late systole. During late systole, the rms axial velocities dropped but overall remained elevated. A small "shoulder" can be seen at window 20 when maximum reverse flow occurred.

The average rms axial velocities plotted in Figure 44 also show that the rms axial velocities measured in steady flow were generally larger than those found in pulsatile flow. Thus, the rms velocities for steady flow tended to be an upper bound on the rms velocities for pulsatile flow.

For the Björk-Shiley convexo-concave valve, the maximum average rms axial velocity was measured two windows after the maximum flow rate. This two-window delay is consistent with the calculation made earlier which suggested that the flow disturbance measured at the data plane was generated at the valve and convected to the data plane.

The average rms axial velocities plotted in the bottom of Figure 44 seem to have a base-line value near 5 cm/s. This base line is similar to that seen for the Ionescu-Shiley valve and probably also stems from the "cascading" energy from the mean velocity field during diastole.

3.4.5 Conclusions

The flow structure generated by the Björk-Shiley convexo-concave valve was quite unlike that found for the empty flow section. This valve was shown to generate a very acentric flow structure consisting of a large, lenticularly shaped jet near the tube wall and a second, smaller jet near the centerline of the tube. These two jets were shown to have emerged from the major and minor outflow regions, respectively. A region of low velocities was also found which corresponded with the minor outflow region and may indicate that the flow in that region was nearly stagnant and hence thrombogenetic. Also, well-defined

secondary-flow structures were found which may have played a role in generating the lenticularly shaped large jet and the central location of the smaller jet.

The largely acentric flow contained a large wake generated behind the disc occluder which adversely affected the valve's pressure-drop characteristics. The pressure-drop results for this prosthesis were found to be somewhat higher than that found by others.

The acentricity of the flow caused high mean velocity gradients at the wall around much of the tube cross section. The high velocity gradients implied high shear stresses. These high shear stresses were of such a magnitude that they may cause elevated levels of hemolysis to be associated with this valve *in vivo*. Shear stresses in the bulk flow were only moderate in magnitude and were less than the level generally considered hemolytic. Sub-lethal damage of RBCs, however, may occur in the bulk flow. The estimated total shear stresses were sufficient to activate platelets and cause a chemical release reaction. The presence in the flow of activated platelets increases the possibility of thrombus formation and hence valve thrombosis and thromboembolic events.

The low to moderate pressure-drop characteristics of the Björk-Shiley convexo-concave valve were coupled with moderate flow-regurgitation characteristics. Thus the hemodynamics of this valve were not as optimal as are usually attributed to a semi-central tilting-disc valve design.

A comparison of steady-flow and pulsatile-flow results showed that i) the steady-flow results approximated those for pulsatile flow only during the middle of systole and ii) the rms velocities for steady flow provided an upper bound to those found in pulsatile flow. The results indicated that the systolic ejection interval could be divided into three phases: early systole, mid-systole, and late

systole. For each phase of systole the flow structure was significantly different. The flow structure of mid-systole was most similar to that for steady flow. The steady-flow results were quite different from those for pulsatile flow during early and late systole. It was found that early systole could be estimated *a priori* as plug flow. Late systole would be difficult to predict *a priori*. Pulsatile-flow results in diastole were found to have structure which were not predictable from the steady-flow results. The results from the steady-flow experiments, therefore, were limited in their ability to provide an understanding of the pulsatile flow. It was concluded that steady flow results can provide some knowledge of the flow fields downstream from the Björk-Shiley convexo-concave valve but only for a relatively small portion of systole.

3.5 SMELOFF PROSTHESIS

3.5.1 Introduction

The Smeloff prosthesis has been in clinical use since 1966 without modification. This lateral-flow ball-check valve is shown in the top of Figure 5b. When introduced, this valve was a variation on the simple ball-check designs of previous prostheses (Cartwright, et al., 1964; Smeloff, et al., 1966). Features of the Smeloff valve are its open-end downstream cage and its full-orifice design. When the Smeloff valve is open, its ball occluder is restrained by a three-pronged, open-end cage. The open-end design of the downstream cage was incorporated to eliminate cage structure in the region of flow stasis downstream from the ball occluder during forward flow. The length of the downstream cages for each valve size has been carefully worked out so that the area available for flow in the open position between the ball occluder and the downstream face of the valve base-ring is equal to the area available for flow through the base-ring orifice (Cartwright, et al, 1964; Davey and Smeloff, 1977). When the Smeloff valve is closed, its ball occluder is restrained by a smaller three-pronged, open-end cage. In the full-orifice design, the ball occluder of the closed Smeloff valve rests on the smaller cage such that the ball's equator is level with the valve's base-ring orifice. Thus the smallest possible ball occluder is used with the largest possible base-ring orifice. The full-orifice design allows a measure of regurgitant flow. This controlled regurgitation is thought to "wash" the valve base-ring and upstream cage free of adherent material which could become thrombogenetic.

The features of the Smeloff valve designed to minimize thromboembolic complications have been successful to a degree. Clinically, thromboembolic rates reported for well anticoagulated patients with a Smeloff valve have been relatively small (Bloodwell, et al., 1969; Smeloff, 1974; Brawley, et al., 1975; Sarma, et al., 1977).

The features of the Smeloff valve designed to optimize its hemodynamic performance have not been as successful. Despite its optimally small ball occluder and optimally large base-ring orifice, this valve creates one of the largest pressure drops of the prostheses currently available (Yoganathan, et al., 1979b). Some of this large pressure drop is probably related to the large wake generated downstream from the ball occluder in forward flow (Yoganathan, 1978). The full-orifice design has also been reported to allow significant of flow regurgitation (Suobank, 1983).

In the present investigation, a Smeloff prosthesis with a TAD of 25 mm was studied *in vitro* in both steady and pulsatile flow regimes. Pressure and volumetric-flow data were collected to insure that the pressure and flow fields encountered by the valve in the experimental rig were similar to that which the valve might encounter when implanted in a patient. For pulsatile flow, the pulse-duplicator was operated at pressures and flows found *in vivo* in a resting state, i.e., as might be measured in the catheterization laboratory. After establishing these pressure and flow fields, the assessment of the *in vitro* states was extended to i) an extensive evaluation of the mean and rms velocities in the axial and non-axial directions across a data plane downstream from the mounted prosthesis, ii) the estimation of the total shear stresses at the data plane from the rms velocity results, iii) the estimation of the total regurgitant flow associated with this prosthesis to be used in comparison with other valves studied, and iv) the comparison of steady and pulsatile flow results to give insights into the relevance of steady-flow analyses of flow fields downstream from prosthetic valves.

This extensive analysis was primarily undertaken to gain a better insight into the structure of the flow downstream from the Smeloff prosthesis. It was expected that this extensive analysis would allow more definitive comments

regarding the hydrodynamic performance of this improved, semi-central flow valve prosthesis. In particular, the magnitude and extent of the wakes generated downstream from this valve were to be interpreted in light of the moderate pressure drop found for this valve. Detailed estimations of shear stresses was undertaken in the hope that better correlation between *in vitro* results and *in vivo* levels of hemolysis could be achieved.

3.5.2 Methodology and Apparatus

The experimental methodology and apparatus used to obtain the results for the Smeloff valve were those discussed in detail in Chapter 2.

3.5.3 Results

3.5.3.1 Pressure and Volumetric-Flow Results

The pressure and volumetric-flow results for the Smeloff valve were computed during each experiment in the same fashion as for the Ionescu-Shiley valve. These two sets of results are presented in Tables 8 and 9, respectively.

3.5.3.2 Velocity Results

The velocity results are presented for steady and pulsatile flow in the same fashion as for the Ionescu-Shiley valve. No data were collected for the Smeloff valve at data-plane locations other than at z = 31.8 mm. The temporal locations of the pulsatile-flow windows for the Smeloff valve are shown in Figure 45. For the Smeloff valve, pulsatile-flow windows 4 through 20 encompassed the systolic ejection interval. The diastolic interval thus extended from windows 20 through 43 and then up to window 3 of the next cycle. Window 8 corresponded to the time when the flow experienced maximum acceleration, window 13 corresponded to the time of maximum forward flow, window 17 to the time when the flow

Table 8

Parameters Computed from the Pressure Data for the Smeloff (24 mm) Prosthesis*

	Pressure (kPa)	Relative time** of occurrence in the cycle (ms)
Pulsatile Flow:		
ΔP_{max}	3.3 ± 0.3	160 ± 12
VP_{max}	18.4 ± 0.5 +	182 ± 10
P_{x1}	11.7 ± 0.8 +	0 ± 7
P_{x2}	10.5 ± 0.9 +	282 ± 8
$\left(\frac{dP}{dt}\right)_{max}$	178 ± 7 (kPa/s)	-30 ± 6
$\left(\frac{dP}{dt}\right)_{min}$	-254 ± 26 (kPa/s)	335 ± 7
$\overline{\Delta P}_{sys}$	1.3 ± 0.2	-
$\overline{\Delta P}_{dias}$	9.3 ± 0.4	-
$\overline{\Delta P}$	10.3 ± 0.4 +	-
Steady Flow:		
$\overline{\Delta P}$	2.2 ± 0.1	-

*Results given as mean ± standard deviation.

**Relative to the beginning of systolic ejection.

+Gauge pressure.

Table 9

Parameters Computed from the Volumetric-Flow Data for the Smeloff (24 mm) Prosthesis*

	Flow (L/min)	Relative time** of occurrence in the cycle (ms)
Pulsatile Flow:		
Q_{max}	30.4 ± 0.4	186 ± 8
Q_{min}	-7.8 ± 1.0	326 ± 5
Q_{beg}	0.0 (by def.)	-15 ± 6
Q_{end}	0.0 (by def.)	305 ± 4
Q_F	6.65 ± 0.09	-
Q_C	-0.09 ± 0.04	-
Q_L	-1.55 ± 0.10	-
Q_{rms}	21.0 ± 0.1	-
Steady Flow:		
$\bar{Q}$	27 (rotameter)	-

*Results given as mean ± standard deviation.

**Relative to the beginning of systolic ejection.

SMELOFF (24 mm)

KEY TO WINDOW LOCATIONS

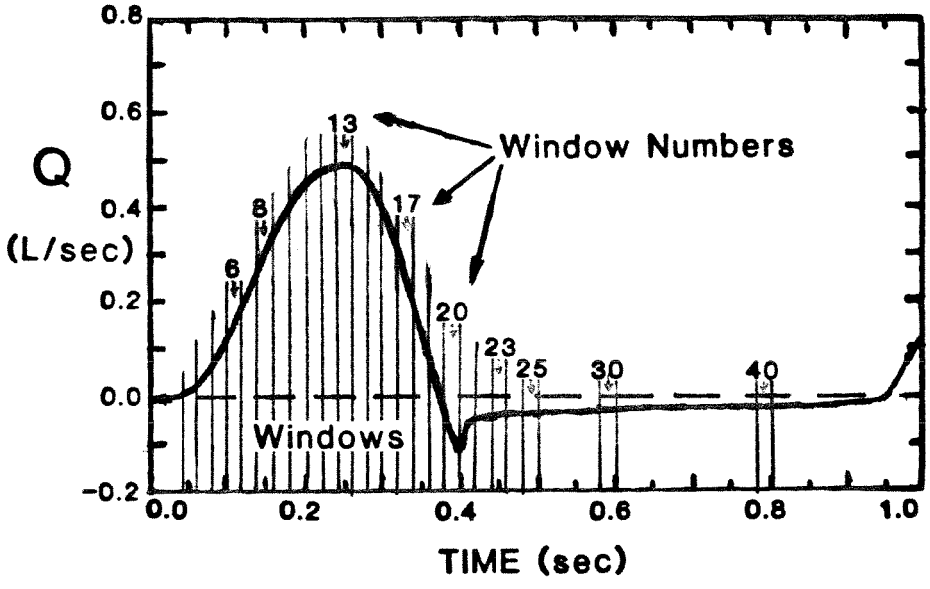

Figure 45. Idealized volumetric-flow curve showing temporal location of pulsatile-flow windows 6 through 25, 30, and 40 for the Smeloff (24 mm) prosthesis.

experienced maximum deceleration, and window 20 to the time of maximum reverse flow.

Mean axial velocity results for pulsatile flow are presented in 3-D perspective in Figure 46. Results are shown for windows 6 through 23, 25, and 30.

Three maxima in the axial velocities can be seen in Figure 46 during much of the systolic ejection interval. These maxima appear to be located near the wall and distributed somewhat evenly around the tube cross section. A type of "saddle point" in the mean velocity contour was thus generated near the tube centerline. The maxima were distinct by window 10 and persisted for at least 150 milliseconds until window 17. No regions of flow separation are notable during the systolic ejection interval until the flow begins to reverse to close the valve. During diastole the axial velocities settled out.

Mean axial velocities are presented in Figure 47 for steady flow and for windows 8, 13, 17, and 20 of the pulsatile flow. For steady flow the three maxima were again evident. These steady-flow maxima, however, generate a less pronounced "saddle point" at the centerline of the tube. For pulsatile flow the flow structure at window 13 was similar to that for steady flow. Early in systole at window 8 the flow had an almost flat velocity profile across the data plane in all directions. A slight annular elevation is noticeable in the results with the highest velocities located near the tube wall. Late in systole at window 17 the maxima were still noticeable but had diminished significantly. By window 21, immediately preceding valve closure, the flow had fully reversed.

Mean axial velocities are presented in Figure 48 for windows 25, 30, and 40 of the pulsatile flow. These velocities show the settling out of the flow during diastole. Note that though both positive and negative velocities are shown in this figure, the integrated flow rate was negative. By window 40 the negative flow

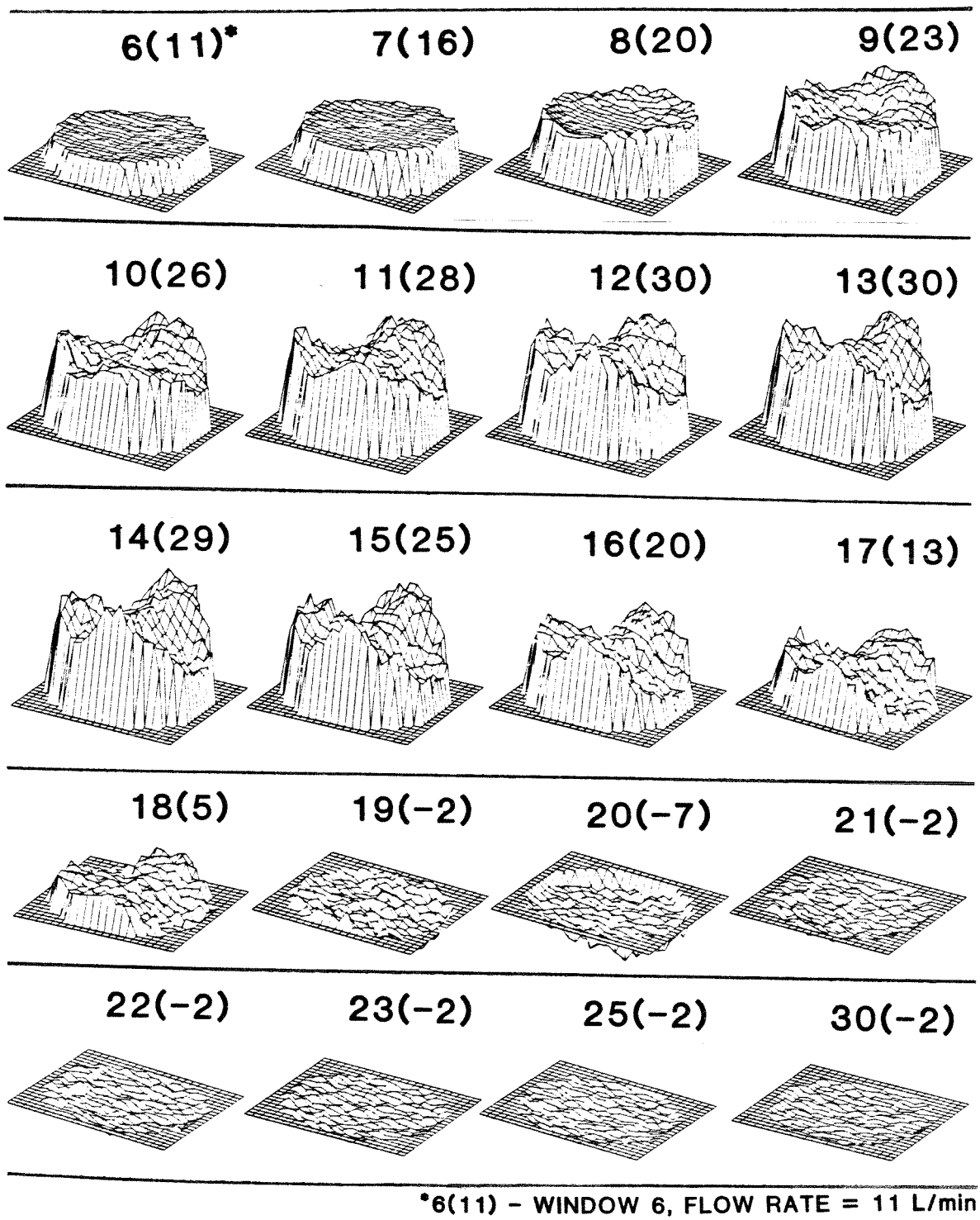

Figure 46. Mean axial velocities in 3-D perspective for pulsatile-flow windows 6 through 23, 25, and 30 downstream from the Smeloff (24 mm) prosthesis at z = 31.8 mm.

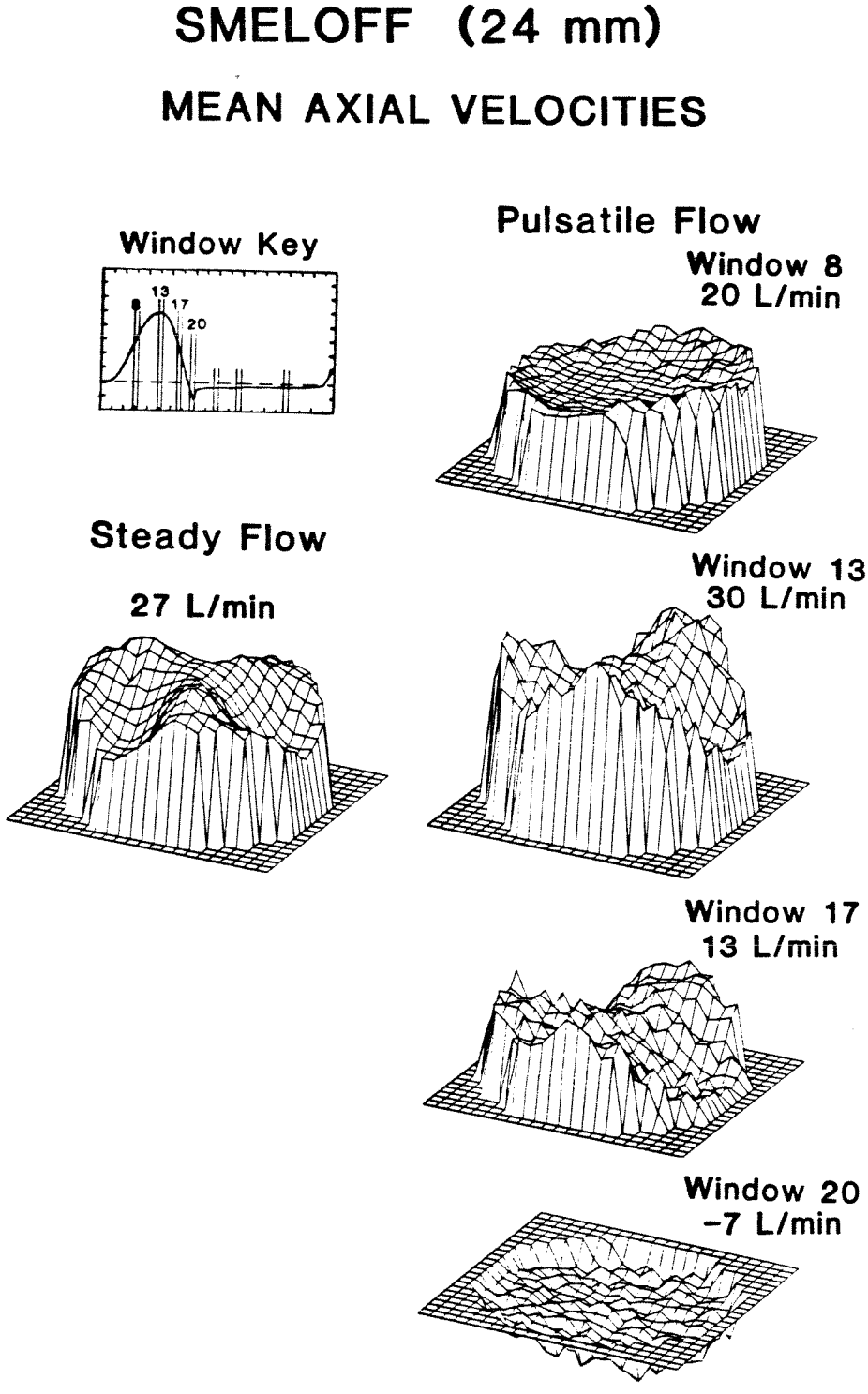

Figure 47. Mean axial velocities in 3-D perspective for steady flow and pulsatile-flow windows 8, 13, 17, and 20 downstream from the Smeloff (24 mm) prosthesis at z = 31.8 mm.

SMELOFF (24 mm)

MEAN AXIAL VELOCITIES

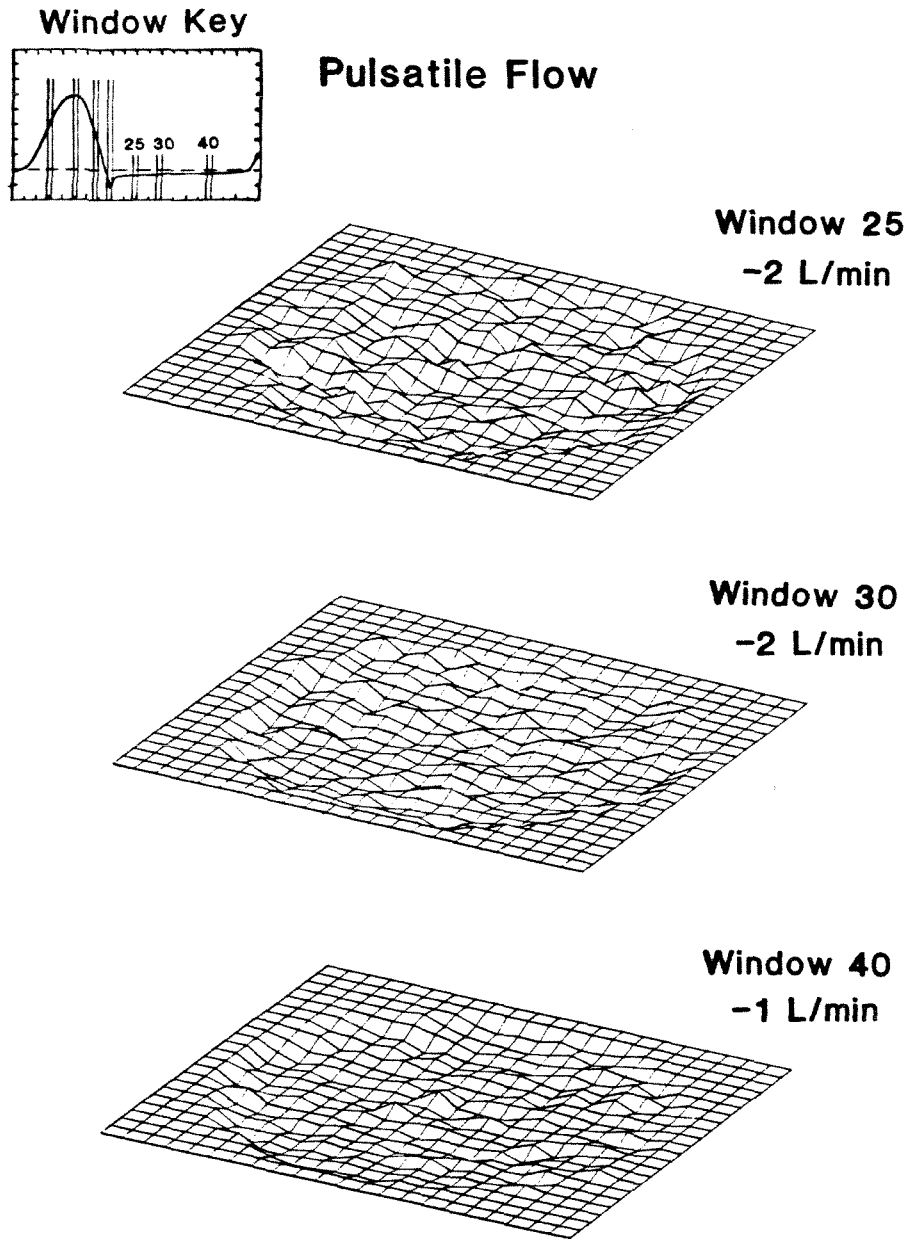

Figure 48. Mean axial velocities in 3-D perspective for pulsatile-flow windows 25, 30, and 40 downstream from the Smeloff (24 mm) prosthesis at z = 31.8 mm.

rate had dropped some in magnitude from -2 L/min to -1 L/min.

The mean axial velocities shown in Figure 47 for steady flow and for windows 8, 13, 17 of the pulsatile flow are presented more quantitatively as contours in Figure 49. The inset showing the valve orientation depicts the orientation of the valve superstructure relative to the structure of the velocity results.

From Figure 49 the magnitude and orientation of the three maxima can be more readily appreciated. For pulsatile flow, the maxima rose up beyond 120 cm/s for two maxima and 140 cm/s for the third. For steady flow, the magnitude of two of the maxima were such that they appear in Figure 49 to be 'ridges' extending out from the center of the tube towards the tube wall. Although these two maxima rose up beyond 100 cm/s, the maximum velocity at the tube centerline was also greater than 100 cm/s. The third maximum for steady flow rose up beyond 120 cm/s. The fluid was therefore found to be accelerated by a factor of about 1.2 and 1.4 for steady and pulsatile flow, respectively, from the maximum velocity of 105 cm/s for the flow upstream from the mounted valve. This factor was less than 1.1 for the flow through the empty flow section. The orientation of the results for steady and pulsatile flow was such that the low-velocity regions between the three maxima corresponded azimuthally with the orientation of the three downstream struts of the valve. These velocity-defect regions appear to be the result of wakes generated downstream from the struts. The three maxima therefore may have been generated by the confinement of the forward flow between two such wakes. Overall, the flow structure as shown in Figure 49 reflected the tri-symmetric aspect of the prosthesis.

The highest mean velocity gradients were generated near the tube wall. These velocity gradients were the greatest at the wall closest to the three maxima.

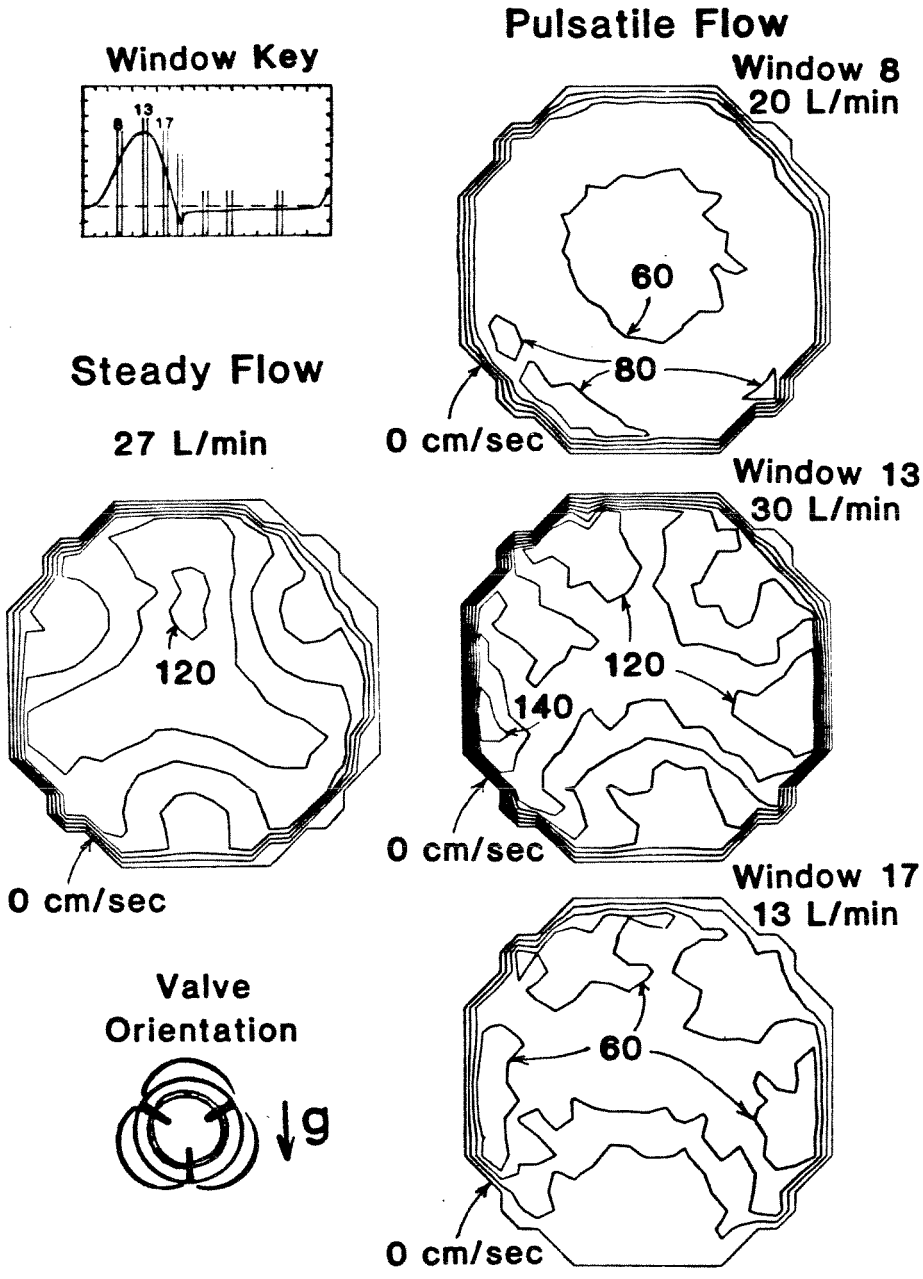

Figure 49. Mean axial velocities as contours for steady flow and pulsatile-flow windows 8, 13, and 17 downstream from the Smeloff (24 mm) prosthesis at z = 31.8 mm. Contour interval: 20 cm/s.

Detailed velocity measurements were not made near the wall but the maximum gradients at the wall appear to have been substantially larger than 500 s^{-1} near the three maxima and lower than 250 s^{-1} elsewhere.

The pulsatile-flow results showed less symmetry and were less distinct than those for steady flow. The three maxima for pulsatile flow were not as evenly distributed around the tube cross section as they were for steady flow. Early in systole at window 8 little flow structure was present. Slightly higher velocities were found around the perimeter of the tube with a minimum in the velocities near the tube centerline. Late in systole at window 17 diminished yet definite maxima were present. The magnitudes of the maxima shown for window 17 had fallen to about half their maximum value at window 13. The tri-symmetric shape of the results was still evident but less pronounced.

Mean axial velocities are presented in Figure 50 as contours for windows 25, 30, and 40 of the pulsatile flow. No mean axial velocities were measured greater than 20 cm/s in absolute value and hence only contours corresponding to zero velocity are plotted. During diastole very few positive mean axial velocities were found.

Mean non-axial velocities are presented in Figure 51 for steady flow and for windows 8, 13, and 17 of the pulsatile flow as resultants of the mean velocities in the x- and y-directions. For both steady and pulsatile flow, the mean non-axial results showed relatively small non-axial velocity components. Some secondary-flow structure is evident from the non-axial velocities near the tube wall but the magnitude of these structures was generally small. That is, overall the flow was mainly directed axially down the tube. For pulsatile flow, larger non-axial velocities were measured than for steady flow. These pulsatile-flow results, however, did not show significant flow structure.

SMELOFF (24 mm)

MEAN AXIAL VELOCITIES

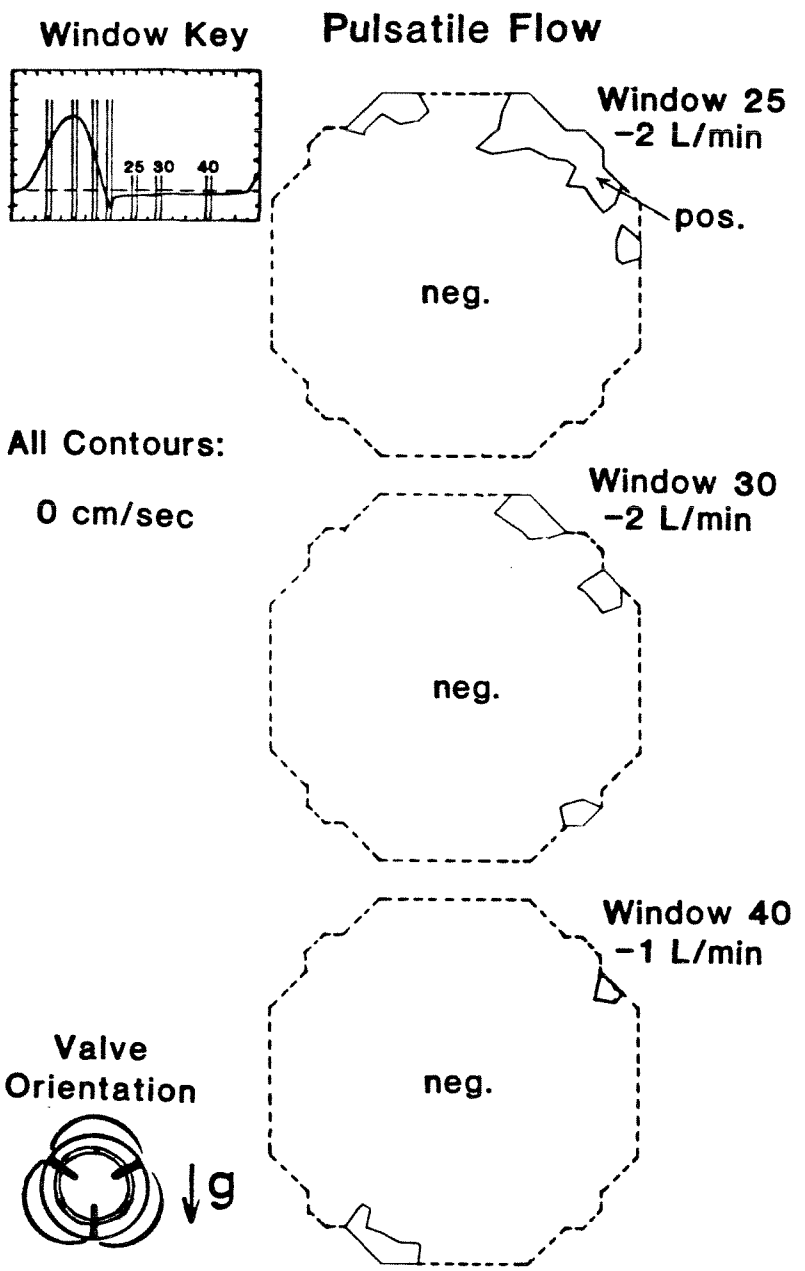

Figure 50. Mean axial velocities as contours for pulsatile-flow windows 25, 30, and 40 downstream from the Smeloff (24 mm) prosthesis at z = 31.8 mm. Contour interval: 20 cm/s.

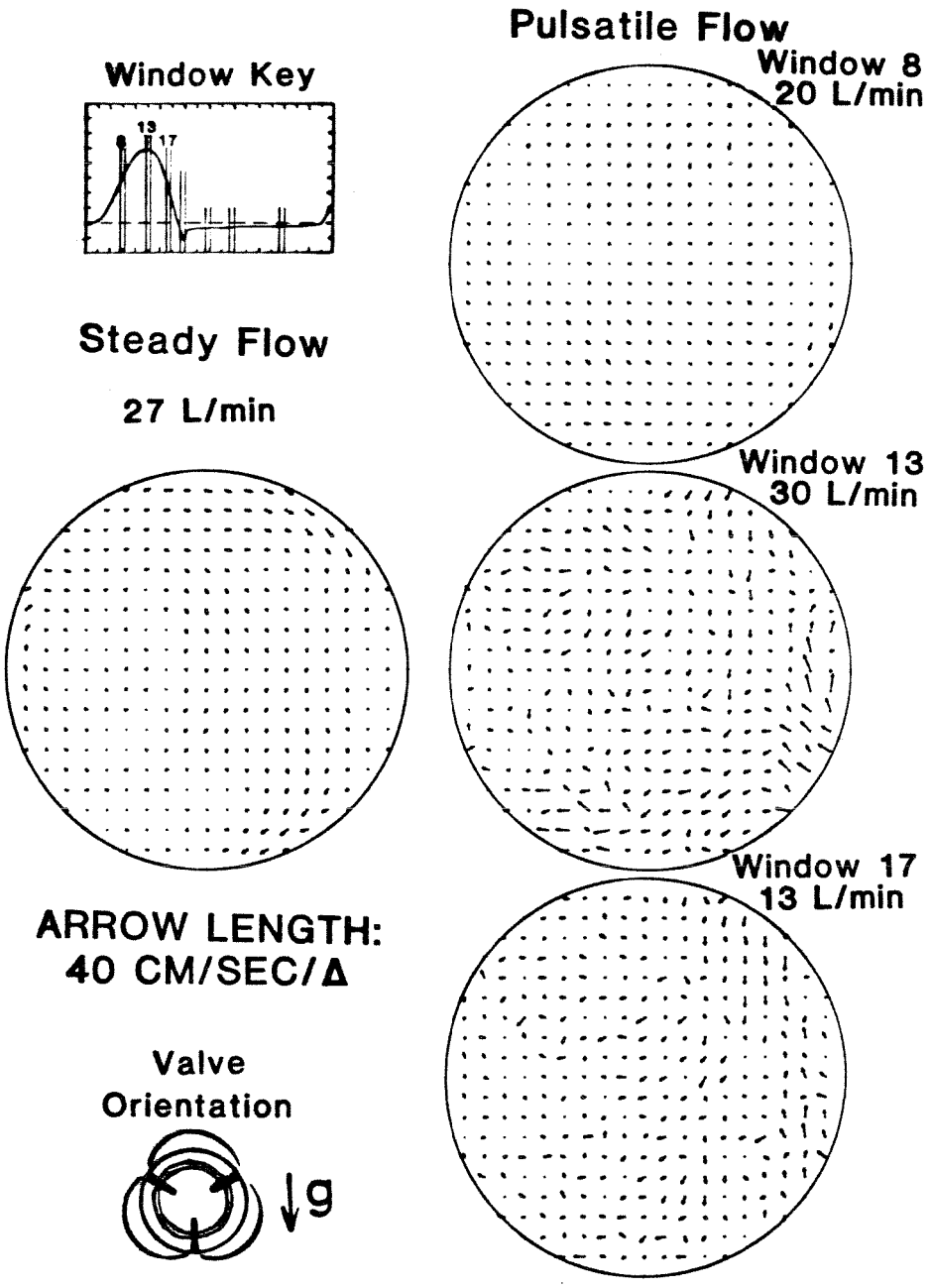

Figure 51. Mean non-axial velocities as resultants for steady flow and for pulsatile-flow windows 8, 13, and 17 downstream from the Smeloff (24 mm) prosthesis at z = 31.8 mm.

The maximum mean velocities in the radial and azimuthal directions were determined as resultants of the velocity components measured in the x- and y-directions. For steady flow, the maximum mean velocities in the radial and azimuthal directions were 7.5 ± 1.0 cm/s and 18.2 ± 1.0 cm/s, respectively. For pulsatile flow, these maximum velocities were 15.0 ± 1.0 cm/s and 37.6 ± 1.0 cm/s, respectively. These pulsatile-flow results were for window 13.

Mean non-axial velocities are presented as resultants in Figure 52 for windows 25, 30, and 40 of the pulsatile flow. Overall, only very small velocity components were observed throughout diastole. There was no appreciable flow structure notable from these diastolic results.

The rms axial velocities are presented in Figure 53 for steady flow and for windows 8, 13, and 17 of the pulsatile flow. For both steady and pulsatile flow, the rms axial velocities reflect the flow structure observed from the mean velocities. The highest rms axial velocities for steady flow and for window 13 of pulsatile flow were found to correspond spatially to the three maxima of the mean velocity results. The lowest rms axial velocities for steady flow and for window 13 of pulsatile flow were found to correspond spatially to the locations of the low-velocity regions of the mean axial velocity results. Generally, the rms axial velocities for steady flow were larger than those for window 13 of the pulsatile flow. The maximum rms axial velocities for steady and pulsatile flow were 39.5 ± 1.0 cm/s and 38.6 ± 1.0 cm/s, respectively. The average rms axial velocity across the data plane for steady flow was 30.8 ± 1.0 cm/s while that for pulsatile flow was 29.6 ± 1.0 cm/s. The pulsatile-flow results are for window 13. The rms axial velocities corresponded to an average turbulence intensity across the data plane of 30% for window 13 of pulsatile flow and 36% for steady flow. The maximum turbulence intensity at the data plane was 45% both for window 13 of pulsatile flow and for steady flow. Early in systole at window 8 the

SMELOFF (24 mm)

MEAN NON-AXIAL VELOCITIES

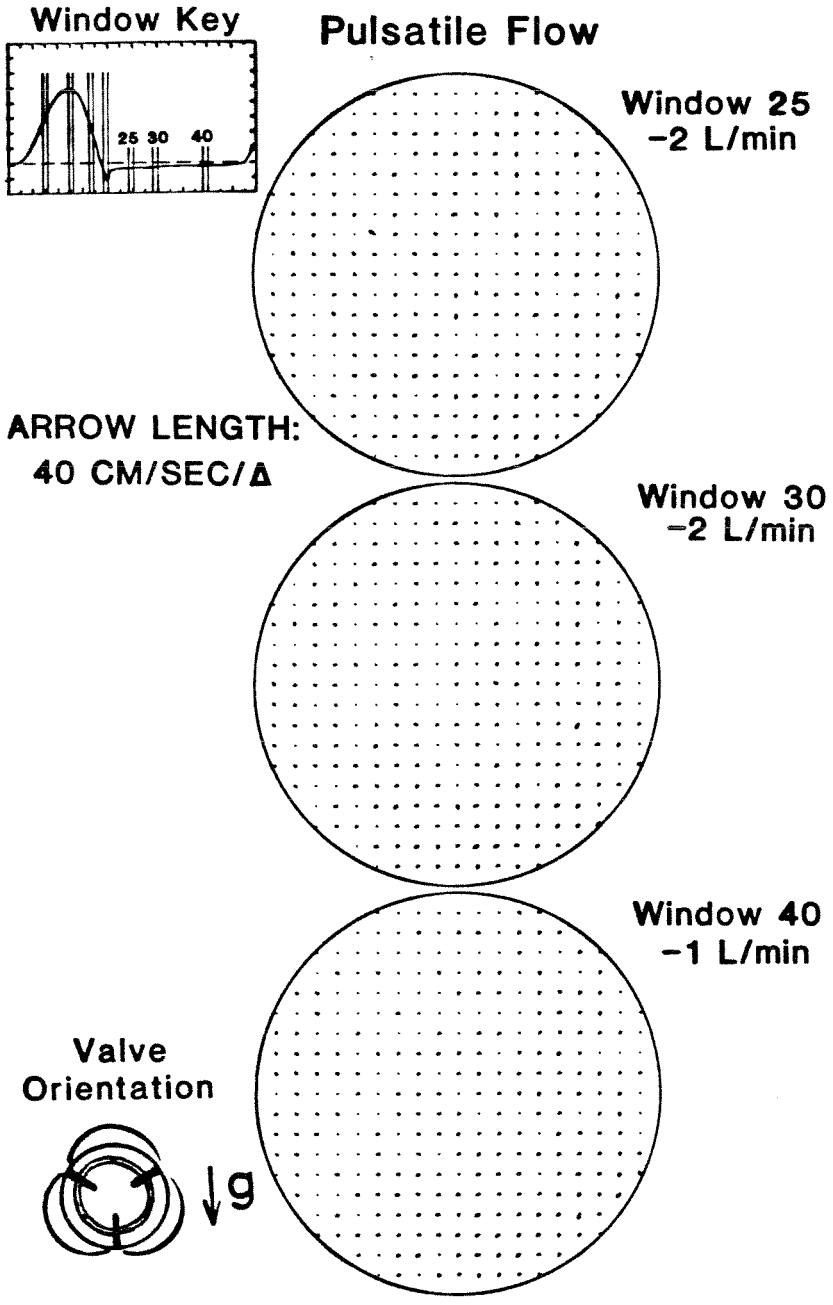

Figure 52. Mean non-axial velocities as resultants for pulsatile-flow windows 25, 30, and 40 downstream from the Smeloff (24 mm) prosthesis at z = 31.8 mm.

SMELOFF (24 mm)

RMS AXIAL VELOCITIES

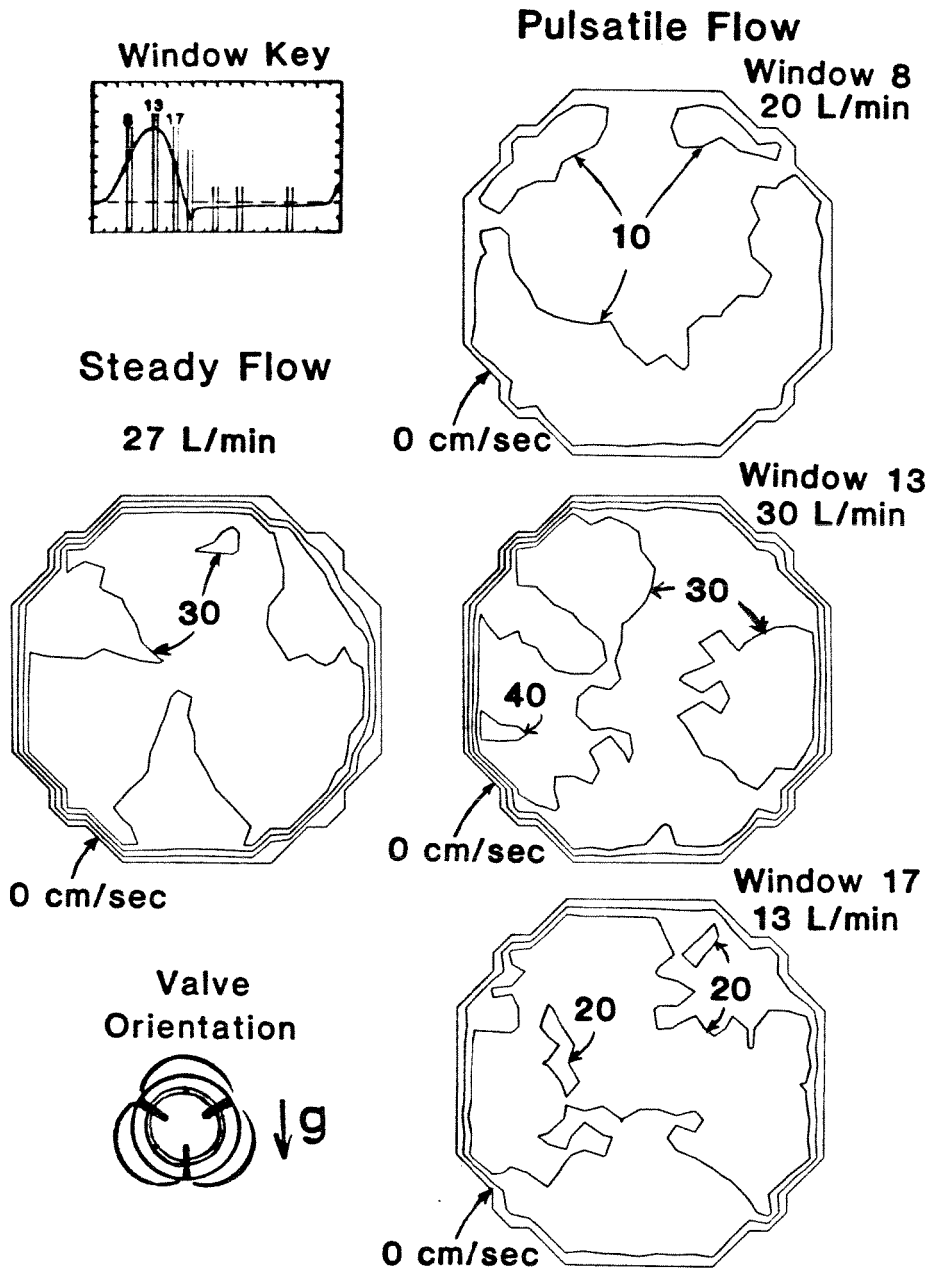

Figure 53. Root-mean-square (rms) axial velocities as contours for steady flow and pulsatile-flow windows 8, 13, and 17 downstream from the Smeloff (24 mm) prosthesis at z = 31.8 mm. Contour interval: 10 cm/s.

rms axial velocities were in comparison very low. The rms axial velocities were elevated somewhat in the annular region of window 8 which corresponded to the higher mean velocities. Late in systole at window 17 the rms axial velocities still remained elevated but were generally smaller than those found at window 13.

The total shear stresses estimated from the velocity data using Equation (11) are presented as contours in Figure 54 for the axial velocity in the x-direction. Ridges of elevated shear stresses are apparent in Figure 54 along the wall of the tube. The estimated total shear stresses were around 80 N/m^2 near the tube wall. In the bulk flow, the estimated total shear stresses were generally low averaging around 30 N/m^2. Early in systole at window 8, some small shear stresses are shown in near the tube wall. Late in systole at window 17, the shear stresses at the wall had dropped considerably from those at window 13. The maximum shear stress shown for window 17 was similar to that for window 8 at about 40 N/m^2.

The maximum total shear stress which was present over at least 10% of the tube cross section was estimated. For steady flow, this maximum shear stress was estimated to be 78 $\pm$ 5 N/m^2. For pulsatile flow, this maximum shear stress was estimated to be 89 $\pm$ 5 N/m^2 at window 13.

Plots of the averaged flow rate and rms axial velocities versus the pulsatile-flow window number are given in Figure 55. The flow rates plotted were determined by averaging the mean axial velocities across the data plane. The average rms axial velocities plotted were determined by averaging the rms axial velocities across the data plane. The steady-flow results plotted in Figure 55 are plotted to correspond to the window that encompassed the maximum flow rate for pulsatile flow.

The flow-rate results in Figure 55 generally agree with those presented in

SMELOFF (24 mm)

TOTAL SHEAR STRESSES* (Z - X)

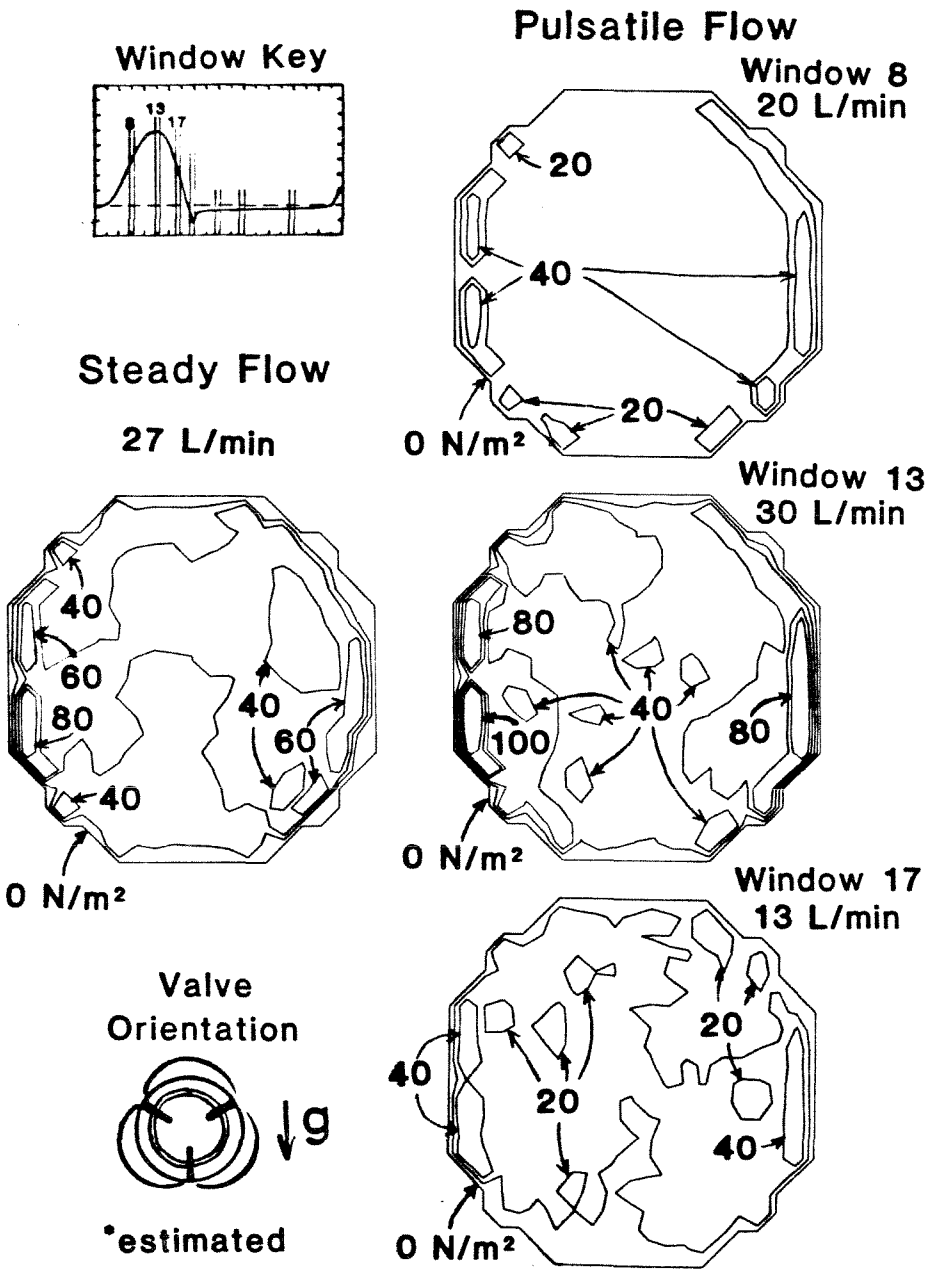

Figure 54. Total estimated shear stresses, τ_{zx}, as contours for steady flow and for pulsatile-flow windows 8, 13, and 17 downstream from the Smeloff (24 mm) prosthesis at z = 31.8 mm. Contour interval: 20 N/m^2.

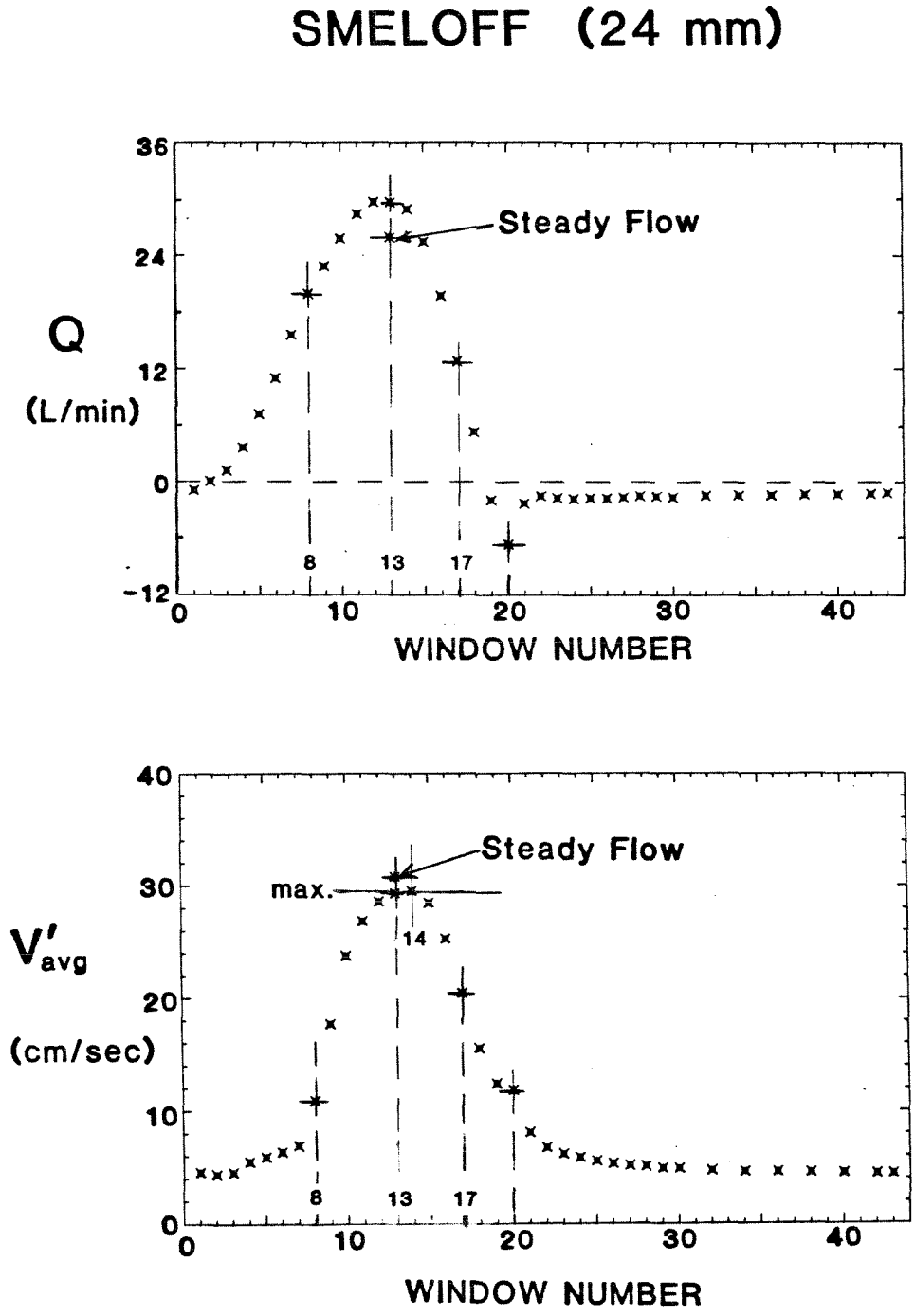

Figure 55. Volumetric-flow rate (top) and average rms velocity (bottom) calculated from the mean and rms velocities, respectively, at the data plane as a function of pulsatile-flow window number for the Smeloff (24 mm) prosthesis.

Table 9. The maximum and minimum flow rates from the velocity data were 30 L/min and -7 L/min, respectively. The corresponding values from Table 9 are 30.4 L/min and -7.8 L/min. The affect of the finite width of the pulsatile-flow window and variability in the timing from one cycle to another probably account for the small differences between these two sets of the maximum and minimum flow rates. Taking the beginning of the systolic ejection interval to be at window 4, the timing of the maximum and minimum flow rates also agree. The velocity data indicate that the maximum and minimum flow rates occurred about 180 and 320 milliseconds after the systolic ejection interval began, respectively. The corresponding values from Table 9 are 186 and 326 milliseconds, within the uncertainty of the width of the 20-millisecond windows.

The leakage-flow rate calculated from the results in Figure 55 differs significantly from that given in Table 9. From the results plotted in Figure 55, the leakage-flow rate was calculated as -0.9 L/min. The leakage-flow rate given in Table 9 is -1.55 ± 0.10 L/min. The forward-flow and closure-flow rates obtained from Figure 55 agree within experimental uncertainty with those reported in Table 9. The forward-flow rate obtained from Figure 55 is 6.7 L/min; that reported in Table 9 is 6.65 ± 0.09 L/min. The closure-flow rate obtained from Figure 55 is -0.1 L/min; that reported in Table 9 is -0.09 ± 0.04 L/min.

The discrepancy between the leakage-flow rate obtained from Figure 55 and that given in Table 9 probably was caused by drift of the electromagnetic flowmeter and biasing of the mean velocity results from the LDA. For the Ionescu-Shiley valve it was shown that during data collection the flowmeter drifted sufficiently to give a value of the leakage-flow rate that was low by about 0.1 L/min. For the Smeloff valve, this drift may have been as much as 0.2 L/min. For the Ionescu-Shiley valve it was also shown that the bias in the

mean velocity results obtained using the LDA was 0.2 L/min for the leakage-flow rate. The bias encountered with the Smeloff valve would most probably be similar to that for the Ionescu-Shiley valve. Subtracting out the bias of 0.2 L/min from the results for the Smeloff valve would give a forward-flow rate of 6.6 L/min and a leakage-flow rate of about -1.1 L/min. With the flowmeter drift and LDA biasing compensated for, the leakage-flow rates become -1.3 ± 0.1 L/min and -1.1 L/min from Table 9 and Figure 55, respectively. The forward-flow rates become 6.7 ± 0.1 L/min and 6.6 L/min, respectively. The closure-flow rates were not affected significantly. Using the forward-flow rate of 6.7 L/min, the closure-flow rate of 0.1 L/min, and the leakage-flow rate of 1.2 L/min, the percentage of regurgitant flow relative to the forward flow was about 19%.

The regurgitant flow for the Smeloff valve would, of course, be a function of the average gap between the valve's base-ring and the ball occluder. The valve used for the current investigation had an average gap width of 0.05 mm at the temperature of the pulsatile-flow experiments. This gap width was within the minimum specifications of the valve manufacturer for an acceptable match of the occluder to its valve.

Another difficulty with the results shown in the top of Figure 55 is that the flow rate at the end of diastole is shown to have risen before the apparent beginning of the systolic ejection phase. The finite flow rates shown in Figure 55 for late diastole are probably a result of the averaging process by which the results were obtained. This phenomenon was seen in the results for the Ionescu-Shiley valve and was again caused here by variations in the time the systolic ejection interval began.

3.5.4 Discussion

3.5.4.1 Discussion of the Pressure and Volumetric-Flow Results

The pressure and volumetric-flow results presented in Tables 8 and 9 indicate that the pressure and flow fields encountered by the mounted prosthesis in the pulse-duplicator were similar to those the valve might have encountered had it been implanted. The maximum rate of change of the ventricular pressure given in Table 8 of 178 ± 7 kPa/s compared well with that of a healthy human ventricle of about 195 ± 37 kPa/s (Yang, et al., 1978). Similarly, the minimum rate of change of the ventricular pressure given in Table 8 of -254 ± 26 kPa/s was not too different from that of a healthy human ventricle of about -355 ± 29 kPa/s (Yang, et al., 1978). For the volumetric-flow results, the forward flow, closure flow, and leakage flow given in Table 9 sum to a mean flow rate, or cardiac output (CO), of 5.01 L/min. This mean flow rate was about 7% below the standard setting of the pulse-duplicator of 5.4 L/min given in Table 2. As was shown above, however, the flow-rate results in Table 9 were subject to adjustment to remove the effects of flowmeter drift. Once adjusted, the flow-rate results in Table 9 become 6.7 L/min, -0.1 L/min, and -1.3 L/min for the forward-flow, closure-flow, and leakage-flow rates, respectively. The sum of these adjusted flow rates is 5.3 L/min which agrees within the experimental error of ± 0.1 L/min with the setting in Table 2. Q_{max} given in Table 9 as 30.4 L/min was physiological in magnitude. The timing results given in Tables 8 and 9 were physiologically appropriate. The systolic ejection interval spanned 33% of the cycle which is similar to that percentage found *in vivo* for a similar pulse rate and cardiac output. The forward-flow phase began and ended at times not significantly different from those of the systolic ejection interval. During systole, ΔP_{max} preceded both Q_{max} and VP_{max} by about 24 milliseconds. Though this difference was not significant, the order of the events was that observed

in vivo. The time of occurrence of $\left(\frac{dP}{dt}\right)_{max}$ was appropriately located in time during the iso-volumetric contraction phase and the time of occurrence of $\left(\frac{dP}{dt}\right)_{min}$ was appropriately located in time during the iso-volumetric relaxation phase. Q_{min} signaled valve closure appropriately by occurring after the end of the systolic ejection interval but before the occurrence of $\left(\frac{dP}{dt}\right)_{min}$ in the iso-volumetric relaxation phase.

The mean systolic pressure drop resulting from these pulsatile pressure and flow fields was within the range reported in the literature *in vitro* (Kaster, et al., 1970; Björk and Olin, 1970; Olin, 1970; Yoganathan, et al., 1979b). The peak systolic pressure drop resulting from these pulsatile pressure and flow fields was lower than the range reported in the literature. *In vitro* pressure-drop results for the Smeloff valve in pulsatile flow have been reported by Kaster, et al. (1970), Björk and Olin (1970), Olin (1971), and Yoganathan, et al. (1979b). Kaster, et al. (1970) operated their pulse-duplicator at 72 beats per minute at a mean flow rate of 5 L/min using a blood-analog fluid of 35% glycerine and 65% saline. With a systolic ejection interval one third of the cycle and a diastolic aortic pressure of 10.7 kPa (gauge), they found a peak systolic pressure drop of 4.2 kPa for a Smeloff valve with a TAD of 24 mm. Björk and Olin (1970) operated their pulse-duplicator at 70 beats per minute at a stroke volume of 0.070 liters per stroke using water as the test fluid. With a maximum aortic pressure of 16.7 kPa (gauge) and a diastolic aortic pressure of 10.0 kPa (gauge), they found a mean systolic pressure drop of 0.5 kPa for a Smeloff valve with a TAD of 24 mm. Olin (1971) operated his pulse-duplicator at 75 beats per minute at a stroke volume of 0.080 liters per stroke using a blood-analog fluid of 37% glycerine and 63% saline. With a systolic interval of 350 milliseconds, a

maximum aortic pressure of 16.7 kPa (gauge), and a diastolic aortic pressure of 10.0 kPa (gauge), they found a mean systolic pressure drop of 1.2 kPa for a Smeloff valve with a TAD of 24 mm. Yoganathan, et al. (1979b) operated their pulse-duplicator at 70 beats per minute at a mean flow rate of 5.0 L/min using both 0.9%-by weight normal saline and a blood-analog fluid of 6%-by-weight Polyol® in water. With a systolic interval of 300 milliseconds, a maximum aortic pressure of about 16.0 kPa (gauge), and a diastolic aortic pressure of about 10.7 kPa (gauge), they found a mean systolic pressure drop of 1.9 kPa and a peak systolic pressure drop of 4.0 kPa for a Smeloff valve with a TAD of 26 mm. ΔP_{max} is reported in Table 8 as 3.3 ± 0.3 kPa. $\overline{\Delta P}_{sys}$ is reported in Table 8 as 1.3 ± 0.2 kPa.

In vivo mean pressure-drop results reported in the literature have been larger than that found in the present investigation. Davey and Smeloff (1977) reported "resting" mean pressure drops averaging 2.3 kPa *in vivo*. McHenry, et al. (1978) reported "resting" mean pressure drops averaging 2.5 kPa *in vivo*. Earlier, McHenry, et al. (1968) had reported "resting" mean pressure drops of 1.9 ± 0.7 kPa *in vivo*.

Regurgitant flow for the Smeloff valve appears to have been significant. The Smeloff valve had the largest percentage of regurgitant flow of the four valves studied in the present investigation. The total regurgitant flow rate for this valve of 1.64 L/min was about 25% of the forward-flow rate of 6.65 L/min. Leakage flow accounted for 95% of the regurgitant flow. The magnitude of the total regurgitant flow, however, was probably less than that shown in Table 9. As was found for the Ionescu-Shiley valve, the electromagnetic flowmeter may have suffered significant drift during data collection. This drift tended to be towards lower flow rates and hence the actual regurgitant-flow rate may have been somewhat smaller, and the forward-flow rate somewhat larger, than that shown

in Table 9. The effect of the performance of the electromagnetic flowmeter on the measured regurgitant-flow rate is discussed in more detail below. $\overline{\Delta P}_{dias}$ and $\overline{\Delta P}$ were consistent with a moderate level of regurgitation. The aortic pressure drops during diastole when there is regurgitant flow and hence $\overline{\Delta P}_{dias}$ and $\overline{\Delta P}$ also drop. The values of $\overline{\Delta P}_{dias}$ and $\overline{\Delta P}$ for the Smeloff valve were the lowest measured of the four valves studied in the present investigation.

For steady flow, $\overline{Q}$ in Table 9 indicates that the steady-flow velocity results were comparable in magnitude to those for pulsatile flow. $\overline{Q}$ at 27 L/min was about 11% smaller than Q_{max}.

The steady-flow pressure drop found in the present investigation was in the range reported in the literature (Forrester, et al., 1969; Yoganathan, et al., 1979b). Forrester, et al. (1969) reported a steady-flow pressure drop of 3.1 kPa for a Smeloff valve with a TAD of 24 mm at a flow rate of 27 L/min. Yoganathan, et al. (1979b) reported a steady-flow pressure drop of 1.8 kPa for a Smeloff valve with a TAD of 26 mm at a flow rate of 25 L/min. The high value measured by Forrester, et al. (1969) was probably not the fully recovered pressure drop. The location of the downstream pressure tap was not indicated but may have been closer to the valve than the approximately 100 mm generally required for pressure recovery downstream from prosthetic valves (Martin, et al., 1981). Using Equation (13) with an exponent of 2.0, the results of Yoganathan, et al. (1979b) predict a steady-flow pressure drop of 2.1 kPa at a flow rate of 27 L/min. An exponent of 2.0 in Equation (13) is consistent with the pressure-drop results presented for the Smeloff valve by Forrester, et al. (1969) and Yoganathan, et al. (1979b). $\overline{\Delta P}$ is reported in Table 8 as 2.2 ± 0.1 kPa.

The pulsatile-flow pressure drops estimated from the pressure-drop results for steady flow in the present investigation compare well with the pulsatile-flow results presented in Table 8. The pulsatile-flow pressure drops can be estimated

using Equations (14) and (16). Substituting into Equation (14) the values for $\overline{\Delta P}$, $\overline{Q}$, and Q_{rms} from Tables 8 and 9, the $\overline{\Delta P}_{sys}$ calculated was 1.33 kPa. $\overline{\Delta P}_{sys}$ in Table 8 was 1.3 ± 0.2 kPa. Substituting into Equation (16) the values of $\overline{\Delta P}$, Q_{max}, and Δt_{sys} yields a value of ΔP_{max} of 3.4 kPa. ΔP_{max} in Table 8 was 3.3 ± 0.3 kPa. Thus the pressure-drop results obtained from the steady-flow and pulsatile-flow experiments in the same flow section were consistent with one another.

3.5.4.2 Discussion of the Velocity Results

The flow downstream from the Smeloff valve was quite different from that downstream from the empty aortic-valve flow section. The flow downstream from the empty flow section, as shown in Figure 16, was axisymmetric and had a global maximum near the centerline of the tube. The rms axial velocities downstream from the Smeloff valve were significantly elevated over those downstream from the empty flow section. The average rms axial velocity across the data plane was 30.8 cm/s for the Smeloff valve and 14.0 cm/s for the empty flow section.

The flow structure downstream for the Smeloff valve appears to have been affected by both the centrally located ball occluder and the struts of the valve. The mean axial velocities near the centerline of the tube were located on a "saddle point" in the plane of the results. The fact that the velocities near the centerline were less than the maximum velocity probably resulted from the disturbance or wake generated downstream from the valve occluder. On the other hand, the fact that the velocities near the centerline of the tube were greater than the minimum velocity probably resulted from the disturbance or wake generated by the valve struts. If the velocity defects attributed to the wakes of the struts were to be removed, then the flow downstream from the

Smeloff valve would have been axisymmetric with a large velocity defect centered on the tube centerline.

The relatively large pressure drop found for the Smeloff valve probably resulted from these flow wakes. As was pointed out in the section 3.3 on the Björk-Shiley convexo-concave valve, the pressure loss in a wake is not recovered. The wakes generated by the valve struts appear to have had a more pronounced effect on the flow structure than the wake generated by the ball. This more pronounced effect is a surprising result since the ball occluder was much larger in size.

The lack of appreciable secondary-flow structure indicates that the azimuthal orientation of the axial velocity results was not changing very rapidly at that location downstream from the valve. Thus, the flow through the valve did not pick up significant azimuthal velocity.

The moderate levels of hemolysis associated with the use of the Smeloff valve were probably not caused by significant destruction of RBCs in the bulk flow. The largest estimated total shear stresses for the Smeloff valve shown in Figure 54 was 80 N/m^2 to 100 N/m^2 for steady and pulsatile flow, respectively. The major source of these estimated shear stresses was the high mean velocity gradients generated near the tube wall. The magnitudes of the estimated total shear stresses were large enough to activate platelets causing a chemical release reaction. As shown in Table 1 of Chapter 1, platelets were shown to undergo chemical release reactions at shear stresses around 20 N/m^2. The total shear stresses estimated in the present investigation were probably ***not*** sufficient to cause damage to platelets. The estimated total shear stresses in the bulk flow were probably not great enough to produce significant hemolysis. Several investigators have reported that the hemolysis associated with the Smeloff valve is significant (Indeglia, et al., 1968; McHenry, et al., 1968; Eyster, et al., 1971;

Sarma, et al., 1977). Therefore the hemolysis associated with the Smeloff valve was probably associated with interactions of the blood with the surface of the prosthesis or in regions of very high shear stress close to the valve superstructure.

The velocity results of the present investigation are more extensive yet consistent with the results presented in previous investigations. The velocity defect near the centerline of the tube has been previously reported. Lu, et al. (1979) and Yoganathan, et al. (1979b) have measured velocities at axial locations near that used in the present investigation and also nearer to the valve. These investigators measured velocities across a single profile of their flow sections. Yoganathan, et al. (1979b) measured velocities in steady flow at 25 L/min. At z = 42.00 mm these investigators found a maximum velocity along the velocity profile of about 110 cm/s. The maximum velocities for the steady-flow results of the present investigation were about 110 cm/s to 120 cm/s at a flow rate of 26 L/min. It should be noted that the velocity profile of Yoganathan and coworkers was not symmetric. This lack of symmetry is quite consistent with the results of the present investigation. Lu, et al. (1979) measured velocities in pulsatile flow. These investigators operated their pulse-duplicator at 70 beats per minute at a mean flow rate of 4.2 L/min using a blood-analog fluid of 36.7% glycerine and 63.3% water. With a systolic interval about 35% of the cycle, a maximum aortic pressure of 16.0 kPa (gauge), and a diastolic aortic pressure of 10.7 kPa (gauge), they found a maximum mean velocity and rms velocity at peak systole of 85 cm/s and 21 cm/s, respectively. The velocity profile reported by Lu and coworkers was measured at about z = 25 mm and was symmetrical across the tube. The lower mean flow rate for the work of Lu, et al. (1979) appears to have caused lower maximum velocities than for the present investigation. The symmetry of their results may have resulted from

the fact that they made their measurements closer to the valve.

Previous investigations have failed to note the wakes downstream from the struts. This failure was because of limitations in the methods by which the results were obtained. In particular, there has been a lack of a systematic, data-plane type approach to the data collection. No information has been presented previously, therefore, which would allow an analysis of the three-dimensional aspects of the wakes generated downstream from this valve design.

Few turbulent shear stresses downstream from the Smeloff valve have been reported in the literature. Lu, et al. (1979) measured these stresses directly using multi-component LDA. They reported maximum turbulent stresses of about 25 to 30 N/m^2 at the point of maximum mean velocity. These values are somewhat smaller than the maximum turbulent stresses of about 35 to 40 N/m^2 reported in the present investigation. The difference probably results from the difference in the flow rates between the present investigation and that of Lu, et al. (1979). Thus the estimated shear stresses of the present investigation were on the order of that found by direct measurement.

3.5.4.3 Steady Versus Pulsatile Flow

The pulsatile-flow results presented in Figures 46 through 53 show that the systolic ejection interval could be divided into three phases. Windows 4 through 9 were taken as encompassing early systole, windows 10 through 16 were taken as encompassing mid-systole, and windows 17 through 20 were taken as encompassing late systole. The flow during early systole was characterized by flat axial velocity profiles, small non-axial velocities, and relatively low rms axial velocities. The flow during mid-systole was similar to that found for steady flow. The flow during late systole was characterized by rapid deceleration and eventual flow reversal, a general lack of secondary-flow structure, and elevated

rms axial velocities. The results thus indicate that the results for early and mid-systole can be approximated *a priori*. Late systole would be difficult to approximate *a priori*.

The pulsatile-flow results were less distinct than the steady-flow results. These differences can be attributed to the relative amount of data available from the pulsatile-flow experiments and the reproducibility of the flow from one cycle to the next. The reproducibility of the pulse-duplicator may have also contributed to the "raggedness" and "scatter" of the pulsatile flow results.

During diastole the flow structure was affected by the fact that the occluding mechanism of the Smeloff valve allowed a controlled amount of flow regurgitation. As shown in Figures 46, 48, and 50, the mean velocities in the flow after valve closure decreased rapidly but did not vanish entirely. Small, negative mean velocities were present throughout diastole. The mean non-axial velocities shown in Figure 52 did not show a tendency to vanish during diastole either. These finite velocities resulted from the small area available for reverse flow through the fully closed valve and the diastolic pressure gradient which provided the driving force for flow.

The flow at the beginning of each cycle was not entirely quiescent. During a pulsatile-flow experiment the results for a given cycle were based on the flow generated by the previous cycle at the end of diastole and not on a perfectly quiescent fluid.

The amount of regurgitant flow during diastole was determined separately by the electromagnetic flowmeter and the mean axial velocity results. The regurgitant-flow rate results from the flowmeter were given in Table 9. The regurgitant-flow rate results from the mean axial velocity results were given in Figure 55. As discussed earlier the results in Table 9 and Figure 55 required

adjustment to remove the effects of flowmeter drift and data biasing. Once these effects had been removed, the closure-flow and leakage-flow rates were calculated to be 2% and 18%, respectively, of the forward-flow rate. The total regurgitant-flow rate was 19% of the forward flow. The closure-flow and leakage-flow rate percentages do not sum to the total regurgitant flow rate because of round-off errors.

Earlier investigations reported relatively low values for the percentage of total regurgitation through the Smeloff valve in pulsatile flow. Björk and Olin (1970) and Olin (1971) reported total regurgitation values of 7% and 8%, respectively. The average gap width between the occluder and the inner diameter of the base-ring was not given for these two investigations. Suobank (1983) recently reported flow regurgitation as 26% of forward flow. The average gap width for the work of Suobank (1983) was given as 0.10 mm at the testing temperature. This larger gap width was at the upper limit of that allowed by the valve manufacturer for an acceptable match of the occluder to the inner diameter of the base-ring. Thus the percentage of flow regurgitation found in the present investigation was in the range reported in the literature but agreed more closely with the higher reported value.

A further comparison of the results for steady flow with those for pulsatile flow can be made from the results shown in Figure 55. The flow-rate results in Figure 55 show that the flow rate during the middle of systole was comparable to that for steady flow. The pulsatile-flow results were within 10% of the steady-flow result over much of mid-systole.

The average rms axial velocities plotted in the bottom of Figure 55 show that the magnitude of the fluctuating velocities was dependent upon the systolic phase. During early systole, the average rms axial velocities were not very different from those during diastole. During mid-systole, the average rms axial

velocities went through a well-defined maximum and began to decrease before late systole. During late systole, the rms axial velocities dropped but overall remained elevated. A small "shoulder" can be seen at window 20 when maximum reverse flow occurred.

The average rms axial velocities shown in Figure 55 show that the rms axial velocities measured in steady flow were generally larger than those found in pulsatile flow. Thus, the rms velocities for steady flow tended to be an upper bound on the rms velocities for pulsatile flow.

For the Smeloff valve, the maximum average rms axial velocity was measured one window after the maximum flow rate. This one-window delay is shorter than the delay of two windows found for the other valves studied in the present investigation. The one-window delay, nonetheless, is consistent with the flow disturbance being generated at the valve and convected to the data plane. For the Smeloff valve much of the flow disturbance generated by the valve was generated by the flow past the ball occluder and downstream cage struts. Thus much of the flow disturbance generated by the valve was generated much closer to the data plane than the valve's base-ring orifice. Therefore, the one-window delay found for the Smeloff valve represents the time it took for the flow disturbance to be convected from the valve superstructure to the data plane.

The average rms axial velocities plotted in the bottom of Figure 55 seem to have a base-line value near 4 cm/s. This base line is similar to that seen for the Ionescu-Shiley valve and probably also stems from the "cascading" energy from the mean velocity field during diastole.

3.5.5 Conclusions

The flow structure generated by the Smeloff valve was quite unlike that found for the empty flow section. The flow showed evidence of wakes generated by the

ball occluder and by the downstream struts of the valve superstructure. The ball occluder of the valve was shown to generate a large wake centered about the centerline of the tube. The three struts of the downstream cage were shown to generate three large wakes near the tube wall. Only small secondary-flow structures were found indicating that the lateral-flow occluding mechanism of this valve imparted very little azimuthal sense to the forward flow.

The extent of the flow disturbance associated with the wakes generated by the struts suggest that these wakes may play a significant role in producing the relatively large pressure drop found for the Smeloff valve. The pressure-drop results for this prosthesis were higher than those found for the other three valves studied in the present investigation.

The mean velocity gradients were elevated at the tube wall which implied high shear stresses in the flow near the wall. These high shear stresses were probably not of such a magnitude as to cause significant hemolysis *in vivo*. Shear stresses in the bulk flow were only moderate in magnitude and were less than the level generally considered hemolytic. Sub-lethal damage of RBCs, however, could occur in the bulk flow. The estimated total shear stresses were sufficient to activate platelets and cause a chemical release reaction. The presence in the flow of activated platelets increases the possibility of thrombus formation and hence valve thrombosis and thromboembolic events.

The moderate pressure-drop characteristics of the Smeloff valve were coupled with moderate flow-regurgitation characteristics. Thus the full-orifice design of this prosthesis has not been entirely successful in producing a valve with superior hemodynamics relative to the other valves currently available for implantation.

A comparison of steady-flow and pulsatile-flow results showed that i) the

steady-flow results approximated those for pulsatile flow only during the middle of systole and ii) the rms velocities for steady flow provided an upper bound to those found in pulsatile flow. The results indicated that the systolic ejection interval could be divided into three phases: early systole, mid-systole, and late systole. For each phase of systole the flow structure was significantly different. The flow structure of mid-systole was most similar to that for steady flow. The steady-flow results were quite different from those for pulsatile flow during early and late systole. It was found that early systole could be estimated *a priori* as plug flow. Late systole would be difficult to predict *a priori*. Pulsatile-flow results in diastole were found to have structure which were not predictable from the steady-flow results. The results from the steady-flow experiments, therefore, were limited in their ability to provide an understanding of the pulsatile flow. It was concluded that steady flow results can provide some knowledge of the flow fields downstream from the Smeloff valve but only for a relatively small portion of systole.

3.6 ST. JUDE PROSTHESIS

3.6.1 Introduction

The St. Jude prosthesis is a relatively new low-profile bi-leaflet valve covered entirely with pyrolytic carbon. This unique valve is shown in the bottom of Figure 5b. The two semicircular leaflets of the occluding mechanism of this valve rotate out to 85° in response to forward flow leaving an orifice 85% to 90% free from obstruction to the flow (Emery and Nicoloff, 1979; Gombrich, et al., 1979; Nicoloff and Emery, 1979).

The St. Jude valve has generally been described as having relatively undisturbed forward flow and low pressure drops *in vitro* and *in vivo* (Emery, et al., 1978; Chaux, et al., 1979; Emery and Nicoloff, 1979; Gombrich, et al., 1979; Nicoloff and Emery, 1979). The two leaflets of the opened divide the area available for forward flow into three regions, as shown in Figure 5b. The two large portions of flow emerge from between each leaflet and the valve base-ring and a third, smaller portion emerges from between the two leaflets.

Because the St. Jude prosthesis was first implanted in late 1977, its long-term success as a substitute heart valve has yet to be demonstrated.

In the present investigation, a St. Jude prosthesis with a TAD of 25 mm was studied *in vitro* in both steady and pulsatile flow regimes. Pressure and volumetric-flow data were collected to insure that the pressure and flow fields encountered by the valve in the experimental rig were similar to that which the valve might encounter when implanted in a patient. For pulsatile flow, the pulse-duplicator was operated at pressures and flows found *in vivo* in a resting state, i.e., as might be measured in the catheterization laboratory. After establishing these pressure and flow fields, the assessment of the *in vitro* states was extended to i) an extensive evaluation of the mean and rms velocities in the

axial and non-axial directions across a data plane downstream from the mounted prosthesis, ii) the estimation of the total shear stresses at the data plane from the rms velocity results, iii) the estimation of the total regurgitant flow associated with this prosthesis to be used in comparison with other valves studied, and iv) the comparison of steady and pulsatile flow results to give insights into the relevance of steady-flow analyses of flow fields downstream from prosthetic valves.

This extensive analysis was primarily undertaken to gain a better insight into the structure of the flow downstream from the St. Jude prosthesis. It was expected that this extensive analysis would allow more definitive comments regarding the hydrodynamic performance of this unique valve prosthesis. In particular, the magnitude and extent of the wakes generated downstream from this valve were to be interpreted in light of the relatively small pressure drop found for this valve. Detailed estimations of shear stresses was undertaken in the hope that better correlation between *in vitro* results and *in vivo* levels of hemolysis could be achieved.

3.6.2 Methodology and Apparatus

The experimental methodology and apparatus used to obtain the results for the St. Jude valve were those discussed in detail in the previous chapter.

3.6.3 Results

3.6.3.1 Pressure and Volumetric-Flow Results

The pressure and volumetric-flow results for the St. Jude valve were computed during each experiment in the same fashion as for the Ionescu-Shiley valve. These two sets of results are presented in Tables 10 and 11, respectively.

Table 10

Parameters Computed from the Pressure Data for the St. Jude (25 mm) Prosthesis*

	Pressure (kPa)	Relative time** of occurrence in the cycle (ms)
Pulsatile Flow:		
ΔP_{max}	2.1 ± 0.2	159 ± 36
VP_{max}	19.3 ± 0.4 +	197 ± 5
P_{x1}	12.3 ± 0.4 +	0 ± 34
P_{x2}	13.1 ± 0.9 +	283 ± 19
$\left(\frac{dP}{dt}\right)_{max}$	177 ± 17 (kPa/s)	-31 ± 30
$\left(\frac{dP}{dt}\right)_{min}$	-307 ± 42 (kPa/s)	347 ± 17
$\overline{\Delta P}_{sys}$	0.6 ± 0.1	-
$\overline{\Delta P}_{dias}$	10.8 ± 0.2	-
$\overline{\Delta P}$	12.5 ± 0.3 +	-
Steady Flow:		
$\overline{\Delta P}$	1.0 ± 0.1	-

*Results given as mean ± standard deviation.

**Relative to the beginning of systolic ejection.

+Gauge pressure.

Table 11

Parameters Computed from the Volumetric-Flow Data for the St. Jude (25 mm) Prosthesis*

	Flow (L/min)	Relative time** of occurrence in the cycle (ms)
Pulsatile Flow:		
Q_{max}	29.6 ± 0.4	201 ± 6
Q_{min}	-7.4 ± 0.8	340 ± 5
Q_{beg}	0.0 (by def.)	-12 ± 15
Q_{end}	0.0 (by def.)	318 ± 4
Q_F	5.60 ± 0.09	-
Q_C	-0.09 ± 0.04	-
Q_L	-0.53 ± 0.10	-
Q_{rms}	19.7 ± 0.1	-
Steady Flow:		
$\bar{Q}$	27 (rotameter)	-

*Results given as mean ± standard deviation.

**Relative to the beginning of systolic ejection.

3.6.3.2 Velocity Results

The velocity results are presented for steady and pulsatile flow in the same fashion as for the Ionescu-Shiley valve. No data were collected for the St. Jude valve at data-plane locations other than at z = 31.8 mm. The temporal locations of the pulsatile-flow windows for the St. Jude valve are shown in Figure 56. For the St. Jude valve, pulsatile-flow windows 4 through 20 encompassed the systolic ejection interval. The diastolic interval thus extended from windows 20 through 43 and then up to window 3 of the next cycle. Window 8 corresponded to the time when the flow experienced maximum acceleration, window 13 corresponded to the time of maximum forward flow, window 17 to the time when the flow experienced maximum deceleration, and window 20 to the time of the maximum reverse flow.

Mean axial velocity results for pulsatile flow are presented in 3-D perspective in Figure 57. Results are shown for windows 6 through 23, 25, and 30. Two parallel 'ridges' in the axial velocities can be seen in Figure 57 during much of the systolic ejection interval. The ridges were noticeable by window 10 and were distinct by window 11 persisting for 120 milliseconds until window 16. A small peak can be seen between these ridges. The peak was distinct by window 12 and persisted until window 16. No regions of flow separation were notable during the systolic ejection interval until the flow began to reverse to close the valve. During diastole the axial velocities settled out.

Mean axial velocities are presented in Figure 58 for steady flow and for windows 8, 13, 17, and 20 for pulsatile flow. For steady flow, the ridges were again evident. The peak between the ridges is also seen for steady flow. For pulsatile flow, the flow structure at window 13 was similar to that for steady flow. Early in systole at window 8 the flow had a flat velocity profile across the data plane in all directions. Late in systole at window 17 only remnants of the

ST. JUDE (25 mm)

KEY TO WINDOW LOCATIONS

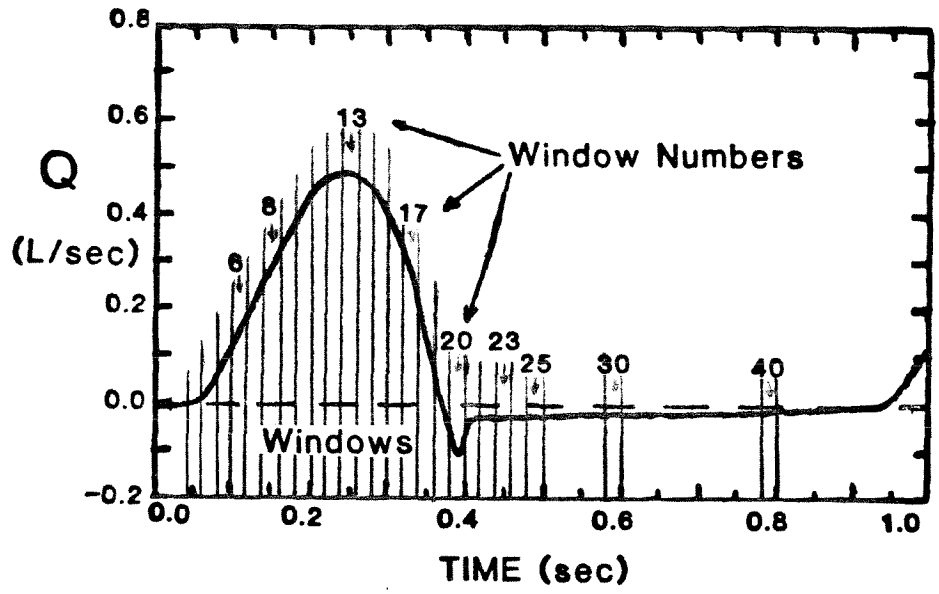

Figure 56. Idealized volumetric-flow curve showing temporal location of pulsatile-flow windows 6 through 25, 30, and 40 for the St. Jude (25 mm) prosthesis.

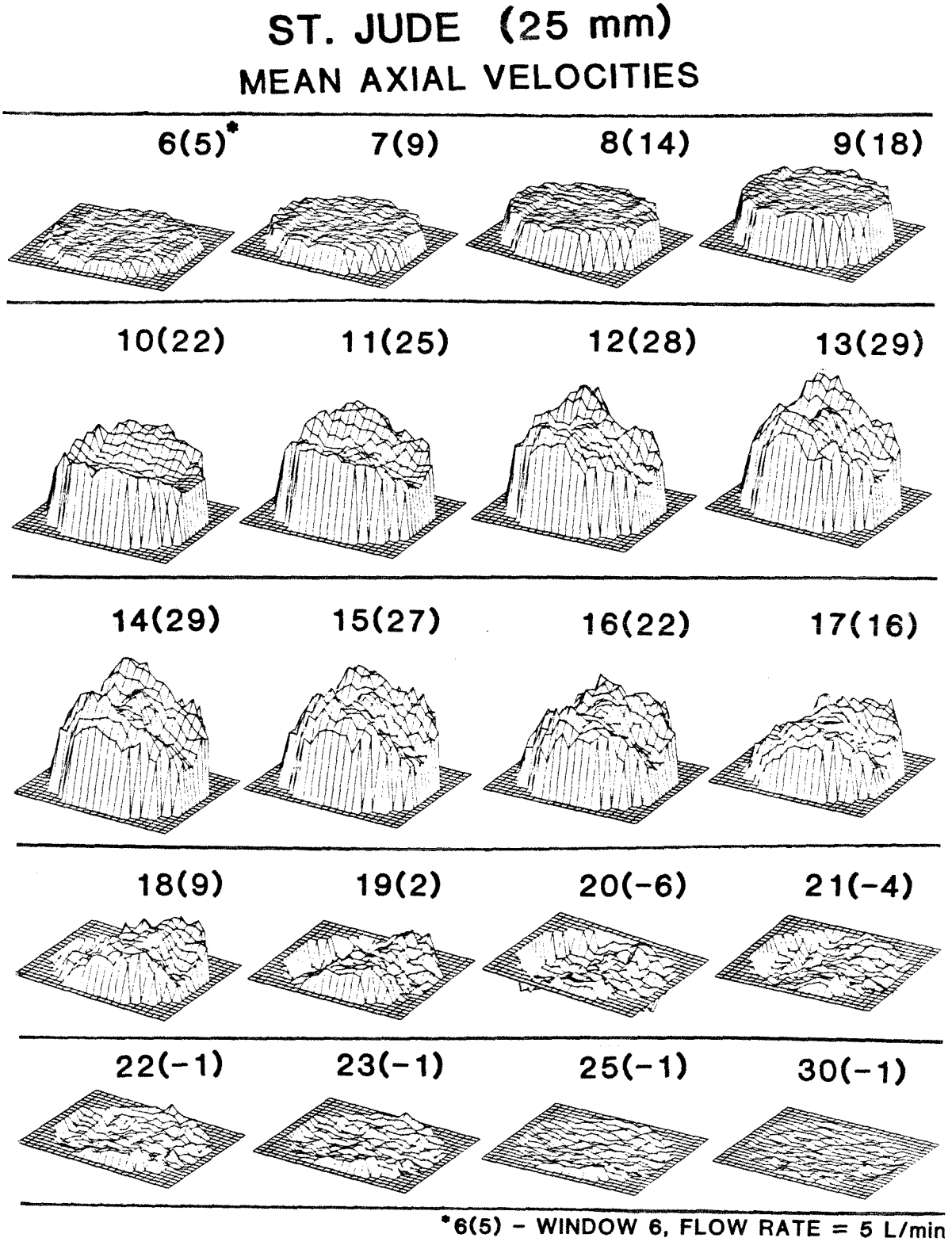

Figure 57. Mean axial velocities in 3-D perspective for pulsatile-flow windows 6 through 23, 25, and 30 downstream from the St. Jude (25 mm) prosthesis at z = 31.8 mm.

ST. JUDE (25 mm)

MEAN AXIAL VELOCITIES

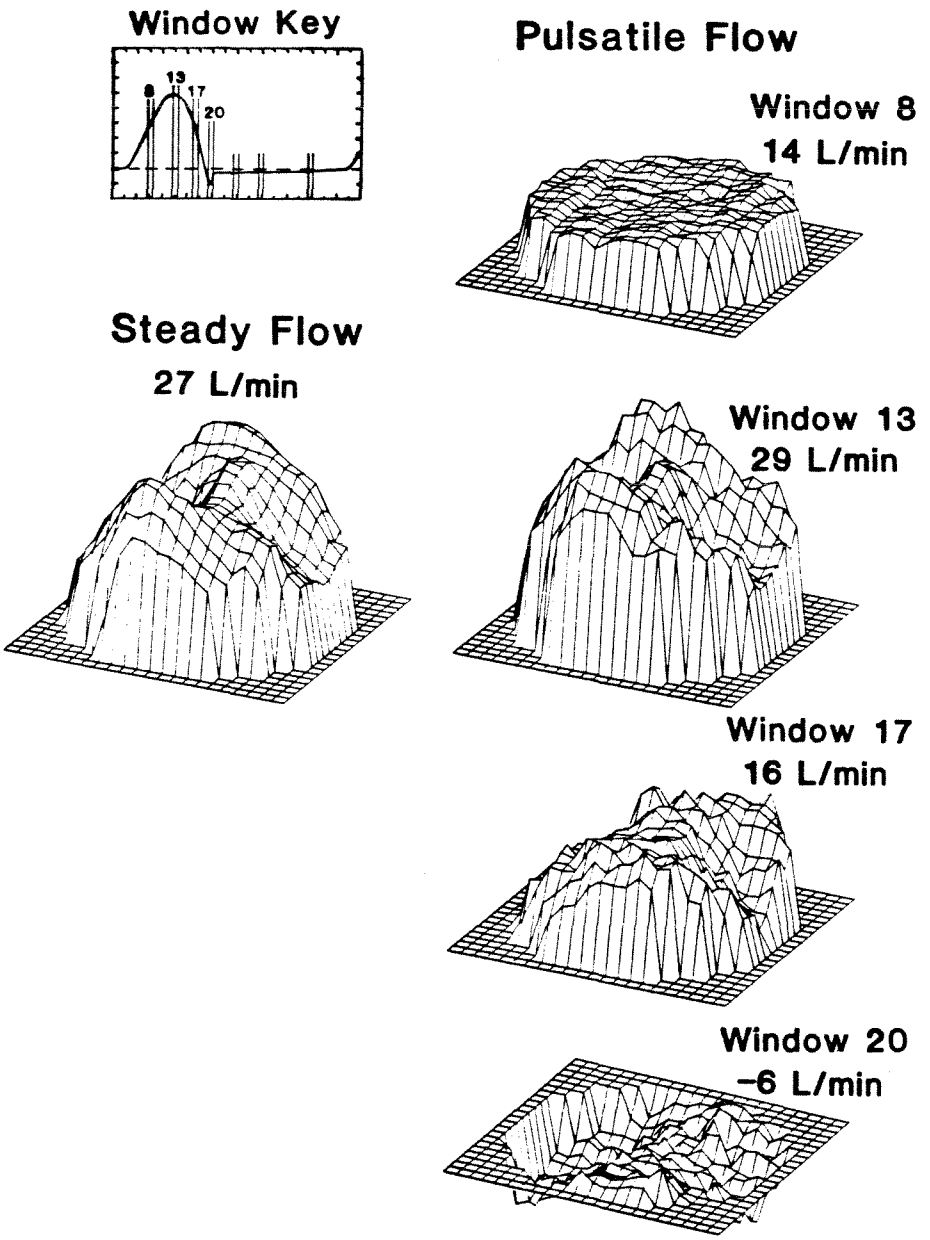

Figure 58. Mean axial velocities in 3-D perspective for steady flow and pulsatile-flow windows 8, 13, 17, and 20 downstream from the St. Jude (25 mm) prosthesis at z = 31.8 mm.

two ridges were still noticeable. By window 21, immediately preceding valve closure, the flow had reversed. Some positive mean axial velocities can be seen for window 21 which appear to correspond spatially to the locations of the two ridges earlier in the cycle.

Mean axial velocities are presented in Figure 59 for windows 25, 30, and 40 of the pulsatile flow. These velocities show the settling out of the flow during diastole. Very small ridges of positive mean axial velocities were still present as late in the cycle as window 25. Note that though both positive and negative velocities are shown in this figure, the integrated flow rate was negative. The negative flow rate throughout diastole was about -1 L/min.

The mean axial velocities shown in Figure 58 for steady flow and for windows 8, 13, 17 of the pulsatile flow are presented more quantitatively as contours in Figure 60. The inset showing the valve orientation depicts the orientation of the valve superstructure relative to the structure of the velocity results.

From Figure 60 the magnitude and structure of the two ridges can be more readily appreciated. For steady flow, the maximum mean axial velocities along the two ridges ranged from 120 cm/s to 140 cm/s. For pulsatile flow, the maximum mean axial velocities along the two ridges was 140 cm/s. The fluid was therefore found to be accelerated by a factor of about 1.4 from the maximum velocity of 105 cm/s for the flow upstream from the mounted valve. This factor was less than 1.1 for the flow through the empty flow section. The "peak" between the ridges can be seen in Figure 60 to form a third, smaller 'ridge' connecting the other two larger ridges in an "H" pattern. Thus there was a type of "saddle point" in the mean axial velocity surface near the centerline of the tube. The orientation of the results for steady and pulsatile flow was such that the two larger ridges corresponded with the orientation of the two leaflets

ST. JUDE (25 mm)

MEAN AXIAL VELOCITIES

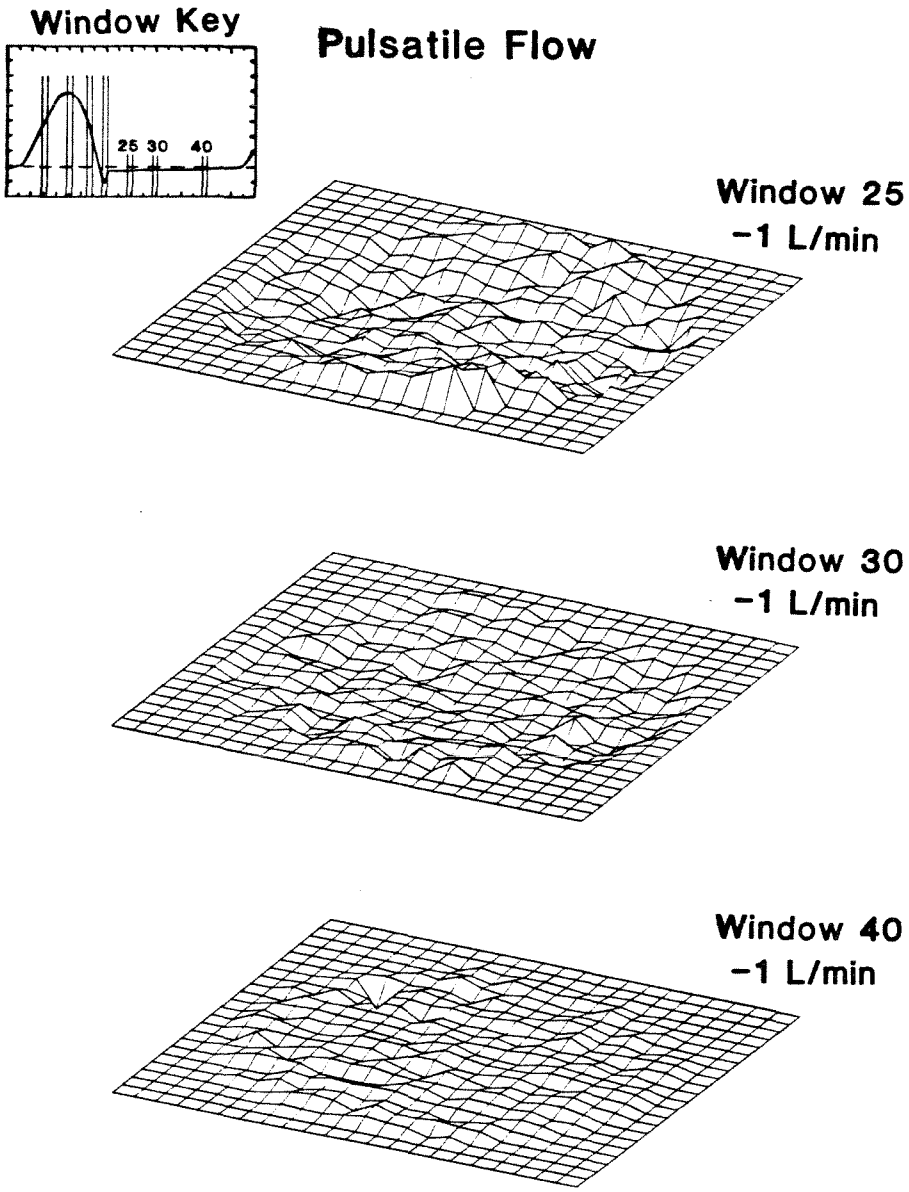

Figure 59. Mean axial velocities in 3-D perspective for pulsatile-flow windows 25, 30, and 40 downstream from the St. Jude (25 mm) prosthesis at z = 31.8 mm.

ST. JUDE (25 mm)

MEAN AXIAL VELOCITIES

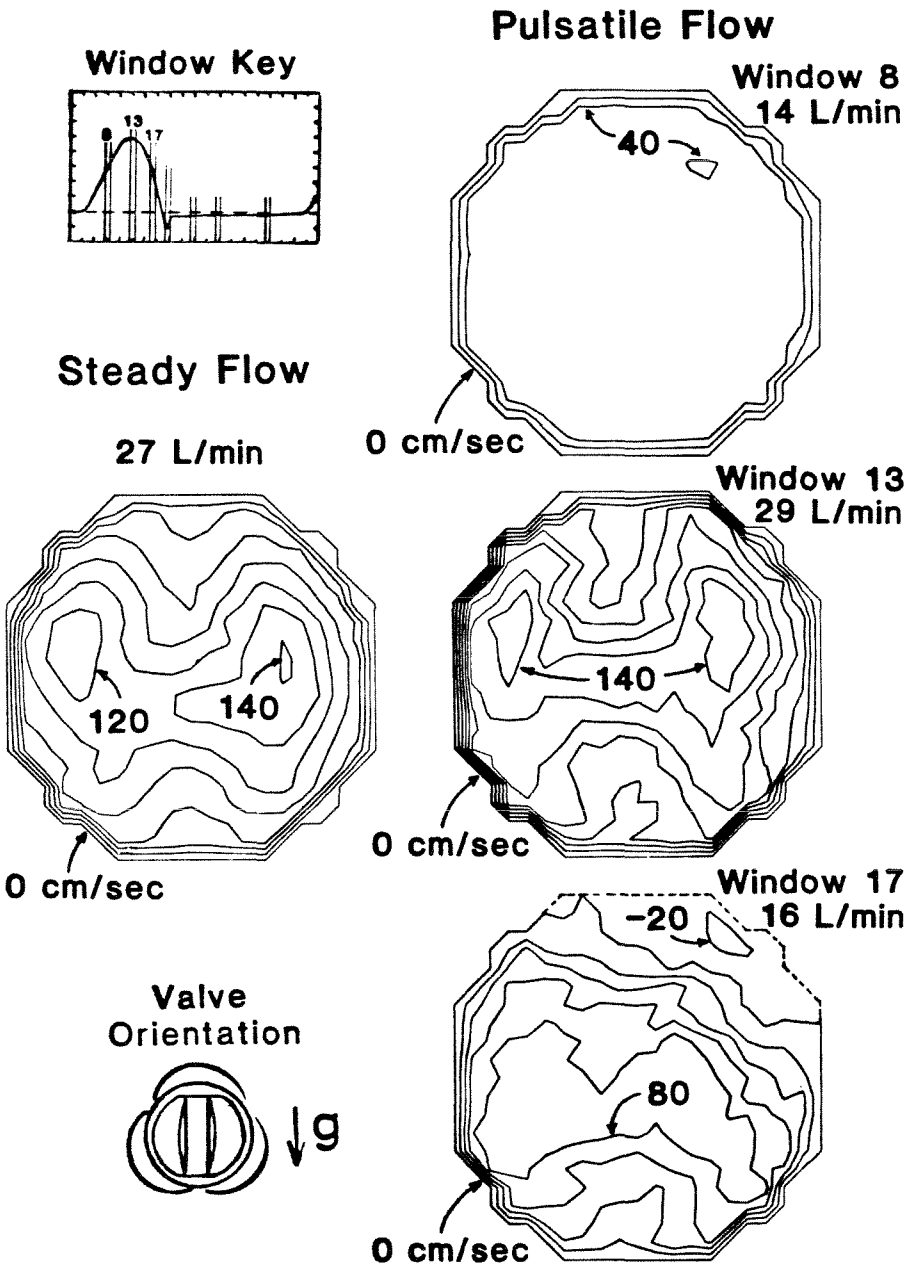

Figure 60. Mean axial velocities as contours for steady flow and pulsatile-flow windows 8, 13, and 17 downstream from the St. Jude (25 mm) prosthesis at z = 31.8 mm. Contour interval: 20 cm/s.

of the valve's occluding mechanism. The third ridge, or "peak," was oriented near the center of the tube. Overall, the flow structure as shown in Figure 60 reflected the bi-symmetric aspect of the prosthesis.

The highest mean velocity gradients were generated near the tube wall. These velocity gradients were more elevated at the wall closest to the two larger ridges. Detailed velocity measurements were not made near the wall but the maximum gradients at the wall appear to have been substantially larger than 500 s^{-1} near the two ridges and lower than 500 s^{-1} elsewhere.

The pulsatile-flow results were less distinct than those for steady flow. The pulsatile-flow results, however, were somewhat more symmetrical than those for steady flow. Early in systole at window 8 very little flow structure was present. Late in systole at window 17 flow reversal was already evident and the two large ridges had diminished significantly. The magnitudes of the maxima shown for window 17 had fallen to a little more than half their maximum value at window 13. The bi-symmetric shape of the results was still somewhat evident but had become much less pronounced.

Mean axial velocities are presented in Figure 61 as contours for windows 25, 30, and 40 of the pulsatile flow. No mean axial velocities were measured greater than 20 cm/s in absolute value and hence only contours corresponding to zero velocity are plotted. During diastole, positive mean axial velocities are presented on the sides of the plots for windows 25, 30, and 40. The most extensive positive velocities were found at window 25. The positive velocities at window 25 correspond in orientation with the two leaflets of the valve's occluding mechanism which in turn corresponded with the two large ridges present during the systolic ejection interval. The extent of the positive velocities diminishes as diastole proceeds.

ST. JUDE (25 mm)

MEAN AXIAL VELOCITIES

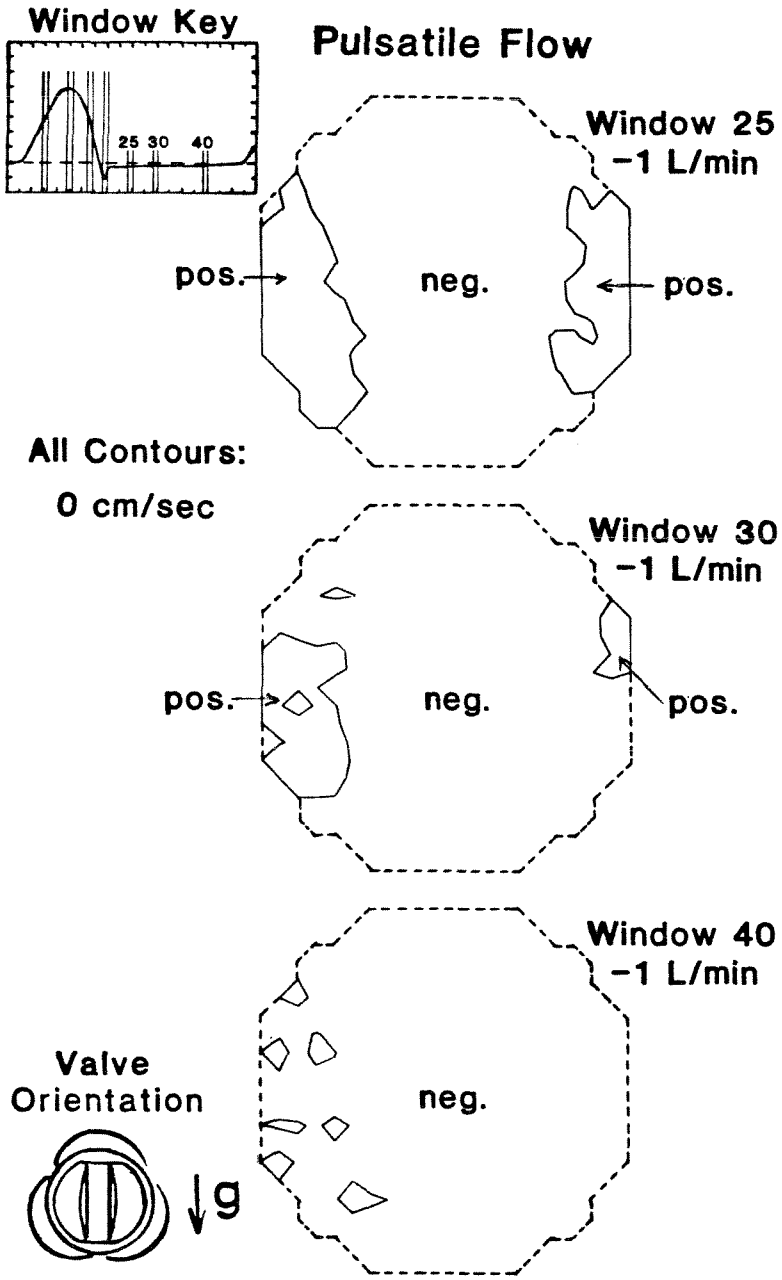

Figure 61. Mean axial velocities as contours for pulsatile-flow windows 25, 30, and 40 downstream from the St. Jude (25 mm) prosthesis at z = 31.8 mm. Contour interval: 20 cm/s.

Mean non-axial velocities are presented in Figure 62 for steady flow and for windows 8, 13, and 17 of the pulsatile flow as resultants of the mean velocities in the x- and y-directions. For both steady and pulsatile flow, the mean non-axial results showed relatively small non-axial velocity components. Some secondary-flow structure is evident from the non-axial velocities near the tube wall but the magnitude of these structures was generally small. For steady flow, the non-axial velocity components were oriented away from the tube centerline towards the left and right sides of the plot in Figure 62. The non-axial velocity components of the flow near the wall were generally directed along the wall toward the top and bottom of the plot in Figure 62. Finally, the non-axial velocity components of the flow near the top and bottom of Figure 62 were directed back towards the tube centerline. A weak vortex system was thus evident consisting of four vortices. For pulsatile flow, these vortices were less distinct than for steady flow. Early in systole at window 8 very small mean non-axial velocities were present. Late in systole at window 17 the structure of the flow had degenerated considerably.

The maximum mean velocities in the radial and azimuthal directions were determined as resultants of the velocity components measured in the x- and y-directions. For steady flow, the maximum mean velocities in the radial and azimuthal directions were 8.2 ± 1.0 cm/s and 6.7 ± 1.0 cm/s, respectively. For pulsatile flow, these maximum velocities were 17.2 ± 1.0 cm/s and 12.1 ± 1.0 cm/s, respectively. These pulsatile-flow results were for window 13.

Mean non-axial velocities are presented as resultants in Figure 63 for windows 25, 30, and 40 of the pulsatile flow. Overall, only very small velocity components were observed throughout diastole. By window 40 these small components were almost all less than 2.0 cm/s. There was no appreciable flow structure notable from these diastolic results.

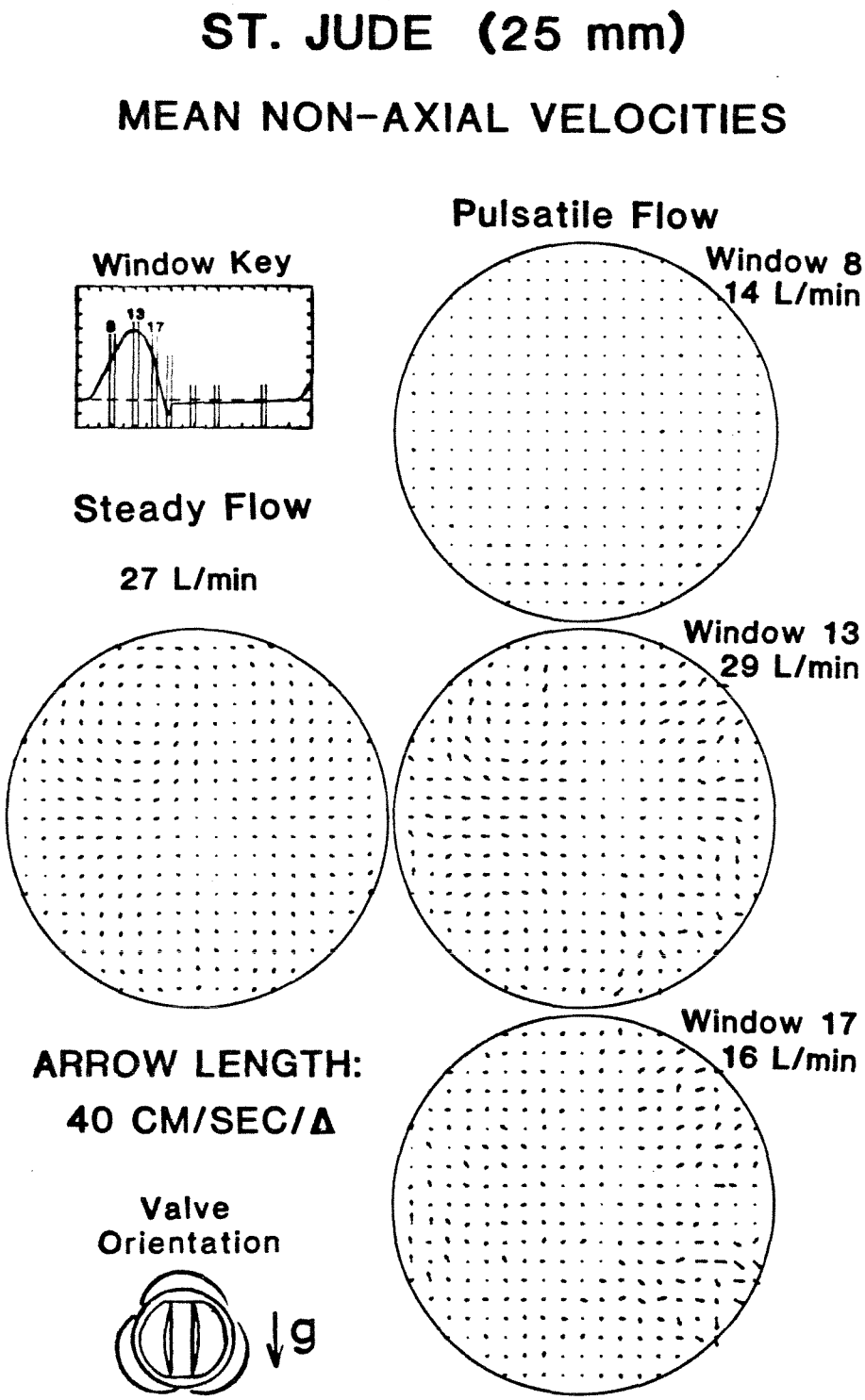

Figure 62. Mean non-axial velocities as resultants for steady flow and for pulsatile-flow windows 8, 13, and 17 downstream from the St. Jude (25 mm) prosthesis at z = 31.8 mm.

ST. JUDE (25 mm)

MEAN NON-AXIAL VELOCITIES

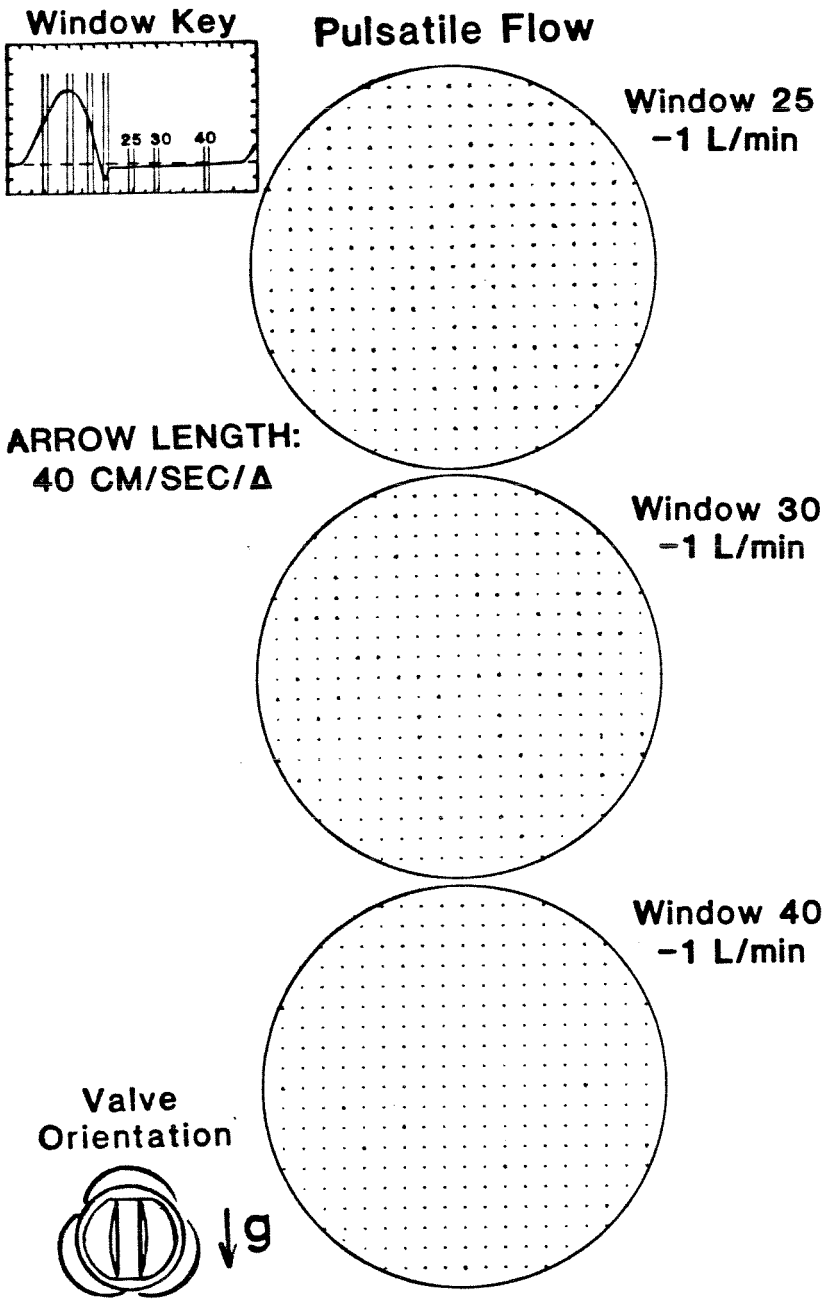

Figure 63. Mean non-axial velocities as resultants for pulsatile-flow windows 25, 30, and 40 downstream from the St. Jude (25 mm) prosthesis at z = 31.8 mm.

The rms axial velocities are presented in Figure 64 for steady flow and for windows 8, 13, and 17 of the pulsatile flow. For both steady and pulsatile flow, the rms axial velocities reflect the flow structure observed from the mean velocities. The highest rms axial velocities for steady flow and for window 13 of pulsatile flow were found to correspond spatially to the two large ridges of the mean velocity results. Generally, the rms axial velocities for steady flow were larger than those for window 13 of the pulsatile flow. The maximum rms axial velocity for pulsatile flow was, however, slightly but insignificantly greater than that for steady flow. The maximum rms axial velocities for steady and pulsatile flow were 38.3 ± 1.0 cm/s and 39.1 ± 1.0 cm/s, respectively. The average rms axial velocity across the data plane for steady flow was 27.7 ± 1.0 cm/s while that for pulsatile flow was 24.2 ± 1.0 cm/s. The pulsatile-flow results are for window 13. The rms axial velocities corresponded to an average turbulence intensity across the data plane of 23% for window 13 of pulsatile flow and 32% for steady flow. The maximum turbulence intensity at the data plane was 36% for window 13 of pulsatile flow and 43% for steady flow. Early in systole at window 8 the rms axial velocities were very low. Late in systole at window 17 the rms axial velocities still remained elevated but were generally smaller than those found at window 13.

The total shear stresses estimated from the velocity data using Equation (11) are presented as contours in Figure 65 for the axial velocity in the x-direction. Ridges of elevated shear stresses are apparent in Figure 65 along the wall of the tube. The estimated total shear stresses were around 80 N/m^2 near the tube wall. In the bulk flow, the estimated total shear stresses were generally low, averaging around 25 N/m^2. Early in systole at window 8, some small shear stresses are shown in near the tube wall. Late in systole at window 17, the shear stresses at the wall had dropped considerably from those at window 13.

ST. JUDE (25 mm)

RMS AXIAL VELOCITIES

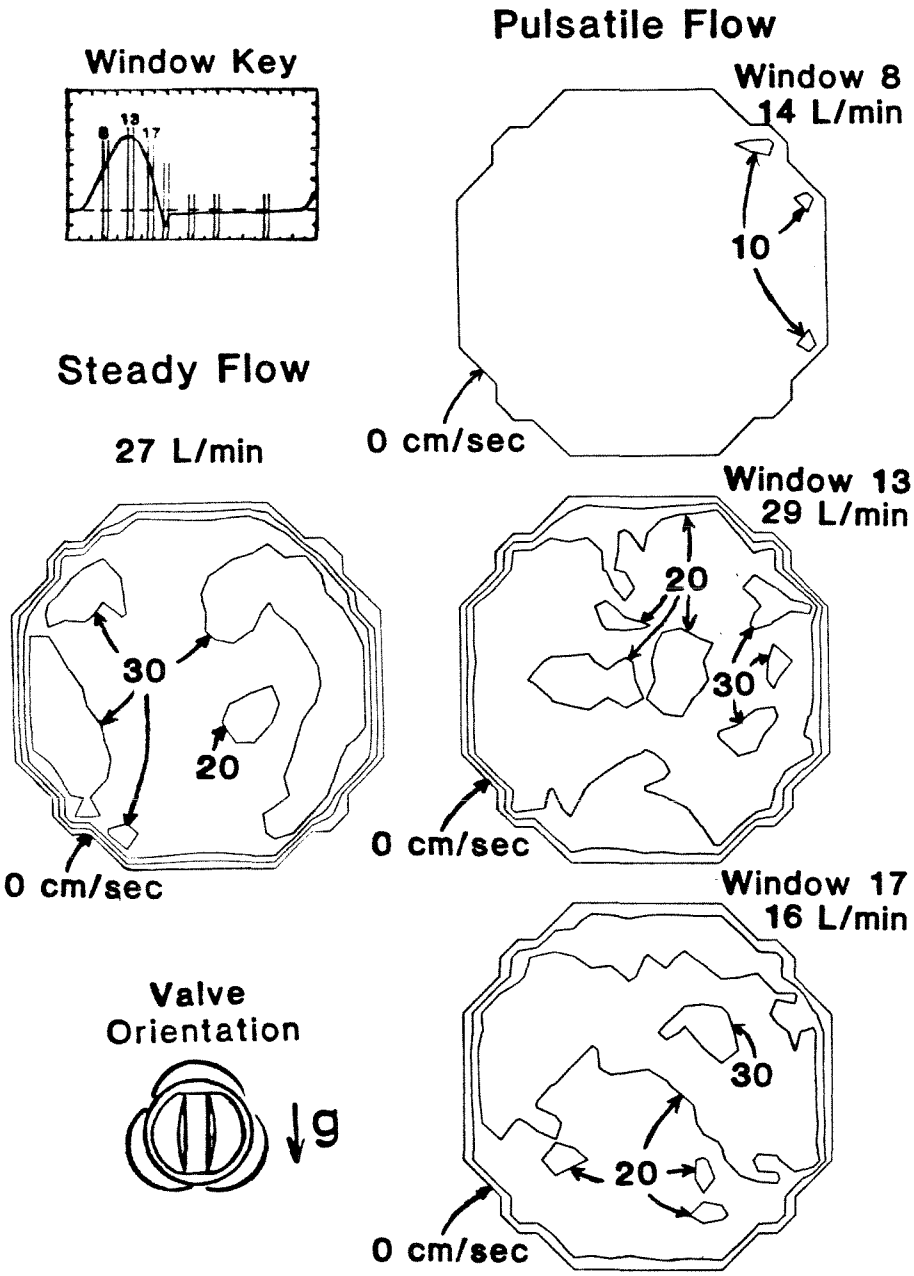

Figure 64. Root-mean-square (rms) axial velocities as contours for steady flow and pulsatile-flow windows 8, 13, and 17 downstream from the St. Jude (25 mm) prosthesis at z = 31.8 mm. Contour interval: 10 cm/s.

ST. JUDE (25 mm)

TOTAL SHEAR STRESSES* (Z - X)

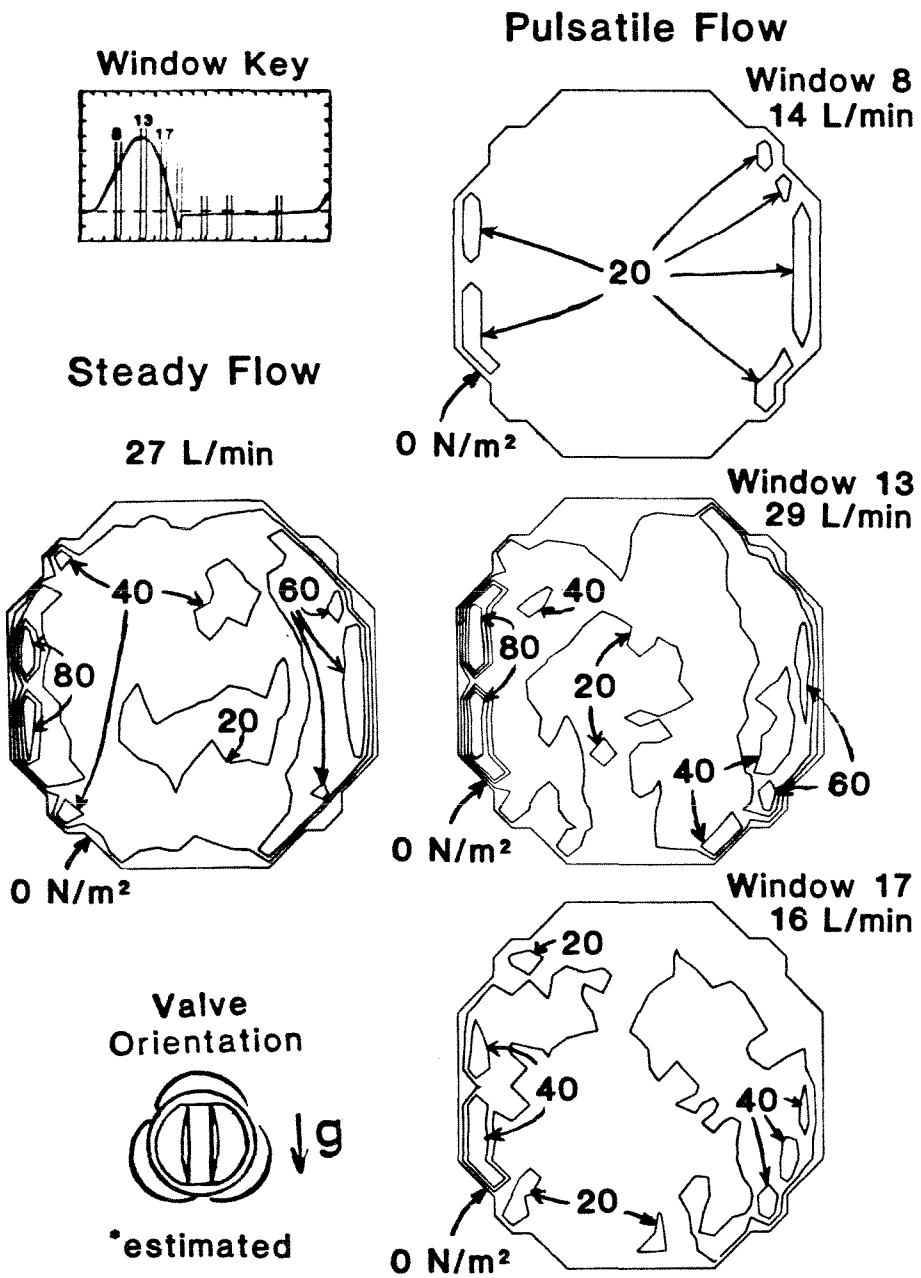

Figure 65. Total estimated shear stresses, τ_{zx}, as contours for steady flow and for pulsatile-flow windows 8, 13, and 17 downstream from the St. Jude (25 mm) prosthesis at z = 31.8 mm. Contour interval: 20 N/m^2.

The maximum total shear stress was estimated which was present over at least 10% of the tube cross section. For steady flow, this maximum shear stress was estimated to be 76 ± 5 N/m^2. For pulsatile flow, this maximum shear stress was estimated to be 74 ± 5 N/m^2 at window 13.

Plots of the averaged flow rate and rms axial velocities versus the pulsatile-flow window number, are given in Figure 66. The flow rates plotted here were determined by averaging the mean axial velocities across the data plane. The average rms axial velocities plotted here were determined by averaging the rms axial velocities across the data plane. The steady-flow results plotted in Figure 66 are plotted to correspond to the window that encompassed the maximum flow rate for pulsatile flow.

The flow-rate results in Figure 66 generally agree with those presented in Table 11. The maximum and minimum flow rates from the velocity data were 29 L/min and -6 L/min, respectively. The corresponding values from Table 11 are 29.6 L/min and -7.4 L/min. The effect of the finite width of the pulsatile-flow window and variability in the timing from one cycle to another probably account for the small differences between these two sets of the maximum and minimum flow rates. Taking the beginning of the systolic ejection interval to be at window 4, the timing of the maximum and minimum flow rates also agree. The velocity data indicate that the maximum and minimum flow rates occurred about 200 and 330 milliseconds, respectively, after the systolic ejection interval began. The corresponding values from Table 11 are 201 and 340 milliseconds, within the uncertainty of the width of the 20-millisecond windows.

The forward-flow and leakage-flow rates calculated from the results in Figure 66 differ significantly from the those given in Table 11. From the results plotted in Figure 66, the forward-flow and leakage-flow rates were calculated as 6.0 L/min and -0.4 L/min, respectively. The forward-flow and leakage-flow rates

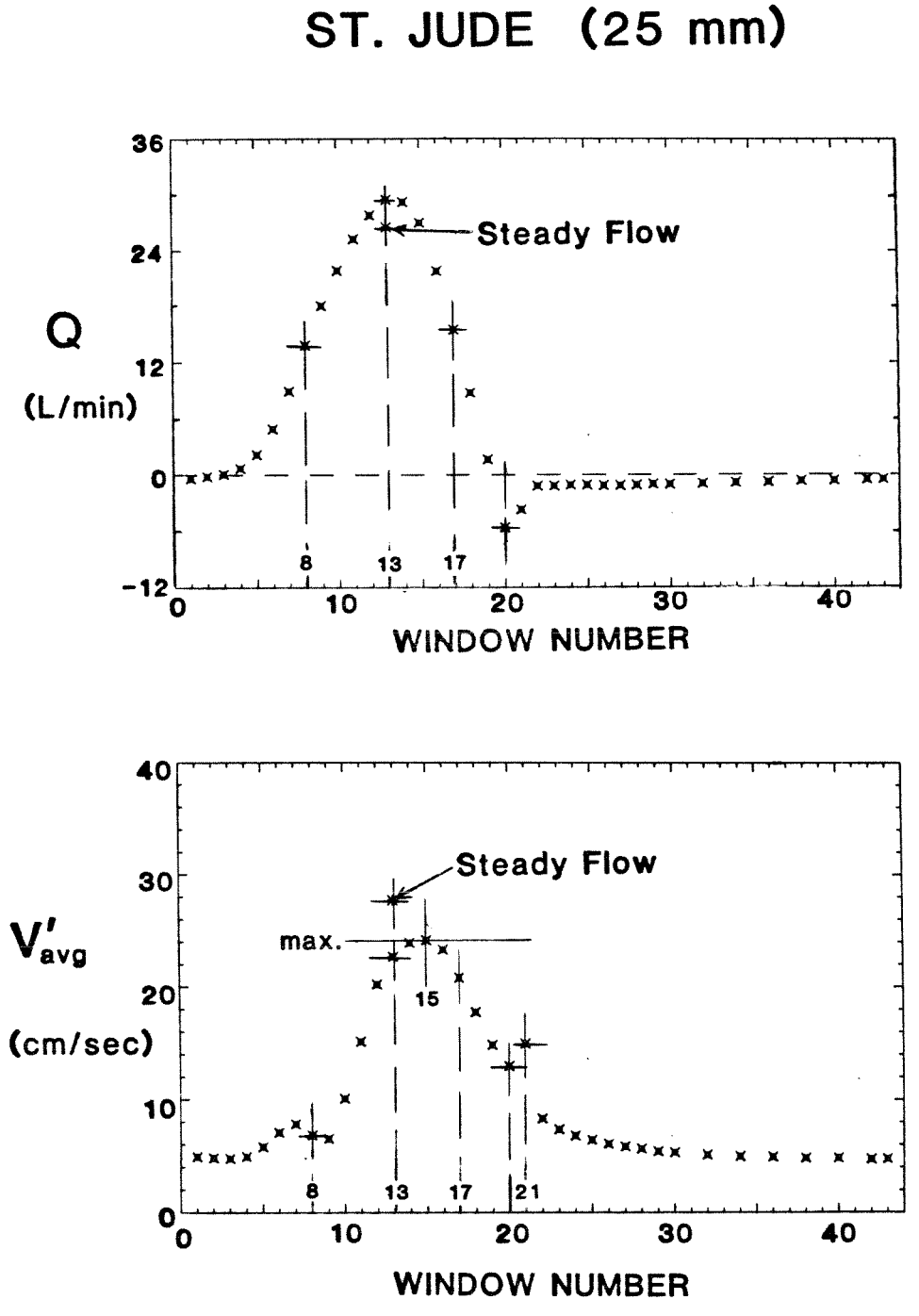

Figure 66. Volumetric-flow rate (top) and average rms velocity (bottom) calculated from the mean and rms velocities, respectively, at the data plane as a function of pulsatile-flow window number for the St. Jude (25 mm) prosthesis.

given in Table 11 are 5.60 ± 0.09 L/min and -0.53 ± 0.10 L/min, respectively. The closure-flow rate obtained from Figure 66 agrees within experimental uncertainty with that reported in Table 11. The closure-flow rate obtained from Figure 66 is -0.1 L/min; that reported in Table 11 is -0.09 ± 0.04 L/min.

The discrepancy between the leakage-flow rate obtained from Figure 66 and that given in Table 11 probably was caused by drift of the electromagnetic flowmeter and biasing of the mean velocity results from the LDA. For the Ionescu-Shiley valve it was shown that during data collection the flowmeter drifted sufficiently to give a value of the leakage-flow rate that was low by about 0.1 L/min. For the St. Jude valve, this drift may have been similar. The closure-flow rate would have remained essentially the same. For the Ionescu-Shiley valve it was also shown that the bias in the mean velocity results obtained using the LDA was 0.2 L/min for the leakage-flow rate. The bias for the St. Jude valve was probably less. As discussed above, the biasing of the mean velocity results becomes worse as the rms velocity results become greater. The average rms axial velocity was significantly less for the St. Jude valve at 27.7 cm/s than that for the Ionescu-Shiley valve at 33.5 cm/s. Thus less biasing would be expected for the St. Jude valve on the basis of the relative values of the average rms axial velocities for the two valves. Assuming a bias for the St. Jude valve of 0.1 L/min gives a forward-flow rate of 5.9 L/min and a leakage-flow rate of about -0.5 L/min. The closure-flow rate was again relatively unaffected. With the flowmeter drift and LDA biasing compensated for, the leakage-flow rates become -0.4 ± 0.1 L/min and -0.5 L/min from Table 11 and Figure 66, respectively. The forward-flow rates become 5.7 ± 0.1 L/min and 5.9 L/min, respectively. The closure-flow rates were not affected significantly. Using the forward-flow rate of 5.9 L/min, the closure-flow rate of -0.1 L/min, and the leakage-flow rate of -0.5 L/min, the percentage of regurgitant flow relative to the forward flow was

about 10%.

The adequate agreement of the results presented in Table 11 with those given in Figure 66 indicate that the LDA bias of 0.1 L/min assumed above was more nearly correct than a bias of 0.2 L/min. Had the bias been taken as 0.2 L/min, the forward-flow and leakage-flow rates would have been 5.9 L/min and -0.6 L/min, respectively. Thus, the flow rates implied by the greater biasing of 0.2 L/min agreed less well with the compensated flowmeter results than the flow rates implied by the smaller biasing of 0.1 L/min. The assumption that the LDA bias was 0.1 L/min, therefore, gives better agreement with the experimental results.

Another difficulty with the results shown in the top of Figure 66 is that the flow rate at the end of diastole is shown to have risen before the apparent beginning of the systolic ejection phase. The finite flow rates shown in Figure 66 for late diastole are probably a result of the averaging process by which the results were obtained. This phenomenon was seen in the results for the Ionescu-Shiley valve and was again caused here by variations in the time the systolic ejection interval began.

3.6.4 Discussion

3.6.4.1 Discussion of the Pressure and Volumetric-Flow results

The pressure and volumetric-flow results presented in Tables 10 and 11 indicate that the pressure and flow fields encountered by the mounted prosthesis in the pulse-duplicator were similar to those the valve might have encountered had it been implanted. The maximum rate of change of the ventricular pressure given in Table 10 of 177 ± 17 kPa/s compared well with that of a healthy human ventricle of about 195 ± 37 kPa/s (Yang, et al., 1978). Similarly, the minimum rate of change of the ventricular pressure given in

Table 10 of -307 ± 42 kPa/s was not too different from that of a healthy human ventricle of about -355 ± 29 kPa/s (Yang, et al., 1978). For the volumetric-flow results, the forward, closure, and leakage flow given in Table 11 sum to a mean flow rate, or cardiac output (CO), of 4.98 L/min. This mean flow rate was about 8% below the standard setting of the pulse-duplicator of 5.4 L/min given in Table 2. As was shown above, however, the flow-rate results in Table 11 were subject to adjustment to remove the effects of flowmeter drift. Once adjusted, the flow-rate results in Table 11 become 5.7 L/min, -0.1 L/min, and -0.4 L/min for the forward-flow, closure-flow, and leakage-flow rates, respectively. The sum of these adjusted flow rates is 5.2 L/min which is less than 4% below the setting in Table 2. Q_{max} given in Table 11 as 29.6 L/min was physiological in magnitude. Also, the timing results given in Tables 10 and 11 were physiologically appropriate. The systolic ejection interval spanned 33% of the cycle which is similar to that percentage found *in vivo* for a similar pulse rate and cardiac output. The forward-flow phase began and ended at times not significantly different from those of the systolic ejection interval. During systole, ΔP_{max} preceded both Q_{max} and VP_{max} by about 40 milliseconds. Though this difference was not significant, the order of the events was that observed *in vivo*. The time of occurrence of $\left(\frac{dP}{dt}\right)_{max}$ was appropriately located in time during the iso-volumetric contraction phase and the time of occurrence of $\left(\frac{dP}{dt}\right)_{min}$ was appropriately located in time during the iso-volumetric relaxation phase. Q_{min} signaled valve closure appropriately by occurring after the end of the systolic ejection interval but before the occurrence of $\left(\frac{dP}{dt}\right)_{min}$ in the iso-volumetric relaxation phase.

The mean systolic pressure drop resulting from these pulsatile pressure and

flow fields was similar to those reported in the literature (Emery and Nicoloff, 1979; Gombrich, et al., 1979). Emery and Nicoloff (1979) operated their pulse-duplicator at 72 beats per minute at a mean flow rate of 5.25 L/min using a blood-analog fluid of 37% glycerine and 65% saline. With a maximum aortic pressure of 16.0 kPa (gauge) and a diastolic aortic pressure of 10.7 kPa (gauge), they found a mean systolic pressure drop of of 0.9 kPa for a St. Jude valve with a TAD of 25 mm. Gombrich, et al. (1979) operated their pulse-duplicator at 72 beats per minute at a mean flow rate of 5.25 L/min using a blood-analog fluid of 37% glycerine and 65% saline. With a maximum aortic pressure of 16.0 kPa (gauge) and a diastolic aortic pressure of 10.7 kPa (gauge), they found a mean systolic pressure drop of of 0.7 kPa for a St. Jude valve with a TAD of 25 mm. $\overline{\Delta P}_{sys}$ is reported in Table 10 as 0.6 ± 0.1 kPa.

In vivo mean pressure-drop results reported in the literature have been similar to that found in the present investigation. Chaux, et al. (1979) reported "resting" mean pressure drops of 0.5 ± 0.2 kPa *in vivo* at a mean flow rate of 4 L/min. Emery, et al. (1979) reported "resting" mean pressure drops of 0.3 ± 0.1 kPa *in vivo*.

Regurgitant flow for the St. Jude valve was relatively small. The total regurgitant flow rate for this valve of 0.62 L/min was about 11% of the forward-flow rate of 5.60 L/min. Leakage flow accounted for 88% of the regurgitant flow. The magnitude of the total regurgitant flow, however, was probably less than that shown in Table 11. As was found for the Ionescu-Shiley valve, the electromagnetic flowmeter may have suffered significant drift during data collection. This drift tended to be towards lower flow rates and hence the actual regurgitant-flow rate may have been somewhat smaller, and the forward-flow rate somewhat larger, than that shown in Table 11. The effect of the performance of the electromagnetic flowmeter on the measured regurgitant-

flow rate is discussed in more detail below. $\overline{\Delta P}_{dias}$ and $\overline{\Delta P}$ were consistent with a lower level of regurgitation.

For steady flow, $\overline{Q}$ in Table 11 indicates that the steady-flow velocity results were comparable in magnitude to those for pulsatile flow. At 27 L/min, $\overline{Q}$ was about 9% smaller than Q_{max}.

The steady-flow pressure drop found in the present investigation was in the range reported in the literature (Emery and Nicoloff, 1979; Schramm, et al., 1980; Yoganathan, et al., 1983a). Emery and Nicoloff (1979) reported a steady-flow pressure drop of 0.9 kPa for a St. Jude valve with a TAD of 25 mm at a flow rate of 27 L/min. Schramm, et al. (1980) reported a steady-flow pressure drop of 0.3 kPa for a St. Jude valve with a TAD of 25 mm at a flow rate of 18 L/min. From the data of Yoganathan, et al. (1983a), a steady-flow pressure drop of 1.3 kPa was extrapolated for a St. Jude valve with a TAD of 25 mm at a flow rate of 27 L/min. Using Equation (13) with an exponent of 2.0, the results of Schramm, et al. (1980) predict a steady-flow pressure drop of 0.7 kPa at a flow rate of 27 L/min. An exponent of 2.0 in Equation (13) is consistent with the pressure-drop results presented for the St. Jude valve by Gombrich, et al. (1979), Emery and Nicoloff (1979), Gabbay, et al. (1980), Bruss, et al. (1983) and Yoganathan, et al. (1983a). $\overline{\Delta P}$ is reported in Table 10 as 1.0 ± 0.1 kPa.

The pulsatile-flow pressure drops estimated from the pressure-drop results for steady flow in the present investigation compare well with the pulsatile-flow results presented in Table 10. The pulsatile-flow pressure drops can be estimated using Equations (14) and (16). Substituting into Equation (14) the values for $\overline{\Delta P}$, $\overline{Q}$, and Q_{rms} from Tables 10 and 11, the $\overline{\Delta P}_{sys}$ calculated was 0.53 kPa. $\overline{\Delta P}_{sys}$ in Table 10 was 0.6 ± 0.1 kPa. Substituting into Equation (16) the values of $\overline{\Delta P}$, Q_{max}, and Δt_{sys} yields a value of ΔP_{max} of 2.2 kPa. ΔP_{max} in

Table 10 was 2.1 ± 0.2 kPa. Thus the pressure-drop results obtained from the steady-flow and pulsatile-flow experiments in the same flow section were consistent with one another.

3.6.4.2 Discussion of the Velocity Results

The flow downstream from the St. Jude valve was quite different from that downstream from the empty aortic-valve flow section. The flow downstream from the empty flow section, as shown in Figure 16, was axisymmetric and had a global maximum near the centerline of the tube. The rms axial velocities downstream from the St. Jude valve were significantly elevated over those downstream from the empty flow section. The average rms axial velocity across the data plane was 27.7 cm/s for the St. Jude valve and 14.0 cm/s for the empty flow section.

The flow structure downstream from the St. Jude valve appears to have been affected by the two semicircular leaflet occluders. As mentioned earlier, these two leaflets divide the base-ring orifice of the valve into three regions. Two of these regions are themselves roughly semicircular in shape. The third region is rectangular in shape with a height-to-width ratio of about five. The areas of the two semicircularly shaped regions are equal, and together represent about 78% of the area available for forward flow. The rectangularly shaped region represents about 22% of the area for forward flow. The rectangularly shaped region has an area of about 57% of that for one of the two semicircularly shaped regions. The measurements for these areas were made from photographs of a St. Jude prosthesis with a TAD of 23 mm and may be slightly different for a prosthesis with a TAD of 25 mm as used in the present investigation. The results shown in Figure 60 seem to indicate that by far the larger portion of the forward flow emerged from the two semicircularly shaped regions. The flow near the

centerline of the tube shows evidence of wakes in the flow generated by the two leaflet occluders. By the time the flow had reached the data plane the presence of these wakes had caused the velocity near the centerline of the tube to be less than the maximum. At the data plane, these wakes caused the flow through the rectangularly shaped region of the valve base-ring orifice to decelerate considerably with respect to the flow through the semicircularly shaped regions. Thus the leaflet occluders affected the flow downstream from the St. Jude valve both by triply dividing the forward flow and by generating significant flow wakes.

The relatively unobstructed flow path past the occluding mechanism of the St. Jude valve resulted in the relatively small pressure drops measured for this valve. The wakes generated by the two leaflet occluders probably contributed significantly to the pressure-drop characteristics of this valve.

The small secondary-flow structure downstream from the St. Jude valve was strongly influenced by the expanding wakes generated by the leaflet occluders. The forward flow emerging from the semicircularly-shaped regions of the valve base-ring orifice was directed only slightly outward by the 85° opening angle of the leaflet occluders. The wakes in the flow would tend to expand downstream and hence "push" that forward flow outward towards the wall even more. Vortex motion was generated in response to this forward flow that was trending outward. These vortices were, however, small in magnitude since the outward trend of the forward flow was not pronounced.

The low levels of hemolysis associated with the use of the St. Jude valve do not appear to be produced in the bulk flow. The largest estimated total shear stresses for the St. Jude valve shown in Figure 65 was 80 N/m^2 for steady and pulsatile flow, respectively. The major source of these estimated shear stresses was the high mean velocity gradients generated near the tube wall. The magnitudes of the estimated total shear stresses were large enough to activate

platelets, causing a chemical release reaction. As shown in Table 1 of Chapter 1, platelets were shown to undergo chemical release reactions at shear stresses around 20 N/m^2. The total shear stresses estimated in the present investigation were, however, probably *not* sufficient to cause damage to platelets. The estimated total shear stresses of the present investigation in the bulk flow were probably also not sufficiently elevated to account for significant hemolysis rates. Hehrlein, et al. (1980) and Wortham, et al. (1981) have reported that the hemolysis associated with the use of the St. Jude valve was insignificant. These results, however, are only preliminary and represent patient follow-up times ranging upwards to only a few years. Nonetheless, the relatively low estimated total shear stresses of the present investigation indicate that low rates of intravascular hemolysis may continue to be reported for the St. Jude valve for longer patient follow-up times. The small amount of hemolysis that has been associated with the St. Jude valve might be generated by interactions of the RBCs with the surface of the prosthesis or in high-shear regions very close to the valve superstructure.

The velocity results of the present investigation are more extensive yet consistent with the few results that have been presented in previous investigations (Schramm, et al., 1980; Bruss, et al., 1983; Yoganathan, et al., 1983a). Schramm, et al. (1980) made velocity measurements using laser ultramicroscope anemometry in steady flow at 18 L/min. They reported two large, lateral jets and a central, smaller jet emerging from a St. Jude valve with a TAD of 25 mm. Bruss, et al. (1983) made velocity measurements at about $z = 15$ mm using LDA in pulsatile flow. These investigators reported results for a single profile of the flow which showed three small peaks separated by two small dips. Yoganathan, et al. (1983a) measured the mean axial velocities at several locations downstream from a St. Jude valve with a TAD of 27 mm in steady flow

at 25 L/min. These investigators found that the flow through the rectangularly shaped region generated a strong central peak in the velocity profile at z = 5.79 mm but that by z = 44.79 mm the peak was almost gone. No peak was found by these investigators at z = 77.79 mm.

Previous investigations have failed to note the extent of the wakes downstream from the valve leaflets. This failure was because of limitations in the methods by which the results were obtained. In particular, there has been a lack of a systematic, data-plane type approach to the data collection. No information has been presented previously, therefore, which would allow an analysis of the three-dimensional aspects of the wakes generated downstream from this valve design.

Few turbulent shear stresses downstream from the St. Jude valve have been reported in the literature. Yoganathan, et al. (1983a) measured these stresses directly using multi-component LDA. They reported turbulent shear stresses in the range of 10 to 60 N/m^2 downstream from the St. Jude valve. The values reported in the present investigation are in that range. Thus the estimated shear stresses of the present investigation were on the order of that found by direct measurement.

3.6.4.3 Steady Versus Pulsatile Flow

A comparison of the steady-flow and pulsatile-flow results for the Pulsatile-flow results presented in Figures 57 through 64 show that the systolic ejection interval could be divided into three phases. Windows 4 through 9 were taken as encompassing early systole, windows 10 through 16 were taken as encompassing mid-systole, and windows 17 through 20 were taken as encompassing late systole. The flow during early systole was characterized by flat axial velocity profiles, small non-axial velocities, and relatively low rms axial velocities. The

flow during mid-systole was similar to that found for steady flow. The flow during late systole was characterized by rapidly deceleration and eventual flow reversal, a general lack of secondary-flow structure, and elevated rms axial velocities. The results thus indicate that the results for early and mid-systole can be approximated *a priori*. Late systole would be difficult to approximate *a priori*.

The pulsatile-flow results were less distinct than the steady-flow results. These differences can be attributed to the relative amount of data available from the pulsatile-flow experiments and the reproducibility of the flow from one cycle to the next. The reproducibility of the pulse-duplicator may have also contributed to the "raggedness" and "scatter" of the pulsatile-flow results.

During diastole the flow structure was affected by the fact that the occluding mechanism of the St. Jude valve allowed a small amount of flow regurgitation. As shown in Figures 57, 59, and 61, the mean velocities in the flow after valve closure decreased rapidly but did not vanish entirely. Small, negative mean velocities were present throughout diastole. The mean non-axial velocities, which were very small at the beginning of diastole as shown in Figure 63, became even smaller as diastole progressed. The finite axial velocities resulted from the small area available for reverse flow through the fully closed valve and the diastolic pressure gradient which provided the driving force for flow.

The flow at the beginning of each cycle thus was not entirely quiescent. During a pulsatile-flow experiment, therefore, the results for a given cycle were based on the flow generated by the previous cycle at the end of diastole and not *on a perfectly quiescent fluid.*

The amount of regurgitant flow during diastole was determined both with the electromagnetic flowmeter and using the mean axial velocity results. The

regurgitant-flow rate results from the flowmeter were given in Table 11. The regurgitant-flow rate results from the mean axial velocity results were given in Figure 66. As discussed earlier, however, the results in Table 11 and Figure 66 required adjustment to remove the effects of flowmeter drift and data biasing. Once these effects had been removed, the closure-flow and leakage-flow rates were calculated to be 2% and 8%, respectively, of the forward-flow rate. The total regurgitant-flow rate was 10% of the forward flow.

Other investigations have reported similar values for the percentage of total regurgitation through the St. Jude valve in pulsatile flow. Emery and Nicoloff (1979) measured flow regurgitation for a St. Jude valve with a TAD of 25 mm. For a pulse rate of 72 beats per minute, a mean flow rate of 5.25 liters per minute, a maximum aortic pressure of 13.3 kPa, and a diastolic aortic pressure of 10.7 kPa, they found the total regurgitant flow to be 9% of the forward flow. Gombrich, et al. (1983) measured flow regurgitation for size 25 and 27 St. Jude valves. For a pulse rate of 72 beats per minute, a mean flow rate of 5.25 liters per minute, a maximum aortic pressure of 13.3 kPa, and a diastolic aortic pressure of 10.7 kPa, they found the total regurgitant flow to be 8% of the forward flow. Dellsperger, et al. (1983) also measured flow regurgitation for a St. Jude valve with a TAD of 27 mm. For a pulse rate of 80 beats per minute, a mean flow rate of 6 liters per minute, and an average aortic pressure of 13.3 kPa, they found the total regurgitant flow to be 11.9% of the forward flow.

A further comparison of the results for steady flow with those for pulsatile flow can be made from the results shown in Figure 66. The flow-rate results in Figure 66 show that the flow rate during the middle of systole was comparable to that for steady flow. The pulsatile-flow results were within 10% of the steady-flow result over much of mid-systole.

The average rms axial velocities plotted in the bottom of Figure 66 show that the magnitude of the fluctuating velocities was dependent upon the systolic phase. During early systole, the average rms axial velocities were not very different from that for windows during diastole. During mid-systole, the average rms axial velocities went through a well-defined maximum and began to decrease before late systole. During late systole, the rms axial velocities dropped but overall remained elevated. A small "peak" can be seen at window 21, one window after maximum reverse flow occurred. This one-window delay may not be significant. It appears from the top of Figure 66 that the maximum reverse flow occurred near the end of window 20. The value of the flow rate at window 21 was relatively close to that at window 20. The inherent uncertainty in timing events using the 20-millisecond windows was ± 10 milliseconds. Thus, the "peak" in the plot on the bottom of Figure 66 may have occurred at a time not significantly different from the maximum reverse flow. This apparent one-window delay may be a manifestation of the delay in the maximum average rms velocity relative to the maximum forward flow discussed in earlier sections and mentioned again below.

The average rms axial velocities shown in Figure 66 show that the rms axial velocities measured in steady flow were generally larger than those found in pulsatile flow. Thus, the rms velocities for steady flow tended to be an upper bound on the rms velocities for pulsatile flow.

For the St. Jude valve, the maximum average rms axial velocity was measured two windows after the maximum flow rate. This two-window delay is consistent with the calculation made earlier which suggested that the flow disturbance measured at the data plane was generated at the valve and convected to the data plane.

The average rms axial velocities plotted in the bottom of Figure 66 seem to have a base-line value near 4 cm/s. This base-line is similar to that seen for the Ionescu-Shiley valve and probably also stems from the "cascading" energy from the mean velocity field during diastole.

3.6.5 Conclusions

The flow structure downstream from the St. Jude valve was in many aspects unlike that found downstream from the empty aortic-valve flow section. The flow showed evidence of wakes generated by the two leaflets of the occluding mechanism of the valve. The extent of the flow disturbance associated with these wakes suggest that they may play a significant role in generating the pressure drop found for this valve. Only small secondary-flow structures were found indicating that the occluding mechanism of this valve imparted very little lateral or azimuthal sense to the forward flow.

The mean velocity gradients were elevated at the tube wall which implied high shear stresses in the flow near the wall. These high shear stresses were probably not of a magnitude that would be associated with significant hemolysis *in vivo*. Shear stresses in the bulk flow were only moderate in magnitude and were less than the level generally considered hemolytic. Sub-lethal damage of RBCs, however, may occur in the bulk flow. The estimated total shear stresses were sufficient to activate platelets and cause a chemical release reaction. The presence in the flow of activated platelets increases the possibility of thrombus formation and hence valve thrombosis and thromboembolic events.

The St. Jude valve was found to have a relatively small pressure drop in both steady and pulsatile flow and to allow only limited flow regurgitation in pulsatile flow. Thus the bi-leaflet design of this prosthesis has shown relatively superior hemodynamics.

A comparison of steady-flow and pulsatile-flow results showed that i) the steady-flow results approximated those for pulsatile flow only during the middle of systole and ii) the rms velocities for steady flow provided an upper bound to those found in pulsatile flow. The results indicated that the systolic ejection interval could be divided into three phases: early systole, mid-systole, and late systole. For each phase of systole the flow structure was significantly different. The flow structure of mid-systole was most similar to that for steady flow. The steady-flow results were quite different from those for pulsatile flow during early and late systole. It was found that early systole could be estimated *a priori* as plug flow. Late systole would be difficult to predict *a priori*. Pulsatile-flow results in diastole were found to have structure which were not predictable from the steady-flow results. The results from the steady-flow experiments, therefore, were limited in their ability to provide an understanding of the pulsatile flow. It was concluded that steady flow results can provide some knowledge of the flow fields downstream from the St. Jude valve but only for a relatively small portion of systole.

4. VALVE COMPARISON STUDIES

4.1 COMPARISON OF PRESSURE AND VOLUMETRIC-FLOW RESULTS

The four valves of the present investigation are compared in this section with regard to their pressure-drop and regurgitant-flow characteristics. The St. Jude valve was found to generate the lowest pressure drop of the four valves while the Smeloff valve generated the highest. The forward flow-rate results for the four valves were comparable. The hydraulic performance, which depended on both the pressure-drop and flow-rate results, was therefore best for the St. Jude valve and least favorable for the Smeloff valve. The Smeloff valve also allowed the most regurgitant flow of the four valves while the Ionescu-Shiley valve allowed the least. The Ionescu-Shiley valve as expected allowed the least regurgitant flow because it was the only totally-occluding valve of the four valves studied. The St. Jude valve allowed the least regurgitant flow of the three valves studied which were *not* totally-occluding valves.

4.1.1 Pressure-Drop Comparison

Table 12 shows the pressure-drop results for the four valves studied in the present investigation. The valves are listed in the order of increasing pressure drop. The Ionescu-Shiley and Björk-Shiley convexo-concave valves had similar mean pressure drops in steady and pulsatile flow, the Ionescu-Shiley valve had a higher maximum pressure drop in pulsatile flow. The higher maximum pressure drop for the Ionescu-Shiley valve was not, however, significantly different from that for the Björk-Shiley convexo-concave valve as is indicated by the values for the standard deviations.

The results presented in Table 12 were obtained for valves tested under identical testing conditions in the same experimental rig. For steady flow, the flow rate was 27 L/min for all four valves. For pulsatile flow, the pulse-

Table 12

Comparison of the Pressure-Drop Results for the Four Prosthetic Aortic Heart Valves Studied in the Present Investigation*

	Mean Steady Flow Pressure Drop (kPa)	Maximum Pulsatile Flow Pressure Drop (kPa)	Mean Systolic Pressure Drop (kPa)	Systolic Ejection Interval (ms)
St. Jude (25 mm)	1.0 ± 0.1	2.1 ± 0.2	0.6 ± 0.1	283 ± 19
Björk-Shiley convexo-concave (25 mm)	1.4 ± 0.1	2.6 ± 0.2	0.8 ± 0.2	289 ± 14
Ionescu-Shiley (25 mm)	1.3 ± 0.1	2.9 ± 0.2	0.8 ± 0.1	293 ± 16
Smeloff (24 mm)	2.2 ± 0.2	3.3 ± 0.3	1.3 ± 0.2	282 ± 8

*Results given as mean ± standard deviation.

duplicator was operated at the settings given in Table 2 for all four valves. For both steady and pulsatile flow the valves were mounted in the aortic-valve flow section squarely so that in turn the axis of each valve was made coincident with the centerline of the flow section tube.

The systolic ejection intervals given in Table 12 are the time intervals over which the mean systolic pressure drops were averaged for each valve. The maximum difference of these intervals between the four valves was less than 4%. The mean systolic pressure drops can thus be compared directly since they were calculated on an equal basis.

The results presented in Table 12 indicate that the St. Jude valve generated a significantly smaller pressure drop than the other three valves in the present investigation in both steady and pulsatile flow. The difference between the mean systolic pressure drops of the St. Jude valve and the Björk-Shiley convexo-concave valve, the valve with the next lowest pressure drops, was insignificant. The mean systolic pressure drop for the St. Jude valve averaged, however, 25% less than that for the Björk-Shiley convexo-concave valve. The Björk-Shiley convexo-concave valve generated a pressure drop insignificantly different from the Ionescu-Shiley valve in steady and pulsatile flow but generated a maximum pressure drop in pulsatile flow which averaged more than 10% lower than that for the Ionescu-Shiley valve. Finally, the Smeloff valve generated a significantly larger pressure drop than the Ionescu-Shiley valve. The difference between the maximum systolic pressure drops of the Smeloff valve and the Ionescu-Shiley valve was not significant. The maximum systolic pressure drop for the Smeloff valve averaged, however, more than 12% greater than that for the Ionescu-Shiley valve.

4.1.2 Flow-Rate Comparison

Table 13 shows the flow-rate results for the four valves studied in the present investigation. The valves are listed in the order of increasing regurgitant flow. The total flow rate was the sum of the forward, closure, and leakage flow rates. Flow-rate results are presented in Table 13 which were determined both from measurements made by the electromagnetic flowmeter and from integrating the mean axial velocity results from the LDA. As discussed in Chapter 3, the flow-rate results obtained for the Ionescu-Shiley valve indicated that the flowmeter had suffered some drifting during data collection and that the LDA had allowed the mean axial velocities to be slightly biased. Quantitatively compensating for the flowmeter drift and the LDA bias was possible based on the fact that the Ionescu-Shiley valve allowed no leakage flow when closed. The values of zero (0.0) for the leakage-flow rate of the Ionescu-Shiley valve in Table 13, therefore, were established on practical grounds. The remaining flow rates reported in Table 13 were then determined after giving due consideration to this flowmeter drift and LDA biasing. The close agreement between the flowmeter and LDA results as presented in Table 13, indicates that these independently compensated sets of results are accurate within their experimental uncertainty. Generally, the experimental uncertainty for both the flowmeter and LDA results was about 0.1 L/min. The experimental uncertainty for the closure flow was smaller at about 0.05 L/min.

The results presented in Table 13 show that as the closure-flow and leakage-flow rates increased, the forward-flow rate did also. The increases of these flow rates were balanced so that the total flow rate remained relatively constant from valve design to valve design.

The forward-flow rate for the Ionescu-Shiley valve was about 15% lower than that for the Smeloff valve. It is interesting to note that in spite of this 15%

Table 13

Comparison of the Flow-Rate Results for the Four Prosthetic Aortic Heart Valves Studied in the Present Investigation

	Forward Flow Rate* (L/min)		Closure Flow Rate** (L/min)		Leakage Flow Rate* (L/min)		Total Flow Rate* (L/min)	
	flow-meter+	LDA++	flow-meter+	LDA++	flow-meter+	LDA++	flow-meter+	LDA++
Ionescu-Shiley (25 mm)	5.6	5.7	-0.2	-0.2	0.0	0.0	5.4	5.5
St. Jude (25 mm)	5.7	5.9	-0.1	-0.1	-0.4	-0.5	5.2	5.3
Björk-Shiley convexo-concave (25 mm)	6.5	6.4	-0.1	-0.1	-1.0	-0.9	5.4	5.4
Smeloff (24 mm)	6.7	6.6	-0.1	-0.1	-1.3	-1.1	5.3	5.4

*Experimental uncertainty: ± 0.1 L/min.

**Experimental uncertainty: ± 0.05 L/min.

+Flow rate measured using the electromagnetic flowmeter.

++Flow rate determined from the axial velocities measured using the LDA.

difference, the maximum flow rate for the Ionescu-Shiley valve was not significantly different from that for the Smeloff valve. As given in Tables 5 and 9, the maximum flow rate for the Ionescu-Shiley and Smeloff valves was 29.8 ± 0.3 L/min and 30.4 ± 0.4 L/min, respectively. To allow for the additional forward flow, the flow rate for the Smeloff valve increased more rapidly than that for the Ionescu-Shiley valve, achieved a comparable maximum, and then decreased more slowly. This more rapid acceleration of the flow rate helps explain the early appearance at the data plane of the flow disturbance generated at the valve. In Figure 46 it was shown that the flow disturbance arrived at the data plane during window 8 for the Smeloff valve. The disturbance manifested itself by causing the flow structure to deviate noticeably from the flat velocity profiles characteristic of early systole. In Chapter 3 this early arrival of the flow disturbance for the Smeloff valve was attributed to the fact that the disturbance may have been generated on the superstructure of the valve nearer the data plane. The phenomenon of rapid flow acceleration, however, probably also contributed to the early arrival of the disturbance. Moreover, this same phenomenon probably also occurred for the Björk-Shiley convexo-concave valve. In Figure 34 it can be seen that some flow disturbance is noticeable at the data plane also by window 8. The disturbance again manifested itself by causing the flow structure to deviate from the flat velocity profiles of early systole. For the Ionescu-Shiley and St. Jude valves, disturbance was not noticeable until windows 9 and 10, respectively.

The closure-flow rate given in Table 13 for the Ionescu-Shiley valve probably includes effects of the compliance of the tissue of which the valve was constructed. The closure-flow rate for the Ionescu-Shiley valve was larger than that for the other three valves. The occluding mechanism of the Ionescu-Shiley valve would not, however, be expected to require significantly more regurgitant

flow to close. Some of the closure flow which was *measured* was probably not flow back through the Ionescu-Shiley valve. Once the leaflets of the Ionescu-Shiley had sealed the orifice, their compliance allowed them to "balloon" slightly backwards in response to the rapidly increasing diastolic pressure drop. If the volume of fluid displaced by this "ballooning" was about one cubic centimeter each cycle, then the closure-flow rate for this valve would have been closer to -0.1 L/min.

4.1.3 Hydraulic Performance Comparison

The relative hydraulic performance of the valves studied in the present investigation can be determined from the pressure-drop and flow-rate results for both steady and pulsatile flow. Using the energy balance of Equation (18), an expression can be derived for the orifice area of the valve in terms of the pressure drop and flow rate. The pertinent equations for both steady and pulsatile flow are derived below. The orifice area determined by these equations, however, is generally smaller than the actual orifice area of the valve base-ring. As indicated in Chapter 3, the occluding mechanisms of most prosthetic valves generate large wakes or separated-flow regions, or both. These separated-flow regions and wakes serve to increase the pressure drop across the valves beyond that pressure drop which would be attributed only to the constriction of the flow through the primary flow orifice of the valve. This generally smaller, calculated orifice area is called the "effective orifice area," or EOA, of the valve.

An expression for the EOA of a valve can be derived from the steady-state macroscopic mechanical energy balance assuming negligible friction losses and using continuity. Assuming negligible friction losses, Equation (18) becomes

$$\frac{1}{2}(\bar{v}_2^2 - \bar{v}_1^2) = \frac{1}{\rho}(p_1 - p_2) . \tag{27}$$

From continuity, for ρ constant,

$$Q = \bar{v} A_f , \tag{28}$$

where Q is the volumetric flow, $\bar{v}$ is the average flow across the flow section, and A_f is the cross-sectional area available for flow. Let $A_{f,1}$ and $\bar{v}_1$ be the cross-sectional area of the flow section and the mean axial velocity across the flow section, respectively, upstream from the valve mount. Also, let $A_{f,2}$ and $\bar{v}_2$ be the cross-sectional area of the valve base-ring orifice and the mean axial velocity across the base-ring orifice, respectively. Then substituting Equation (28) into Equation (27) gives

$$\frac{Q^2}{2}\left[\frac{1}{A_2^2} - \frac{1}{A_1^2}\right] = \frac{1}{\rho}(p_1 - p_2) . \tag{29}$$

Rearranging and taking the square root, Equation (29) becomes

$$\frac{1}{\left[\frac{1}{A_2^2} - \frac{1}{A_1^2}\right]^{\frac{1}{2}}} = \frac{Q}{2^{\frac{1}{2}}\left[\frac{p_1 - p_2}{\rho}\right]^{\frac{1}{2}}} . \tag{30}$$

Now let $A_2 = \alpha A_1$, where $\alpha < 1$, and substitute into Equation (30), then

$$A_2 = \frac{(1 - \alpha^2)^{\frac{1}{2}}}{2^{\frac{1}{2}}} \frac{Q}{\left[\frac{p_1 - p_2}{\rho}\right]^{\frac{1}{2}}} . \tag{31}$$

For small α, $(1 - \alpha^2)^{\frac{1}{2}} \approx 1$ and Equation (31) becomes finally

$$A_2 = \frac{1}{2^{\frac{1}{2}}} \frac{Q}{\left[\frac{p_1 - p_2}{\rho}\right]^{\frac{1}{2}}} . \tag{32}$$

Although it is not strictly correct, the pressure drop in Equation (32), $\Delta P = p_1 - p_2$, has usually been taken as the total pressure drop across the valve.

This practice has come about because of the very common use of expressions similar to Equation (32) for clinical evaluations (Gorlin and Gorlin, 1951). Equation (32) was derived for the pressure drop from just upstream from the valve to the valve base-ring. This latter pressure drop is, however, much more difficult to measure *in vivo* than the former. Thus, for steady flow, Equation (32) becomes

$$EOA = \frac{1}{8.49} \frac{\bar{Q}}{(\overline{\Delta P})^{\frac{1}{2}}} \qquad \text{(steady flow)} . \qquad (33)$$

where EOA is in cm^2, Q is in L/min, and ΔP is in kPa. In Equation (33) ρ has been taken as 1000 kg/m^3. In the medical literature Q and ΔP are often given in cm^3/s and torr (mm Hg). For Q and ΔP given in cm^3/s and torr, respectively, the constant in Equation (33) becomes $\frac{1}{51.6}$. Equation (33) is valid for steady flow only. Using Equation (14), however, a similar equation to Equation (33) can be derived for pulsatile flow, thus

$$EOA = \frac{1}{8.49} \frac{Q_{rms}}{(\overline{\Delta P}_{sys})^{\frac{1}{2}}} \qquad \text{(pulsatile flow)} . \qquad (34)$$

Equations (33) and (34) were used to determine the EOA for the four valves of the present investigation in steady and pulsatile flow, respectively.

Table 14 shows the steady-flow EOA's calculated using Equation (33) for the four valves studied in the present investigation. The performance index (PI) is given in Table 14 along with the EOA results. The PI is defined as the EOA divided by the area of an orifice with an inner diameter equal to the valve's mounting diameter. The valves are listed in the same order as in Table 12.

The results in Table 14 show that all of the valves generated some effective constriction of the flow. The performance index was considerably less than one for all four valves. Note that the order of the ranking of the valves by pressure

Table 14

Comparison of the Effective Orifice Areas and Performance Indices in Steady Flow for the Four Prosthetic Aortic Heart Valves Studied in the Present Investigation

	Mean Pressure Drop (kPa)	Mean Flow Rate (L/min)	Effective Orifice Area (cm^2)	Performance Index*
St. Jude (25 mm)	1.0 ± 0.1	27	3.18	0.65
Björk-Shiley convexo-concave (25 mm)	1.4 ± 0.1	27	2.69	0.55
Ionescu-Shiley (25 mm)	1.3 ± 0.1	27	2.79	0.57
Smeloff (24 mm)	2.2 ± 0.1	27	2.14	0.47

*Performance index based on the valve mounting diameter.

**Mean ± standard deviation.

drop from Table 12 was similar to that by EOA or PI. The order of these rankings were expected to be similar since the mounting diameters and the steady-flow mean flow rates were similar for all four valves. The steady-flow results were essentially the same for the Björk-Shiley convexo-concave and Ionescu-Shiley valves.

Table 15 shows the pulsatile-flow EOA's calculated using Equation (34) for the four valves studied in the present investigation. The PI in Table 15 is again defined for the valves as the EOA divided by the area of an orifice with an inner diameter equal to the valve's mounting diameter. The rms systolic flow rates given in Table 12 are those from Tables 5, 7, 9, and 11 for the respective valves. The valves are listed in the same order as in Table 12.

The results in Table 15 show that in pulsatile flow as for steady flow, all of the valves generated some effective constriction of the flow. The performance index was considerably less than one for all four valves. Note again that the order of the ranking of the valves by pressure drop from Table 12 was similar to that by EOA or PI. The order of these rankings was expected to be similar since the mounting diameters and the rms systolic flow rates were similar for all four valves.

The results in Tables 14 and 15 allow a further comparison of results for steady flow versus those for pulsatile flow. For the Björk-Shiley convexo-concave and Smeloff valves, the PI for pulsatile flow was essentially that for steady flow. For the St. Jude and Ionescu-Shiley valves the PI for pulsatile flow was somewhat smaller than that for steady flow. The order of the ranking of the valves, however, was not affected by these differences between steady and pulsatile flow. Thus EOA and PI results in steady flow determined using Equation (33) were similar to those results in pulsatile flow determined using Equation (34).

Table 15

Comparison of the Effective Orifice Areas and Performance Indices in Pulsatile Flow for the Four Prosthetic Aortic Heart Valves Studied in the Present Investigation

	Mean Systolic Pressure Drop (kPa)	rms Systolic Flow Rate (L/min)	Effective Orifice Area (cm^2)	Performance Index*
St. Jude (25 mm)	0.6 ± 0.1**	19.7 ± 0.1**	3.00	0.61
Björk-Shiley convexo-concave (25 mm)	0.8 ± 0.2	20.6 ± 0.1	2.71	0.55
Ionescu-Shiley (25 mm)	0.8 ± 0.1	19.5 ± 0.1	2.57	0.52
Smeloff (24 mm)	1.3 ± 0.2	21.0 ± 0.1	2.17	0.48

*Performance index based on the valve mounting diameter.

**Mean ± standard deviation.

4.1.4 Regurgitant-Flow Comparison

Table 16 shows the regurgitant-flow results for the four valves studied in the present investigation. An attempt was made in the present investigation to keep the total flow rate constant and not the mean aortic pressure as in the work of Dellsperger, et al. (1983). The valves are listed in the order of increasing regurgitant flow. The regurgitant flow is given in Table 16 as percentages of the forward flow. The flow rates used for the percentage calculations were the averages of the two respective values given in Table 13. The percentages for the closure and leakage flow do not sum to the percentage for the total regurgitant flow for the Björk-Shiley convexo-concave and Smeloff valves because of rounding off of the results.

The mean diastolic pressure drop and the mean aortic pressure are presented in Table 16 along with the regurgitant-flow results. As alluded to in Chapter 3, both the mean diastolic pressure drop and the mean aortic pressure decrease as the percentage of the total regurgitant flow increases. For the mean aortic pressure, the decrease was not significant between the valve designs except between the Björk-Shiley convexo-concave and Smeloff valves. For the mean diastolic pressure drop, the decrease was significant between all valve designs.

The results presented in Table 16 show that the four valves studied in the present investigation allowed total regurgitant flows over a wide range of the percentage of the forward flow. As a totally occluding valve, the Ionescu-Shiley was found to have no leakage flow. Thus only the flow required by this prosthesis for closure contributed to the total regurgitant flow. The total regurgitant flow for the Ionescu-Shiley valve was therefore very small at 3% of the total regurgitant flow. The discussion above regarding the compliance of this valve's leaflets suggests that the actual total regurgitant flow was somewhat

Table 16

Comparison of the Regurgitant-Flow Results for the Four Prosthetic Aortic Heart Valves Studied in the Present Investigation

	Mean Diastolic Pressure Drop (kPa)	Mean Aortic Pressure (kPa)**	Closure Flow* (percent of forward flow)	Leakage Flow* (percent of forward flow)	Total Regurgitant Flow* (percent of forward flow)
Ionescu-Shiley (25 mm)	11.9 ± 0.4+	13.3 ± 0.6+	3%	0%	3%
St. Jude (25 mm)	10.8 ± 0.2	12.5 ± 0.3	2%	8%	10%
Björk-Shiley convexo-concave (25 mm)	10.2 ± 0.3	12.1 ± 0.4	2%	15%	16%
Smeloff (24 mm)	9.3 ± 0.4	10.3 ± 0.4	2%	18%	19%

*Flow rates used for percentage calculations were the averages of the two respective values given in Table 13.

**Gauge pressure.

+Mean ± standard deviation.

smaller even than that shown in Table 16. The St. Jude valve allowed only a modest leakage flow of 8%. When summed with the apparently obligatory 2% closure flow, the leakage flow resulted in a total regurgitant flow of 10%. The Björk-Shiley convexo-concave valve allowed a surprisingly large leakage flow of about 15%. Summing the closure and leakage flow for this valve gave a total regurgitant flow of 16%. The Smeloff valve allowed a slightly larger leakage flow of 18%. The total regurgitant flow for this valve was 19%.

The cross-sectional area available for regurgitant flow through the closed prostheses correlates qualitatively with the total regurgitant flow measured. Figure 67 shows a photograph of each of the valves of the present investigation oriented so that the cross-sectional area available for regurgitant flow through the closed prostheses can be seen. The photographs were taken in air at atmospheric pressure. The three mechanical valves' occluding mechanisms were held closed by the force of gravity. A small, unoccluded area in the center of the Ionescu-Shiley valve can be seen in Figure 67. This small area vanished when the pressure drop across the valve during diastole was applied. Thus the occluding mechanism of the valve totally occluded the valve's orifice and allowed no leakage flow.

For the St. Jude valve, a thin, interrupted annular unoccluded area can be seen between the curved edges of the leaflet occluders and the valve base-ring. Between the straight edges of the two leaflets a very thin unoccluded region is visible with small rectangularly shaped areas at either end near the hinge mechanisms. Because of the design of the St. Jude valve some of these areas may have decreased in size when the pressure drop across the valve was applied during diastole. Additional pressure on the downstream face of the two leaflets attempted to rotate these leaflets back through the base-ring orifice. The net effect of diastolic pressure was thus to push i) the curved edges of the leaflets

Figure 67. Prosthetic aortic heart valves used in the present investigation showing area available for regurgitant flow through the closed prostheses.

closer to the inner aspect of the valve base ring and ii) the straight edges of the leaflets closer to one another. The unoccluded area of the closed St. Jude valve under diastolic pressure was therefore smaller than that shown in Figure 67.

For the Björk-Shiley convexo-concave valve, a thin, interrupted annular unoccluded area can be seen between the edge of the occluder and the valve base-ring. Unlike the previous two valves, the unoccluded area for regurgitant flow through the closed Björk-Shiley convexo-concave valve did not change when the diastolic pressure was applied. Thus the unoccluded area of the closed valve under diastolic pressure was that unoccluded area visible in Figure 67. In Figure 67, the unoccluded area of the Björk-Shiley convexo-concave valve appears to be only slightly larger than that for the St. Jude valve. As discussed above, however, the unoccluded area of the St. Jude valve under diastolic pressure was smaller than that shown in Figure 67. Hence, the smaller leakage flow for the St. Jude valve was likely due to the fact that this valve occluded more of its orifice under diastolic pressure.

For the Smeloff valve, a thin annular unoccluded area can be seen between the diameter of the ball and the valve base-ring. Like the Björk-Shiley convexo-concave valve, the unoccluded area for regurgitant flow through the Smeloff valve did not change when the diastolic pressure was applied. Thus the unoccluded area of the closed valve under diastolic pressure was that unoccluded area visible in Figure 67. In Figure 67, the unoccluded area of the Smeloff valve appears to be considerably larger than that for the Björk-Shiley convexo-concave valve. Since neither of these two valves occluded more of its orifice under diastolic pressure, the larger total regurgitant flow for the Smeloff valve was due to its larger unoccluded area when closed.

The unoccluded areas visible in Figure 67 thus correlate qualitatively with the leakage flows in Table 16. Since the leakage flow makes up between 80% and 90%

of the total regurgitant flow, the unoccluded areas visible in Figure 67 also correlate qualitatively with the total regurgitant flows in Table 16.

4.2 COMPARISON OF VELOCITY RESULTS

4.2.1 Forward-Flow Results

The four valves of the present investigation were compared with regard to velocity results obtained downstream during forward flow at the data plane at z = 31.8 mm. The Ionescu-Shiley generated the highest mean axial velocities of the four valves compared. The Ionescu-Shiley valve also generated the highest mean velocity gradients and rms axial velocities in the bulk flow away from the tube wall. The Ionescu-Shiley valve was the only valve to generate regions of separated flow which could be measured at the data plane. The Björk-Shiley convexo-concave valve generated the highest mean velocity gradients near the tube wall and also generated the largest mean non-axial velocity components. The high gradients at the wall and the large non-axial velocities resulted from the considerable acentricity of the forward flow generated by this tilting disc valve. The Smeloff and St. Jude valves generated relatively low values for the maximum mean axial velocity across the data plane. The mean non-axial and rms axial velocities for these two valves were also relatively small.

The mean axial velocity results for the four valves are presented as contours in Figures 68 and 69 for steady flow and for the window in pulsatile flow corresponding to maximum forward flow. The results presented in Figures 68 and 69 were presented earlier in Figures 22, 37, 49, and 60.

The results presented in Figures 68 and 69 indicate that the valve designs studied in the present investigation all generated axial flow structures unique to their design. The Ionescu-Shiley valve generated a triangularly shaped centrally located jet of fluid containing very high mean axial velocities up to more than

FORWARD FLOW

MEAN AXIAL VELOCITIES

Steady Flow Pulsatile Flow

IONESCU-SHILEY (25 mm)

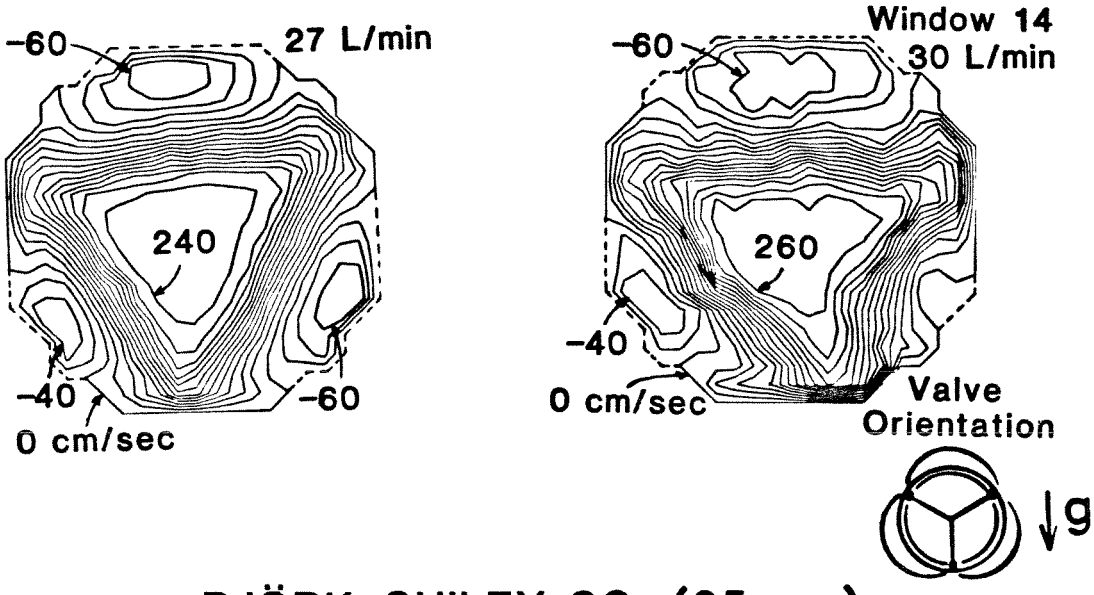

BJÖRK-SHILEY CC (25 mm)

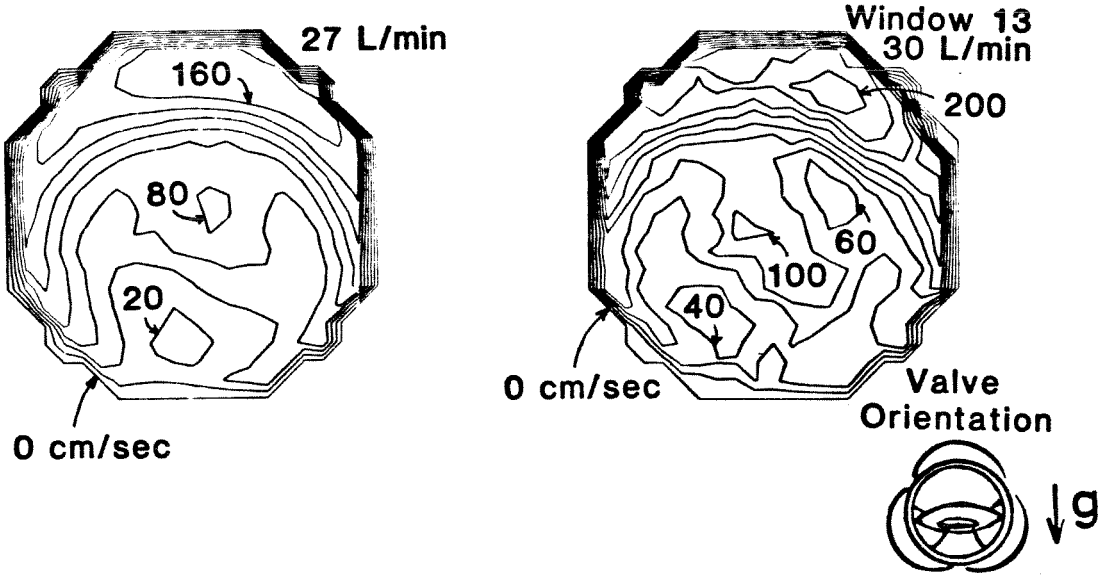

Figure 68. Mean axial velocities for steady flow and during maximum forward flow for pulsatile flow downstream from the Ionescu-Shiley (25 mm) and Björk-Shiley convexo-concave (25 mm) prostheses at z = 31.8 mm. Contour interval: 20 cm/s.

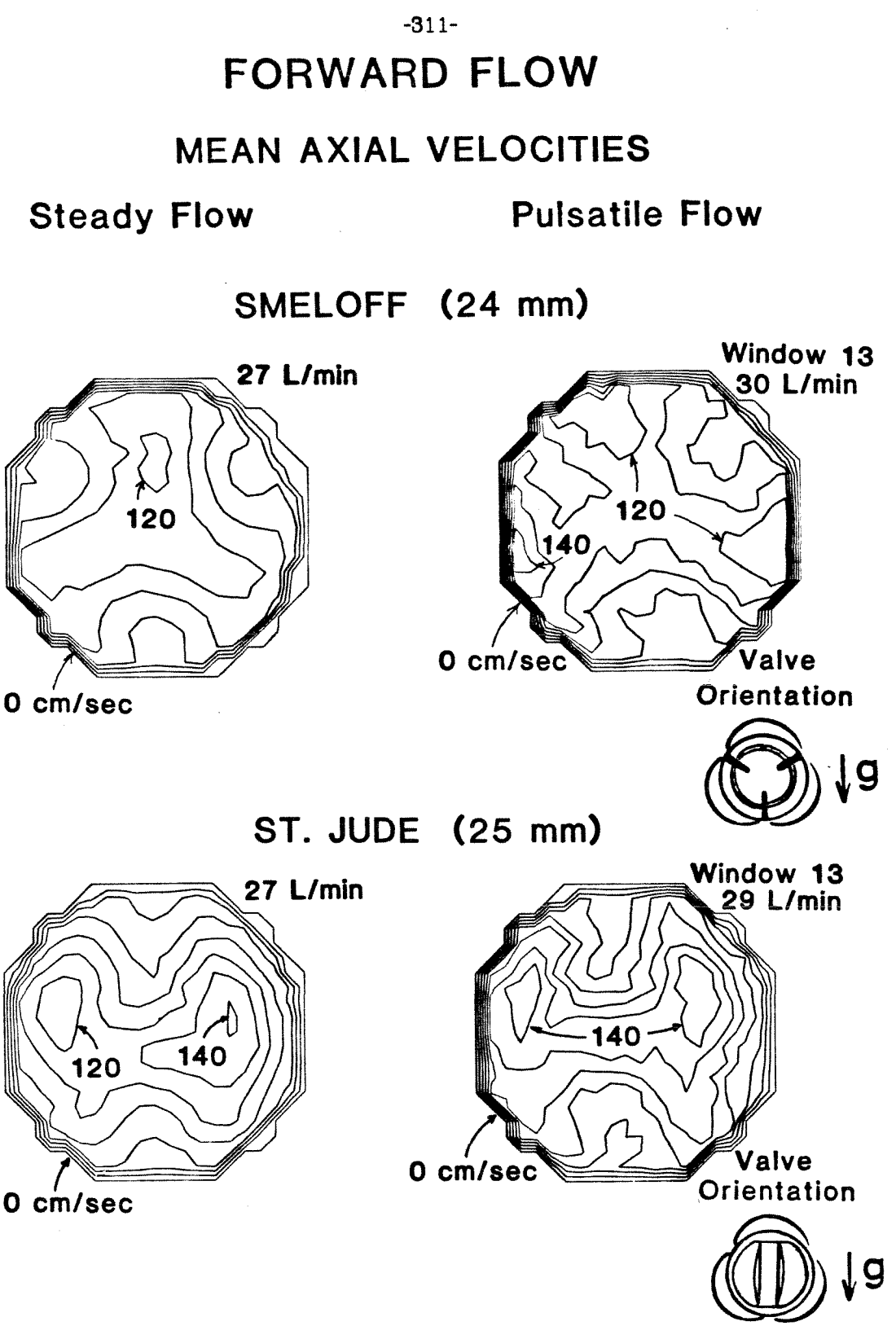

Figure 69. Mean axial velocities for steady flow and during maximum forward flow for pulsatile flow downstream from the Smeloff (24 mm) and St. Jude (25 mm) prostheses at z = 31.8 mm. Contour interval: 20 cm/s.

240 cm/s. These high mean axial velocities dropped off quickly away from the tube centerline giving rise to relatively large mean velocity gradients in the bulk flow. The Ionescu-Shiley valve also generated regions of flow separation which were observable downstream at the data plane located at z = 31.8 mm. The Björk-Shiley convexo-concave valve generated a large, lenticularly shaped jet of fluid which was located very close to approximately half of the circumference of the tube wall. This large, acentric jet contained high mean axial velocities rising beyond 160 cm/s. A second, much smaller jet was generated by the Björk-Shiley convexo-concave valve near the centerline of the tube. This centrally located jet, which was much smaller in cross-sectional area than the first and contained mean axial velocities only about half that of the the first, was generated by the flow through the minor outflow region. Regions of low velocity were also generated by the Björk-Shiley convexo-concave valve which were observed at the data plane. The largest of these low-velocity regions were located near the tube wall on the opposite side of the tube from the maximum of the large, lenticularly shaped jet. The Smeloff valve generated three maxima in the mean axial velocities interspersed with three regions of lower velocities. A "saddle point" in the mean axial velocities was observed near the center of the tube. The maxima for the Smeloff valve were not very distinct and rose to only about 120 cm/s. Thus only very small mean velocity gradients were generated in the bulk flow. The St. Jude valve generated two maxima in the mean axial velocities interspersed with two regions of lower velocities. Thus a "saddle point" in the mean axial velocities was also observed for the St. Jude valve as was observed for the Smeloff valve. The maxima for the St. Jude valve rose to about 140 cm/s and were a little more distinct than those for the Smeloff valve. Only very small mean velocity gradients were generated by the St. Jude valve in the bulk flow.

From Figures 68 and 69 it is clear that some valve designs subject the

forward flow to considerably more acceleration than other designs. The valve designs which cause greater relative acceleration of the fluid are those which more narrowly constrict the flow through them. Large flow constrictions imply high mean velocity gradients which, in turn, imply high shear stresses. The relative acceleration of the fluid flowing through the mounted valves can be compared by defining an acceleration ratio. The acceleration ratio is the maximum mean axial velocity measured downstream from the valve at z = 31.8 mm divided by the maximum mean axial velocity measured for the fully developed turbulent pipe flow at 27 L/min of 105 cm/s. The developed pipe flow represents flow totally unaffected by valve superstructure and flow-section geometry. The acceleration ratios thus defined are given in Table 17 as determined for each of the four valves in steady and pulsatile flow and for the empty flow section. Predictably, the acceleration ratio for the empty flow section was the lowest of those in Table 17. No pulsatile-flow results were obtained for the empty flow section. The four valves are listed in the order of increasing acceleration ratio. At the data plane location of z = 31.8 mm, the Smeloff valve had the smallest acceleration ratio at 1.2 for steady flow and 1.4 for pulsatile flow. The Ionescu-Shiley valve had the largest acceleration ratio at 2.4 for steady flow and 2.6 for pulsatile flow. The experimental uncertainty in these ratios was ± 0.1. The acceleration ratio for pulsatile flow was equal to or greater than that for steady flow but the order of ranking remained essentially the same in either case.

The mean non-axial velocity results for the four valves are presented as resultants in Figures 70 and 71 for steady flow and for the window in pulsatile flow corresponding to maximum forward flow. The results presented in Figures 70 and 71 were presented earlier in Figures 24, 39, 51, and 62.

Table 17

Comparison of the Maximum Acceleration of the Fluid through the Four Prosthetic Aortic Heart Valves Studied in the Present Investigation*

	Acceleration Ratio**	
	Steady Flow+	Pulsatile Flow++
Empty Flow Section (25.4 mm)	1.1	-
Smeloff (24 mm)	1.2	1.4
St. Jude (25 mm)	1.4	1.4
Björk-Shiley convexo-concave (25 mm)	1.6	2.0
Ionescu-Shiley (25 mm)	2.4	2.6

*Results for empty flow section also included as base-line.

**The acceleration ratio is defined as the maximum mean axial velocity measured across the data plane at z = 31.8 mm divided by the maximum mean velocity measured for fully developed turbulent pipe flow at 27 L/min. Experimental uncertainty: ± 0.1.

+At a steady-flow rate of 27 L/min.

++At a maximum pulsatile-flow rate of 30 L/min for Ionescu-Shiley, Björk-Shiley convexo-concave, and Smeloff valves and 29 L/min for St. Jude valve. No pulsatile-flow results were obtained for the empty flow section.

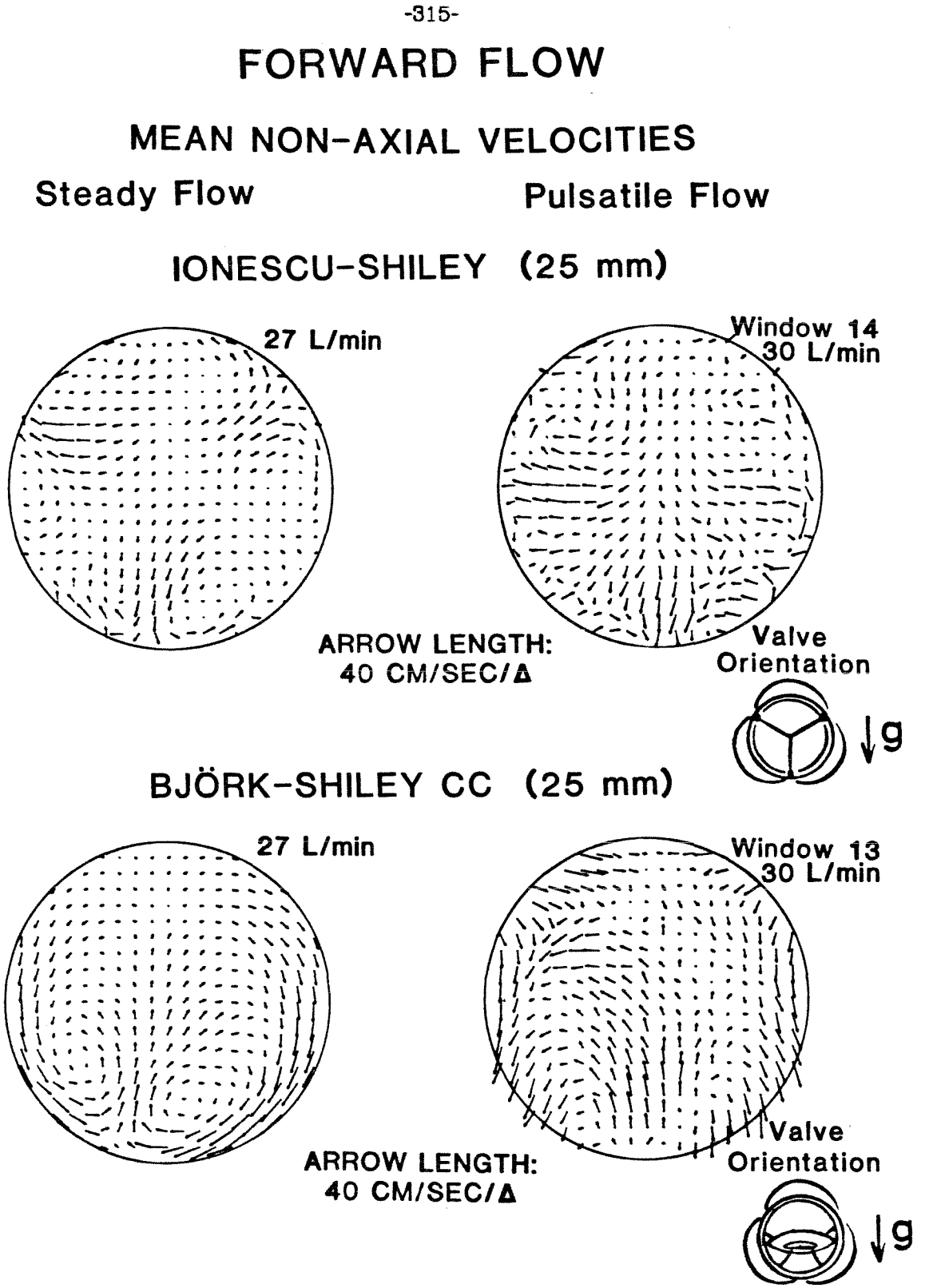

Figure 70. Mean non-axial velocities for steady flow and during maximum forward flow for pulsatile flow downstream from the Ionescu-Shiley (25 mm) and Björk-Shiley convexo-concave (25 mm) prostheses at z = 31.8 mm.

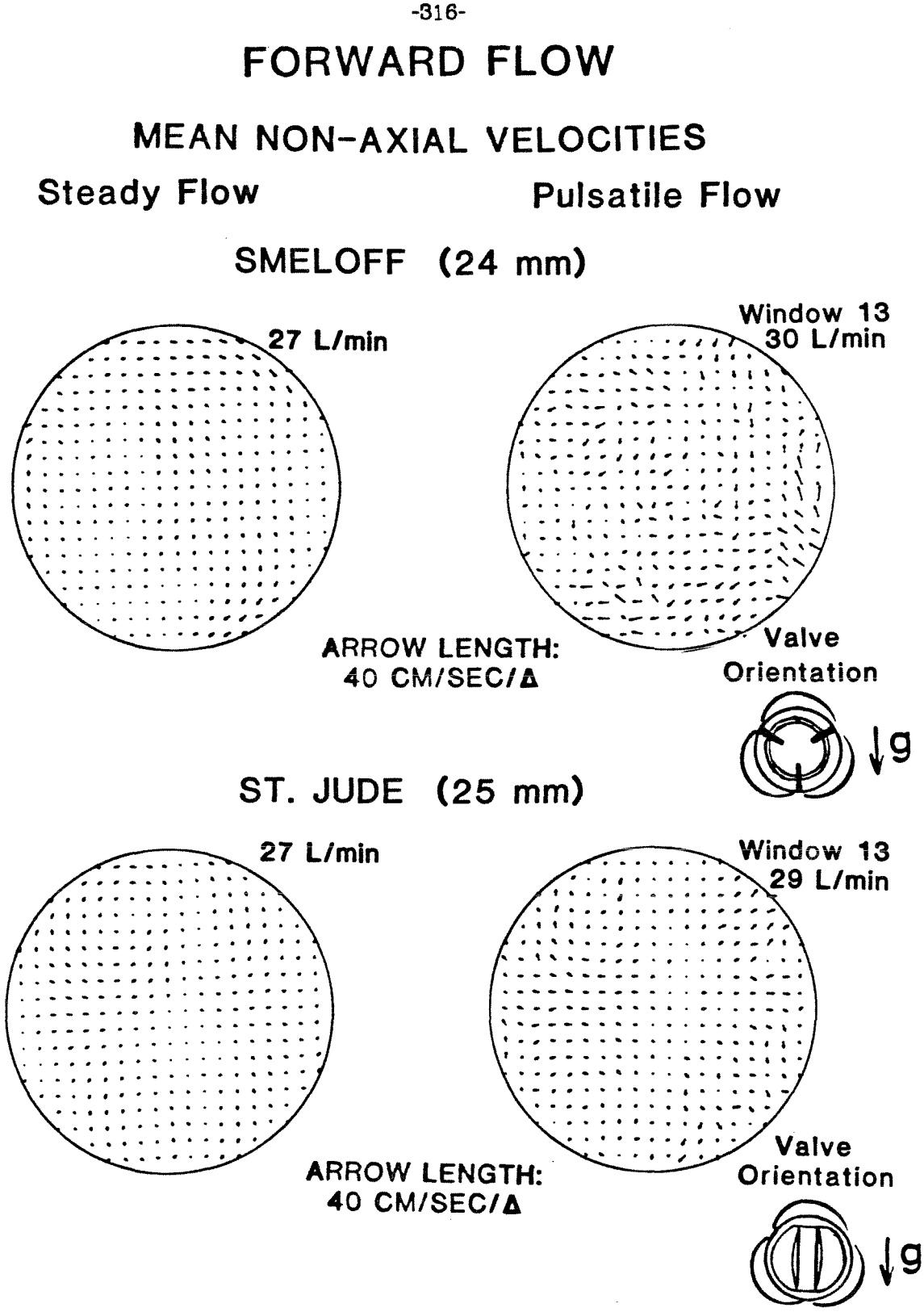

Figure 71. Mean non-axial velocities for steady flow and during maximum forward flow for pulsatile flow downstream from the Smeloff (24 mm) and St. Jude (25 mm) prostheses at z = 31.8 mm.

The results presented in Figures 70 and 71 indicate that, of the valve designs studied in the present investigation, the Ionescu-Shiley and Björk-Shiley convexo-concave valves generated well-defined secondary-flow structures characteristic of their respective designs. The secondary-flow structures generated by the Smeloff and St. Jude valves were lower in magnitude and less distinct than the secondary-flow structures for the other two valves. The Ionescu-Shiley valve generated relatively large, wall-directed mean non-axial velocity components. Also, the Ionescu-Shiley valve generated relatively large azimuthal velocities near the tube wall. These wall-directed and azimuthal non-axial velocities were part of a secondary-flow pattern which included six vortices. These vortices were roughly equal in diameter and were spaced evenly around the centerline of the tube. The Björk-Shiley convexo-concave valve generated very high mean non-axial velocity components near the tube wall. These high non-axial velocities were oriented azimuthally and were part of two distinct vortices in the secondary-flow pattern for this valve. The centers of these two vortices were located near the tube wall such that the vortices were similar in size but non-circular in diameter. The Smeloff and St. Jude valves generated only small mean non-axial velocity components at the data plane. Some low-magnitude vortices were observable in the secondary-flow patterns but these were much less distinct than those for the Ionescu-Shiley and Björk-Shiley convexo-concave valves. For the St. Jude valve, four vortices appear to have been present in the flow. These four vortices were similar in diameter and each was located in a quadrant of the tube cross-section.

The relative magnitude of the secondary-flow structure generated downstream from the four valves can be compared by determining the maximum radial and azimuthal mean velocity components. These two velocity components were determined as resultants of the the non-axial velocity

components measured in the x- and y-directions. The radial and azimuthal velocity components thus determined are given in Table 18 for each of the four valves in steady and pulsatile flow and for the empty flow section. The non-axial velocity components for the empty flow section were the lowest of those in Table 18. No pulsatile-flow results were obtained for the empty flow section. The four valves are listed in the order of increasing non-axial velocity components. At the data plane location of z = 31.8 mm, the St. Jude valve had the smallest non-axial velocity components. The Björk-Shiley convexo-concave valve had the largest non-axial velocity components. The experimental uncertainty in these ratios was ± 1.0 cm/s. The results in Table 18 for steady flow were therefore significantly lower than those for pulsatile flow.

The rms axial velocity results for the four valves are presented as contours in Figures 72 and 73 for steady flow and for the window in pulsatile flow corresponding to maximum forward flow. The results presented in Figures 72 and 73 were presented earlier in Figures 26, 41, 53, and 64.

The results presented in Figures 72 and 73 indicate that the valve designs studied in the present investigation all generated elevated rms axial velocities relative to the flow through the empty flow section. The Ionescu-Shiley valve generated relatively large rms axial velocities in the bulk flow. The rms axial velocities for this valve were as high as 50 cm/s. The rms axial velocities also dropped down to less than 10 cm/s at the tube centerline. The average rms axial velocity for the Ionescu-Shiley valve was 33.5 cm/s for steady flow and 29.3 cm/s for pulsatile flow. In comparison, the average rms axial velocity for the empty flow section was 14.0 cm/s for steady flow. The turbulent shear stresses implied by the rms velocities are discussed below along with the shear stresses associated with the mean velocity gradients. The Björk-Shiley convexo-concave valve generated moderate rms axial velocities in the bulk flow. For this

Table 18

Comparison of the Magnitude of the Secondary-Flow Structure Generated Downstream from the Four Prosthetic Aortic Heart Valves Studied in the Present Investigation*

	Maximum Radial** Mean Velocity Component (cm/s)		Maximum Azimuthal** Mean Velocity Component (cm/s)	
	Steady Flow+	Pulsatile Flow++	Steady Flow+	Pulsatile Flow++
Empty Flow Section (25.4 mm)	4.2	-	3.9	-
St. Jude (25 mm)	8.2	17.2	6.7	12.1
Smeloff (24 mm)	7.5	15.0	18.2	37.6
Ionescu-Shiley (25 mm)	42.0	53.1	38.9	43.1
Björk-Shiley convexo-concave (25 mm)	59.8	62.0	40.1	45.2

*Results for empty flow section also included as base-line.

**Radial and azimuthal mean velocity components determined as resultants of the velocity components measured in the x- and y-directions. Experimental uncertainty: ± 1.0 cm/s.

+At a steady-flow rate of 27 L/min.

++At a maximum pulsatile-flow rate of 30 L/min for Ionescu-Shiley, Björk-Shiley convexo-concave, and Smeloff valves and 29 L/min for St. Jude valve. No pulsatile-flow results were obtained for the empty flow section.

FORWARD FLOW

RMS AXIAL VELOCITIES

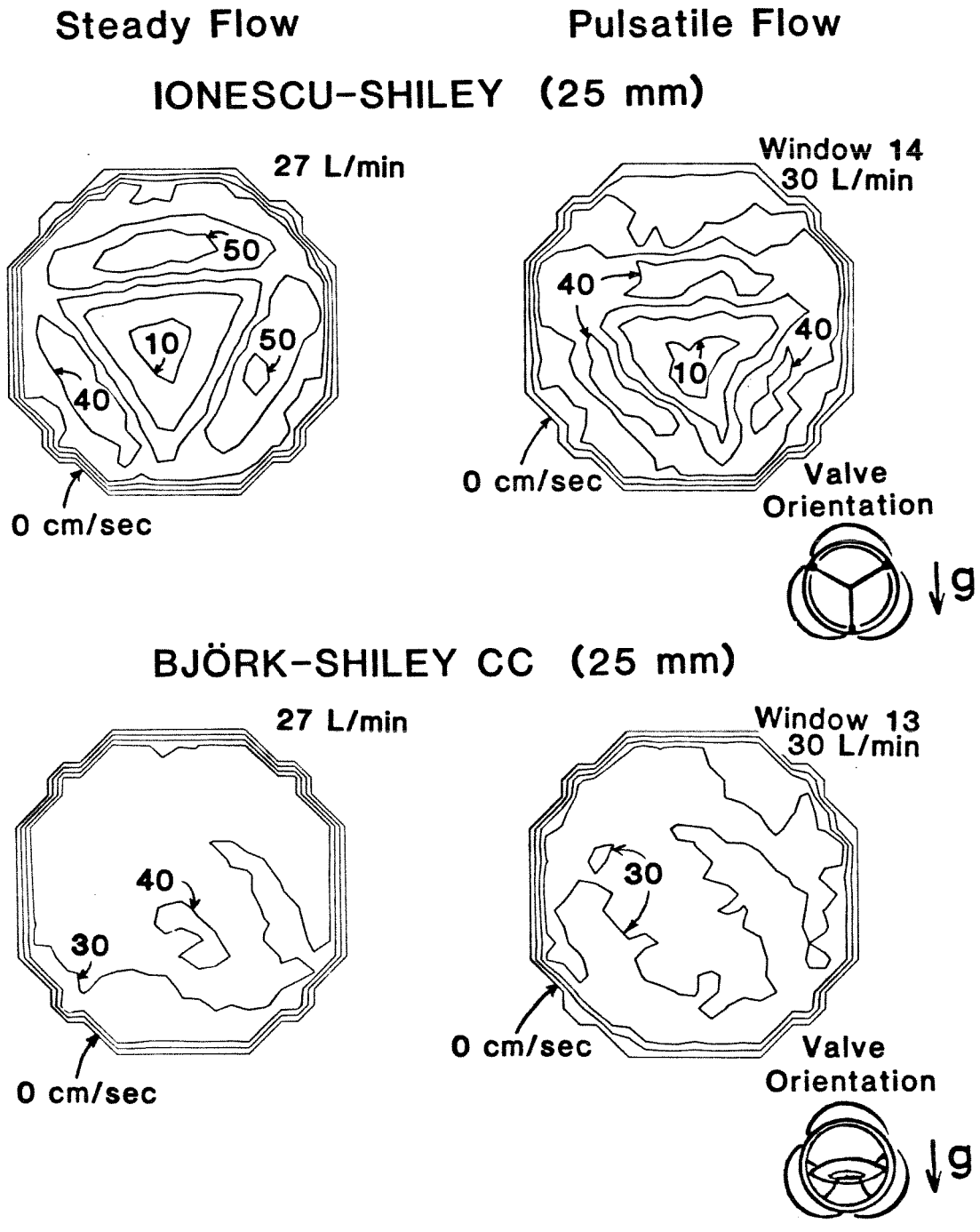

Figure 72. Root-mean-square (rms) axial velocities for steady flow and during maximum forward flow for pulsatile flow downstream from the Ionescu-Shiley (25 mm) and Björk-Shiley convexo-concave (25 mm) prostheses at z = 31.8 mm. Contour interval: 10 cm/s.

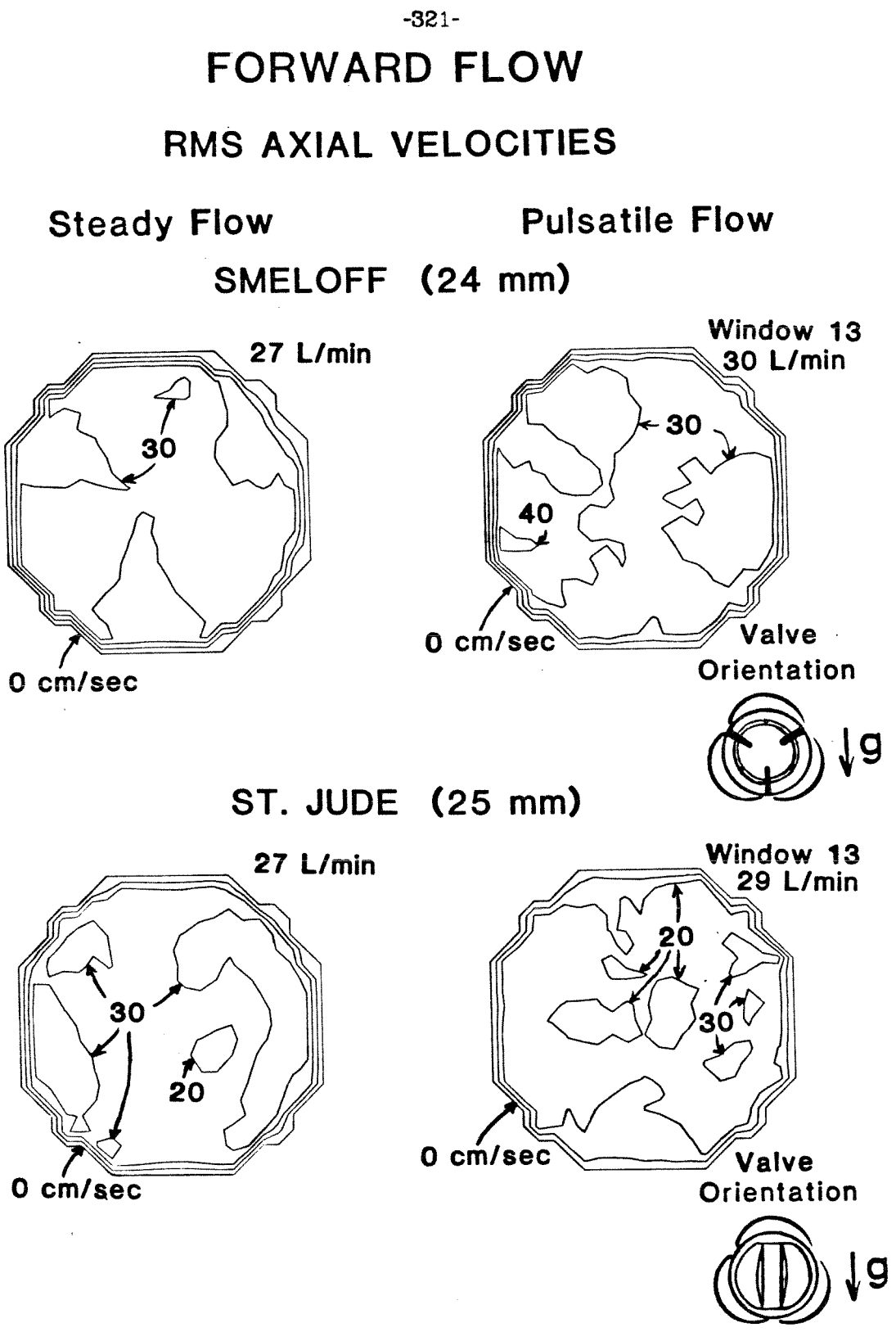

Figure 73. Root-mean-square (rms) axial velocities for steady flow and during maximum forward flow for pulsatile flow downstream from the Smeloff (24 mm) and St. Jude (25 mm) prostheses at z = 31.8 mm. Contour interval: 10 cm/s.

valve, however, these rms velocities were elevated across the entire tube cross section. The average rms axial velocity for this valve was thus similar to that for the Ionescu-Shiley valve at 32.5 cm/s for steady flow and 30.7 cm/s for pulsatile flow. The Smeloff valve generated moderate rms axial velocities in the bulk flow which were of lesser magnitude overall than those for the Björk-Shiley convexo-concave valve. The average rms axial velocity for the Smeloff valve was 30.8 cm/s for steady flow and 29.6 cm/s for pulsatile flow. The St.Jude valve generated the lowest rms axial velocities in the bulk flow of the four valves. The average rms axial velocity for this valve was 27.7 cm/s for steady flow and 24.2 cm/s for pulsatile flow.

The relative magnitude of the fluctuating velocities generated downstream from the four valves can be compared by determining the maximum and average rms axial velocities in both steady and pulsatile flow. These rms velocities are given in Table 19 for each of the four valves in steady and pulsatile flow and for the empty flow section. The rms velocities in the axial direction are given in Table 19 because they were larger in magnitude than the non-axial rms velocities. The rms axial velocities for the empty flow section were the lowest of those in Table 19. No pulsatile-flow results were obtained for the empty flow section. The four valves are listed in the order of increasing rms axial velocities. At the data plane location of z = 31.8 mm, the St. Jude valve overall had the smallest rms axial velocities. The Ionescu-Shiley valve had the largest rms axial velocities. The experimental uncertainty in these ratios was ± 1.0 cm/s. Thus, in general, the results in Table 19 for pulsatile flow were significantly lower than those for steady flow.

In summary, the velocity results for forward flow showed that the axial flow structures generated by each valve design were unique to that design relative to the others. Two of the valves, the Ionescu-Shiley and Björk-Shiley convexo-

Table 19

Comparison of the Magnitude of the Fluctuating Velocities Generated Downstream from the Four Prosthetic Aortic Heart Valves Studied in the Present Investigation*

	Maximum Axial** rms Velocity (cm/s)		Average Axial** rms Velocity (cm/s)	
	Steady Flow+	Pulsatile Flow++	Steady Flow+	Pulsatile Flow++
Empty Flow Section (25.4 mm)	30.8	-	14.0	-
St. Jude (25 mm)	38.3	39.1	27.7	24.2
Smeloff (24 mm)	39.5	38.6	30.8	29.6
Björk-Shiley convexo-concave (25 mm)	44.8	44.8	32.5	30.7
Ionescu-Shiley (25 mm)	58.0	52.5	33.5	29.3

*Results for empty flow section also included as base-line.

**Axial rms velocities are given because they were greater in magnitude than the non-axial rms velocities. Experimental uncertainty: ± 1.0 cm/s.

+At a steady-flow rate of 27 L/min.

++At a maximum pulsatile-flow rate of 30 L/min for Ionescu-Shiley, Björk-Shiley convexo-concave, and Smeloff valves and 29 L/min for St. Jude valve. No pulsatile-flow results were obtained for the empty flow section.

concave also generated well-defined secondary-flow structures in combination with their respective axial flow structures. All valves generated elevated rms axial velocities at the data plane. It is interesting to note that the order of the valves listed in Tables 17, 18, and 19 are similar. The St. Jude and Smeloff valves generated smaller flow acceleration, non-axial velocities, and rms axial velocities than the Björk-Shiley convexo-concave and Ionescu-Shiley valves. Both the shear stresses associated with the high mean axial velocity gradients and those implied by the elevated rms velocities are discussed further in the section below on the shear stress analysis.

4.2.2 Reverse-Flow Results

The four valves of the present investigation were compared with regard to the velocity results obtained downstream at the time of maximum reverse flow. For this comparison all velocity results were obtained for the data plane located at z = 31.8 mm. The Ionescu-Shiley valve generated an annular type of reverse flow with slightly elevated rms axial velocities. The Björk-Shiley convexo-concave and Smeloff valves generated centrally reversing flows with low rms axial velocities. The St. Jude valve generated a "saddle-point" reverse flow with low rms axial velocities. None of the four valves generated large mean non-axial velocity components and no secondary-flow structures were observable.

The mean axial velocity results for the four valves are presented in 3-D perspective in Figure 74 and as contours in Figure 75 for the window in pulsatile flow corresponding to maximum reverse flow. The results presented in Figure 74 were presented earlier in Figures 20, 35, 47, and 58.

The results in Figures 74 and 75 show that the structure of the reverse flow was roughly similar in structure to the forward flow. For the Ionescu-Shiley valve, the reverse flow contained a region of positive mean axial velocities near

REVERSE FLOW

MEAN AXIAL VELOCITIES

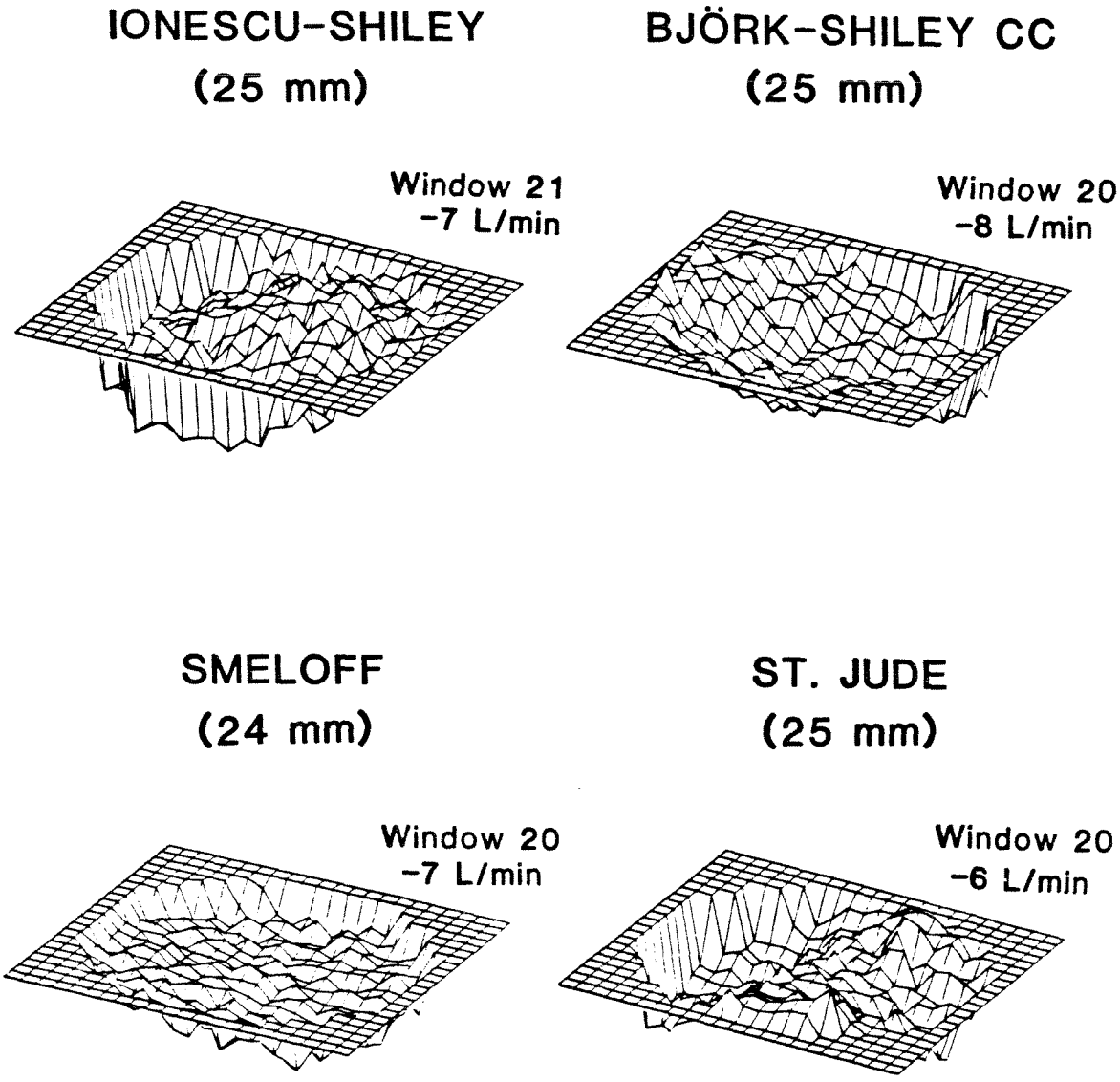

Figure 74. Mean axial velocities at z = 31.8 mm in 3-D perspective during maximum reverse flow for the four prostheses studied in the present investigation.

REVERSE FLOW

MEAN AXIAL VELOCITIES

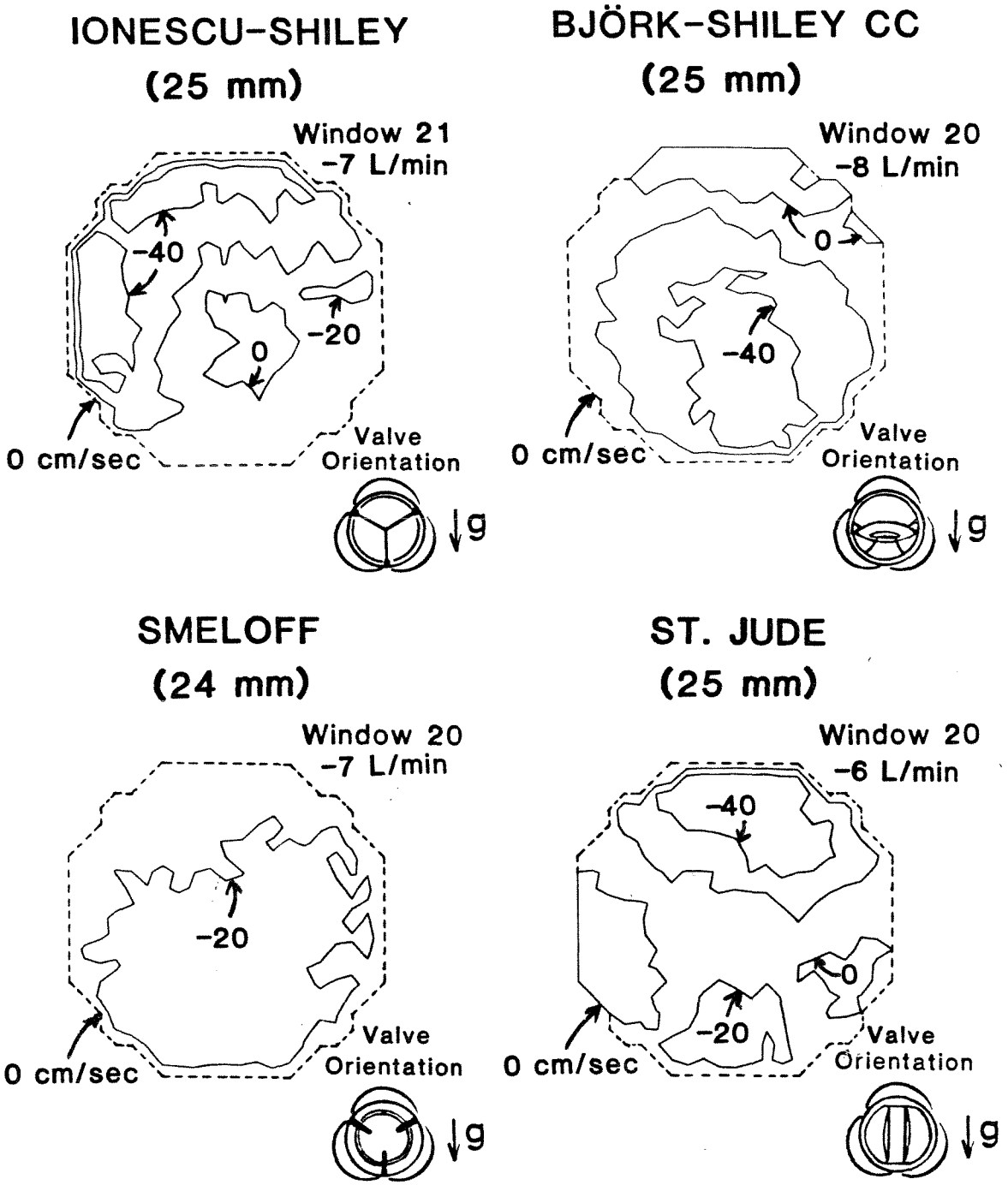

Figure 75. Mean axial velocities at z = 31.8 mm as contours during maximum reverse flow for the four prostheses studied in the present investigation. Contour interval: 20 cm/s.

the centerline of the tube. The negative mean axial velocities were thus in the annular region between this central region and the wall of the tube. These negative velocities are located in the tube cross section in similar fashion to those for the forward flow. The reverse flow for the Ionescu-Shiley valve, therefore, had a central-peak structure similar to that for this valve during forward flow. For the Björk-Shiley convexo-concave valve, the reverse flow contained a region of positive mean axial velocities near the top of the plot in Figure 75. The location of this region of positive velocities coincided with the location of the maximum mean axial velocities in the lenticularly shaped jet during forward flow. The reverse flow for the Björk-Shiley convexo-concave valve, therefore, had an acentric structure similar to that for this valve during forward flow. For the Smeloff valve, the reverse flow contained no regions of positive mean axial velocities. The flow thus reversed somewhat uniformly across the tube cross section with its minimum mean axial velocity near the centerline of the tube. Although no effect of the maxima and low-velocity regions of the forward flow were observable for the Smeloff valve in Figures 74 and 75, the reverse flow for this valve had an axisymmetric structure similar to that during forward flow. For the St. Jude valve, the reverse flow contained two regions of positive mean axial velocities, one on either side of the plot in Figure 75. The location of these regions of positive velocities coincided with the location of the maximum mean axial velocities in the forward flow for this valve. The reverse flow for the Björk-Shiley convexo-concave valve, therefore, had a bi-symmetric structure similar to that for this valve during forward flow.

The mean non-axial velocity results for the four valves are presented as resultants in Figure 76 for the window in pulsatile flow corresponding to maximum reverse flow. The results presented in Figure 76 were not presented earlier.

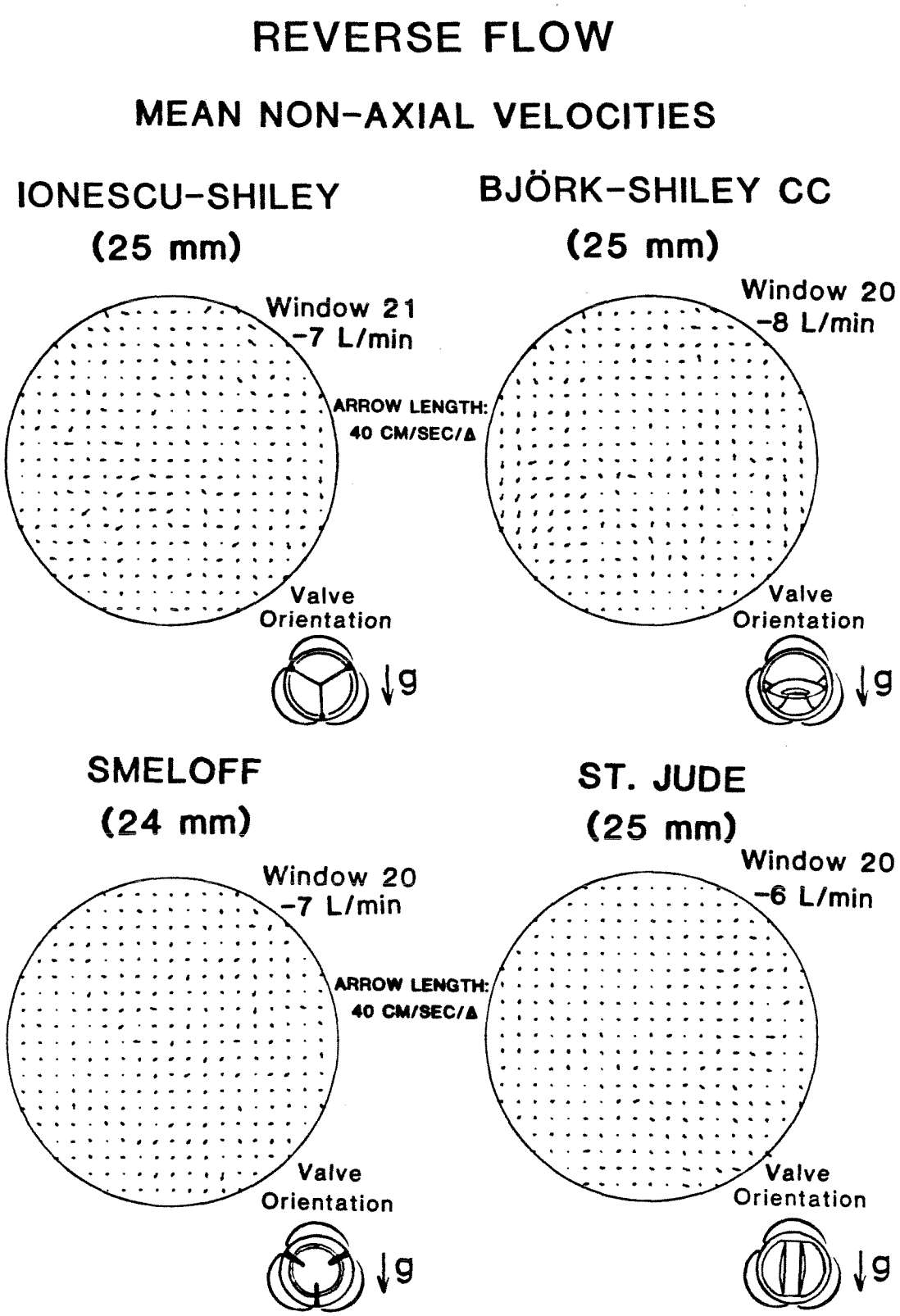

Figure 76. Mean non-axial velocities at z = 31.8 mm as resultants during maximum reverse flow for the four prostheses studied in the present investigation.

The results shown in Figure 76 indicate that upon flow reversal the secondary-flow structure of the forward flow was largely destroyed. For all four valves there was a general lack of secondary-flow structure at the time of the maximum reverse flow. Some remnants of the secondary-flow structure present during the forward flow are observable in Figure 76, especially for the Björk-Shiley convexo-concave valve, but these remnants are very much less distinct and small in magnitude. For each of the four valves, therefore, the reversing flow generally proceeded directly back towards the closing valve.

The rms axial velocity results for the four valves are presented as contours in Figure 77 for the window in pulsatile flow corresponding to maximum reverse flow. The results presented in Figure 77 were not presented earlier.

The small rms axial velocities shown in Figure 77 indicate that the fluctuating velocity field was quickly damped by viscous dissipation once the pressure-drop driving force was removed. For all four valves the rms axial velocities were relatively small at the time of the maximum reverse flow. For the Ionescu-Shiley valve the rms axial velocities were somewhat larger than those for the other valves. The average rms axial velocity for the Ionescu-Shiley valve was 19.1 cm/s. The average rms axial velocities for the Björk-Shiley convexo-concave, Smeloff, and St. Jude valves were 12.5 cm/s, 11.9 cm/s, and 13.0 cm/s, respectively. The slightly elevated rms velocities found for the Ionescu-Shiley valve reflect the higher rms velocities present for that valve during forward flow.

In summary, the velocity results for reverse flow showed that the structure of the flow at maximum reverse flow retained some semblance to that during forward flow. The secondary-flow structure at maximum reverse flow, however, was much less distinct for reverse flow than that for forward flow. The rms axial velocities were much lower at the maximum reverse flow than that for forward flow.

REVERSE FLOW

RMS AXIAL VELOCITIES

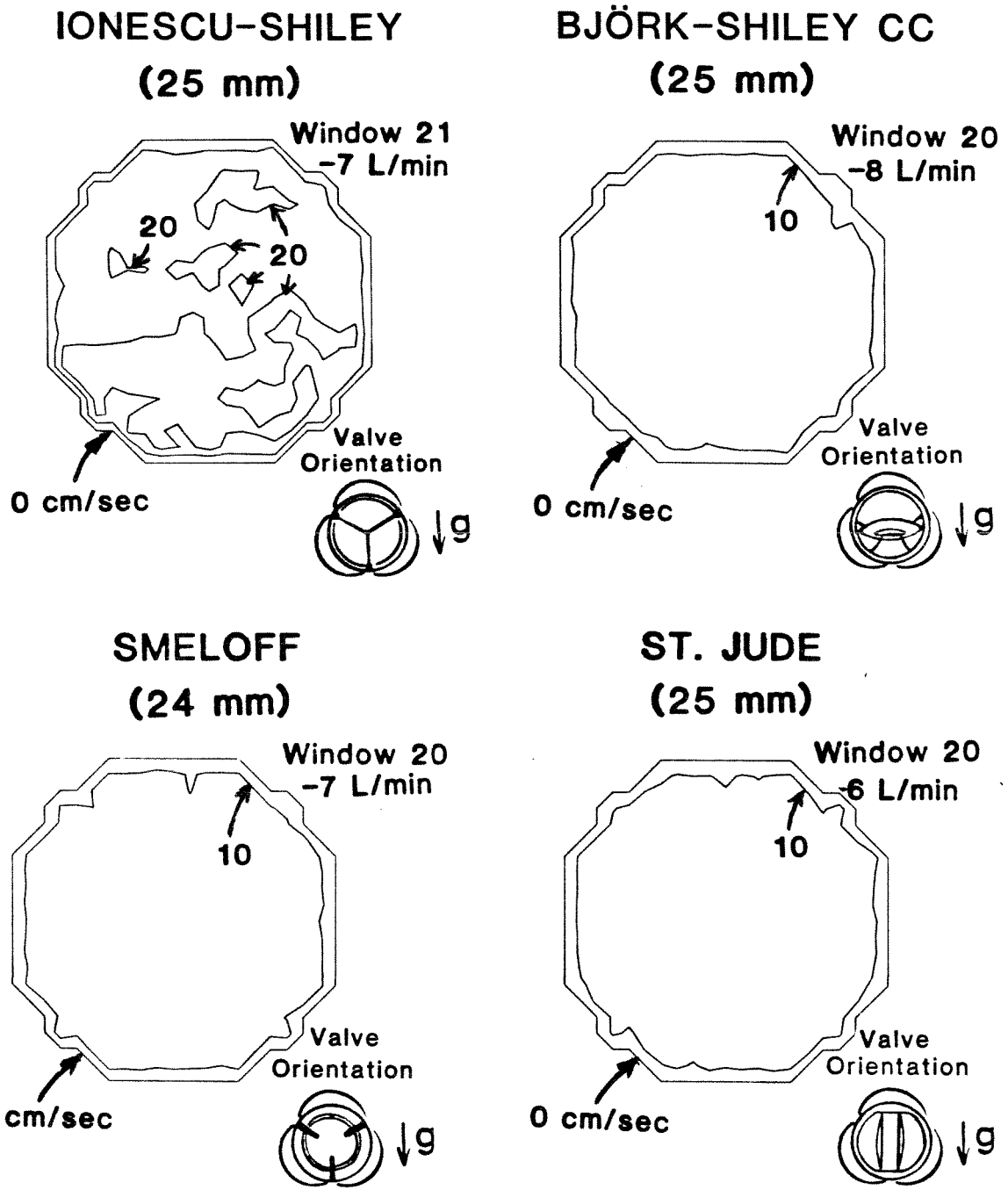

Figure 77. Root-mean-square (rms) axial velocities at z = 31.8 mm as contours during maximum reverse flow for the four prostheses studied in the present investigation. Contour interval: 10 cm/s.

4.3 COMPARATIVE SHEAR-STRESS ANALYSIS

The four valves of the present investigation were also compared with regard to the total shear stresses estimated from the velocity results measured downstream at the time of maximum forward flow. For this comparison all velocity results were obtained for the data plane located at z = 31.8 mm. The total shear stresses were estimated from the mean axial velocities and the rms axial and rms non-axial velocities using Equation (11). The Ionescu-Shiley valve generated large estimated total shear stresses in the bulk flow. The Björk-Shiley convexo-concave, Smeloff, and St. Jude valves generated large estimated total shear stresses near the tube wall.

The estimated total shear stresses for the four valves are presented as contours in Figures 78 and 79 for steady flow and for the window in pulsatile flow corresponding to maximum flow. The results presented in Figures 78 and 79 were presented earlier in Figures 30, 42, 54, and 65.

The results in Figures 78 and 79 show that the valve design affected both the general location and the magnitude of the largest estimated total shear stresses downstream from that valve. The central-flow design of the Ionescu-Shiley valve generated relatively high shear stresses in the bulk flow. The mean axial velocity gradients and the elevated rms velocities both contributed to the high total shear stresses of more than 120 N/m^2 estimated in the bulk flow. The semi-central flow design of the Björk-Shiley convexo-concave valve generated high shear stresses close to the tube wall. Near the tube wall, the mean axial velocity gradients contributed the largest part of the magnitude of the total shear stresses which were estimated to be higher than 100 N/m^2. The lateral-flow design of the Smeloff valve also generated high shear stresses close to the tube wall. The total shear stresses estimated for the Smeloff valve were somewhat smaller than those for the Björk-Shiley convexo-concave valve. For

FORWARD FLOW

TOTAL SHEAR STRESSES* (Z - X)

Steady Flow

Pulsatile Flow

IONESCU-SHILEY (25 mm)

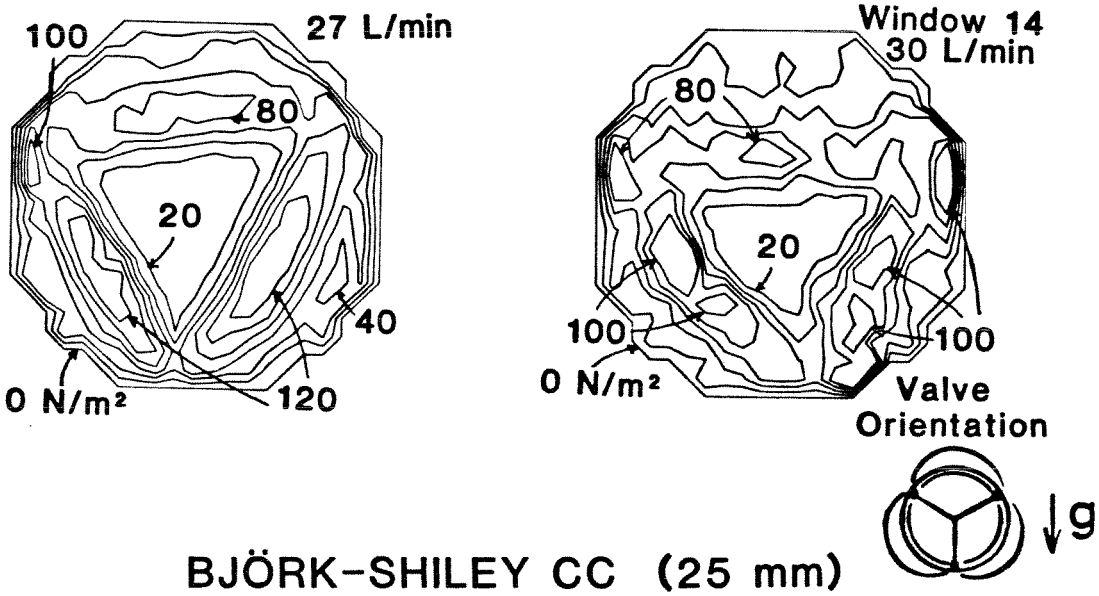

BJÖRK-SHILEY CC (25 mm)

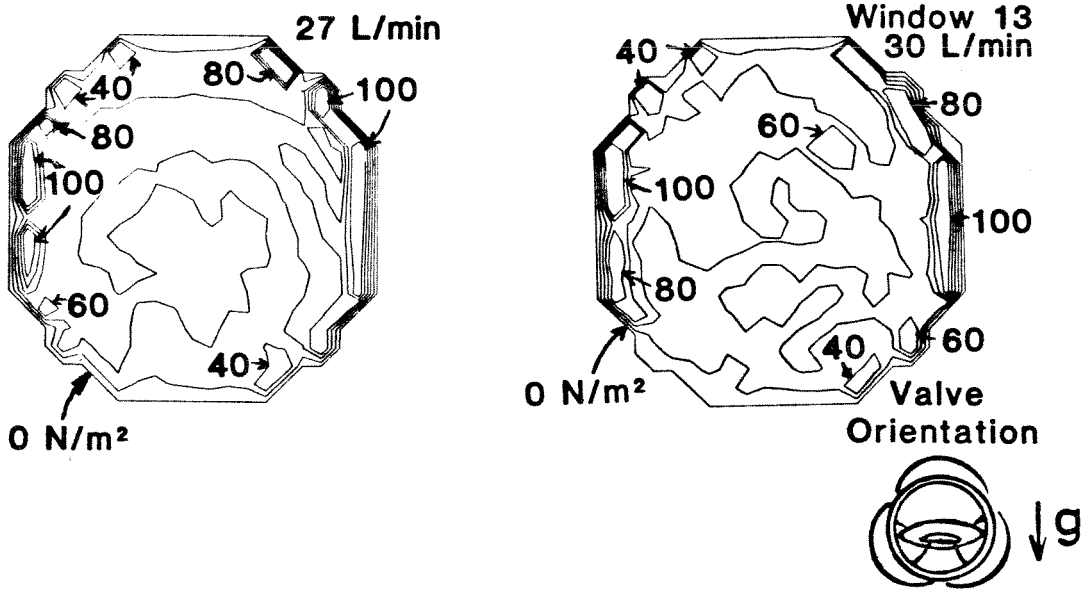

Figure 78. Total estimated shear stresses, τ_{zx}, for steady flow and during maximum forward flow for pulsatile flow downstream from the Ionescu-Shiley (25 mm) and Björk-Shiley convexo-concave (25 mm) prostheses at z = 31.8 mm. Contour interval: 20 N/m^2.

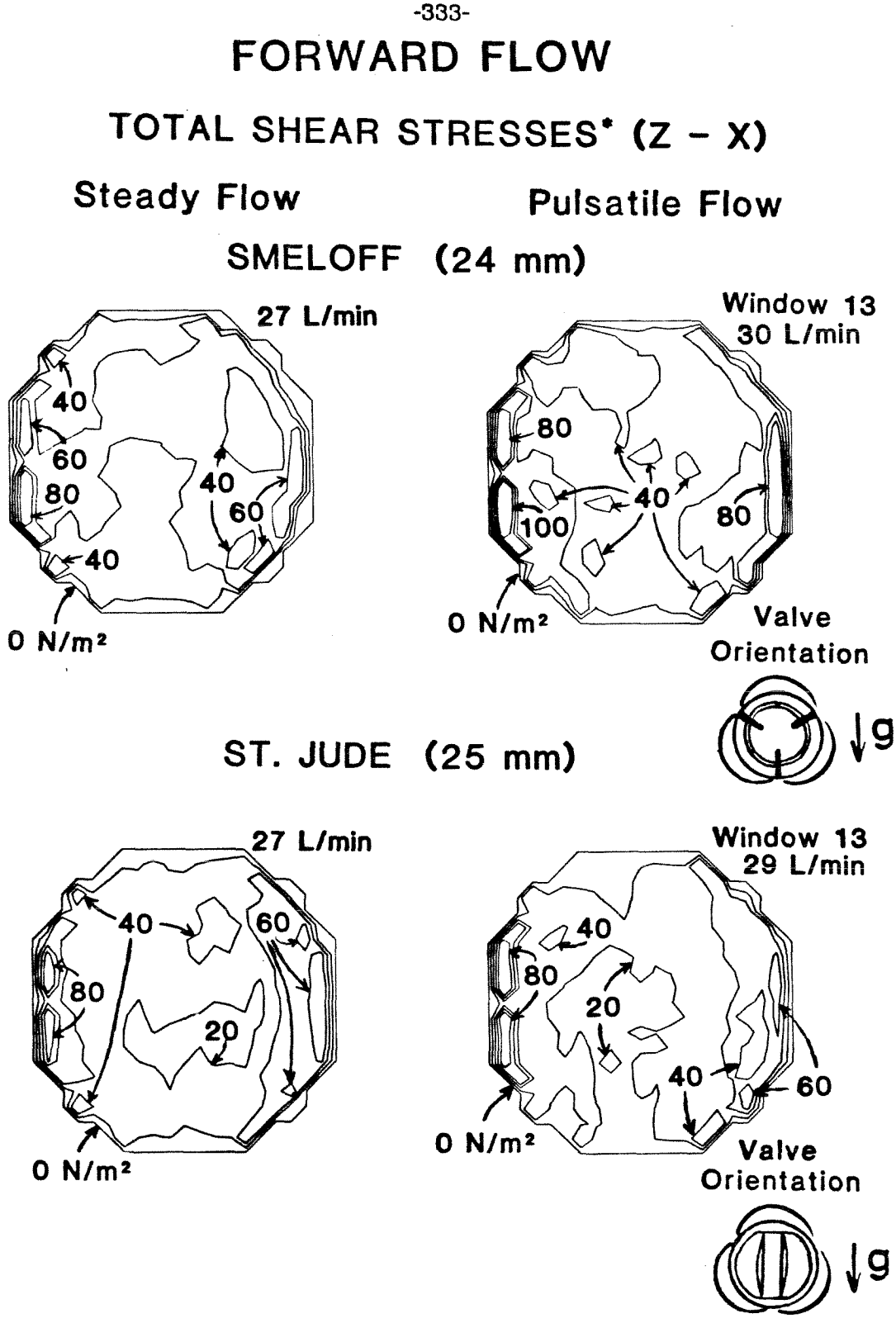

Figure 79. Total estimated shear stresses, τ_{zx}, for steady flow and during maximum forward flow for pulsatile flow downstream from the Smeloff (24 mm) and St. Jude (25 mm) prostheses at z = 31.8 mm. Contour interval: 20 N/m^2.

the Smeloff valve, as for the Björk-Shiley convexo-concave valve, the mean axial velocity gradients contributed the largest part of the magnitude of the total shear stresses. Shear stresses for the Smeloff valve in Figure 79 were greater than 100 N/m^2 for a much shorter distance along the wall than for the Björk-Shiley convexo-concave valve. The flow design of the St. Jude valve generated elevated shear stresses near the tube wall but these stresses were estimated to be the lowest of the four valves studied. For the St. Jude valve, as for the Björk-Shiley convexo-concave and Smeloff valves, the mean axial velocity gradients contributed the largest part of the magnitude of the total shear stresses. No shear stresses are shown in Figure 79 greater than 100 N/m^2 for the St. Jude valve.

The relative magnitude and extent of the shear stresses generated downstream from the four valves can be compared by estimating the maximum total shear stress which was present over at least 10% of the tube cross section. These maximum estimated total shear stresses are given in Table 20 for each of the four valves in steady and pulsatile flow and for the empty flow section. The maximum estimated total shear stresses for the empty flow section were the lowest of those in Table 20. No pulsatile-flow results were obtained for the empty flow section. The four valves are listed in the order of increasing maximum estimated total shear stresses. At the data-plane location of $z = 31.8$ mm, the St. Jude valve overall had the smallest maximum estimated total shear stresses. The Ionescu-Shiley valve had the largest. The experimental uncertainty in these ratios was $\pm$ 5 N/m^2. Thus, the results in Table 20 for pulsatile flow were only significantly lower than those for steady flow for the Ionescu-Shiley valve. The results in Table 20 for pulsatile flow were actually significantly higher than those for steady flow for the Smeloff valve. The shear stress values given in Table 20 for the Ionescu-Shiley valve were those found out

Table 20

Comparison of the Magnitude of the Estimated Total Shear Stresses, τ_{zx}, Generated Downstream from the Four Prosthetic Aortic Heart Valves Studied in the Present Investigation*

	Maximum Estimated Total Shear Stress** (N/m^2)	
	Steady Flow+	Pulsatile Flow++
Empty Flow Section (25.4 mm)	43	-
St. Jude (25 mm)	76	74
Smeloff (24 mm)	78	89
Björk-Shiley convexo-concave (25 mm)	112	106
Ionescu-Shiley (25 mm)	128	112

*Results for empty flow section also included as base-line.

**The maximum total shear stress is given which was estimated to be present over at least 10% of the tube cross-section. Experimental uncertainty: ± 5 N/m^2.

+At a steady-flow rate of 27 L/min.

++At a maximum pulsatile-flow rate of 30 L/min for Ionescu-Shiley, Björk-Shiley convexo-concave, and Smeloff valves and 29 L/min for St. Jude valve. No pulsatile-flow results were obtained for the empty flow section.

in the bulk flow away from the tube wall whereas those values given for the other three valves were those found very near the tube wall.

It should be noted that the highest mean velocity gradients at the tube wall were in the radial direction. Hence the largest laminar shear stresses were those in the radial direction. Thus only the shear-stress results on the left and right sides of the plots shown in Figures 78 and 79 included the maximum mean velocity gradient at the tube wall. At the top and bottom of the plots in Figures 78 and 79 the mean velocity gradient used to estimate the laminar shear stress at the tube wall was that gradient in the direction almost ***parallel*** with the wall. Therefore, the spatial extent of the elevated shear stresses at the tube wall is not indicated in its entirety for the plots in Figures 78 and 79. For the Ionescu-Shiley, Smeloff, and St. Jude valves, the mean velocity gradients which occurred near the wall on the left and right of the plots in Figures 78 and 79, were either the maximum gradients or insignificantly different from the maximum gradients at the tube wall for those respective valves. For these three valves, therefore, the shear-stress results in Figures 78 and 79 include the highest, or very nearly the highest, laminar shear stresses close to the tube wall. For the Björk-Shiley convexo-concave valve, however, the maximum mean velocity gradient at the wall occurred near the top of the plots in Figure 78, as was shown in Figure 43. The highest estimated total shear stress near the tube wall for the Björk-Shiley convexo-concave valve was about 140 N/m^2.

From the results presented in Figures 78 and 79 it is clear that the Ionescu-Shiley valve generated the highest shear stresses by far in the bulk flow of the four valves studied in the present investigation. Total shear stresses were estimated as high as 120 N/m^2 in the bulk flow downstream from the Ionescu-Shiley valve. There were relatively large regions of the tube cross section downstream from the Ionescu-Shiley valve where the total shear stresses were

estimated to be greater than 100 N/m^2.

Although the three mechanical valves of the present investigation generated relatively low shear stresses in the bulk flow, all three generated high shear stresses near the tube wall. The full spatial extent of the highest shear stresses at the tube wall was not shown by the plots in Figures 78 and 79, as discussed above. The full extent of the high laminar shear stresses near the tube wall can be inferred, however, from the mean axial velocity results shown in Figures 68 and 69. The highest laminar shear stresses for the Björk-Shiley convexo-concave valve at the tube wall were greater than 100 N/m^2 and occurred along about half of the circumference of the tube cross section. The high shear stresses produced by the Björk-Shiley valve are demonstrated along the top of the plots in Figure 78. The highest laminar shear stresses produced by the Smeloff valve at the tube wall were 80 N/m^2 to 100 N/m^2 and they occurred around the entire circumference of the tube cross section. The highest laminar shear stresses produced by the St. Jude valve at the tube wall were 80 N/m^2 to 100 N/m^2 and they occurred along about half the circumference of the tube cross section. The high shear stresses produced by the St. Jude valve are seen on the left and right of the plots in Figure 79.

The Ionescu-Shiley valve also generated relatively large total shear stresses near the tube wall. The large total shear stresses near the tube wall for this valve were, however, relatively limited in spatial extent. These stresses were only large near the wall where the non-circular axial jet impinged upon the tube wall, as shown in Figure 68. Thus for the Ionescu-Shiley valve the highest shear stresses near the tube wall only occurred along about one third of the circumference of the tube cross-section.

It should be reiterated here that in the present investigation a systematic study of the velocities very close to the tube wall was not done. Hence, the total

shear stresses estimated close to the tube wall should be considered rough estimates only. The total shear stresses very close to the wall were probably larger than those found in the present investigation. As mentioned above, the largest part of the total shear stresses estimated near the tube wall was that shear stress contribution from the mean axial velocity gradient. Yoganathan, et al. (1978a) have shown that very close to the wall the mean axial velocity gradient rises considerably as the wall is approached. Thus the actual total shear stresses very near the tube wall were probably considerably higher than those shown in Figures 78 and 79.

The shear stresses estimated downstream from the valves studied in the present investigation could be hemolytic in magnitude. The estimated total shear stresses shown in Figures 78 and 79 and inferred by Figures 68 and 69 were larger than 100 N/m^2 for three of the four valves studied in the present investigation. Only the St. Jude valve generate total shear stresses estimated to be less than 100 N/m^2. Table 1 in Chapter 1 presents these levels of the total shear stress which may be detrimental to RBCs in flowing blood. For the Ionescu-Shiley valve, the estimated total shear stresses greater than 100 N/m^2 were located in relatively large regions of the bulk flow. Thus, for the Ionescu-Shiley valve, a relatively large number of the RBCs flowing in the bulk flow could encounter highly elevated shear stresses. For the other three valves studied in the present investigation, the estimated total shear stresses greater than 100 N/m^2 were located close to tube wall only. Thus, for the three mechanical valves, only the RBCs flowing near the tube wall could encounter highly elevated shear stresses. The relative volume of the fluid which encountered the elevated shear stresses was thus in general different for each valve design. In theory, such volumes could be calculated from the shear-stress results given in Figures 78 and 79 along with the mean axial velocity results given in Figures 68

and 69. In practice, however, these volumes could not be reliably determined for the present investigation. Much of the large estimated total shear stresses occurred very near the tube wall where, as discussed above, a systematic study of the velocities was not done. Nonetheless, it is clear that the potential for damage to RBCs in the bulk flow is much higher for the Ionescu-Shiley valve than for the other three valves and that the reverse is true for damage occurring near the wall.

A final point is that for pulsatile flow, the highest shear stresses were present for only a short interval in mid-systole. This interval was on the order of four to six window lengths, or about 100 milliseconds. Thus the question of the reversibility of damage to the RBC becomes important. That is, as shown in Table 1, very high shear stresses are necessary to lethally damage RBCs for short exposure times. It is unlikely therefore that a healthy RBC would be destroyed in a single pass through the flow field generated by each of the valves studied in the present investigation. An RBC which encountered the prosthesis repeatedly may, however, suffer damage and eventual destruction.

5. SUMMARY AND RECOMMENDATIONS

5.1 SUMMARY

Laser-Doppler anemometry has been applied in a systematic way to determine the structure of the flow downstream from prosthetic aortic heart valves in steady flow at a flow rate of 27 L/min and in pulsatile flow at a pulsing rate of 70 beats per minute, a mean flow rate of 5.4 L/min, a systolic interval of 0.300 seconds, and for an aortic pressure range of 16.0 kPa to 10.7 kPa (gauge). The results show that all four of the valves studied generated very disturbed flow fields. Flow structures which have been previously shown to be potentially thrombogenetic were found and analyzed to determine their origins and significance. Turbulence intensities were measured in steady flow as high as 65% at a distance of 31.8 mm downstream from the downstream face of the valve base-ring. At this same axial distance, shear stresses were estimated in the bulk flow to be greater than 120 N/m^2 over more than 10% of the tube cross section. If these elevated shear stresses were to occur *in vivo*, they could damage red blood cells and activate platelets, and lead to hemolysis and thrombus formation.

Velocity measurements revealed that the central-flow design of the occluding mechanism of the Ionescu-Shiley prosthesis significantly constricted forward flow. The maximum acceleration of the flow through the valve was determined to be a factor of 2.4 for steady flow and 2.6 for pulsatile flow relative to the upstream velocity profile. This flow constriction generated relatively large separated-flow regions which contributed to the low to moderate pressure drop found for this valve. Also, this flow constriction generated high mean velocity gradients and rms velocities in the bulk flow which implied elevated shear stresses. The maximum turbulence intensity was determined to be 65% and 55% in steady flow and in pulsatile flow at maximum forward flow, respectively, at a

distance of 31.8 mm downstream from the downstream face of the valve base-ring. For both steady and pulsatile flow, the estimated shear stresses were greater than 110 N/m^2 over more than 10% of the tube cross section. Quantitative evaluation of the spatial extent of the flow constriction and separated-flow regions generated by this central-flow valve design have not been previously reported in the literature.

The semi-central flow design of the Björk-Shiley convexo-concave valve was found to generate a very acentric flow structure. The occluding mechanism of this valve directed forward flow towards the tube wall generating high mean velocity gradients over much of the circumference of the tube wall. The large, azimuthal extent of the elevated shear stresses at the tube wall generated by this semi-central flow valve has not been previously reported in the literature. For both steady and pulsatile flow, the estimated shear stresses near the wall were greater than 105 N/m^2 over more than 10% of the tube cross section. Regions of low velocity were also found which implied large stagnant zones in the flow closer to the valve superstructure. If present *in vivo* such stagnant zones may be thrombogenetic.

The lateral-flow design of the Smeloff valve created significant wakes in the forward flow downstream from the valve superstructure. Besides the large flow wake generated by the ball occluder, three additional wakes were found which were generated by the struts on the downstream cage of the occluding mechanism of the valve. The additional wakes appeared to be of sufficient magnitude to have contributed significantly to the moderate pressure drop attributed to this prosthesis. The spatial extent of these three additional wakes in the flow downstream from the Smeloff valve has not been previously reported in the literature. The largest shear stresses estimated downstream from this lateral-flow valve were located near the tube walls. For both steady and pulsatile

flow, the estimated shear stresses near the wall were greater than about 80 N/m^2 over more than 10% of the tube cross section.

The unique design of the St. Jude valve allowed for relatively unobstructed forward flow. The forward flow through this valve, however, was found to consist of sizable wakes which were generated by the leaflet occluders and to contain relatively intense velocity fluctuations. The flow wakes generated by the leaflets of this valve probably contribute significantly to its pressure-drop characteristics. The intense velocity fluctuations implied elevated shear stresses in the bulk flow. The largest shear stresses estimated downstream from this valve, however, were located near the tube walls. For both steady and pulsatile flow, the estimated shear stresses near the wall were greater than about 75 N/m^2 over more than 10% of the tube cross section.

A comparative analysis of steady and pulsatile flow showed that steady-flow results only approximated the pulsatile-flow results obtained during the middle of the systolic ejection phase of the pulse cycle. Early in systole, the flow was found to be of a plug-flow type. Late in systole, the flow was highly disturbed and would have been difficult to predict *a priori*. Generally, the intensity of the velocity fluctuations was found to be greater for steady flow than for pulsatile flow. Thus, steady-flow analyses of prosthetic heart valves were found to give an upper bound on the velocity fluctuations which would be determined in pulsatile flow. The estimated shear stresses in steady flow, therefore, were also an upper bound on those in pulsatile flow.

The pressure-drop and regurgitant-flow characteristics were also determined for the four valves studied in the present investigation. A comparative analysis showed that there was a significant range in the hemodynamic performance of the four prosthetic heart valves.

The comparison of the pressure-drop results showed that the St. Jude valve generated the lowest pressure drops in both steady and pulsatile flow, while the Smeloff valve generated the highest. Accordingly, the St. Jude valve had the largest effective orifice area (EOA) in both steady and pulsatile flow and the Smeloff valve had the smallest. The Björk-Shiley convexo-concave and Ionescu-Shiley valves each had intermediate pressure-drop characteristics which were similar in magnitude between the two prostheses.

The comparison of the regurgitant-flow results showed that the Ionescu-Shiley had the smallest percentage of regurgitant flow relative to the forward flow. Of the valves which did not totally occlude the base-ring orifice when closed, the St. Jude valve had the smallest percentage of regurgitant flow. The percentage of regurgitant flow determined for the Björk-Shiley convexo-concave valve was intermediate between that for the St. Jude valve and that for the Smeloff valve.

5.2 RECOMMENDATIONS

In the present investigation a single-component LDA was used in the forward-scatter mode to obtain detailed velocity measurements in the bulk flow for both steady and pulsatile flow. The measurements were made in each of the three Cartesian coordinate directions. The velocity results thus obtained were then used to estimate the total shear stresses in the bulk flow downstream from several prosthetic aortic valves.

As direct extensions of the present investigation i) the data-plane grid should be modified to allow detailed velocity measurements very close to the tube wall, ii) a multi-component LDA should be employed to measure turbulent stresses directly, iii) velocity measurements should be made closer to the superstructure of the valves to seek out small regions of flow stagnation, iv) more pulsatile-flow

states should be investigated to cover the spectrum of cardiac states encountered *in vivo*, and v) additional valve designs should be studied including a natural aortic valve. Each of these five recommendations is discussed in order below.

Detailed velocity measurements close to the tube wall would complement the results obtained in the present investigation for the bulk flow. To make the detailed velocity measurements, a data-plane grid could be laid out to have a finer matrix near the tube wall. These measurements close to the wall would allow for better characterization of the shear stresses near those surfaces. The relative importance of hemolytic forces in the bulk flow versus those very close to the wall could then be studied in regard to the maximum shear stresses and the cross-sectional area involved.

Direct measurement of turbulent stresses would improve the experimental uncertainty over that of the present investigation and would significantly reduce the time required for data collection. To directly measure the turbulent stresses, a multi-component LDA could be employed wherein the velocity in two or more of the three mutually orthogonal coordinate directions is measured simultaneously. The total shear stress results from these direct measurements would allow an even better characterization of the hemolytic potential of various prosthetic aortic valve designs.

Velocity measurements very close to the superstructure of a valve would provide some indication of the tendency for that valve to thrombose or to be associated with a high rate of thromboembolic events, or both. These measurements close to the valve would delineate small, potentially thrombogenetic regions of stagnant fluid adjacent to the prosthetic surfaces. The data collection could be approached by making measurements across data planes which "intersected" the valve superstructure. The data planes would be

located at incremental axial distances from one another. The grid for these data planes would be designed to have a finer matrix near all prosthetic surfaces as well as the wall of the flow section.

In making many of the velocity measurements very close to the valve, it would be necessary to modify the LDA to operate in the backward-scatter mode. An optically clear path for the laser beams would then only be required from one direction and would allow velocity measurements near the opaque surfaces.

The cardiovascular dynamics can range over quite a spectrum of heart rates, cardiac outputs, and systemic pressures. To analyze and compare valve performance adequately, the prostheses should be studied by simulating several cardiovascular states in the pulse-duplicator. Rapid heart rates and high cardiac outputs could be used to simulate the "exercise" state wherein larger pressure drops and shearing stresses would be present. Elevated systemic pressures could be used to simulate a hypertensive state in which the regurgitant flow would increase through valves that were not totally occluding. Low cardiac outputs and high systemic pressures could be used to simulate the cardiac state during that critical time immediately following valve-replacement surgery. Several steady-flow states could also be studied which are related to the pulsatile-flow states investigated.

Several more important designs of prosthetic valves are available for implantation that were not studied in the present investigation. These designs also need to be investigated in the more systematic manner of the present investigation. Numerous designs of low-profile pericardial valves have been or are being developed. A study comparing the flow dynamics of these pericardial valves is thus needed. Also, porcine bioprostheses have become very popular and comparative studies are needed between the porcine and pericardial valves. Further studies could also include comparative analyses of the many tilting-disc

prostheses currently available or under development. The natural, human aortic valve also needs to be investigated in a similar way as the four valves were for the present investigation. The results from the study of the natural valve would provide the standard flow dynamics for comparison with the prostheses.

Another very important extension of the present investigation would be to mock-up clinically relevant failure modes of prostheses and study the changes in the flow dynamics. Small thrombus formations could be simulated on key parts of the valve superstructure. The propensity for accelerating thrombus formation could then be studied as a function of the stagnant-flow regions generated by the small thrombus.

Finally, explanted valves could be studied to correlate hemodynamic findings before explantation with flow dynamics found later *in vitro*. This type of investigation would be most helpful for tissue valves that had suffered tissue degeneration or were calcific. Care would be necessary to take into account the differences in the *in vivo* state of the valves compared with the *in vitro* state, especially after sterilization of the explanted valve. The differences in the flow dynamics of the explanted valve when compared to a new valve would give insight into the relative importance of the notable deficiencies of the explanted valves.

6. REFERENCES

1. Åberg, B. and Henze, A. (1979), Comparison Between the *In Vitro* Flow Dynamics of the Standard and Convexo-Concave Björk-Shiley Tilting Disc Valve Prostheses, *Scand. J. Thorac. Cardiovasc. Surg.*, **13**, 177-189.

2. Anderson, R., Bonchek, L., Grunkemeier, G., Lambert, L. and Starr, A. (1974), Analysis and Presentation of Surgical Results by Actuarial Methods, *J. Surg. Research*, **16**, 224-230.

3. Alchas, P., Snyder, A. and Phillips, W. (1980), Pulsatile Prosthetic Valve Flows: Laser-Doppler Studies, in **Biofluid Mechanics**, ed. Schneck, D., Plenum Publishing Corp., New York, NY, pp. 243-265.

4. Au, A. and Greenfield, H. (1975), Computer Graphics Analysis of Stresses in Blood Flow Through a Prosthetic Heart Valve, *Comput. Biol. Med.*, **4**, 279-291.

5. Barnett, D. and Bentley, H., III (1974), Statistical Bias of Individual Realization Laser Velocimeters, *Proc. 2nd Int. Workshop in Laser Velocimetry*, **1**, 428-444.

6. Becker, R., Strom, J., Frishman, W., Oka, Y., Lin, Y., Yellin, E. and Frater, R. (1980), Hemodynamic Performance of the Ionescu-Shiley Valve Prosthesis, *J. Thorac. Cardiovasc. Surg.*, **80**, 613-620.

7. Bellhouse, B. (1969), Velocity and Pressure Distributions in the Aortic Valve, *J. Fluid Mech.*, **37**, 587-600.

8. Bellhouse, B. and Talbot, L. (1969), The Fluid Mechanics of the Aortic Valve, *J. Fluid Mech.*, **35**, 721-735.

9. Ben-Zvi, J., Hildner, F., Chandraratna P. and Samet P. (1974), Thrombosis on Björk-Shiley Aortic Valve Prosthesis, *Amer. J. Cardiol.*, **34**, 538-544.

10. Berman, N. and Dunning, J. (1973), Pipe Flow Measurements of Turbulence and Ambiguity Using Laser-Doppler Velocimetry, *J. Fluid Mech.*, **61**, 289-299.

11. Bernstein, E. (1976), Mechanisms of Hemolysis, Annual Summary Report, Contract No. DADA 17-73-C-3115, Supported by U.S. Army Medical Research and Development Command, Washington, DC.

12. Bernstein, E., Blackshear, P., Jr. and Keller, K. (1967), Factors Influencing Erythrocyte Destruction in Artificial Organs, *Amer. J. Surg.*, **114**, 126-138.

13. Bernstein, E., Marzec, U. and Johnston, G. (1977), Structural Correlates of Platelet Functional Damage by Physical Forces, *Trans. Amer. Soc. Artif. Intern. Organs*, **23**, 617-625.

14. Bird, R., Stewart, W. and Lightfoot, E. (1960), **Transport Phenomena**, John Wiley and Sons, Inc., New York, NY.

15. Björk, V. (1978), The Improved Björk-Shiley Tilting Disc Valve Prosthesis, *Scand. J. Thorac. Cardiovasc. Surg.*, **12**, 81-84.

16. Björk, V. and Henze, A. (1975), Management of Thrombo-Embolism After Aortic Valve Replacement with the Björk-Shiley Tilting Disc Valve, *Scand. J. Thorac. Cardiovasc. Surg.*, **9**, 183-191.

17. Björk, V. and Henze, A. (1979), Ten Years' Experience with the Björk-Shiley Tilting Disc Valve, *J. Thorac. Cardiovasc. Surg.*, **78**, 331-342.

18. Björk, V., Holmgren, A., Olin, C. and Ovenfors, C. (1971), Clinical and Hemodynamic Results of Aortic Valve Replacement with the Björk-Shiley Tilting Disc Valve Prosthesis, *Scand. J. Thorac. Cardiovasc. Surg.*, **5**, 177-191.

19. Björk, V. and Olin, C. (1970), A Hydrodynamic Comparison Between the New Tilting Disc Aortic Valve Prosthesis (Björk-Shiley) and the Corresponding Prostheses of Starr-Edwards, Kay-Shiley, Smeloff-Cutter and Wada-Cutter in the Pulse Duplicator, *Scand. J. Thorac. Cardiovasc. Surg.*, **4**, 31-36.

20. Björk, V., Olin, C. and Rodriguez, L. (1972), Comparative Results of Aortic Valve Replacement with Different Prosthetic Heart Valves, *J. Cardiovasc. Surg.*, **13**, 268-271.

21. Blackshear, P., Jr. (1972), Mechanical Hemolysis in Flowing Blood, in **Biomechanics: Its Foundations and Objectives**, eds. Fung, Y., Perrone, N. and Anliker, M., Prentice-Hall, Inc., Philadelphia, PA, pp. 501-528.

22. Blackshear, P., Jr., Dorman, F. and Steinbach, J. (1965), Some Mechanical Effects that Influence Hemolysis, *Trans. Amer. Soc. Artif. Intern. Organs*, **11**, 112-117.

23. Bloodwell, R., Okies, J., Hallman, G. and Cooley, D. (1969), Aortic Valve Replacement. Long-Term Results, *J. Thorac. Cardiovasc. Surg.*, **58**, 457-466.

24. Bodnar, E., Wain, W. and Haberman, S. (1982), Assessment and Comparison of the Performance of Cardiac Valves, *Ann. Thorac. Surg.*, **34**, 146-156.

25. Bonchek, L. (1981), Current Status of Cardiac Valve Replacement: Selection of a Prosthesis and Indications for Operation, *Amer. Heart J.*, **101**, 96-106.

26. Bonchek, L. and Starr, A. (1975), Ball Valve Prostheses: Current Appraisal of Late Results, *Amer. J. Cardiol.*, **35**, 843-854.

27. Bozer, A. and Karamehmetoglu, A. (1972), Thrombosis Encountered with Björk-Shiley Prosthesis, *J. Cardiovasc. Surg.*, **13**, 141-143.

28. Braunwald, E. (1980), **Heart Disease. A Textbook of Cardiovascular Medicine**, W. B. Saunders Co., Philadelphia, PA.

29. Brawley, R., Donahoo, J. and Gott, V. (1975), Current Status of the Beall, Björk-Shiley, Braunwald-Cutter, Lillehei-Kaster and Smeloff-Cutter Cardiac Valve Prostheses, *Amer. J. Cardiol.*, **35**, 855-865.

30. Brodeur, M., Sutherland, D., Koler, R., Starr, A., Kimsey, I. and Griswold, H. (1965), Red Blood Cell Survival in Patients with Aortic Valvular Disease and Ball-Valve Prostheses, *Circ.*, **32**, 570-581.

31. Brown, C., III, Lemuth R., Hellums, J., Leverett, L. and Alfrey, C., Jr. (1975), Response of Human Platelets to Shear Stress, *Trans. Amer. Soc. Artif. Intern. Organs*, **21**, 35-38.

32. Brown, C., III, Leverett, L., Lewis, C., Alfrey C., Jr. and Hellums, J. (1975), Morphological, Biochemical, and Functional Changes in Human Platelets Subjected to Shear Stress, *J. Lab. Clin. Med.*, **86**, 462-471.

33. Bruss, K., Reul, H., Gilse, J. van and Knott, E. (1983), Pressure Drop and Velocity Fields at Four Mechanical Heart Valve Prostheses: Björk-Shiley Standard, Björk-Shiley Concave-Convex, Hall-Kaster and St. Jude Medical, *Life Support Systems*, **1**, 3-22.

34. Buchhave, P., George, W., Jr. and Lumely, J. (1979), The Measurement of Turbulence with the Laser-Doppler Anemometer, *Ann. Rev. Fluid Mech.*, **11**, 443-503.

35. Cartwright, R., Smeloff, E., Davey, T. and Kaufman, B. (1964), Development of a Titanium Double-Caged Full-Orifice Ball Valve, *Trans. Amer. Soc. Artif. Intern. Organs*, **10**, 231-236.

36. Casci, C., Fumero, R. and Montevecchi, F. (1977), Prosthetic Heart Valves, in **Cardiovascular Flow Dynamics and Measurements**, eds. Hwang, N. and Normann, N., University Park Press, Baltimore, MD, pp. 851-875.

37. Chaux, A., Gray, R., Matloff, J., Feldman, H. and Sustaita, H. (1981), An Appreciation of the New St. Jude Valvular Prosthesis, *J. Thorac. Cardiovasc. Surg.*, **81**, 202-211.

38. Chaux, A., Matloff, J., Sustaita, H., MacKay, D. and McCarthy, K. (1979), Thromboembolism and Survival After Mitral and Aortic Valve Replacement. Comparison Between Porcine Xenografts and Nonbiologic Valve Prostheses, in **Prosthetic Heart Valves**, eds. Yoganathan, A., Harrison, E. and Corcoran W., Caltech Press, Pasadena, CA, pp. 321-340.

39. Chuang, H. and Cermak, J. (1967), Electrokinetic-Potential Fluctuations Produced by Pipe Flow Turbulence, *AIChE J.*, **13**, 266-272.

40. Clark, C. (1976), The Fluid Mechanics of Aortic Stenosis - I. Theory and Steady Flow Experiments, *J. Biomech.*, **9**, 521-528.

41. Clark, C. (1976), The Fluid Mechanics of Aortic Stenosis - II. Unsteady Flow Experiments, *J. Biomech.*, **9**, 567-573.

42. Cokkinos, D., Voridis, E., Bakoulas, G., Theodossiou, A. and Skalkeas, G. (1971), Thrombosis of Two High-Flow Prosthetic Valves, *J. Thorac. Cardiovasc. Surg.*, **62**, 947-949.

43. Colantuoni, G., Hellums, J., Moake, J. and Alfrey, C., Jr. (1977), The Response of Human Platelets to Shear Stress at Short Exposure Times, *Trans. Amer. Soc. Artif. Intern. Organs*, **23**, 626-631.

44. Corrsin, S. and Uberoi, M. (1951), Spectra and Diffusion in a Round Turbulent Jet, *NACA Tech. Reports*, **1040**.

45. Cox, J., Hoften, J. van and Hwang, N. (1979), Investigation of a Pulsatile Flowfield Downstream from a Model Stenosis, *J. Biomech. Eng.*, **101**, 141-150.

46. Crexells, C., Aerichide, N., Bonny, Y., Lepage, G. and Campeau, L. (1972), Factors Influencing Hemolysis in Valve Prosthesis, *Amer. Heart J.*, **84**, 161-170.

47. Dale, J. (1977), Arterial Thromboembolic Complications in Patients with Björk-Shiley and Lillehei-Kaster Aortic Disc Valve Prostheses, *Amer. Heart J.*, **93**, 715-722.

48. Dale, J., Levang, O. and Enge, I. (1980), Long-Term Results After Aortic Valve Replacement with Four Different Prostheses, *Amer. Heart J.*, **99**, 155-162.

49. Dale, J. and Myhre, E. (1978), Intravascular Hemolysis in the Late Course of Aortic Valve Replacement. Relation to Valve Type, Size, and Function, *Amer. Heart J.*, **96**, 24-30.

50. Davey, T., Kaufman, B. and Smeloff, E. (1966), Pulsatile Flow Studies of Prosthetic Heart Valves, *J. Thorac. Cardiovasc. Surg.*, **51**, 264-267.

51. Davey, T. and Smeloff, E. (1977), Development of a Cardiac Valve Substitute: The Smeloff-Cutter Prosthesis, *Med. Instrum.*, **11**, 95-97.

52. Davila, J., Enriquez, F. and Palmer, T. (1963), Thrombosis in Artificial Heart Valves: Role of Turbulence due to Design, *Circ.*, **28**, 708-709.

53. De Bernardinis B., Graham, J. and Parker, K. (1981), Oscillatory Flow Around Disks and Through Orifices, *J. Fluid Mech.*, **102**, 279-299.

54. Dellsperger, K., Wieting, D., Baehr, D., Bard, R., Brugger, J. and Harrison, E. (1983), Regurgitation of Prosthetic Heart Valves: Dependence on Heart Rate and Cardiac Output, *Amer. J. Cardiol.*, **51**, 321-328.

55. Dimotakis, P. (1976), Single Scattering Particle Laser-Doppler Measurements of Turbulence, AGARD Conference Proceedings No. 193.

56. Duff, W. (1969), Ph.D. Thesis, Purdue University, IN.

57. Dutton, R., Baier, R., Dedrick, R., and Bowman, R. (1968), Initial Thrombus Formation on Foreign Surfaces, *Trans. Amer. Soc. Artif. Intern. Organs*, **14**, 57-62.

58. Edmiston, W., Harrison, E., Parnassus, W., Mitani, G. Sarma, R., Carlock, S., Lampman, M., Batista, E., and Masaki, B. (1979), Thromboembolism in Aortic and Mitral Prosthetic Valve Recipients, in **Prosthetic Heart Valves**, eds. Yoganathan, A., Harrison, E. and Corcoran, W., Caltech Press, Pasadena, CA, pp. 357-367.

59. Edwards, R. (1981), A New Look at Particle Statistics in Laser-Anemometer Measurements, *J. Fluid Mech.*, **105**, 317-325.

60. Emery, R., Anderson, R., Lindsay, W., Jorgensen, C., Wang, Y. and Nicoloff, D. (1979), Clinical and Hemodynamic Results with the St. Jude Medical Aortic Valve Prosthesis, *Surg. Forum*, **30**, 235-238.

61. Emery, R. and Nicoloff, D. (1979), St. Jude Medical Cardiac Valve Prosthesis. *In Vitro* Studies, *J. Thorac. Cardiovasc. Surg.*, **78**, 269-276.

62. Emery, R., Palmquist W., Mettler, E. and Nicoloff, D. (1978), A New Cardiac Valve Prosthesis: *In Vitro* Results, *Trans. Amer. Soc. Artif. Intern. Organs*, **24**, 550-556.

63. Evans, E. (1973), New Membrane Concept Applied to the Analysis of Fluid Shear- and Micropipette-Deformed Red Blood Cells, *Biophys. J.*, **13**, 941-954.

64. Eyster, E., Rothchild, J. and Mychajliw, O. (1971), Chronic Intravascular Hemolysis After Aortic Valve Replacement, *Circulation*, **44**, 657-665.

65. Falk, R., MacKinnon, J., Wainscoat, J., Melikian, V. and Bignell, A. (1979), Intravascular Hemolysis After Valve Replacement: Comparative Study Between Starr-Edwards (Ball Valve) and Björk-Shiley (Disc Valve) Prosthesis, *Thorax*, **34**, 746-748.

66. Febres-Roman, P., Bourg, W., Crone, R., Davis, R., Jr. and Williams, T. (1980), Chronic Intravascular Hemolysis After Aortic Valve Replacement with Ionescu-Shiley Xenograft: Comparative Study with Björk-Shiley Prosthesis, *Amer. J. Cardiol.*, **46**, 735-738.

67. Fernandez, J., Samuel, A., Yang, S., Sumathisena, Gooch, A., Maranhao, V., Lemole, G. and Goldberg, H. (1976), Late Thrombosis of the Aortic Björk-Shiley Prosthesis, *Chest*, **70**, 12-16.

68. Figliola, R. (1979), Ph.D. Thesis, University of Notre Dame, IN.

69. Figliola, R. and Mueller, T. (1977), Fluid Stresses in the Vicinity of Disk, Ball, and Tilting Disk Prosthetic Heart Valves from *In Vitro* Measurements, *J. Biomech. Eng.*, **99**, 173-177.

70. Figliola, R. and Mueller, T. (1976), *In Vitro* Measurements of Fluid Stresses in the Vicinity of a Disc-Type Prosthetic Heart Valve, Proc. 29th ACEMB, Boston, MS, p. 340.

71. Figliola, R. and Mueller, T. (1979), *In Vitro* Determination of Fluid Stresses in the Vicinity of Occluder-Type Prosthetic Heart Valves, in **Prosthetic Heart Valves**, eds. Yoganathan, A., Harrison, E. and Corcoran W., Caltech Press, Pasadena, CA, pp. 121-134.

72. Figliola, R. and Mueller, T. (1981), On the Hemolytic and Thrombogenic Potential of Occluder Prosthetic Heart Valves from *In Vitro* Measurements, *J. Biomech. Eng.*, **103**, 83-90.

73. Forrester, J., Wieting, D., Hall, C. and DeBakey, M. (1969), A Comparative Study of the Fluid Flow Resistance of Prosthetic Heart Valves, *Cardiovasc. Res. Center Bull.*, **7**, 83-99.

74. Frater, R., Gabbay, S., McQueen, S., Becker, R., Borg, M., Strom, J., Lin, T., Oka, Y. and Yellin, E. (1979), Bioprostheses: Hemodynamic Performance Thromboembolic Incidence and Symptomatic Benefits, in **Prosthetic Heart Valves**, eds. Yoganathan, A., Harrison, E. and Corcoran, W., Caltech Press, Pasadena, CA, pp. 341-355.

75. Friedli, B., Aerichide, N., Grondin, P. and Campeau, L. (1971), Thromboembolic Complications of Heart Valve Prostheses, *Amer. Heart J.*, **81**, 702-708.

76. Fung, Y. and Tong, P. (1968), Theory of the Sphering of Red Blood Cells, *Biophys. J.*, **8**, 175-198.

77. Gaarder, A., Jonsen, J., Laland, S., Hellem, A. and Owren, P. (1961), Adenosine Diphosphate in Red Cells as a Factor in the Adhesiveness of Human Blood Platelets, *Nature*, **192**, 531-532.

78. Gabbay, S., Yellin, E., Frishman, W. and Frater, R. (1980), *In Vitro* Hydrodynamic Comparison of St. Jude, Björk-Shiley and Hall-Kaster Valves, *Trans. Amer. Soc. Artif. Intern. Organs*, **26**, 231-236.

79. Gehrman, G., Bleifeld, W. and Kauler, D. (1966), Hertzklappenfehler und Hämolyse, *Klinische Wochenschrift*, **44**, 1229-1235.

80. George, W. (1974), The Measurement of Turbulence Intensities Using Real-Time Laser-Doppler Velocimetry, *J. Fluid Mech.*, **66**, 11-16.

81. George, W. and Lumely, J. (1973), The Laser-Doppler Velocimeter and Its Application to the Measurement of Turbulence, *J. Fluid Mech.*, **60**, 321-362.

82. Gombrich, P., Villafana, M. and Palmquist, W. (1979), From Concept to Clinical. The St. Jude Medical Bi-Leaflet Pyrolytic Carbon Cardiac Valve, in **Prosthetic Heart Valves**, eds. Yoganathan, A., Harrison, E. and Corcoran, W., Caltech Press, Pasadena, CA, pp. 181-212.

83. Gonzalez-Lavin, L., Chi, S., Blair, T., Jung, J., Fabaz, A., McFadden, P., Lewis, B. and Daughters, G. (1983), Five-Year Experience with the Ionescu-Shiley Bovine Pericardial Valve in the Aortic Position, *Ann. Thorac. Surg.*, **36**, 271-280.

84. Gorlin, R. and Gorlin, S. (1951), Hydraulic Formula for Calculation of the Area of the Stenotic Mitral Valve, Other Cardiac Valves, and Central Circulatory Shunts. I., *Amer. Heart J.*, **44**, 1-29.

85. Gray, R., Chaux, A., Matloff, J. and Raymond, M. (1979), Early Postoperative Hemodynamic Performance of the Porcine Xenograft Compared to Non-Biologic Prosthesis, in **Prosthetic Heart Valves**, eds. Yoganathan, A., Harrison, E. and Corcoran, W., Caltech Press, Pasadena, CA, pp. 213-229.

86. Grunkemeier, G., Lambert, L., Bonchek, L. and Starr, A. (1975), An Improved Statistical Method for Assessing the Results of Operation, *Ann. Thorac. Surg.*, **20**, 289-298.

87. Grunkemeier, G. and Starr, A. (1977), Actuarial Analysis of Surgical Results: Rationale and Method, *Ann. Thorac. Surg.*, **24**, 404-408.

88. Guttman, I., Wilks, S. and Hunter, S. (1971), **Introductory Engineering Statistics**, John Wiley and Sons, Inc., New York, NY, p. 36.

89. Hagelberg, M. (1973), **Physics. An Introduction for Students of Science and Engineering**, Prentice-Hall, Inc., Englewood, Cliffs, NJ, p. 334.

90. Hancock, W., Nolan, S., Roschke, J. (co-Chairmen) and Members (1981), American National Standard For Cardiac Valve Prostheses, by the Association for the Advancement of Medical Instrumentation, Arlington, VA.

91. Hanle, D., Harrison, E., Corcoran, W. and Yoganathan, A. (1983), The Measurement of the Three-Dimensional Velocity Fields Downstream from Artificial Heart Valves *In Vitro* using Laser-Doppler Anemometry, presented at ASME Biomechanics Symposium, Houston, TX, pp. 225-228.

92. Harrison, E., Roschke, E., Meyers, H., Edmiston, W., Chan, L., Tatter, D. and Lau, F. (1978), Cholelithiasis: A Frequent Complication of Artificial Heart Valve Replacement, *Amer. Heart J.*, **95**, 483-488.

93. Hehrlein, F., Gottwik, M., Mulch, J., Walter, P. and Fraedrich, G. (1980), Heart Valve Replacement with the New All-Pyrolytic Bi-Leaflet St. Jude Medical Prosthesis, *J. Cardiovasc. Surg.*, **21**, 395-398.

94. Hellums, J. and Brown, C., III (1977), Blood Cell Damage by Mechanical Forces, in **Cardiovascular Flow Dynamics and Measurements**, eds. Hwang, N. and Normann, N., University Park Press, Baltimore, MD, pp. 799-823.

95. Henze, A. and Fortune, R. (1974), Regurgitation and Hemolysis in Artificial Heart Valves, *Scand. J. Thorac. Cardiovasc. Surg.*, **8**, 167-175.

96. Herr, R., Starr, A., McCord, C. and Wood, J. (1965), Special Problems Following Valve Replacement. Embolus, Leak, Infection, Red Cell Damage, *Ann. Thorac. Surg.*, **1**, 403-415.

97. Hinze, J. (1976), **Turbulence**, 2nd ed., McGraw-Hill Co., New York, NY.

98. Hochmuth, R. and Mohandas, N. (1972), Uniaxial Loading of the Red-Cell Membrane, *J. Biomech.*, **5**, 501-509.

99. Hochmuth, R., Mohandas, N. and Blackshear, P., Jr. (1973), Measurement of the Elastic Modulus for Red Cell Membrane Using a Fluid Mechanical Technique, *Biophys. J.*, **13**, 747-762.

100. Hochmuth, R., Mohandas, N., Spaeth, E., Williamson, J., Blackshear, P., Jr. and Johnson, D. (1972), Surface Adhesion, Deformation and Detachment at Low Shear of Red Cells and White Cells, *Trans. Amer. Soc. Artif. Intern. Organs*, **18**, 325-334.

101. Hoeber, T. and Hochmuth, R. (1970), Measurement of Red Cell Modulus of Elasticity by *In Vitro* and Model Cell Experiments, *J. Basic Eng.*, **92**, 604-609.

102. Hung, T., Hochmuth, R., Joist, J. and Sutera, S. (1976), Shear-Induced Aggregation and Lysis of Platelets, *Trans. Amer. Soc. Artif. Intern. Organs*, **22**, 285-291.

103. Hung, T. Shen, L., Akutsu, T. and Hwang, N. (1978), Some Physical Characteristics of Normal Erythrocyte Membrane from Experimental Animals and Humans, *Trans. Amer. Soc. Artif. Intern. Organs*, **24**, 573-577.

104. Hussain, A. (1977), Mechanics of Pulsatile Flows of Relevance to the Cardiovascular System, in **Cardiovascular Flow Dynamics and Measurement**, eds. Hwang, N. and Normann, N., University Park Press, Baltimore, MD, pp. 541-632.

105. Hussain, A. and Reynolds, W. (1970), The Mechanics of an Organized Wave in Turbulent Shear Flow, *J. Fluid Mech.*, **41**, 241-258.

106. Hwang, N. (1977), Flow Dynamics of Natural Valves in the Left Heart, in **Cardiovascular Flow Dynamics and Measurements**, eds. Hwang, N. and Normann, N., University Park Press, Baltimore, MD, pp. 825-850.

107. Hwang, N., Nan, X. and Gross, D. (1983), Prosthetic Heart Valve Replacements, *CRC Crit. Rev. Biomed. Eng.*, **9**, 99-132.

108. Indeglia, R., Shea, M., Varco, R. and Bernstein, E. (1968), Erythrocyte Destruction by Prosthetic Heart Valves, *Circulation*, **37**, II-86 - II-93.

109. Ionescu M., Tandon, A., Mary, D. and Abid, A. (1977), Heart Value Replacement with the Ionescu-Shiley Pericardial Xenograft, *J. Thorac. Cardiovasc. Surg.*, **73**, 31-40.

110. Ionescu M., Tandon, A., Saunders, N., Chidambaram, M. and Smith, D. (1982), Clinical Durability of the Pericardial Xenograft Valve: 11 Years' Experience, in **Cardiac Bioprostheses**, eds. Cohn, L. and Gallucci, V., Yorke Medical Books, New York, NY, pp. 42-60.

111. Johnson, D. (1973), Insensitivity of Single Particle Time Domain Measurements to Laser Velocimeter "Doppler Ambiguity," *AIAA J.*, **11**, 890-892.

112. Johnston, G., Marzec, U. and Bernstein, E. (1975), Effects of Surface Injury and Shear Stress on Platelet Aggregation and Serotonin Release, *Trans. Amer. Soc. Artif. Intern. Organs*, **21**, 413-421.

113. Karp, R., Cyrus, R., Blackstone, E., Kirklin, J. Kouchoukos, N. and Pacifico, A. (1981), The Björk-Shiley Valve, *J. Thorac. Cardiovasc. Surg.*, **81**, 602-614.

114. Karpuk, M. and Tiederman, W., Jr. (1976), Effect of Finite-Size Probe Volume Upon Laser Doppler Anemometer Measurements, *AIAA J.*, **14**, 1099-1105.

115. Kaster, R., Lillehei, C. and Starek, P. (1970), The Lillehei-Kaster Pivoting Disc Aortic Prosthesis and a Comparative Study of Its Pulsatile Flow Characteristics with Four Other Prostheses, *Trans. Amer. Soc. Artif. Intern. Organs*, **16**, 233-243.

116. Kloster, F. (1979), Complications of Artificial Heart Valves, *J. Amer. Med. Assoc.*, **241**, 2201-2203.

117. Kolmogorov, A. (1941), The Local Structure of Turbulence in Incompressible Viscous Fluid for Very Large Reynold's Numbers, *Comptes Rendus (Doklady) de l'Academie des Sciences de l'URSS*, **30**, 301-305.

118. Komasawa, I., Kuboi, R. and Otake, T. (1974), Fluid and Particle Motion in Turbulent Diffusion - I. Measurement of Turbulence of Liquid by Continual Pursuit of Tracer Particle Motion, *Chem. Eng. Sci.*, **29**, 641-650.

119. Kreid, D. (1974), Error Estimates for Laser Doppler Velocimeter Measurements in Non-Uniform Flow, *Proc. 2nd Int. Workshop in Laser Velocimetry*, **1**, 398-427.

120. Lawn, C. (1971), The Determination of the Rate of Dissipation in Turbulent Pipe Flow, *J. Fluid Mech.*, **48**, 477-505.

121. Laufer, J. (1954), The Structure of Turbulence in Fully Developed Pipe Flow, *NACA Tech. Reports*, **1174**.

122. Lee, C. and Talbot, L. (1979), A Fluid-Mechanical Study of the Closure of Heart Valves, *J. Fluid Mech.*, **91**, 41-65.

123. Lee, S., Barr, C., Callaghan, J. and Rossall, R. (1975), Long-Term Survival after Aortic Valve Replacement Using Smeloff-Cutter Prosthesis, *Circulation*, **52**, 1132-1137.

124. Leonard, E. (1972), The Role of Flow in Thrombogenesis, *Bull. N.Y. Acad. Med.*, **48**, 273-280.

125. Levang, O. (1979), Aortic Valve Replacement. A Randomized Study Comparing Björk-Shiley and Lillehei-Kaster Disc Valves. Hematological Evaluation, *Scand. J. Thorac. Cardiovasc. Surg.*, **13**, 215-220.

126. Levang, O., Nitter-Hauge, S., Levorstad, K. and Froysaker, T. (1979), Aortic Valve Replacement. A Randomized Study Comparing the Björk-Shiley and Lillehei-Kaster Disc Valves. Late Hemodynamics Related to Clinical Results, *Scand. J. Thorac. Cardiovasc. Surg.*, **13**, 199-213.

127. Leverett, L., Hellums, J., Alfrey, C. and Lynch, E. (1972), Red Blood Cell Damage by Shear Stress, *Biophys. J.*, **12**, 257-273.

128. Lindsay, R. (Chairman), Mason, R., Kim, S., Andrade, J. and Hakim, R. (1980), Panel Conference on Blood Surface Interactions, *Trans. Amer. Soc. Artif. Intern. Organs*, **26**, 603-610.

129. Lloyd, J. (1979), Electrochemical Techniques Applied to Evaluation of Prosthetic Heart Valve Performance, in **Prosthetic Heart Valves**, eds. Yoganathan, A., Harrison, E. and Corcoran, W., Caltech Press, Pasadena, CA, pp. 135-153.

130. Love, J., Jr., Advani, S. and Tarnay, T. (1971), Comparative Turbulence of Heart Valves (Natural and Prosthetic), *Trans. Amer. Soc. Artif. Intern. Organs*, **17**, 497-504.

131. Lu, P., Sallam, A. and Hwang, N. (1979), Measurement of Turbulence in Aortic Valve Prostheses: An Assessment by Laser Doppler Anemometer, in **Prosthetic Heart Valves**, eds. Yoganathan, A., Harrison, E. and Corcoran, W., Caltech Press, Pasadena, CA, pp. 91-119.

132. Madras, P., Morton., W. and Petschek, H. (1971), Dynamics of Thrombus Formation, *Fed. Proc.*, **30**, 1665-1676.

133. Martin, G. and Johanson, L. (1965), Turbulence Characteristics of Liquids in Pipe Flow, *AIChE J.*, **11**, 29-33.

134. Martin, T., Tindale, W., Noort, R. van and Black, M. (1981), *In Vitro* Heart Valve Evaluation: Fact or Fantasy?, *Trans. Amer. Soc. Artif. Intern. Organs*, **27**, 475-479.

135. Mazumdar, J. and Thalassoudis, K. (1983), A Mathematical Model for the Study of Flow through Disc-Type Prosthetic Heart Valves, *Med. Biol. Eng. Comp.*, **21**, 400-409.

136. McHenry, M., Smeloff, E. and Hattersky, P. (1968), Complications of Heart Valve Replacement. Embolism, Bleeding, and Hemolysis, *Calif. Med.*, **109**, 1-8.

137. McHenry, M., Smeloff, E., Matlof, H., Rice, J. and Miller, G., Jr. (1978), Long-Term Survival after Single Aortic or Mitral Valve Replacement with the Present Model of Smeloff-Cutter Valves, *J. Thorac. Cardiovasc. Surg.*, **75**, 709-715.

138. McLaughlin, D. and Tiederman, W. (1973), Biasing Correction for Individual Realization of Laser Anemometer Measurements in Turbulent Flows, *Phys. of Fluids*, **16**, 2082-2088.

139. Menon, R. (1982), Laser Doppler Velocimetry: Performance and Applications. *Amer. Lab.*, **14**, 122-143.

140. Merendino, K. and Manhas, D. (1973), Man-Made Gallstones: A New Entity Following Cardiac Valve Replacement, *Ann. Surg.*, **177**, 694-704.

141. Nevaril, C., Hellums, J., Alfrey C., Jr. and Lynch, E. (1969), Physical Effects in Red Blood Cell Trauma, *AIChE J.*, **15**, 707-711.

142. Nevaril, C., Lynch, E., Alfrey, C., Jr. and Hellums, D. (1968), Erythrocyte Damage and Destruction Induced by Shearing Stress, *J. Lab. Clin. Med.*, **71**, 784-790.

143. Nicoloff, D. and Emery, R. (1979), Current Status of the St. Jude Cardiac Valve Prosthesis, *Contemp. Surg.*, **15**, 11-26.

144. Nworgu, O., McHugh, B., Bellingham, A. and Wright, J. (1979), An *In Vitro* Assessment of Hemolysis caused by Prosthetic Heart Valves, in **Prosthetic Heart Valves**, eds. Yoganathan, A., Harrison, E. and Corcoran, W., Caltech Press, Pasadena, CA, pp. 285-299.

145. Olin, C. (1971), Pulsatile Flow Studies of Prosthetic Aortic Valves, *Scand. J. Thorac. Cardiovasc. Surg.*, **5**, 1-12.

146. Perry, R. and Chilton, C. (1973), **Chemical Engineers' Handbook**, 5th ed., McGraw-Hill Co., New York, NY, p. 5-62.

147. Peskin, C. (1982), The Fluid Dynamics of Heart Valves: Experimental, Theoretical, and Computational Methods, *Ann. Rev. Fluid Mech.*, **14**, 235-258.

148. Petschek, H., Adamis, D. and Kantrowitz, A. (1968), Stagnation Flow Thrombus Formation, *Trans. Amer. Soc. Artif. Intern. Organs*, **14**, 256-260.

149. Phillips, W., Brighton, J. and Pierce, W. (1972), Artificial Heart Evaluation Using Flow Visualization Techniques, *Trans. Amer. Soc. Artif. Intern. Organs*, **18**, 194-201.

150. Phillips, W., Lenker, J., Brighton, J. and Pierce, W. (1976), Flow Visualization Methods for *In Vitro* Cardiovascular Flow Studies, *Proc. 29th ACEMB*, Boston, MS, p. 337.

151. Phillips, W., Rosenberg, G., Furkay, S. and Pierce, W. (1979), An *In Vitro* and *In Vivo* Evaluation of Mitral Valves in a Prosthetic Ventricle, in **Prosthetic Heart Valves**, eds. Yoganathan, A., Harrison, E. and Corcoran, W., Caltech Press, Pasadena, CA, pp. 43-57.

152. Phillips, W., Snyder, A., Alchas, P., Rosenberg, G. and Pierce, W. (1980), Pulsatile Prosthetic Valve Flows, *Trans. Amer. Soc. Artif. Intern. Organs*, **26**, 43-49.

153. Rahimtoola, S. (1983), Valvular Heart Disease: A Perspective, *J. Amer. Coll. Cardiol.*, 199-215.

154. Ramstack, J., Zuckerman, L. and Mockros L. (1979), Shear-Induced Activation of Platelets, *J. Biomech.*, **12**, 113-125.

155. Rand, R. and Burton, A. (1964), Mechanical Properties of the Red Cell Membrane, *Biophys. J.*, **4**, 115-135.

156. Reul, H., Lu, P., Hoften, J. van and Hwang, N. (1977), Flow Patterns of Artificial Heart Valves Analyzed by a New Laser Technique, *Proc. 30th ACEMB*, Los Angeles, CA, p. 413.

157. Roberts, W. (1976), Choosing a Substitute Cardiac Valve: Type, Size, Surgeon, *Amer. J. Cardiol.*, **38**, 633-644.

158. Roeser, W., Powell, L. and O'Brien, M. (1970), Hemolysis After Heterograft and Prosthetic Valve Replacement, *Amer. Heart J.*, **79**, 281-283.

159. Rooney, J. (1970), Hemolysis Near an Ultrasonically Pulsating Gas Bubble, *Science*, **169**, 869-871.

160. Roschke, E. (1973), An Engineer's View of Prosthetic Heart Valve Performance, *Biomater. Med. Dev. Artif. Org.*, **1**, 249-290.

161. Roschke, E. and Harrison, E. (1977), Fluid Shear Stress in Prosthetic Heart Valves, *J. Biomech.*, **10**, 299-311.

162. Ross, D. (1982), The Evolution of the Biologic Valve, in **Cardiac Bioprostheses**, eds. Cohn, L. and Gallucci, V., Yorke Medical Books, New York, NY, pp. 1-8.

163. Sallam, A. and Hwang, N. (1983), Red Blood Cell Hemolysis in a Turbulent Jet, presented at ASME Biomechanics Symposium, Houston, TX, pp. 83-86.

164. Sallam, I., Shaw, A. and Bain, W. (1976), Experimental Evaluation of Mechanical Hemolysis with Starr-Edwards, Kay-Shiley and Björk-Shiley Valves. An *In Vitro* Study, *Scand. J. Thorac. Cardiovasc. Surg.*, **10**, 117-122.

165. Sandborn, V. (1955), Experimental Evaluation of Momentum Terms in Turbulent Pipe Flow, *NACA Tech. Reports*, **3266**.

166. Santinga, J., Batsakis, J., Flora, J. and Kirsh, M. (1976), Hemolysis in the Aortic Prosthetic Valve, *Chest*, **69**, 56-61.

167. Sarma, R., Roschke, E., Harrison, E., Edmiston, W. and Lau, F. (1977), Clinical Experience with the Smeloff-Cutter Aortic Valve Prosthesis: An 8-Year Follow-Up Study, *Amer. J. Cardiol.*, **40**, 338-344.

168. Schlichting, H. (1968), **Boundary Layer Theory**, McGraw-Hill Co., New York, NY, p. 531.

169. Schoen, F., Titus, J. and Lawrie, G. (1982), Bioengineering Aspects of Heart Valve Replacement, *Ann. Biomed. Eng.*, **10**, 97-128.

170. Schramm, D., Baldauf, W. and Meisner, H. (1980), Flow Pattern and Velocity Field Distal to Human Aortic and Artificial Heart Valves as Measured Simultaneously by Ultramicroscope Anemometry in Cylindrical Glass Tubes, *Thorac. Cardiovasc. Surg.*, **28**, 133-140.

171. Schramm, D., Müller-Mohnssen H., Baldauf, W. and Meisner, H. (1982), Fresh Human Aortic and Artificial Heart Valves Studied *In Vitro* Using Ultramicroscope Anemometry. Further Results, *Thorac. Cardiovasc. Surg.*, **30**, 273-280.

172. Schwarz, F., Baumann, P., Manthey, J., Hoffmann, M., Schuler, G. and Mehmel, H. (1982), The Effect of Aortic Valve Replacement on Survival, *Circulation*, **66**, 1105-1110.

173. Shulman, I., Edmiston, W., Harrison, E., Parnassus, W., Mitani, G., Yoganathan, A., Corcoran, W. and Turkel, S. (1979), Description of Material Adherent to Recovered Rigid Heart Valve Prostheses, in **Prosthetic Heart Valves**, eds. Yoganathan, A., Harrison, E. and Corcoran, W., Caltech Press, Pasadena, CA, pp. 385-395.

174. Silver, M. and Wilson G. (1983), Pathology of Cardiovascular Prostheses Including Coronary Artery Bypass and Other Vascular Grafts, in **Cardiovascular Pathology**, ed. Silver, M., Churchill-Livingstone, New York, NY, pp. 1225-1296.

175. Sixma, J. and Wester, J. (1977), The Hemostatic Plug, *Sem. Hematol.*, **14**, 265-299.

176. Slater, S., Sallam, I., Bain, W., Turner, M. and Lawrie, T. (1974), Hemolysis with Björk-Shiley and Starr-Edwards Prosthetic Heart Valves: A Comparative Study, *Thorax*, **29**, 624-632.

177. Smeloff, E. (1974), Isolated Single Valve Replacement with Smeloff-Cutter Prosthesis, 1966-1972, *Adv. Cardiol.*, **11**, 211-215.

178. Smeloff, E., Huntley, A., Davey, T., Kaufman, B. and Gerbode, F. (1966), Comparative Study of Prosthetic Heart Valves, *J. Thorac. Cardiovasc. Surg.*, **52**, 841-848.

179. Smith, R., Blick, E., Coalson, J. and Stein, P. (1972), Thrombus Production by Turbulence, *J. App. Physiol.*, **32**, 261-264.

180. Starr, A., Lawrie, G., Howell, J. and Morris, G. (1980), Clinical Experience with the Smeloff-Cutter Prosthesis: 1- to 12-year Follow-up, *Ann. Thorac. Surg.*, **30**, 448-453.

181. Steenhoven, A. van and Dongen, M. van (1979), Model Studies of the Closing Behaviour of the Aortic Valve, *J. Fluid Mech.*, **90**, 21-35.

182. Steenhoven, A. van, Duppen, T. van, Cauwenberg, J. and Renterghem R. van (1982), *In Vitro* Closing Behaviour of Björk-Shiley, St. Jude and Hancock Heart Valve Prostheses in Relation to the *In Vivo* Recorded Aortic Valve Closure, *J. Biomech.*, **15**, 841-848.

183. Stein, P. and Sabbah, H. (1974), Measured Turbulence and Its Effect on Thrombus, *Circ. Res.*, **35**, 608-614.

184. Stein, P. and Sabbah, H. (1976), Turbulent Blood Flow in the Ascending Aorta of Humans with Normal and Diseased Aortic Valves, *Circ. Res.*, **39**, 58-65.

185. Stein, P., Walburn, F. and Sabbah, H. (1982), Turbulent Stresses in the Region of Aortic and Pulmonary Valves, *J. Biomech. Eng.*, **104**, 238-244.

186. Stettler, J. and Hussain, A. (1983), On Transition of the Unsteady Pipe Flow, presented at ASME Biomechanics Symposium, Houston, TX, pp. 179-180.

187. Stormorken, H. (1971), Platelets, Thrombosis and Hemolysis, *Fed. Proc.*, **30**, 1551-1555.

188. Streeter, V. and Wylie, E. (1975), **Fluid Mechanics**, 6th ed., McGraw-Hill Co., New York, NY, pp. 169-170.

189. Suobank, D. (1983), Ph.D. Thesis, California Institute of Technology, CA.

190. Suobank, D., Yoganathan, A., Harrison, E. and Corcoran, W. (1984), A Quantitative Method for the *In Vitro* Study of Sounds Produced by Prosthetic Aortic Heart-Valves, Part I: Analytical Considerations, to be published in *Med. Biol. Eng. Comput.*

191. Suobank, D., Yoganathan, A., Harrison, E. and Corcoran, W. (1984), A Quantitative Method for the *In Vitro* Study of Sounds Produced by Prosthetic Aortic Heart-Valves, Part II: An Experimental, Comparative Study of the Sounds Produced by a Normal and Simulated-Abnormal Starr-Edwards Series 2400 Aortic Prosthesis, to be published in *Med. Biol. Eng. Comput.*

192. Suobank, D., Yoganathan, A., Harrison, E. and Corcoran, W. (1984), A Quantitative Method for the *In Vitro* Study of Sounds Produced by Prosthetic Aortic Heart-Valves, Part III: An Experimental, Comparative Study of the Sounds Produced by Normal and Simulated-Abnormal Smeloff Aortic Prosthesis, to be published in *Med. Biol. Eng. Comput.*.

193. Sutera, S., Croce, P. and Mehrjardi, M. (1972), Hemolysis and Subhemolytic Alterations of Human RBC Induced by Turbulent Shear Flow, *Trans. Amer. Soc. Artif. Intern. Organs*, **18**, 335-341.

194. Sutera, S. and Mehrjardi, M. (1975), Deformation and Fragmentation of Human Red Blood Cells in Turbulent Shear Flow, *Biophys. J.*, **15**, 1-10.

195. Swanson, W., Ou, S. and Clark, R. (1978), Vortex Motion and Induced Pressures in a Model of the Aortic Valve, *J. Biomech. Eng.*, **100**, 216-222.

196. Swope, R. and Falsetti, H. (1976), Velocity Profiles in Prosthetic Heart Valves under Steady Flow Conditions, *Proc. 29th ACEMB*, Boston, MS, p. 339.

197. Talukder, N., Reul, H. and Müller, E. (1977), Fluid Mechanics of the Natural Aortic Valve, *INSERM - Euromech 92, Cardiovascular and Pulmonary Dynamics*, **71**, 335-350.

198. Tandon, A., Smith, D., Mary, D. and Ionescu, M. (1977), Sequential Hemodynamic Studies in Patients Having Aortic Valve Replacement with the Ionescu-Shiley Pericardial Xenograft, *Ann. Thorac. Surg.*, **24**, 149-155.

199. Tennekes, H. and Lumely, J. (1972), **A First Course in Turbulence**, MIT Press, Cambridge, MA.

200. Tindale, W., Black, M. and Martin, T. (1982), *In Vitro* Evaluation of Prosthetic Heart Valves: Anomalies and Limitations, *Clin. Phys. Physiol. Meas.*, **3**, 115-130.

201. Torobin, L. and Gauvin, W. (1961), Turbulent Flow Ballistics Facility for Particle Momentum Transfer Studies, *AIChE J.*, **7**, 406-410.

202. Turitto, V. and Baumgartner, H. (1978), Inhibited Platelet Adhesion and Irreversible Thrombus Formation under High Shear Conditions, *Trans. Amer. Soc. Artif. Intern. Organs*, **24**, 719-726.

203. Underwood, F. and Mueller, T. (1977), Numerical Study of the Steady Axisymmetric Flow Through a Disk-Type Prosthetic Heart Valve in a Constant Diameter Chamber, *J. Biomech. Eng.*, **99**, 91-97.

204. Venkataraman, K., Beer, R., Mathews, N., Carl, J., Harrison, E., Turner, A. and Finck, E. (1980), Thrombosis of Björk-Shiley Aortic Valve Prostheses, *Radiology*, **137**, 43-47.

205. Walburn, F. and Stein, P. (1981), Effect of Vessel Tapering on the Transition to Turbulent Flow: Implications in the Cardiovascular System, *J. Biomech. Eng.*, **103**, 116-120.

206. Wallace, R. (1975), Tissue Valves, *Amer. J. Cardiol.*, **35**, 866-871.

207. Walsh, J., Starr, A. and Ritzmann, L. (1969), Intravascular Hemolysis in Patients with Prosthetic Valves and Valvular Heart Disease, *Circ.*, **39**, I-135 - I-140.

208. Whalen, R. and Keiser, J. (1977), Prosthetic Valves in Cardiac Assist Devices, *30th ACEMB*, Los Angeles, CA, p. 409.

209. Whatley, G. (1981), Ph.D. Thesis, California Institute of Technology, CA.

210. Whicher, S., Uniyal, S. and Brash, J. (1980), Platelet-Foreign Surface Interactions: The Release Reaction From Singly Adherent Platelets and Adherent Platelet Aggregates, *Trans. Amer. Soc. Artif. Intern. Organs*, **26**, 268-273.

211. Wieting, D. (1969), Ph.D. Thesis, University of Texas at Austin, TX.

212. Williams, A., Hughes, D. and Nyborg, W. (1970), Hemolysis Near a Transversely Oscillating Wire, *Science*, **169**, 871-873.

213. Wintrobe, M., Lee, G., Boggs, D., Bithell, T., Foerster, J., Athens, J. and Lukens, J. (1981), **Clinical Hematology**, 8th ed., Lea and Febiger, Philadelphia, PA.

214. Wortham, D. Tri, T. and Bowen, T. (1981), Hemodynamic Evaluation of the St. Jude Medical Valve Prosthesis in the Small Aortic Annulus, *J. Thorac. Cardiovasc. Surg.*, **81**, 615-620.

215. Wright, J. (1972), The Heart, its Valves and their Replacement, *Biomed. Eng.*, **7**, 26-33.

216. Wright, J. (1979), Hydrodynamic Evaluation of Tissue Valves, in **Tissue Heart Valves**, ed. Ionescu, M., Butterworths, Boston, MA, pp. 29-87.

217. Wright, J. (1977), *In Vitro* Comparison Between the Hydrodynamic Characteristics of the Hancock 250 (Modified Orifice) Xenografts and the Björk-Shiley Aortic Valve Prostheses, *Trans. Amer. Soc. Artif. Intern. Organs*, **23**, 89-94.

218. Wright, J. (1978), Leaflet Opening Characteristics of Tissue Valve Prostheses in Current Clinical Use, *Trans. Amer. Soc. Artif. Intern. Organs*, **24**, 537-541.

219. Wright, J. (1972), Prosthetic Heart Valves: Clinical Requirements, Design and Performance, *Biomed. Eng.*, **7**, 160-170.

220. Wright, J. and Temple, L. (1977), A Flow Visualization Study of Prosthetic Aortic and Mitral Heart Valves in a Model of the Aorta and Left Heart, *Engineering in Med.*, **6**, 31-45.

221. Wyatt, D. (1977), Theory, Design, and Use of Electromagnetic Flowmeters, in **Cardiovascular Flow Dynamics and Measurements**, eds. Hwang, N. and Normann, N., University Park Press, Baltimore, MD,pp. 89-149.

222. Yang, S., Bentivoglio, L., Maranhão, V. and Goldberg, H. (1978), **From Cardiac Catheterization Data To Hemodynamic Parameters**, F.A. Davis Co., Philadelphia, PA.

223. Yellin, E. (1966), Laminar - Turbulent Transition Process in Pulsatile Flow, *Circ. Res.*, **19**, 791-804.

224. Yellin, E. and Peskin, C. (1975), Large Amplitude Pulsatile Water Flow Across an Orifice, *J. Dyn. Syst. Meas. Contr.*, **97**, 92-95.

225. Yoganathan, A. (1978), Ph.D. Thesis, California Institute of Technology, CA.

226. Yoganathan, A., Chaux, A., Gray, R., Robertis, M. and Matloff, J. (1982), Flow Characteristics of the St. Jude Prosthetic Valve: An *In Vitro* and *In Vivo* Study, *Artificial Organs*, **6**, 288-294.

227. Yoganathan, A., Corcoran, W. and Harrison, E. (1977), *In Vitro* Measurements of Pressure Drops Across Prosthetic Aortic Valves Under Steady and Pulsatile Flow, *Proc. 30th ACEMB*, Los Angeles, CA, p. 410.

228. Yoganathan, A., Corcoran, W. and Harrison, E. (1979), *In Vitro* Velocity Measurements in the Vicinity of Aortic Prostheses, *J. Biomech.*, **12**, 135-152.

229. Yoganathan, A., Corcoran, W. and Harrison, E. (1979), Pressure Drops Across Prosthetic Aortic Heart Valves Under Steady and Pulsatile Flow - *In Vitro* Measurements, *J. Biomech.*, **12**, 153-164.

230. Yoganathan, A., Corcoran, W. and Harrison, E. (1978), Wall Shear Stress Measurements in the Near Vicinity of Prosthetic Aortic Heart Valves, *J. Bioeng.*, **2**, 369-379.

231. Yoganathan, A., Corcoran, W., Harrison, E. and Carl, J. (1978), The Björk-Shiley Aortic Prosthesis: Flow Characteristics, Thrombus Formation and Tissue Overgrowth, *Circulation*, **58**, 70-76.

232. Yoganathan, A., Corcoran, W., Harrison, E. and Carl, J. (1977), Steady-Flow *In Vitro* Velocity Measurements in the Near Vicinity of the Björk-Shiley Aortic Prosthesis, *Proc. 30th ACEMB*, Los Angeles, CA, p. 414.

233. Yoganathan, A., Reamer, H., Corcoran, W. and Harrison, E. (1980), The Björk-Shiley Aortic Prosthesis: Flow Characteristics of the Present Model vs. the Convexo-Concave Model, *Scand. J. Thorac. Cardiovasc. Surg.*, **14**, 1-5.

234. Yoganathan, A., Reamer, H., Corcoran, W., Harrison, E., Shulman, I. and Parnassus, W. (1981), The Starr-Edwards Aortic Ball Valve: Flow Characteristics, Thrombus Formation, and Tissue Overgrowth, *Artificial Organs*, **5**, 6-17.

235. Yoganathan, A., Reamer, H., Harrison, E. and Corcoran, W. (1979), Laser-Doppler Anemometer to Study Velocity Fields in the Vicinity of Prosthetic Heart Valves, *Med. Biol. Eng. Comput.*, **17**, 38-44.

236. Yoganathan, A., Woo, Y., Williams, F., Stevenson, D., Franch, R. and Harrison, E. (1983), *In Vitro* Fluid Dynamic Characteristics of Ionescu-Shiley and Carpentier-Edwards Tissue Bioprostheses, *Artificial Organs*, **7**, 459-460.

237. Young, D. and Tsai, F. (1973), Flow Characteristics in Models of Arterial Stenoses - I. Steady Flow, *J. Biomech.*, **6**, 395-410.

238. Young, D. and Tsai, F. (1973), Flow Characteristics in Models of Arterial Stenoses - II. Unsteady Flow, *J. Biomech.*, **6**, 547-559.

APPENDIX A

This appendix contains a table, Table A1, showing mean axial velocities measured downstream from the Ionescu-Shiley (25 mm) prosthesis studied in the present investigation. These velocity results were obtained at the grid points indicated in Table A1 with the data plane located at z = 31.8 mm. The measurements were made in steady flow at 27 L/min. A figure, Figure A1, is also presented which shows the spatial orientation of the velocity results in Table A1. For obtaining the velocity results, the Ionescu-Shiley valve was oriented such that the stents of the valve were aligned with the maximum of the dilatation of the sinuses of Valsalva, as indicated in the valve orientation inset. The orientation of the valve here, therefore, was rotated 60° from that for the results shown in Figures 19 through 31 of the main body of the thesis.

Table A1

Mean Axial Velocities at z = 31.8 mm for the Ionescu-Shiley (25 mm) Bioprosthesis in Steady Flow*

Data Plane Index Number	Velocity (cm/s)
6	65
12	-10
22	-23
56	-70
72	-74
82	239
150	-28
159	248
168	-6
232	221
240	228
246	62
262	120
296	37
306	19
312	-61

*Valve rotated in flow section 60° with respect to its orientation for the results shown in Figures 18 through 33.

IONESCU-SHILEY (25 mm)

MEAN AXIAL VELOCITIES

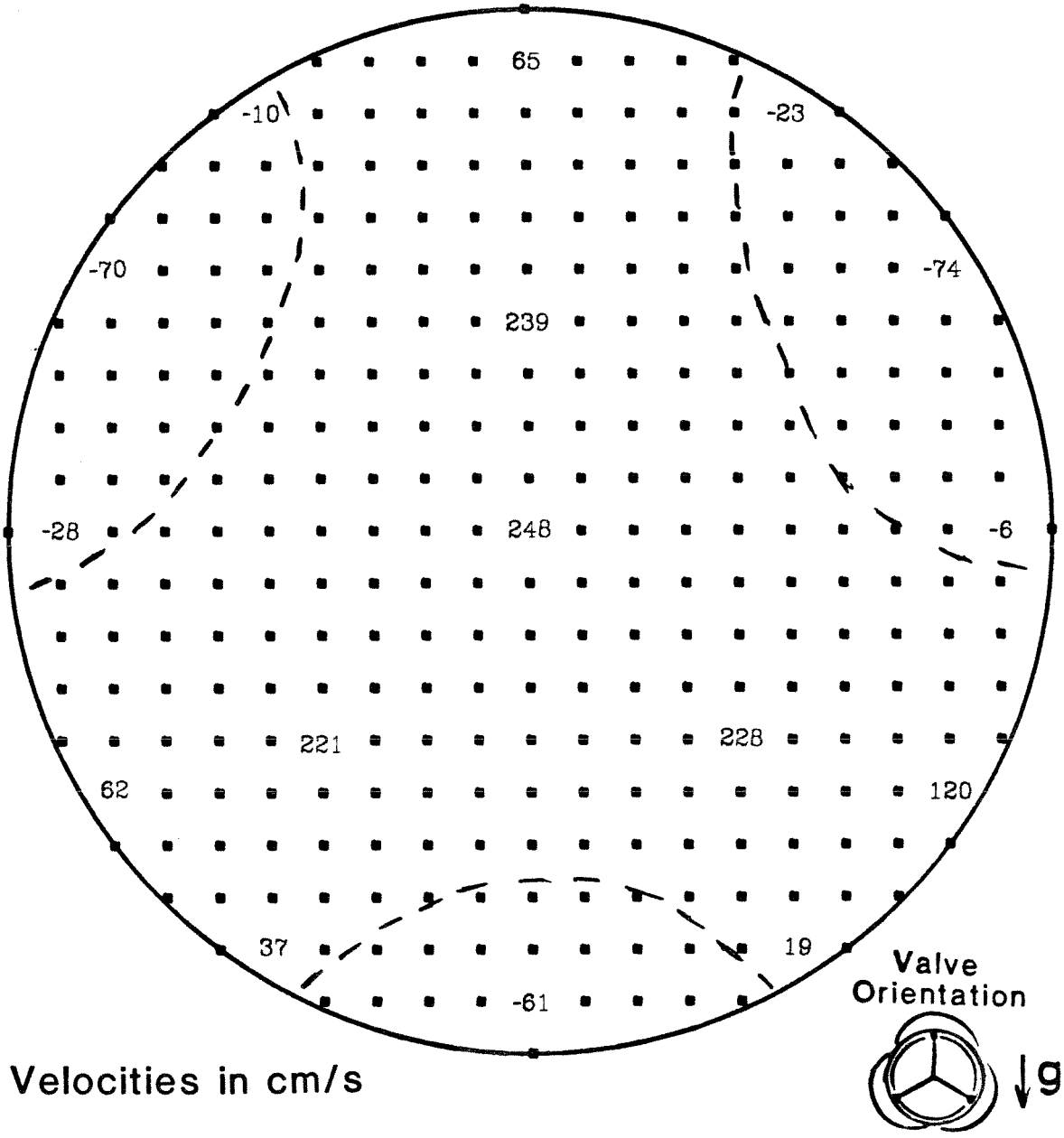

Figure A1. Mean axial velocities for steady flow downstream from the Ionescu-Shiley (25 mm) bioprosthesis at z = 31.8 mm.